ANALYSIS OF THE CORRELATION BETWEEN RE FILAMENT SURFACE FEATURES AND TIMS PERFORMANCE

THESIS

Chris J. Mihal, Major, USA

AFIT-ENP-MS-20-M-107

DEPARTMENT OF THE AIR FORCE
AIR UNIVERSITY

AIR FORCE INSTITUTE OF TECHNOLOGY

Wright-Patterson Air Force Base, Ohio

AFIT-ENP-MS-20-M-107

ANALYSIS OF THE CORRELATION BETWEEN RE FILAMENT SURFACE FEATURES AND TIMS PERFORMANCE

THESIS

Presented to the Faculty

Department of Nuclear Engineering and Physics

Graduate School of Engineering and Management

Air Force Institute of Technology

Air University

Air Education and Training Command

In Partial Fulfillment of the Requirements for the

Degree of Master of Science in Nuclear Engineering

Christopher J. Mihal, MS

Major, USA

March 2020

DISTRIBUTION STATEMENT A

APPROVED FOR PUBLIC RELEASE; DISTRIBUTION UNLIMITED

AFIT-ENP-MS-20-M-107

ANALYSIS OF THE CORRELATION BETWEEN RE FILAMENT SURFACE FEATURES AND TIMS PERFORMANCE

Christopher J. Mihal, MS

Major, USA

Committee Membership:

Dr. Abigail Bickley
Chair

Dr. Larry Burggraf
Member

Dr. Bill Johnson
Member

Dr. George Peterson
Member

AFIT-ENP-MS-20-M-107

Abstract

Thermal Ionization Mass Spectrometry (TIMS) is an invaluable tool in nuclear forensics as it enables isotopic assays of actinides to be measured, permitting analysis to include special nuclear material isotopic assays, nuclear reactor monitoring, and treaty verification. In one method of measurement for the TIMS system, samples are deposited in solution form on high-purity rhenium filaments. The filaments are heated to evaporate the solvent, and then further heated to cause sample ionization, permitting the sample to be transmitted through a magnetic field which separates ions based on mass to charge ratio into detectors for counting. Heavier ions will be deflected less by the magnetic field than lighter ions with equivalent charges.

Critical to the function of TIMS is the rhenium filaments themselves; any variability that suppresses ionization of the samples can lead to reduction in the number of ions detected. This research examines twenty-four filaments utilized in TIMS that have already been used for actinide analysis, with varying degrees of ionization efficiency. By examining the surface of the filaments using scanning electron microscopy (SEM), energy-dispersive x-ray spectroscopy (EDS), optical microscopy and electrical conductivity analysis, this research determined that there was correlation between filament shape and reported filament efficiency.

Acknowledgments

I would like to express the utmost love and appreciation to my wife and my son for being my constant sources of strength and inspiration throughout this journey. This thesis is the culmination of many hours of work on the part of many individuals, to include Dr. Abigail Bickley, Dr. George Peterson, and Major Nick Herr, among others. I also would like to thank my fellow Nuclear Engineering graduate students for making the past 18 months enlightening, entertaining, and most illuminating.

Christopher J. Mihal

Table of Contents

Page

List of Figures

Page

List of Tables

Page

List of Appendices

Page

ANALYSIS OF THE CORRELATION BETWEEN RE FILAMENT SURFACE FEATURES AND TIMS PERFORMANCE

1. Introduction

1.1 Motivation

Nuclear forensics has come to the forefront of the geopolitical sphere in recent years as monitoring of emergent nuclear nations has become of greater emphasis in the 2018 Nuclear Posture Review (NPR), whereas the previous NPR placed an emphasis on the use of improvised nuclear devices by violent extremist organizations (VEOs). [1] The ability to determine if nuclear reactors are being utilized for peaceful means, such as power generation and medical isotope production, as opposed to production of plutonium for weapons, is critical. The International Atomic Energy Agency (IAEA) retains a central role in advancing the goals of the Treaty on the Non-Proliferation of Nuclear Weapons (NPT). The IAEA does so by establishing and verifying safeguards against nuclear weapons proliferation while simultaneously furthering the safe, peaceful development of nuclear power. [2] The agency is tasked with monitoring sites in countries with nuclear capabilities, and is authorized to take samples from these sites to ensure that "each non-nuclear-weapon State Party to the Treaty undertakes not to . . . manufacture or otherwise acquire nuclear weapons or other nuclear explosive devices." [3]

A wide variety of nuclear forensics techniques exist, ranging from near-instantaneous feedback mechanisms to laboratory techniques that can take several weeks, but provide much more in-depth data. The IAEA has a suggested sequence for analysis

techniques and methods with the associated timeframe for each, demonstrated in Figure 1 below:

Techniques/Methods	24 hours	One week	Two months
Radiological	Estimated total activity Dose rate (α, β, γ, n) Surface Contamination		
Physical	Visual Inspection Radiography Photography Weight Dimensions Optical Microscopy Density	SEM/EDS XRD	TEM (EDX)
Traditional Forensic	Fingerprints, fibres		
Isotope Analysis	γ spectroscopy α spectroscopy	Mass spectrometry (SIMS, TIMS, ICP-MS)	Radiochemical separation
Elemental/Chemical		ICP-MS XRF Assay (titration, IDMS)	GC-MS

SEM/EDS: Scanning electron microanalysis with energy dispersive sensor; TEM: transmission electron microscopy; SIMS: secondary ion mass spectrometry; TIMS: thermal ionization mass spectrometry; ICP-MS inductively coupled plasma mass spectrometry; XRF: x-ray fluorescence analysis; IDMS: isotope dilution mass spectrometry; GC-MS: gas chromatography-mass spectrometry.

Figure 1. IAEA Suggested Sequence for Laboratory Techniques and Methods. [4]

This research will specifically focus on Thermal Ionization Mass Spectrometry (TIMS), a technique used for isotopic analysis of nuclear forensics samples. TIMS permits isotopic ratios of long-lived (and some relatively short-lived, such as the 14-year half-life plutonium-241) radionuclides to be measured with a precision of better than 0.01%, with sample sizes of as low as tens of femtograms. [5] TIMS with a multiple ion collector system yields the most precise isotope ratios, as low as to 0.001%. [6] [7] Samples are loaded into the TIMS system on, most commonly for uranium, filaments of

ultra-pure (99.7% or greater) rhenium. The filaments being studied were utilized in the single-filament TIMS technique, where the sample is loaded on a single filament facing the extraction voltage and the magnet. As the filament current is increased, the ion beam intensity increases, together with the evaporation and ionization of the sample. [8] Figure 2 provides an example schematic of a TIMS system.

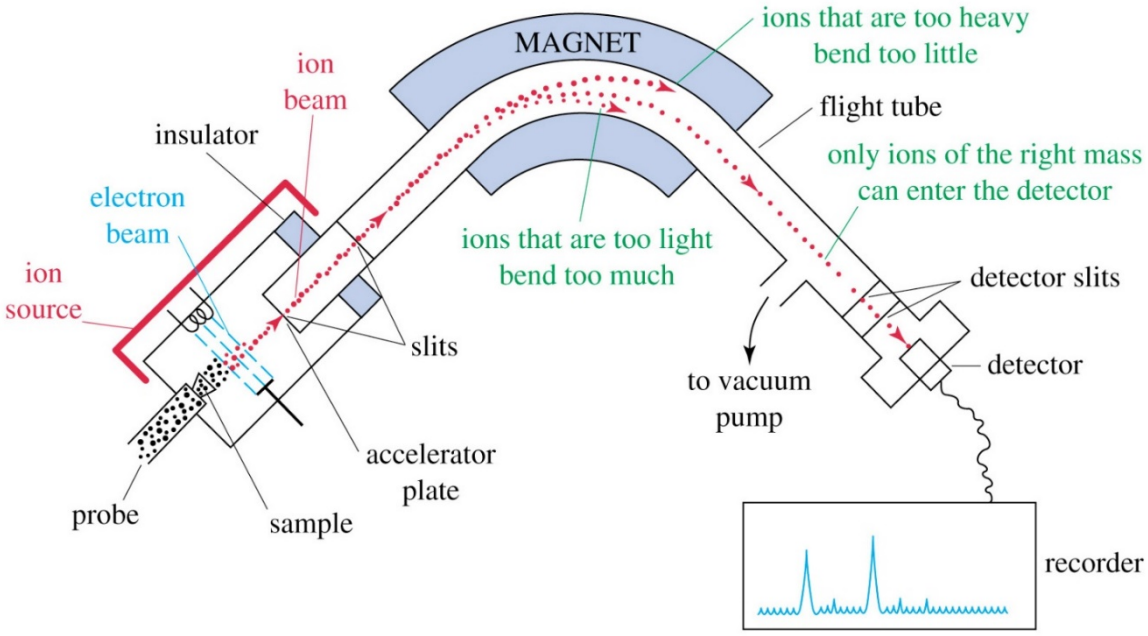

Figure 2. A schematic of a TIMS system [9]

For a mixed sample containing unknown elements with unknown isotopic ratios, individual elements will ionize at different temperatures, and ions will subsequently be separated in the electromagnetic field by their mass to charge ratio, whereupon they will be collected separately for counting.

For uranium and plutonium specifically, TIMS is extremely useful for its ability to provide accurate information on isotopic composition, which in turn aids in distinguishing between materials of different origins, as well as extrapolations on

intended use – e.g. power, weapons, etc. [10] A non-exhaustive sample of some of the relevant isotopes of uranium and plutonium are in Figure 3, along with a general idea of the isotopic ratios expected for a sample of this particular type.

[1] ISOTOPE	FRESH FUEL (LBS/1000 LBS)	SPENT FUEL (LBS/1000 LBS)
Uranium 235	37.00	7.60
Uranium 236	0.00	4.81
Uranium 238	963.00	932.50
Uranium Total	1000.00	944.91
Plutonium 238	0.00	0.21
Plutonium 239	0.00	5.72
Plutonium 240	0.00	2.62
Plutonium 241	0.00	1.60
Plutonium 242	0.00	0.68
Americium 241	0.00	0.05
Plutonium Total	0.00	10.88

Figure 3. A table showcasing some of the common U and Pu isotopes and relative amounts generated following operation of a typical U.S. power reactor. [11]

Ensuring Re filaments are manufactured, prepared, and loaded correctly is paramount for efficient sample analysis in the TIMS system and, therefore, for proper isotopic measurements for forensics analysis. Ensuring that the filaments utilized in TIMS are prepared properly, and thus ionize at maximum efficiency, is crucial to providing proper nuclear forensics analysis for isotopic composition.

1.2 Background

Efficiency in TIMS is determined by the amount of sample detected versus amount of sample loaded, and the proportionality of positive ions to neutral ions is governed by the Saha-Langmuir equation:

$$\frac{n^+}{n} \propto exp^{\left[\frac{e(W-I)}{kT}\right]} \quad \text{(Equation 1)}$$

Where n^+ is the number of evaporated ions, n is the number of evaporated neutral particles, e is the charge of an electron, 1.60 x 10^{-19} coulomb, W is the work function of the metal, I is the ionization potential, k is the Boltzmann constant, and T is the temperature. [12]

Over the last 60 years, carburized rhenium filaments have been the utilized in TIMS measurements due to their relatively large work function and high melting point. The work function is the minimum amount of energy to remove an electron from the element; it is important for filaments to have high work functions to enable the ionization of samples. A high melting point is important because of the temperatures necessary to ionize samples.

Carburized rhenium filaments have been demonstrated to achieve ionization efficiencies of approximately 1% for sample analysis since the late 1950s. [13] [14] Rhenium has an experimentally determined work function of 5.0 eV. [15] Rhenium is desirable for TIMS due to its high work function and high melting point, as well as the fact that carburized rhenium both acts as a reducing agent which decreases oxidation, and the fact that carburization increases rhenium's work function by 0.25 V, which is desirable for ionizing actinides with high ionization potentials. [12] [14] While rhenium

is resistant to forming carbides [16], it can be effectively carburized with benzene for sample preparation.

While rhenium is typically not used in high-temperature applications due to its propensity to form oxides, the high-vacuum (and subsequently low oxygen) environment produced in TIMS systems are what enable the successful use of rhenium as a thermal ionization filament for actinides. [17] While there are a wide variety of filaments currently used with TIMS, as seen in Table 1, for the purposes of this research only rhenium filaments will be examined, as they are most relevant to nuclear forensics missions. In Table I, loading methods are broken down by either single or double filament loading methods, as well as either Positive Ionizing (PI) or Negative Ionizing (NI).

Table 1. An overview of different elements and preferred loading methods in TIMS with preferred filament material. Note the single, rhenium filament preference for uranium. [9]

	PI or NI	Filament	Filament materials
Cr	PI	Single	W
Rb	PI	Double	Re–Ta
Sr	PI	Single	W
Ba	PI	Double	Re–Ta
La	PI	Single	Re
Ce	PI	Double	Re–Re
Nd	PI	Double	Re–Re
Sm	PI	Double	Re–Ta
Lu	PI	Double	Re–Ta
Re	NI	Single	Pt
Os	NI	Single	Pt
Pb	PI	Single	Re
Th	PI	Double	Re–Re
U	PI	Single	Re

While rhenium is the most effective element for loading actinides for TIMS analysis, it is not without complications. Rhenium filaments stored for 79 days or greater following carburization are subject to significant oxidation, forming numerous rhenium oxide compounds, which can then further degenerate into perrhenic acid. [17] [18] Rhenium filaments with oxidation coverage greater than 1% have been proven to lose efficiency, by up to a 20% loss when tested with plutonium. [19] Thus, the longer a filament is unused following preparation, the greater likelihood of performance degradation being introduced into the system.

Rhenium has 10 oxidation states with +7 being the most common, and can form several different oxides, most commonly Re_2O_7, but also including ReO, Re_2O, ReO_2, ReO_3, Re_2O_5, Re_2O_8, and Re_2O_{10}, among others. [20] [21] Most studies focus on the most common +7 oxidation state. This is due to the fact that most rhenium cations very easily oxidize to +7. [21]

Given the importance of the nuclear forensics mission, it is paramount to ensure the best possible data is available for analysis. Low filament efficiency increases the sample size required to determine isotopic assay. When sample sizes are very small, it is crucial to ensure the minimum amount of material is utilized to determine isotopic assay, and correspondingly, the higher ionization efficiency per filament analyzed, the better. Thus, any means by which the isotopic assay measurements can be shielded from uncertainty caused by filament variability is of extreme value.

1.3 Problem Statement

The Air Force Technical Applications Center (AFTAC) utilizes TIMS for uranium isotopic analysis. An overview of filaments previously utilized in TIMS, however, noted a wide variety in efficiencies generated by these filaments, ranging from a low of 0.23% of uranium detected in the TIMS system to a high of 1.30%. Filaments were arrayed in four boxes of six filaments each; filaments and their efficiencies are in Table 2. For the purposes of this research, filaments will be defined by the following nomenclature: The first number signifies the box the filament originated from, and the second number is its place within the box. Thus, 2-5 denotes the fifth filament from box 2.

Table 2. Filament Efficiencies and Organization

Filament	Efficiency (%)		Filament	Efficiency (%)
Box 1			**Box 3**	
1-1	1.08		3-1	0.78
1-2	1.04		3-2	0.36
1-3	1.3		3-3	0.36
1-4	0.45		3-4	0.23
1-5	0.66		3-5	0.87
1-6	0.93		3-6	0.86
Box 2			**Box 4**	
2-1	0.9		4-1	0.79
2-2	0.94		4-2	0.88
2-3	1.1		4-3	0.31
2-4	1.26		4-4	0.53
2-5	1.13		4-5	1.13
2-6	0.99		4-6	0.91

Given the generally accepted mean of 1% efficiency for rhenium filaments, AFTAC seeks to proactively identify whether high-efficiency filaments can be predicted

based on surface features visible through SEM analysis. The broad research objective for this work is defined as the ability to *detect differences in the rhenium filaments, of great enough significance, primarily through the utilization of an SEM system to correlate surface features to the reported low collection efficiencies, and potentially identify ways to increase the collection efficiency*. This research proposes to utilize a variety of means to examine the filaments, including SEM and its attached EDS system for both imaging analysis and elemental composition analysis, respectively. Additional analyses included electroconductivity testing and optical microscopy. Data collected will undergo statistical analysis to correlate observed surface features with measured filament efficiency. Statistical analysis will also provide a confidence interval to determine if the sample of filaments provided is likely to be representative of the entire population of filaments used by AFTAC, and the probability of this subset of 24 filaments being an outlier for the population as a whole.

1.4 Questions and Hypothesis

The research questions and hypotheses associated with the problems outlined in Section 1.3 are detailed below. They are organized by the problem and capability that they support.

1. SEM analysis – are there noticeable differences in appearance/grain orientation/morphology between efficient and inefficient filaments? Are there other identifiable structural trends in efficient or inefficient filaments?

2. EDS analysis – are there any elemental composition differences in efficient and inefficient filaments? What are these differences and how might they impact efficiency?
3. Electroconductivity analysis – is there a difference in electrical conductivity between efficient and inefficient filaments? Do these results line up with hypothesized differences in the previous SEM and EDS analysis?
4. Optical microscopy analysis – are filament defects identified in the SEM imagery optically visible, or are they artifacts of SEM imaging – contrast due to differences in atomic number, orientation, etc? Are there holes through the entire depth of the filament that the SEM cannot detect?
5. Statistical analysis – can identifiable surface features correlate with filament efficiency? Is this sample representative of the overall rhenium filament population, or likely to be an outlier? What statistical trends, if any, are in the data?

Hypothesis: the filaments are representative of the filament population at AFTAC, and there are factors that are decreasing filament efficiency, due to sources external to the filaments themselves, but resultant from filament preparation or storage. These factors manifest as identifiable surface features.

1.5 Assumptions and Limitations

There are numerous assumptions associated with this project. The first is to assume that all of the filaments are manufactured and drawn from the same source. A further assumption is that the filaments were carefully handled post-usage and placed

directly into a clean storage container; that there were no outside contaminants introduced between being taken out of the TIMS and being placed in the box. Also, due to the extremely long half-life, this project assumes that rhenium decay into osmium is negligible.

The primary limitation is the number of filaments available for study. As with any statistical analysis, more data points are always better. The exact process for preparing each individual filament for loading into TIMS, while known, has not been observed by the researcher and so cannot be completely verified for consistency. There may be minor differences in what has been described versus reality in terms of the exact steps in the process and how much variance each step could possibly introduce in the filaments.

1.6 Approach

This research proposes multiple means to determine if there is a correlation in identifiable surface features with disparity in filament efficiency. The SEM will provide an accurate picture of the shape, grain orientation, and the number of surface material defects present per filament. Further analysis utilizing ImageJ and Gwyddion will permit measuring the length of cracks and defects, percentage of the filament covered by foreign material, and accurate measuring of the shape and curve of the filament depressions where the actinide solution is deposited.

Concurrent to SEM imaging is the EDS analysis of filaments. The EDS, which is attached to the SEM, will permit elemental composition analysis of filaments by measuring characteristic x-rays emitted by the sample. This will generate a spectrum

which will give a measurement of the composition of the filament and any foreign material deposited or remaining on the filament.

Other techniques will confirm if the surface features noted via the SEM correlate to efficiency. Electroconductivity analysis will demonstrate if filaments with excess material defects, opacity, or holes are poor conductors compared to clean filaments. Optical microscopy will provide better fidelity on surface features and if they are SEM artifacts or are visible.

2. Theory

2.1 Characteristics of Rhenium

Rhenium is one of the 35 elements critical to U.S. National Security outlined in the Department of the Interior Final List of Critical Minerals 2018, [22] with national supply estimated to last for approximately 40 years before exhaustion at current consumption levels. [23] Rhenium is a transition metal, atomic number 75, with most common isotopes being Re-185, which is stable, and Re-187, with a half-life of 4.12 x 10^{10} years. Unusually, Re-187 is more prevalent in nature than the stable Re-185 isotope, with natural rhenium consisting of 37.4% Re-185 and 62.6% Re-187. Natural rhenium exists at a concentration of about 0.001 parts per million in the Earth's crust. [24]

2.1.1. Physical Characteristics of Rhenium

Rhenium does not have a ductile-to-brittle transition temperature, which means that it retains its ductility from low subzero temperatures to very high temperatures – useful in areas as varied as mass spectroscopy and space travel. [25] Its rarity, combined with myriad uses in jet turbine engines, nuclear forensics, and even lead-free gasoline, make efficient and effective use of rhenium supplies critical. [23] When heated, rhenium, like many other metals, emits positive ions of the alkali metals, with a work function of 5.0 eV. [26] The thermal conductivity of rhenium is 71.2 W/m K at 20 °C. [27] [28]

Rhenium metal typically has a close-packed hexagonal crystalline structure, although cubic structures have been hypothesized. Rhenium oxide is a polytype, with

crystalline forms including cubic, hexagonal, tetragonal, rhombohedral, orthorhombic and monoclinic. [29]

2.1.2. Rhenium Oxidation States and Oxides

Rhenium has an extremely high melting point at 3,180 °C, the third highest of any element after carbon and tungsten, as well as a vaporization temperature of 5,597 °C making it ideal for TIMS analysis where vaporization temperatures for elemental uranium and plutonium are 3,818 °C and 3,228 °C, respectively (all temperatures at standard pressure, 1 atm). However, Re_2O_7, the most common rhenium oxide, has a melting point of only 225 °C and, more importantly, sublimates at approximately 400 °C, making its presence undesirable in large amounts. [27] [29] The presence of rhenium oxide on the surface also causes changes in the structure of the rhenium underneath the rhenium oxide, as well as altering its oxidation state. There has been little research into this due to the difficulties inherent in the analysis and the relative scarcity of rhenium.

How rhenium is stored can affect oxidation rates of the material. Rhenium filaments stored in humid conditions – simulated by a NaCl salt bath for experimental purposes – had 34 times more oxidation than filaments stored in dry conditions, and the oxidation crystallites were up to 12 times larger. [17] Regardless, lengthy storage periods following carburization can still lead to a significant buildup of oxidized rhenium, with grain orientation playing a predominant role in oxidation.

With Re_2O_7 on the surface, buried layers of sub-oxides that contain Re^{4+}, Re^{2+} and $Re^{\delta+}$ ($\delta \sim 1$) occur at the interface between Re_2O_7 and pure Re. Re_2O_7 sublimes at a very low temperature (approximately 400 °C), while the Re^{4+}, Re^{2+} and $Re^{\delta+}$ species

remain stable in oxidizing conditions up to at least 450 °C. [30] The presence of these various oxide species noticeably reduce the ability of rhenium to withstand temperature increases, which may reduce the ability of the rhenium filament to vaporize and ionize samples. An example of how potential oxidation appears in an SEM image is given in Figure 4.

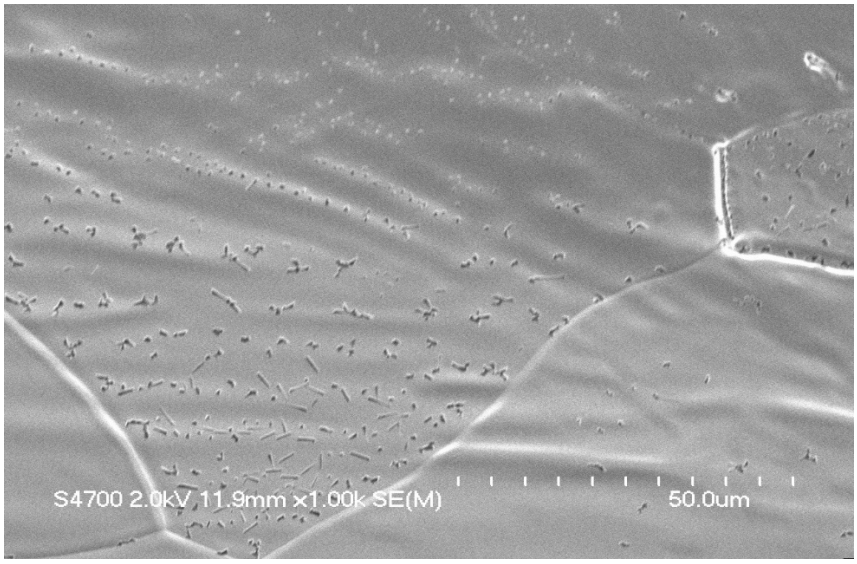

Figure 4. A rhenium grain hypothesized to contain significant oxidation (denoted by black spots); some of the oxidation has begun to spread to the adjacent grain, bottom right.

2.1.3. Rhenium Filament Fabrication

Prior to use in TIMS, the rhenium filaments used in this research underwent two stages of carburization. Carburization is the process of adding carbon to the rhenium filaments. Carbon atoms intersperse within the metallic crystalline structure of rhenium; this has been shown to alter rhenium's work function, [15] and, more importantly, to act as a reducing agent, which also has been shown to increase overall ionization efficiency by preventing the formation of uranium oxide compounds. Pallmer et al. have

demonstrated that proper carburization will increase rhenium's work function by 0.25V, and via Auger depth profiling showed that the surface carbon sits in solution in the rhenium. They also demonstrated that improper carburization will result in a graphitic carbon layer that sits on top of the rhenium, along with lowering the work function to as low as 4.1 eV, which is highly undesirable for ionization efficiency. [15] Some research has shown that uranium carbides form more readily at the temperatures TIMS operates, but uranium carbides are not typically found in the TIMS system at all. [31] Carburization decreases oxide formation in rhenium metal and carburized rhenium thus has a higher ionization efficiency. [16] [32]

Rhenium cannot be hot-worked (hardened at high temperature), but must be worked at room temperature with frequent annealing. [33] For AFTAC's specific process, the rhenium filament must first be cut. Re ribbon currently available to AFTAC was fabricated by the H-Cross Company but at an improper length for TIMS, and so the ribbon is cut to the appropriate length to fit into the filament posts. The filaments are subsequently loaded into a stamping machine, which creates a depression in the filament for the sample solution to be deposited. Following shaping, the filaments are spot-welded onto tantalum posts and placed into a mounting shield. After formation and mounting, the filaments are carburized for the first time. After the first carburization the sample is loaded. In the case of the filaments for this research, the sample was CRM 129-A, uranium oxide in the U_3O_8 form (see Appendix 1 for CRM 129-A specifications) dissolved in nitric acid. The filament is then very gently heated to vaporize the solution while retaining the solute on the filament. The filaments are then carburized a second

time. Filaments are finally degassed, which cleans filaments and removes external contaminants, but can alter grain structure (due to recrystallization after exposure to high heat) and can volatize any existing rhenium oxide compounds. [34] The filaments are loaded into TIMS and are used only once before being discarded.

2.1.4 Rhenium Filament Carburization

As referenced in Equation 1, the Saha-Langmuir equation states that the proportion of positively charged ions to neutral ions emitted from a heated filament is proportional to $exp^{\left[\frac{e(W-I)}{kT}\right]}$ where e is the charge of an electron, 1.60×10^{-19} coulomb, W is the work function of the metal filament, I is the ionization potential of the sample – for uranium, the first ionization energy is 6.19405 eV [15] – k is the Boltzmann constant, 1.3807×10^{-23} $J \cdot K^{-1}$, and T is the temperature in kelvin. The ratio between positive and neutral ions is important, as TIMS detectors cannot detect neutral ions.

Table 3 illustrates a number of potential metals for filament fabrication along with their work functions and melting points. To promote the generation of positive ions, (W-I) must be positive. Therefore, the filament material chosen must have the highest possible work function. Additionally, given the temperatures at which uranium begins to ionize, the filament material also must have a high melting point. Note that the value for rhenium's work function in Table 3 is slightly higher than has been experimentally determined; work function calculations have provided a range of work function values ranging from 4.96 to 5.4 for pure rhenium, though experimental results have yielded a value of 5.0. [15] [35] [36]

Table 3. Work function and melting points of filament materials. [15]

Table 17.1 Work function and melting point of filament materials

Metal	Work function (V)	Melting point (°C)
Nickel	5.03	1453
Niobium	4.0	2468
Rhodium	4.80	1966
Palladium	4.99	1552
Tantalum	4.19	2996
Tungsten	4.52	3410
Rhenium	5.1	3180
Platinum	5.32	1772

Given that rhenium has both a high work function and a high melting point, it is the ideal candidate for ionizing uranium. However, it should be noted that all of these work functions are lower than uranium's first ionization potential, and thus there will be only a small ratio of positive to neutral ions.

Pallmer et. al demonstrated that proper carburization increases rhenium's work function by 0.25V, but carburization's main benefit is to introduce carbon to act as a reducing agent to prevent the formation of uranium oxides in the sample, whose formation would negatively affect ionization collection efficiency. It is preferable to do a uranium isotopic analysis on pure uranium ions rather than uranium oxide, to avoid complications from isotopes of oxygen. [37] Oxide reduction is also beneficial due to the fact that the oxide ReO_3^+ has an atomic mass of 235, the same as U-235, and thus may interfere with isotopic analysis. [38] Furthermore, as TIMS is tuned to detect certain mass/charge ratios, a TIMS system may not be calibrated for the extra weight of oxide species, and so those might also be lost in collection. Thus, the more uranium oxide in a

sample, the lower the collection efficiency; to prevent this, a reducing agent can be added.

Carburization's role as a reducing agent was demonstrated by Studier et. al. by selectively controlling benzene vapors and an oxygen leak to the TIMS chamber. [37] When benzene vapors were directed at the rhenium filament, or carbon in the form of sucrose was added to the filament, the uranium sample was reduced, and only metal U^+ ions were observed. When an oxygen leak was created, a combination of U^+, UO_2^+, and UO_3^+ ions were observed. Studier et. al. also speculated that up to 90% of the sample may be lost before the filament reaches maximum temperatures for metal ion emission. Maintaining a reducing chemical environment for both the rhenium filament and the uranium sample will keep their sublimation and boiling point temperatures higher, helping reduce some of that initial loss while ramping the filament temperature to maximum ionization temperatures. [37] Carburization is the most effective means of maintaining a reducing chemical environment for rhenium filaments.

2.2 Scanning Electron Microscopy (SEM)

This research uses a Hitachi S-4700 Field Emission Scanning Electron Microscope, an example of which can be seen in Figure 5. An SEM consists of an electron gun – in the case of this particular S-4700 utilized in the experiment, a LaB_6 cold field-emission tip, with a radius of approximately 30-50 Å - which accelerates electrons down a column using multiple focal and converging lenses. These lenses concentrate the electrons into a single point on a sample. As the electrons interact with the sample, they scatter both elastically and inelastically, and can generate several relevant species of

electrons – secondary electrons (SEs) and backscattered electrons (BSEs), both of which can be collected by different types of detectors for analysis. For BSEs, the S-4700 uses an Yttrium-Aluminum-Garnet detector, which must be separately connected to the system for operation; the default state for the S-4700 is to detect SEs only.

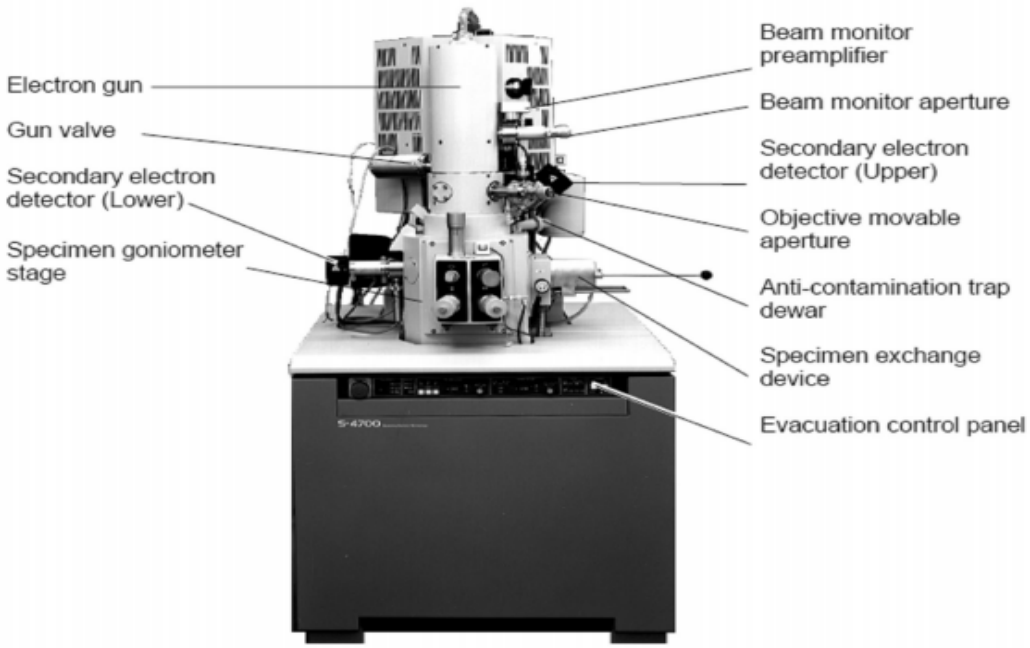

Figure 5. The Hitachi S-4700 SEM utilized in this research, with major parts delineated. [39]

SEM images are typically greyscale, with color differences due to a variety of contrast factors, including topographic and compositional contrast. Topographic contrast occurs due to different amounts of SEs and BSEs being emitted from different parts of the sample geometry; areas where more electrons are emitted, such as sharp corners, will appear significantly brighter on the image. An example of topographic contrast is Figure 6, where the edge of the filament is much lighter in tone than the rest of the filament as secondary electrons are emitted in many different directions and have more possible

means of escape than SEs generated in the center of the filament. This is also partially due to the geometry of the sample, where the filament edge is directly facing the detector.

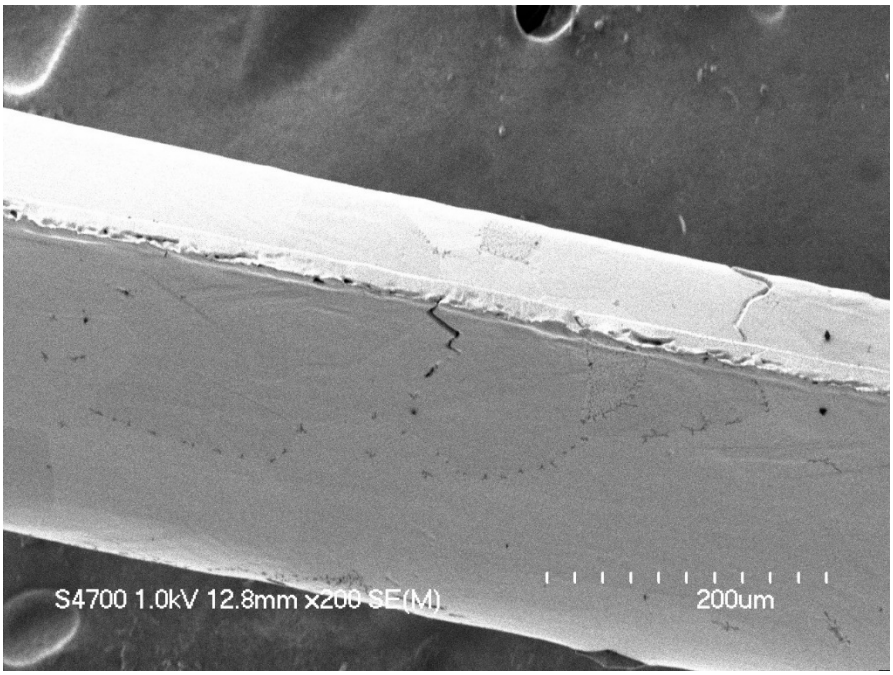

Figure 6. An example of topographic contrast on filament 3-4.

Compositional contrast is also determined by atomic makeup of the sample; areas of the sample dominated by higher-Z materials will be lighter-colored than low-Z materials, which will be significantly darker in tone. Figure 7 demonstrates compositional contrast.

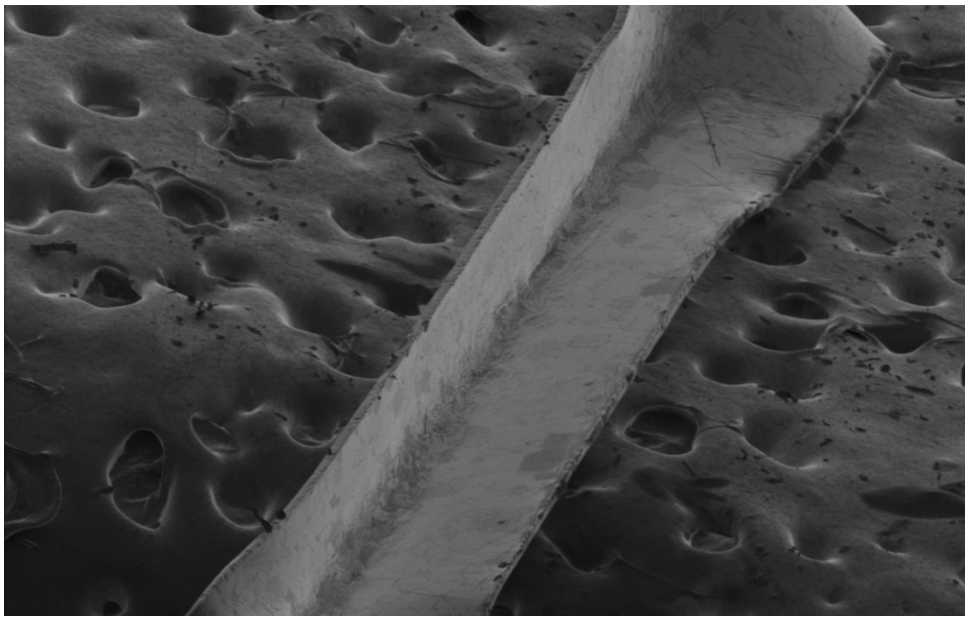

Figure 7. An example of compositional contrast. The rhenium filament in the center is lighter than the surrounding carbon tape, which appears almost black.

To operate the SEM, first a potential difference is generated between the first anode and the lanthanum boride (LaB_6) tip to generate an electric field, causing electron emission down the column towards the specimen. Accelerating voltage (V_0) is determined by the potential difference between the tip and the anode; the higher the V_0, the faster the electrons travel down the column, and subsequently the greater the penetrating power. Electrons pass through several apertures with staggered converging and focal lenses to minimize the size of the beam current. A smaller beam provides greater resolution and focus; widely scattered electron beams produce poor imaging and are undesirable. Higher beam energies improve the visibility of low-contrast objects, but may reduce visibility of surface topology, as the mean free path of the electrons becomes significantly longer, causing them to generate SEs below the surface of the sample rather

than on the surface itself. [40] Higher beam energies can also potentially damage a sample via excess charge build up.

The distance an electron can travel through a medium is dictated by the number of times the electron undergoes inelastic scattering, and is dictated by the Bethe equation:

$$\frac{dE}{ds}\left(\frac{eV}{nm}\right) = -7.85\left(\frac{Z\rho}{AE}\right)\ln\left(\frac{1.166E}{J}\right) \quad \text{(Equation 2)}$$

where E is the beam energy in keV, Z is the atomic number of the target material, ρ is the target density in g/cm^3, A is the atomic weight in g/mol and J is the mean ionization potential, given by:

$$J\,(keV) = (9.76Z + 58.5Z^{-0.19})x10^{-3} \quad \text{(Equation 3)}$$

For the Bethe equation, dE/ds gives the energy lost per nanometer of material for an electron transiting through a sample. [41] A plot of the Bethe equation for rhenium with electron energies varying from 5 to 30 keV is below in Figure 8; code associated with generating this graph is in Appendix 2:

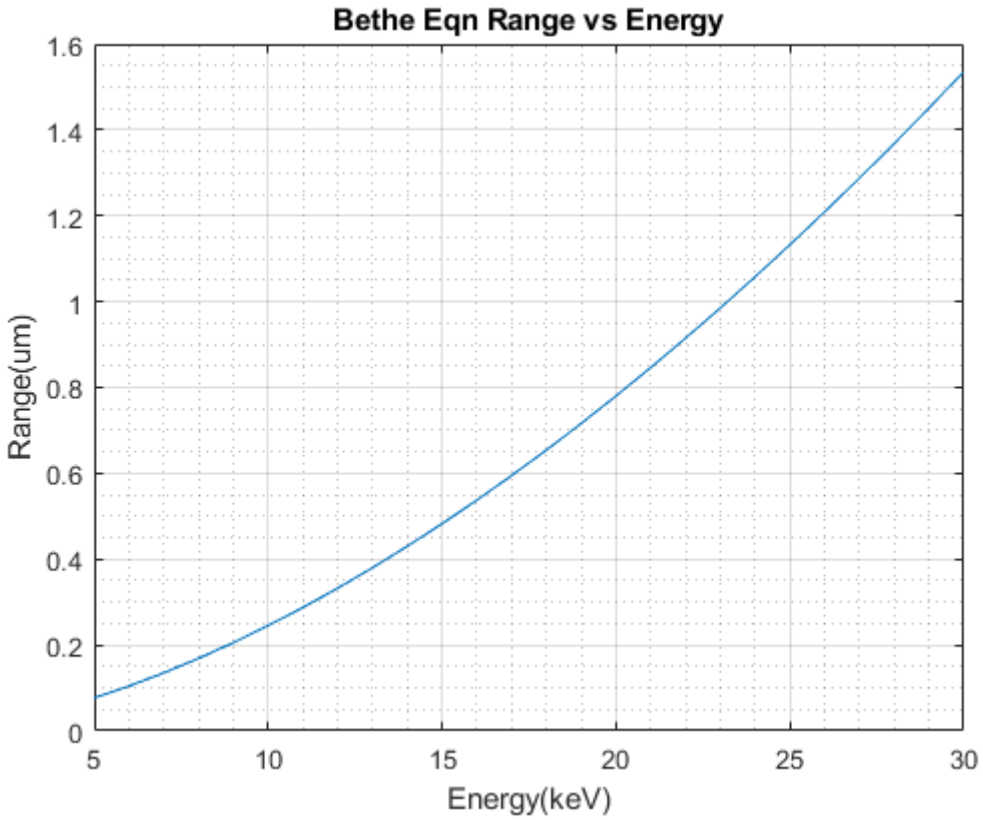

Figure 8. Plot of the Bethe range of electrons in rhenium by energy

This equation governs energy loss for electrons with >5 keV energy; below 5 keV there are a number of approximations for the function as it breaks down at that point, including Joy and Luo, Rao-Sahib and Wittry, and Tung, among other equations. [42] Integrating the expression gives the "Bethe range" of the electron in the medium. It is important to note that electrons can also undergo elastic scattering, where no energy is lost with deflections of the incident electron up to 180 degrees occurring. This can cause the electron to deviate out of the narrow angular range of incident trajectory. Elastic scattering is governed by the following equation, which is heavily dependent on target Z:

$$Q_{elastic} == 1.62X10^{-20} * (\frac{Z^2}{E^2}) * cot^2(\phi_0) \qquad \text{(Equation 4)}$$

where ϕ_0 is a threshold elastic scattering angle. Some sample electron trajectories in different media are modelled in Section 3.1.2 of this document.

The S-4700 is categorized as a cold field emission gun (FEG). In cold FEGs, it is essential that the tip remain free of contaminants, and so Ultra High Vacuum conditions (10^{-10} to 10^{-11} Torr) are required. The electric field produced by the extraction voltage lowers the work function barrier and allows electrons to directly tunnel through it - thus facilitating emission. Cold FEGs must have their tip flashed, or briefly heated periodically to clean the tip for optimal function. [43] It is worthwhile to note that the incident electron beam is capable of charging nonconductive samples. This charging results in decreased image resolution and a noticeable change in the color of the conductive sample; the sample will get substantially whiter the longer the electron beam is focused on it. The only means by which to avoid charging of nonconductive samples is to coat them in some form of metal, such as a chromium mesh or gold foil, which was not done for this experiment. Figure 9 demonstrates charging due to the electron beam interacting with a conductive material. The material to the right of the image is low-Z and typically dark. However, due to the presence of additional unknown material, it is highly non-conductive, and one can see it beginning to whiten significantly, particularly in the center. This is evidence of the buildup of electrons which have no means of escape.

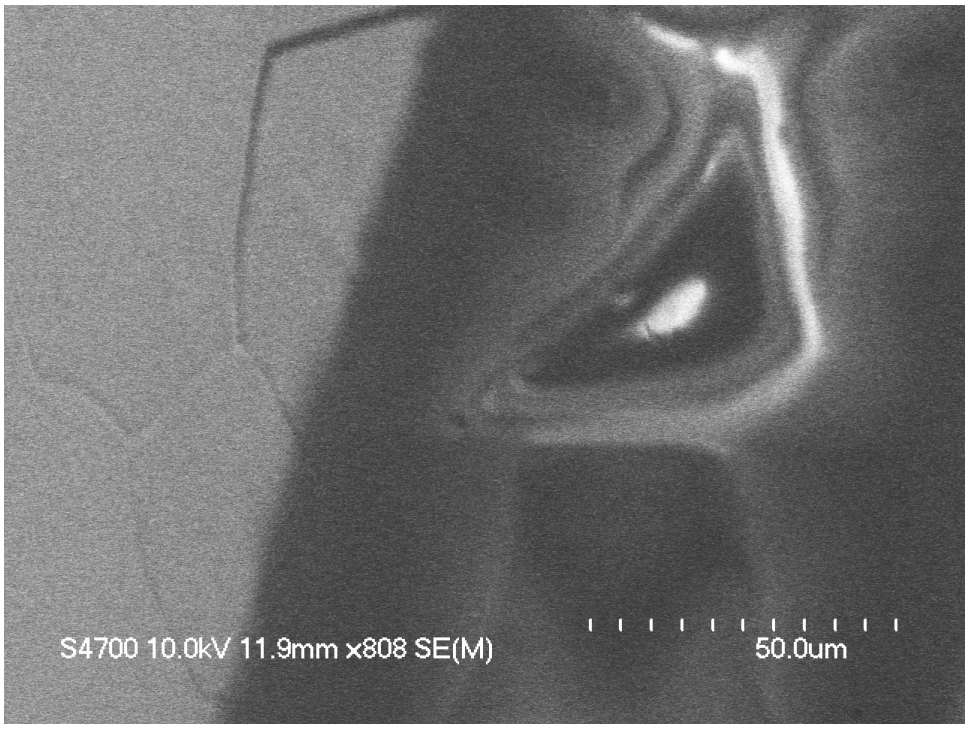

Figure 9. An example of the charging phenomenon.

2.2.1 Secondary Electron Images

SEs are created when inelastic scattering of the beam electrons eject weakly bound valence electrons or conduction band electrons with binding energies of 1-15 eV. By definition, SEs have an energy of less than 50 eV. [43] SEs have extremely low kinetic energy, and thus only a small fraction can escape the sample to be collected by the detector. The lower the beam energy, the greater the SE generation, as the lower mean free path of the electron means there are more SEs generated near the surface of the sample, and thus more can escape. SE generation can be improved by specimen tilt, as this increases the surface area for SEs to escape the sample.

There are three categories of SEs, SE_1, SE_2, and SE_3. Electrons in category SE_1 are generated within the footprint of the incident electron beam from the SEM. These

have a high lateral resolution signal due to proximity to the electron beam. Electrons in category SE_2 are generated by electrons traveling into the sample and backscattering out via inelastic scattering which ejects weakly-bound electrons from the sample. Electrons in category SE_3 are generated when BSEs or SE_2s interact with the chamber walls of the SEM and eject an electron from the SEM itself. The details of the SE image are dependent on the formation of these categories of SE. [41] For low Z materials, SE_1 is dominant as there are very few BSEs produced in low Z materials.

Secondary electron production is less dependent on Z than BSE production, and so provides greater contrast on the surface of materials. As SEs are primarily produced near the surface, they can provide much greater contrast in sample topography compared to BSEs.

2.2.2 Backscattered Electron Images

BSEs are generated by electrons scattering within the sample and then escaping. Due to the probabilistic nature of inelastic scattering, some BSEs will have energies almost equivalent to the incident electron beam energy and some will have the minimum BSE energy, which is defined as 50 eV. However, most BSEs will have approximately 50% of the incident beam energy. [43] BSE production is highly dependent on the atomic number of the sample material; higher Z elements produce significantly greater quantities of BSEs, as there are substantially more electrons in the material for beam electrons to interact with and eject. Thus, BSE images are preferential for demonstrating elemental contrast in images. Both BSEs and SEs have their uses in this experiment.

2.3 Energy-Dispersive X-ray Spectroscopy (EDS)

Energy-dispersive x-ray spectroscopy (EDS) utilizes a semiconductor detector which photoelectrically absorbs x-rays emitted by the sample material after interaction with the electron beam of the SEM. The photon's entire energy is transferred to a bound inner-shell electron of the lithium-drifted silicon detector, which is ejected with a kinetic energy equal to the photon minus the shell ionization energy. As the ejected electron inelastically scatters in the silicon crystal, it moves valence electrons into the conduction band of the semiconductor, leaving positively-charged holes. Electrons collect in the anode; this charge generation requires 3.6 eV per electron hole pair. The original photon energy is determined by the charge deposited in the detector via this mechanism. [43] EDS detectors can detect x-rays with energies ranging from 50 eV to 30 keV.

EDS measures the characteristic x-rays emitted when beam electrons interact with the sample. Characteristic x-rays are emitted when electrons transition between energy levels. The most common and relevant characteristic x-rays for this experiment are below in Table 4:

Table 4: Characteristic X-ray energies for the three most commonly expected elements present on rhenium filament. [44]

Energy (KeV)	Emission	Element
0.282	Kα-Wtd. A	C (Carbon) 6
0.282	Kα1	C (Carbon) 6
0.282	Kα2	C (Carbon) 6
0.283	Kab	C (Carbon) 6
0.523	Kα-Wtd. A	O (Oxygen) 8
0.523	Kα1	O (Oxygen) 8
0.523	Kα2	O (Oxygen) 8
0.531	Kab	O (Oxygen) 8
1.842	Mα1	Re (Rhenium) 75
8.586	Lα2	Re (Rhenium) 75
8.653	Lα1	Re (Rhenium) 75
10.010	Lβ1	Re (Rhenium) 75
10.275	Lβ2	Re (Rhenium) 75
11.685	Lγ1	Re (Rhenium) 75
59.718	Kα2	Re (Rhenium) 75
61.140	Kα1	Re (Rhenium) 75
69.310	Kβ1	Re (Rhenium) 75

Note that Table 4 is not exhaustive and includes only the most commonly detected characteristic x-rays; NIST has a comprehensive list of all characteristic x-rays for all elements, which includes 53 total characteristic x-rays for rhenium. [45]

It is important to note that, for EDS to effectively collect and produce spectra, that the SEM beam energy should be approximately twice the energy of the highest-energy x-ray being detected. This is to maximize the number of characteristic x-rays collected. If the incident electron beam is at exactly the energy required to emit a characteristic x-ray, any inelastically scattered electrons will not have enough energy to produce a characteristic x-ray. Doubling the beam energy allows greater depth of penetration into the material, thus more characteristic x-rays emitted, and subsequently a higher confidence in the EDS spectrum.

Higher beam energy must be balanced against dead time, however. Dead time occurs when an x-ray interacts with the detector while the detector is still processing the

previous x-ray; the second x-ray is thus not counted. Lower beam energies produce fewer x-rays and so dead time is often not a factor, but higher beam energies can produce x-ray fluxes that overwhelm the detector and lead to higher amounts of dead time. [46] For this reason, double the beam energy is generally the best compromise between dead time and confidence. Given the limitation that the SEM in use has a maximum beam energy of 30 keV, it is difficult to confidently analyze the data from the EDS to detect characteristic x-rays significantly above approximately 15 keV.

EDS requires some interpretation to maximize functionality, as many characteristic x-rays are extremely close in energy values. The software which interprets EDS data is known as INCA. While INCA generates most probable elements to match an x-ray spectrum, such estimates must be carefully analyzed by the user. The EDS is also prone to several error-induced artifacts, including peak broadening, escape peaks, and coincidence peaks.

Peak broadening is due to natural statistical fluctuations and ever-present bremsstrahlung radiation, compounded by the resolution of the EDS. EDS resolution can broaden x-ray peaks by a factor of 20 or more; this is particularly deleterious when x-ray peaks of different elements in the sample are close in energy range. These are referred to as mutually interfering peaks and can lead to significant loss of fidelity if not accounted for. Mutually interfering peaks are especially common for elements with atomic numbers above 20 due to their complex x-ray spectra. [41]

Escape peak artifacts are caused by the silicon in the detector generating its own x-ray after absorbing the sample x-ray and thus “robbing” incident photons of the energy

required to generate an x-ray. This additionally generated x-ray will cause a peak exactly 1.74 keV less than the elemental characteristic x-ray peak expected from the sample. Si escape peaks are frequently mislabeled as trace elements.

The final EDS artifact to account for is a coincidence peak, also known as a sum peak. Coincidence peaks occur when the detector is processing one photon and a second photon enters the detector during the measurement period. While in other types of instruments the second photon would be lost due to dead time, in EDS the energy of the second photon is added to the energy of the first, causing a peak to appear at the sum of their energies. For instance, if two Si x-rays entered the detector at approximately the same time, instead of 2 counts at 1.74 keV as expected, the EDS would generate one count at 3.48 keV. Most EDS software has some built-in functionality to account for and eliminate coincidence peaks, but they are a factor to be aware of.

2.4 Statistical Analysis

In this experiment, statistical analysis will focus on determining if the surface features identified have any correlation with the ionization efficiency values given for the filaments. This will primarily be accomplished using design of experiments models, including the factorial and response surface designs. Both designs rely on the data being approximately normally distributed, and use linear algebraic models to estimate the effects of factors on the response.

Design of Experiments (DoE) is a methodology by which data is made to fit linear or quadratic models to permit holistic analysis of the data. DoE is most useful in that it allows multiple variables (known as factors) to be evaluated simultaneously rather than

one at a time. DoE also permits one to observe the interplay between multiple factors and determine which factors, and which interplays of factors, directly affect the outcome of the model.

Design of experiments is typically done beforehand to maximize outputs – that is, to find a model that maximizes the response, and to thus perform an experiment that produces optimal results. They are designed to maximize efficiency prior to use. These models can also be used to evaluate data from an already-conducted experiment, which is what was done for this experiment. Both designs will produce an equation which shows how the response relates to the variables.

2.4.1 Factorial Design

Factorial designs are named because they evaluate a number of factors. Generally speaking, factorial designs are the most efficient type of design of experiments models for a linear model of a multi-factor experiment. [47] For a factorial design, the variables being evaluated are known as factors, and the quantity being measured is known as the response. Factorial designs are useful not just because they can simultaneously evaluate several factors, but they are also capable of evaluating the interaction between factors. Factors are ordered alphabetically, so a three-factor design would have factors A, B, and C, and interactions AB, AC, BC, and ABC, as an example.

Factorial designs calculate the average effect of a factor by evaluating the change in the response produced by a change in the factor. Factorial designs also model the effect of interactions. For example, interaction AB is the average difference of the effect of A at the high level of B and the average effect of B at the high level of A.

The model used for linear analysis is a resolution IV factorial design. The design seeks to solve the equation found below, where E = efficiency:

$$E = \beta_0 + \beta_1 X_1 + \beta_2 X_2 + \beta_3 X_3 + \beta_4 X_4 + \beta_{12} X_1 X_2 + \beta_{13} X_1 X_3 + \beta_{14} X_1 X_4 + \beta_{23} X_2 X_3 + \beta_{24} X_2 X_4 + \beta_{34} X_3 X_4 + \beta_{123} X_1 X_2 X_3 + \beta_{124} X_1 X_2 X_4 + \beta_{134} X_1 X_3 X_4 + \beta_{234} X_2 X_3 X_4 + \beta_{1234} X_1 X_2 X_3 X_4 + \varepsilon \quad \text{(Equation 5)}$$

where all of the β terms are the amount that the factors affect the model, all of the X terms are the factor data, and ε is the error, with Expected Value E(ε) = 0 and Standard Deviation $V(\varepsilon) = \sigma^2 I$, where I is the identity matrix.

Factorial designs are linear models. If the data is not best modelled linearly, a factorial design will not adequately estimate or analyze the data. In the event that a quadratic or polynomial model is required, a response surface design is instead a better model.

2.4.2 Response Surface Design

The response surface design performs a least-squares fit of data to produce a "fitted surface" that approximates the data input. The response surface analysis is then performed using the fitted surface. If the fitted surface is an adequate representation of the true response function – the function that correlates the factors with the response – then analysis of the fitted surface is approximately equivalent to an analysis of the raw data.

The response surface design can do first order – that is, linear – modelling, or higher order – quadratic and polynomial – modelling. [47] It is worthwhile to note that

quadratic models lose some of the fidelity of linear models as they adjust the curves, and also lose some degrees of freedom for error to model squared terms. The equation the response surface design solves for is as follows:

$$E = \beta_0 + \beta_1 X_1 + \beta_2 X_2 + \ldots + \beta_{11} X_1^2 + \beta_{22} X_2^2 + \ldots \beta_{12} X_1 X_2 + \ldots$$

$$+\varepsilon \qquad \text{(Equation 6)}$$

3. Methodology

3.1 Physical Set-Up of SEM

The SEM used for this research depicted in Figure 10 is a Hitachi Model S-4700, with the INCA Analyzer for EDS software. Both systems are linked, and the Hitachi is capable of generating secondary electron (SE) images and backscattered electron (BSE) images.

Figure 10. The SEM, EDS and accompanying computers used for the experiment.

Samples are kept in designated sample holding areas, separated into four boxes of six filaments each. Filaments were analyzed individually, mounted on circular mounting rings for loading into the SEM, as seen in Figure 11. Images are taken at a variety of beam energies, working distances, and to varying degrees of tilt to get a comprehensive set of images for each of the 24 filaments.

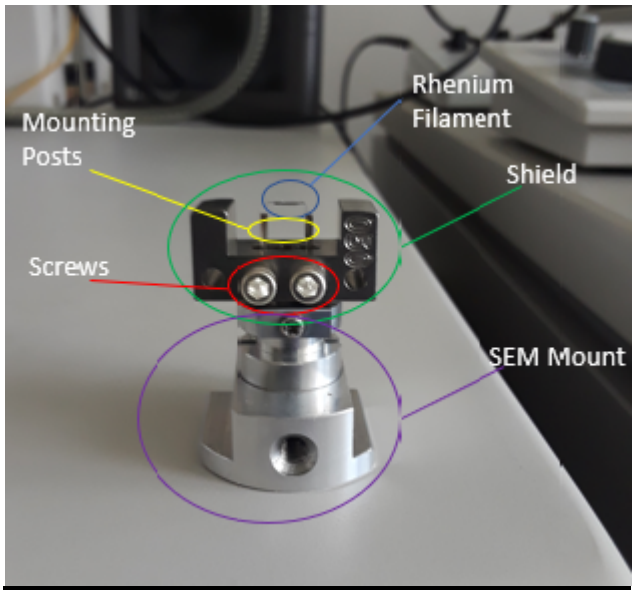

Figure 11. Filament mounted for SEM analysis, with important features labelled.

Liquid nitrogen is added to the SEM to cool the SE/BSE detectors as well as the EDS x-ray detector, enabling the highest resolution images and greatest fidelity in the EDS. The liquid nitrogen increases measurement resolution by condensing particulate that impede observation onto a cold surface within the SEM, reducing electron beam scattering [32].

Samples are loaded. The SEM chamber's pressure is reduced to, at a minimum, $1x10^{-7}$ Pa ($7.5x10^{-11}$ torr), and then the sample is placed onto the SEM stage. The stage permits full 360-degree rotation and sample tilt to just under 90 degrees.

3.1.1 SEM Imagery

Initial images were taken for filaments at the low-range of efficiency; filaments 4-3 and 4-4 were the first candidates, with efficiencies of 0.31% and 0.53%. These initial images were utilized to ascertain optimal working distance, beam energy, and orientation.

All filaments were scanned at 1 kV beam energy and 15 μamps, with a working distance of 12 mm, as 12 mm is optimal for EDS analysis. A low beam energy is desirable as the low beam energy reduces interaction volume, providing greater fidelity of surface features. Primary objectives for the initial run of images were as follows: delineate between curved and v-shaped indentations in the filaments, measure size of filaments, observe defects, and observe level of opacity. At approximately 250x magnification, filaments were raster-scanned, left to right, top to bottom, to get a complete picture of the filament. All images are 256-color, greyscale images.

The SEM utilized in this experiment offers a variety of image resolutions for outputs, essentially at a "range" of 1-6, with 6 being the highest resolution. This range determines how quickly the SEM raster scans through the entire image; the greater the range, the slower the scan, which generates more pixels and consequently, larger image file size. Lower resolutions take significantly shorter amounts of time to generate, but lack detail. For this experiment, images were taken at range 4. The difference in resolution from 4 to 6 is minimal, but the processing time for the machine to generate the image is drastically lengthened. At range 4, each image took approximately 2 minutes to form, and was the best compromise between image utility and time.

In the initial set of images, filaments were imaged every 400 μm at 250x magnification, with two rows of images, which generated between 22 and 28 images per filament. Most of these image sets when stitched together utilizing FIJI did not provide adequate representations of the shape or surface features of the filament. Two filaments, 1-4 and 1-6, had so much opacity in the SEM that stitching was unnecessary, as no

surface features could be identified; these filaments were imaged at 30x magnification once each. After many attempts to optimize the images for adequate analysis, filaments were re-loaded into the SEM several months later, and a new set of images were taken for all filaments whose stitched images were incapable of providing good data for analysis.

In the second run of images, images were instead taken every 300 μm at 250 x magnification, with 3 rows of images per filament, with the exception of filaments 3-1 and 3-2, which only required 2 rows each. This provided a total of 51-57 images per filament (again, except for filaments 3-1 and 3-2, which had 36 images each) with much greater fidelity when stitched together. Filament stitching utilized the FIJI Stitching Plugin and is described in detail in Section 4.2. [48] Certain filaments had imagery that could not adequately stitch for a variety of reasons using the plugin; these were manually stitched together using a combination of Adobe Photoshop and Microsoft Paint. Tables 5 and 6 contain all relevant imaging data used in this experiment:

Table 5. Settings for filament imaging.

	Common to All			
Filament	Beam current for images	Amperage for images	Zoom	Working Distance
1-1	1 keV	15 µamps	250x	12.0 mm
1-2	1 keV	15 µamps	250x	12.0 mm
1-3	1 keV	15 µamps	250x	12.0 mm
1-4	1 keV	15 µamps	30x	12.0 mm
1-5	1 keV	15 µamps	250x	12.0 mm
1-6	1 keV	15 µamps	30x	12.0 mm
2-1	1 keV	15 µamps	250x	12.0 mm
2-2	1 keV	15 µamps	250x	12.0 mm
2-3	1 keV	15 µamps	250x	12.0 mm
2-4	1 keV	15 µamps	250x	12.0 mm
2-5	1 keV	15 µamps	250x	12.0 mm
2-6	1 keV	15 µamps	250x	12.0 mm
3-1	1 keV	15 µamps	250x	12.0 mm
3-2	1 keV	15 µamps	250x	12.0 mm
3-3	1 keV	15 µamps	250x	12.0 mm
3-4	1 keV	15 µamps	250x	12.0 mm
3-5	1 keV	15 µamps	250x	12.0 mm
3-6	1 keV	15 µamps	250x	12.0 mm
4-1	1 keV	15 µamps	250x	12.0 mm
4-2	1 keV	15 µamps	250x	12.0 mm
4-3	1 keV	15 µamps	250x	12.0 mm
4-4	1 keV	15 µamps	250x	12.0 mm
4-5	1 keV	15 µamps	250x	12.0 mm
4-6	1 keV	15 µamps	250x	12.0 mm

Table 6. Differences between first and second sets of images.

	First Image Set				Second Image Set			
Filament	Photo Count	Image spacing	Rows of Images	Images per row	Photo Count	Image Spacing	Rows of Images	Images per row
1-1	22	400 µm	2	11	57	300 µm	3	19
1-2	22	400 µm	2	11	54	300 µm	3	18
1-3	22	400 µm	2	11	-	-	-	-
1-4	1	-	1	1	-	-	-	-
1-5	22	400 µm	2	11	54	300 µm	3	18
1-6	1	-	1	1	-	-	-	-
2-1	22	400 µm	2	11	57	300 µm	3	19
2-2	22	400 µm	2	11	54	300 µm	3	18
2-3	22	400 µm	2	11	57	300 µm	3	19
2-4	22	400 µm	2	11	54	300 µm	3	18
2-5	28	400 µm	2	14	-	-	-	-
2-6	26	400 µm	2	13	54	300 µm	3	18
3-1	28	400 µm	2	14	36	300 µm	2	18
3-2	28	400 µm	2	14	36	300 µm	2	18
3-3	30	400 µm	2	15	54	300 µm	3	18
3-4	28	400 µm	2	14	54	300 µm	3	18
3-5	26	400 µm	2	13	-	-	-	-
3-6	28	400 µm	2	14	57	300 µm	3	19
4-1	28	400 µm	2	14	54	300 µm	3	18
4-2	30	400 µm	2	15	-	-	-	-
4-3	28	400 µm	2	14	54	300 µm	3	18
4-4	30	400 µm	2	15	51	300 µm	3	17
4-5	26	400 µm	2	13	-	-	-	-
4-6	28	400 µm	2	14	54	300 µm	3	18

Further images were taken of individual filaments with unique surface characteristics such as large opaque regions or significant gaps in grain structure. Stereoscopic images, which are multiple images of the same region using the same centerline but taken 1-4 degrees offset of one another, were taken to observe the curvature of depression and angle of depression for curved and v-shaped filaments, respectively.

3.2 INCA and EDS

INCA generates x-ray spectra to analyze the elemental composition of a sample, including providing a visual analysis of where elements occur in the selected image,

atomic percentage of each element and weight percent of each element. INCA provides the user a number of options for data output, including atomic percentage of elements, weight percentage of elements, and photo maps which display where in an image different elements occur.

When analyzing using INCA, it is important to note the resolution the software is capable of obtaining, which is 10 eV per channel with 2000 channels from 0 to 20 keV. [49] Thus, any characteristic x-rays within 10 eV of one another could potentially interfere with one another. Common elements with characteristic x-rays similar to rhenium are silicon (1.838 keV to rhenium's 1.842 keV), zinc (8.639 keV to rhenium's 8.653), mercury (9.987 keV to rhenium's 10.010 keV), and tantalum (11.676 keV to rhenium's 11.685 keV). Distinguishing which element is present in a sample based off of characteristic x-rays requires some interpretation of the data, and is discussed below.

Figure 12 is one example of an image taken with accompanying EDS analysis. The sample included an image with both the filament and a section that appears opaque in the SEM imagery, pictured below:

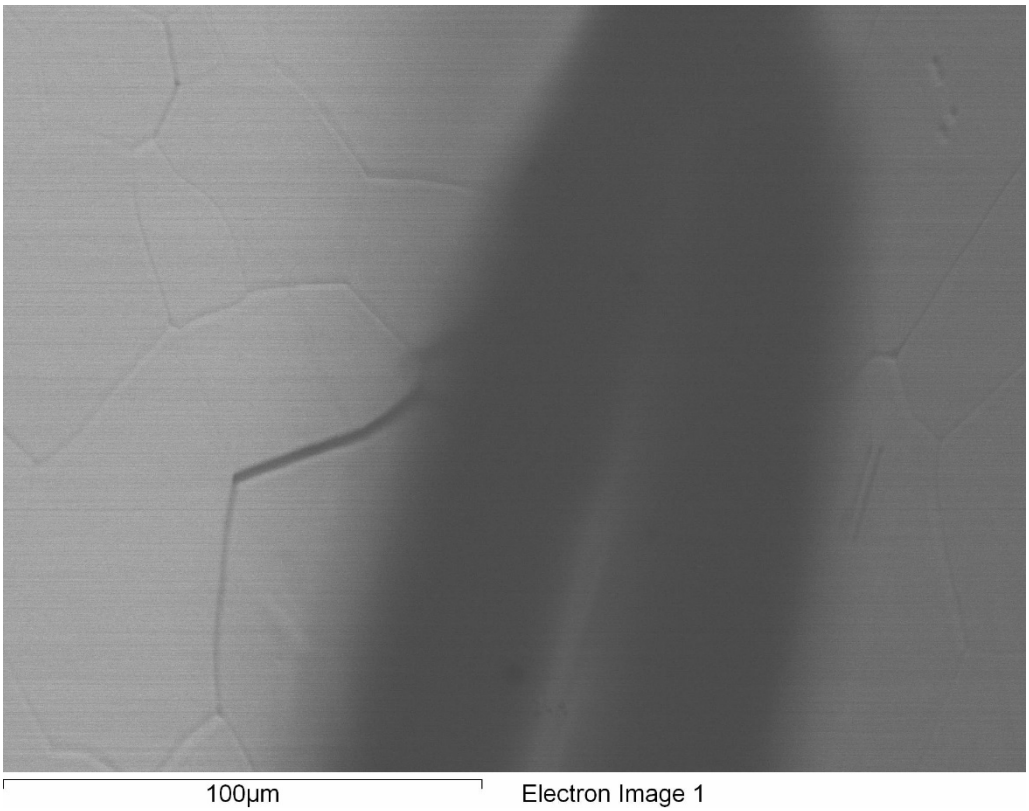

Figure 12. SEM Image on filament 4-4 taken for subsequent EDS spectrum analysis. Rhenium grains can be seen.

INCA Analyzer generated an EDS spectrum which showed rhenium, with significant concentrations of carbon, oxygen and silicon. It is a possibility that the silicon peak is an artifact or mislabeled. This spectrum was taken with a beam current of 20 keV; as such, only characteristic x-rays with energy less than 20 keV are detected.

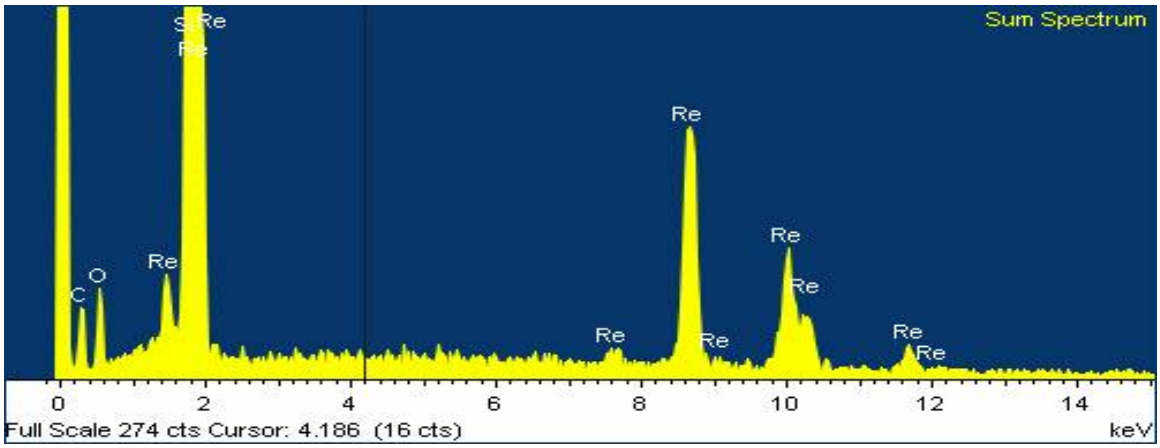

Figure 13. EDS spectrum of rhenium filament 4-4 with significant surface opacity. Note EDS cannot detect hydrogen.

In the EDS spectrum in Figure 13, the INCA analyzer software noted that all of the major peaks at 1.842 keV, 8.586 keV, 8.653 keV, 10.010 keV and 11.685 keV correspond with Re peaks given in Table 2, along with some other minor Re peaks at 1.55 keV, 7.67 keV, and 12.1 keV, which correspond with the NIST database of rhenium's characteristic x-rays. The existence of all of these peaks simultaneously indicates the presence of rhenium; if one or more of the major peaks were not present, it would indicate the absence of that element. All of an element's major characteristic x-ray peaks will be present in a sample containing that element. Carbon's sole peak at 0.282 keV and oxygen's sole peak at 0.523 keV are expected; the variations in x-rays from these two elements are too small to be resolved on the EDS (0.001 keV difference for carbon x-rays and 0.008 keV for oxygen), and so all x-rays appear as one peak.

Following generation of the spectrum, INCA has a number of tools to further analyze the sample and provide visual outputs to better quantify the elemental composition. INCA will provide an image map showing where each element occurs on each image and provide both weight and atomic percentages of the elements it registers.

INCA can provide multiple means of displaying data, such as the box plot in Figure 14, tables, or pictorial representations of where elements occur in the given image.

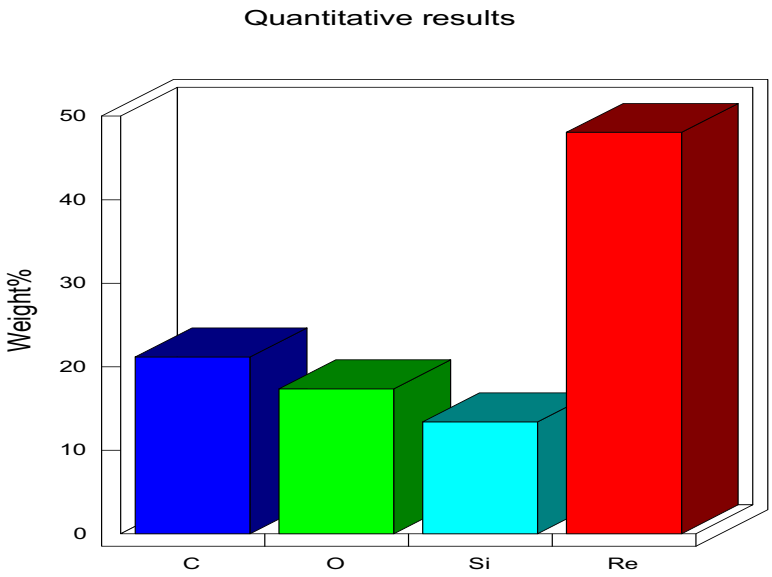

Figure 14. Elemental analysis of filament 4-6 conducted with INCA software, showing elemental composition of selected region of rhenium filament. Unsurprisingly, rhenium is the majority of the weight percentage.

Due to issues with the EDS detector, spectra and elemental composition were not able to be taken for any of the rhenium filaments beyond the two taken for demonstration purposes above. The detector registered insufficient counts for all elements – in the realm of single or double-digit counts over a period of 10 minutes – and was determined to be damaged and unable to be used for any further analysis.

3.3 CASINO Modeling

Modeling electron transport through material was done using the "monte CArlo SImulation of electroN trajectory in sOlids" (CASINO) [50]. CASINO permits a visual estimation of the path that electrons will travel, giving an indication of the interaction

volume in the medium being viewed through the SEM. Secondary electrons and backscattered electrons have vastly different trajectories and interaction volumes, and CASINO provides a good approximation of this. The CASINO image modelled 10,000 electron trajectories at 1 keV – the most common electron energy used for SEM imagery in this experiment. As expected, low Z materials such as benzene have large interaction volumes, as there are fewer electrons for the electron beam to interact, while high Z materials such as pure rhenium have smaller interaction volumes. In the model, yellow is the highest electron beam energy, 1 keV, decrementing to orange, red, green, and with blue the lowest energy, approximately 50 eV. Electrons that lose their energy prior to escaping are lost and not collected by the SEM for imaging.

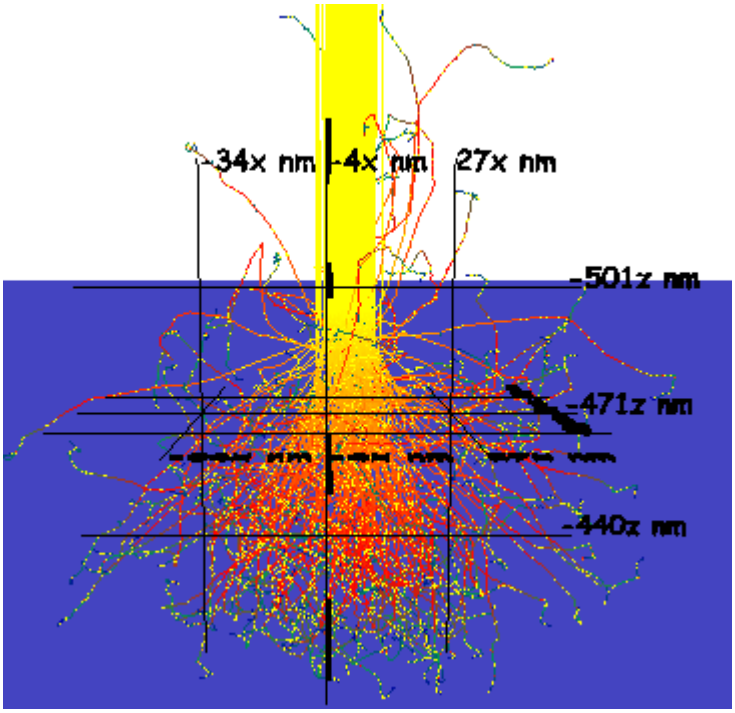

Figure 15. Modelling electron transport through pure rhenium from a 1 keV SEM electron gun. Note the scale, a total depth of approximately 100 nm and a width of approximately 120 nm.

In Figure 15, the rhenium is in blue, with a 30-nm electron beam radius shown. The interaction volume is limited to less than 100 nm; this is because rhenium, with a relatively high Z of 75, has a large number of electrons for the electron beam to interact with, limiting the interaction volume relative to low-Z materials. Note that Figure 15 is for pure rhenium; this particular model assumes no degree of carburization or oxidation.

3.4 Imaging Analysis

FIJI, which stands for Fiji Is Just ImageJ, a play on the fact that Fiji is an expanded version of ImageJ, was the primary image processing software utilized in this experiment. FIJI was utilized for contrast and sharpening adjustments, cropped images, quantified the percentage of opacity for each filament, performed measurements for filament shape, and provided 3-D images of filaments following stereoscopic imaging, such as Figure 16.

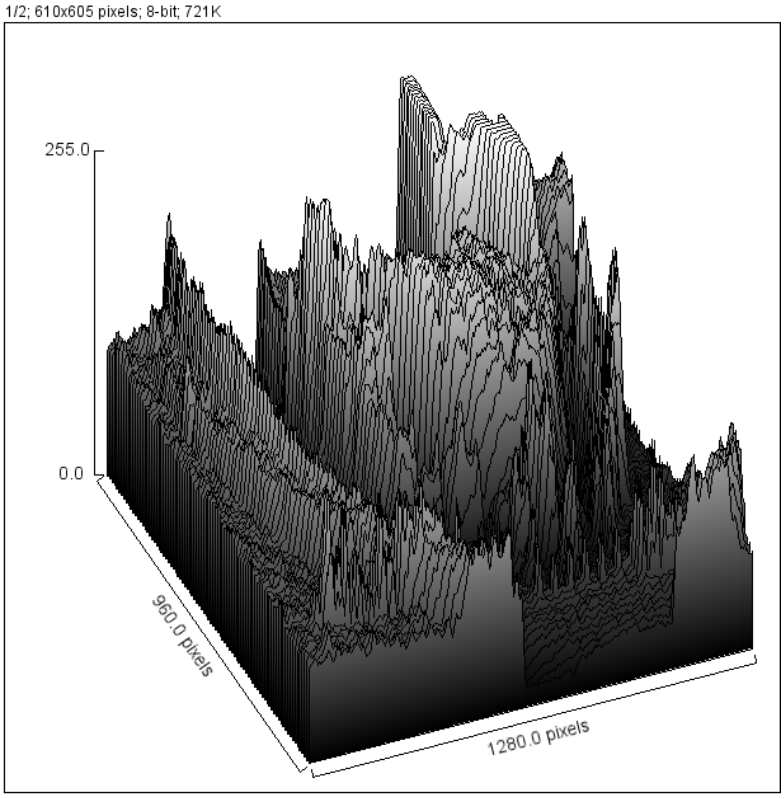

Figure 16. A 3-D surface mapping of filament connection to the mounting bracket generated by ImageJ. The post is in the center, and in the top rear is the beginning of the filament.

Imaging software packets installed separately, known as plugins, stitched together filament images, allowing the raster-scanned images to be collated into one larger, complete filament image. Finally, a FIJI macro was written and used to conduct radius of curvature measurements. All FIJI functions, plugins and macros used for this research are in Table 7.

Table 7. All FIJI functions, plugins and macros used in this research.

FIJI Functions	**FIJI Plugins**	**FIJI Macros**
Smooth	Grid/Collection Stitching	Radius of Curvature
Sharpen	Pairwise Stitching	
Enhance Contrast	Two Shot Anaglyph	
Crop		
Rotate		
Adjust Threshold		
Stacks		
Image Type (Color to 32-bit, 32-bit to 8-bit)		
3-D Surface Plot		
Measure		

4. Experimental Results

4.1 Initial Image Analysis

Raw SEM imagery must be processed for proper analysis. Due to the nature of the SEM, the beam current has a tendency to "drift." This means that, while the SEM was set to 15 μamps for the duration of imaging, actual amperage varied between 11 and 17.5 μamps while images were taken. Given the amount of time an image takes to form (in this experiment, images took approximately 2 minutes to generate), the beam current could vary by as much as 3-4 μamps from the time the SEM began generating the image to the conclusion. Thus, images that are directly adjacent to one another can have different amounts of contrast, and even within the same image filaments can have varied contrast in different regions. Additionally, not all portions of the filaments are orthogonal to the beam current; this can cause some regions, particularly edges, of the filament to appear brighter as electrons have more surface area to escape from.

Figure 17 is a flowchart depicting the steps taken for image processing for filaments from raw SEM imagery to stitched filament images suitable for analysis. In Figure 17, orange rectangles are imagery that still require processing, a dark yellow rectangle is the final stitched image, green rectangles are stitched filament images that have undergone further data analysis, blue circles are FIJI functions or plugins that act upon imagery, and teal circles are Gwyddion functions that act upon imagery.

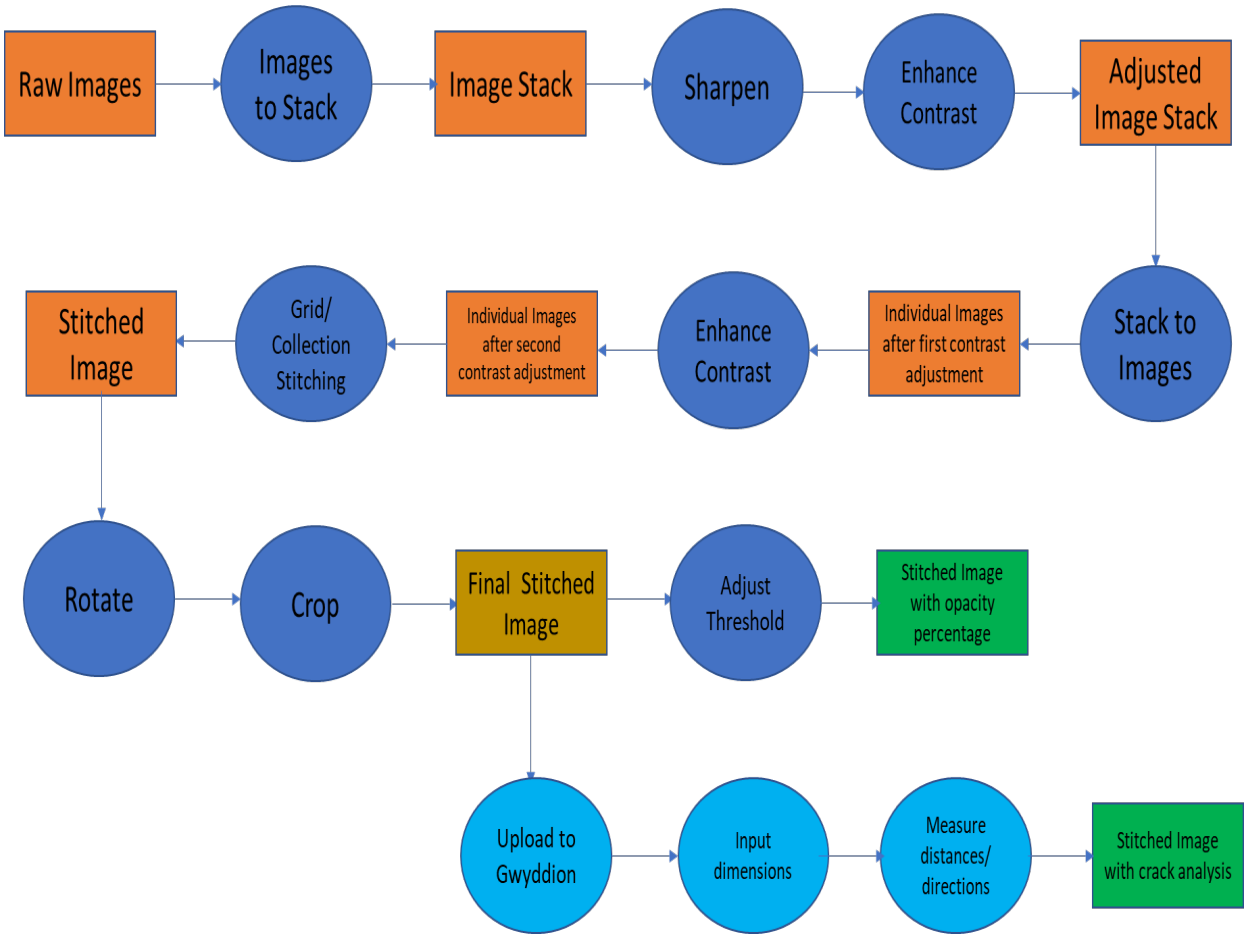

Figure 17. Flowchart of SEM imagery analysis in FIJI and Gwyddion.

FIJI has a number of built-in functions to assist with post-processing. FIJI also allows individual image processing or for a group of images to be added to a stack and all processed simultaneously. FIJI characterizes greyscale images with a histogram ranging from 0 to 255, with 0 being completely black and 255 being completely white. Figure 18 consists of a raw SEM image with its accompanying image histogram; the red in the image are the highlighted regions of the histogram selected. These histograms are essential for the opacity measurements conducted later.

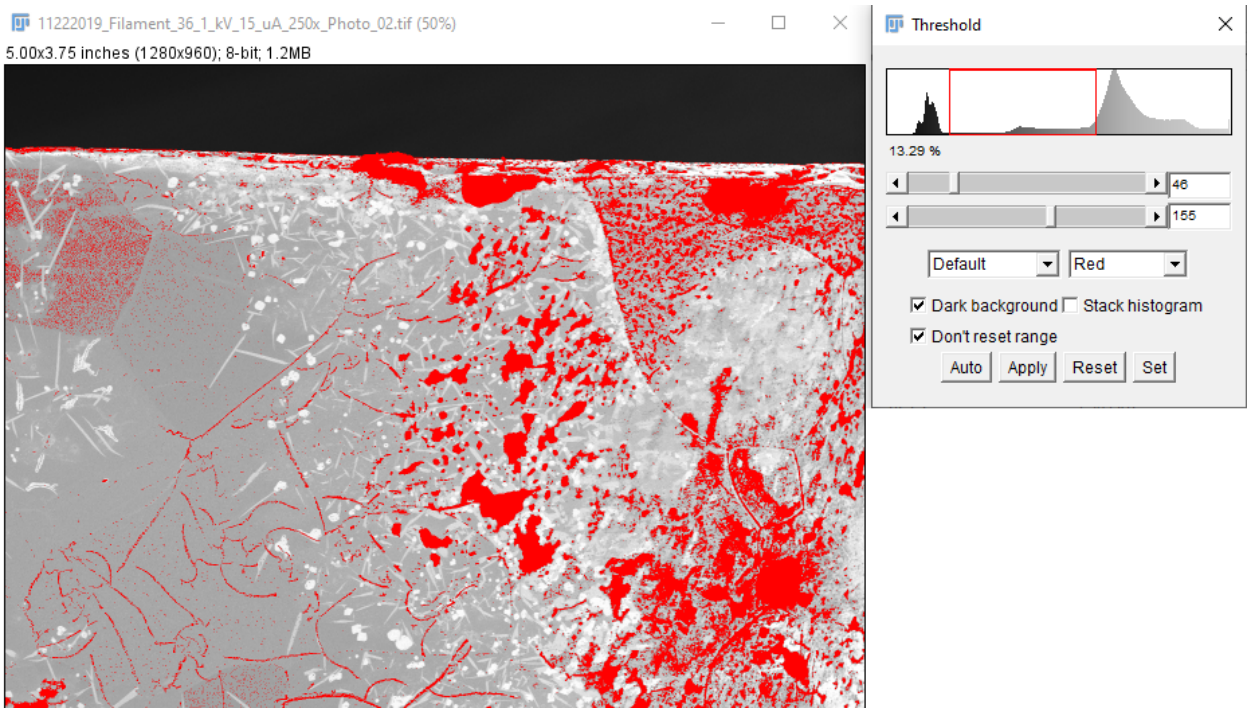

Figure 18. An image histogram (top right) with its associated image (left). The height of the lines represents the percent of pixels of that particular color in the histogram. In this image, 110 pixel bins have been isolated in the red rectangular box, and make up 13.29% of the total image.

All raw SEM images comprised dimensions of 1280x960 pixels, or 1,228,800 pixels per image. For this experiment, all images from a filament were added to a stack, underwent image sharpening – which increases pixilation in areas of extreme contrast difference, such as grain boundaries, providing for a better image for analysis – and then underwent a contrast adjustment using FIJI's integral Enhance Contrast function. For the stack contrast adjustment, the settings were as below in Figure 19. The contrast was normalized across all images, and then the stack histogram was applied to each filament and adjusted the image accordingly. In this instance, there are two images in the stack, hence the phrase "Process all 2 slices."

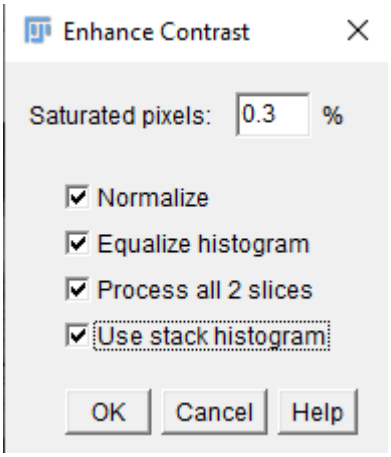

Figure 19. Settings for contrast adjustment for a stack of images.

However, by applying the stack histogram to all images and normalizing the histogram, images at either end of the dark/light spectrum have their issues exacerbated. To remedy this, the images are all taken out of the stack, and each image undergoes an additional set of contrast adjustment, again done with FIJI's Enhance Contrast function, which ensures all facets of the images are as visible as possible. These adjustments provide much clearer imaging of the individual rhenium grains, grain boundaries, and surface opacity. The change in imagery from raw SEM image to processed image is illustrated in Figure 20.

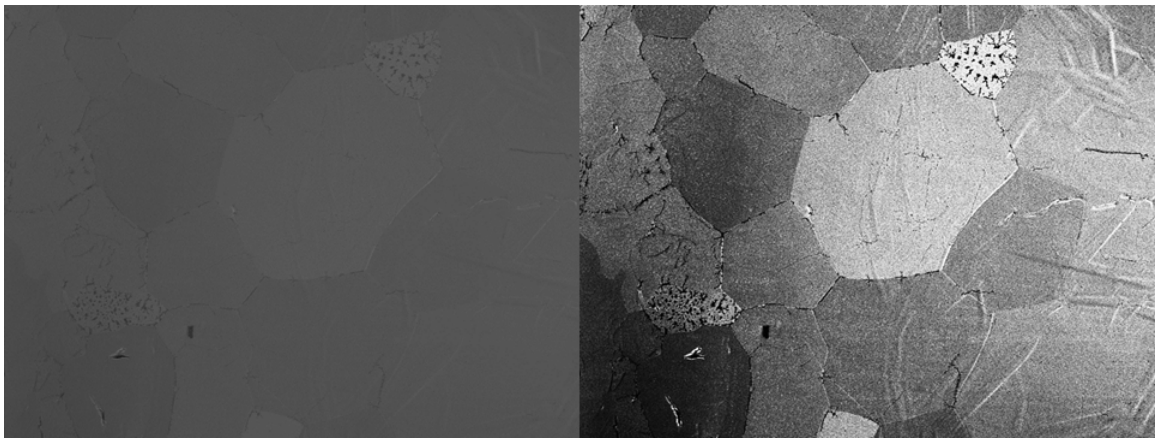

Figure 20. The image on the left is a raw SEM image; the right is the same image after going through the image sharpening and two contrast adjustments as outlined above.

4.2 Image Stitching

Image stitching was primarily conducted using the Image Stitching plugin available in FIJI. [48] The alternative method was to use Microsoft Paint and manually line up images, double-checking with Adobe Photoshop for alignment. As the images were raster-scanned from left to right, top to bottom, in a snakelike pattern, the images were stitched the same way using the plugin. Settings for image stitching are below in Figure 21.

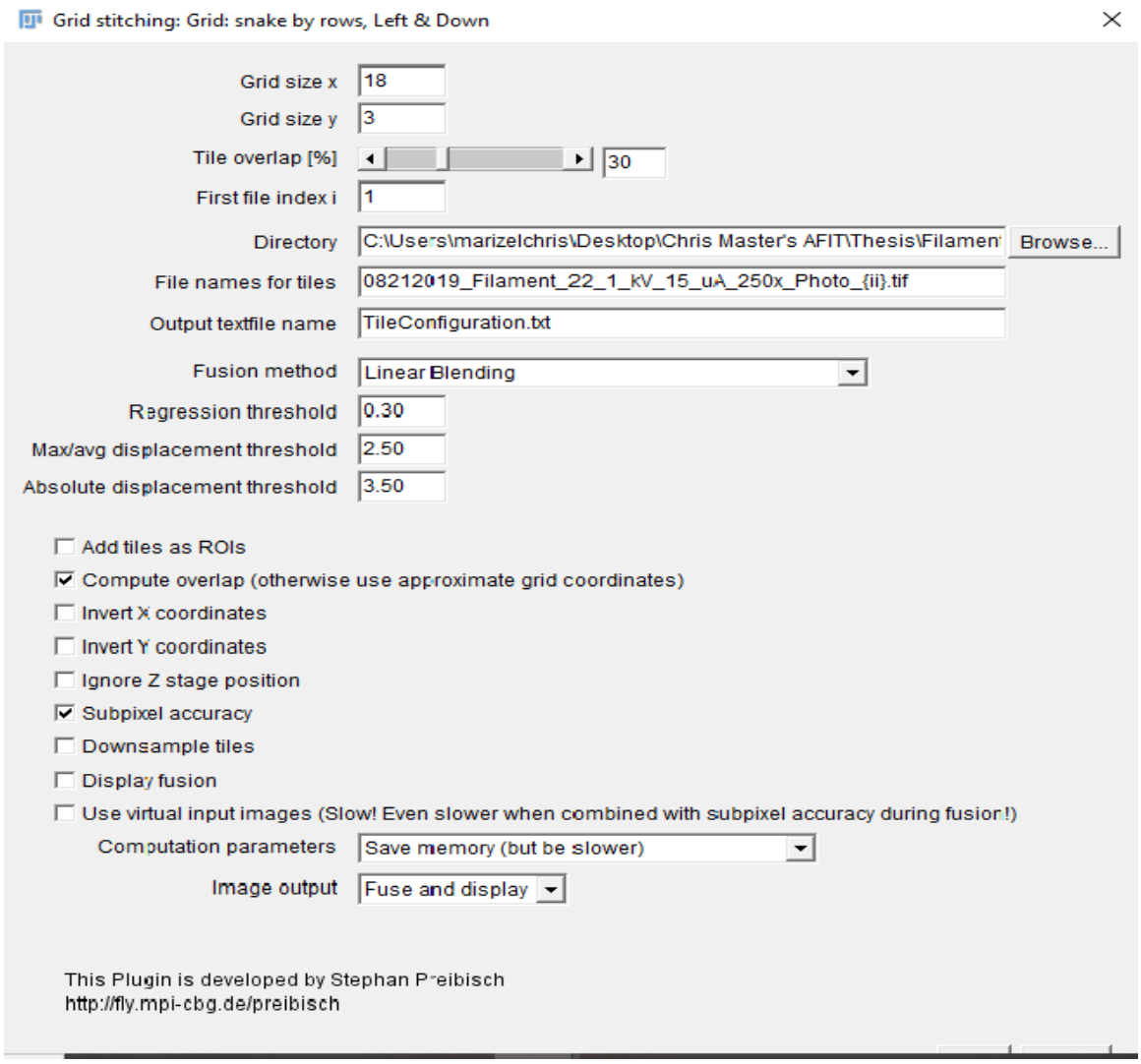

Figure 21. Settings for image stitching with the FIJI Image Stitching plugin.

A few notes on the settings for stitching. The fusion method utilized was linear blending. Linear blending smooths contrast adjustments in stitched areas. Even with the multiple contrast adjustments and image sharpening conducted in initial post-processing, there were still some areas where the contrast did not match. The linear blending algorithm mitigates this by normalizing the greyscale histograms where the images overlap for stitching. This "smooths" the color balance in the images. This method was

chosen as it provided the best images. Other methods, such as taking the average or median of the stack histograms where the images overlap, provided poorer overall images, as demonstrated in Figure 22. Note the cleaner image with linear blending and the fewer instances of lines making it evident where the images overlapped. The red circle delineates one of the areas where the difference between the two methods of stitching is more obvious; in the top image, lines where multiple images blended together is much more obvious than in the linear blending method used for the bottom image.

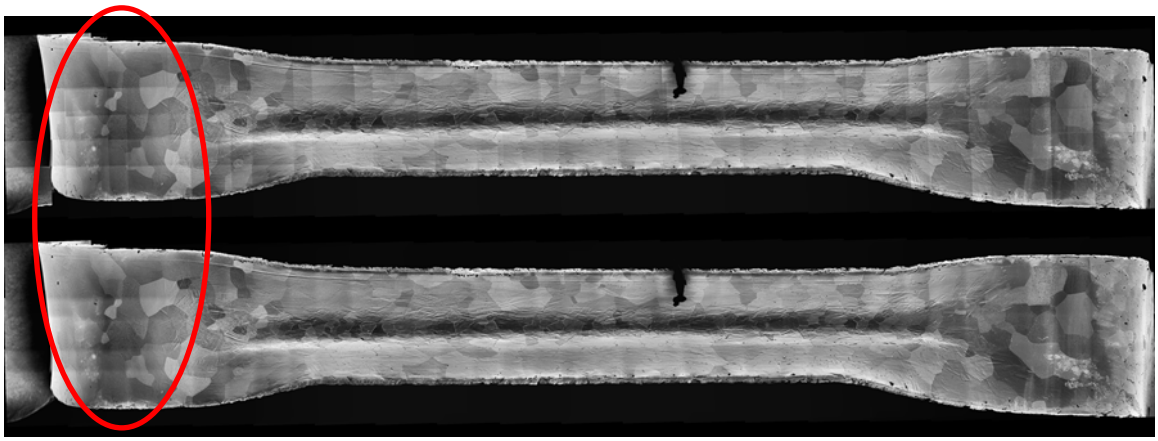

Figure 22. Filament 2-4 with stitching where the image overlaps were averaged (top) or underwent linear blending (bottom).

Initial images had a lower degree of overlap, and only two rows of images as opposed to three. The images produced via the stitching algorithm did not adequately represent the geometry of the filaments; this was due to the low degree of overlap in the images. As the stitching algorithm calculates image placement based on areas of the image that match up, the greater the percentage of overlap, the better the stitched image will be. While the plugin permits very low values of overlap, the images produced using base images with a low percentage of overlap, such as Figure 23, are poor.

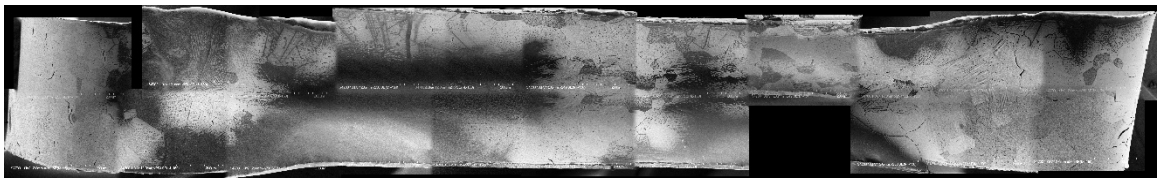

Figure 23. The initial stitching attempt for filament 2-2. Note the voids in the bottom right and top left and how the top edge of the filament does not align.

Figure 24 shows the same filament as Figure 23, but done with the new stitching technique using more images with greater overlap.

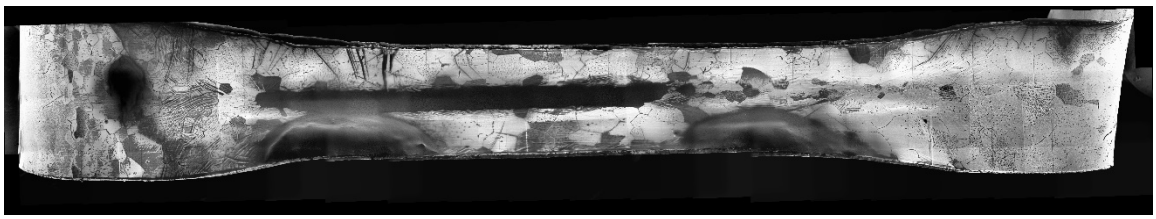

Figure 24. Filament 2-2 utilizing the new imaging procedure. Note how much cleaner the image is and the lack of voids where the software algorithm could not correlate overlap.

Some filaments were unable to be stitched utilizing the plugin – filaments 2-5, 3-5, and 4-5. These filaments had to be manually stitched by aligning areas of overlap by eye using Microsoft Paint and Adobe Photoshop. Three filaments had images that produced adequate stitched images with the first run of images – filaments 1-3, 2-1 and 4-2. These filaments thus did not undergo a second set of imaging.

Calculating uncertainty for stitched images requires calculations comparing predicted versus actual pixel counts for the final stitched image. FIJI gives the pixel count for all source images and for the final stitched image. By calculating the percent of pixels that should be "lost" due to overlap, and comparing the difference between calculated and actual pixel values, one has an approximation of the error associated with the stitching algorithmic process. For instance, for a filament with 54 images with

dimensions of 1280x960 pixels, all 54 images together have a combined pixel count of 66,355,200. For 3 rows of 18 images each, stitched images with an approximate 30% horizontal and vertical overlap should produce an image with a length of 16,512 pixels and with a height of 2,064 pixels, for a total of 34,080,768 pixels. A 19-image row filament would expect 35,930,112 pixels. Comparing the actual numbers of pixels per image in FIJI to the predicted value gives an approximation of the percent error of the stitching algorithm. The values for the various filaments and their percent errors are in Table 8 below; note that the majority of the error was due to an increase in pixels in the vertical direction primarily. Output images had vertical pixel counts very high compared to the expected values. Filaments that are highlighted in red were filaments that only underwent one set of imaging and did not undergo a second set of imaging; these filaments were stitched with 22-28 images. Filaments in yellow were manually stitched due to the stitching algorithm providing incomplete or inaccurate stitches of the filament images. Filaments with a dashed line were not stitched, as their percent opacity was so high as to make stitching unnecessary for evaluation.

Table 8. Predicted and actual pixel counts for stitched images and associated error.

Filament	Number of Images for Stitching	Predicted Pixel Count	Actual Pixel Count	Error
1-1	57	35,930,112	38,828,048	0.074635119
1-2	54	34,080,768	40,290,332	0.154120448
1-3	22	19,464,192	23,361,825	0.166837694
1-4		-	-	-
1-5	54	34,080,768	40,323,795	0.154822407
1-6		-	-	-
2-1	22	19,464,192	21,136,021	0.079098568
2-2	54	34,080,768	37,976,900	0.102592155
2-3	57	35,930,112	45,405,450	0.208682834
2-4	54	34,080,768	37,400,166	0.088753563
2-5	28	24,772,608	18,924,672	0.309011221
2-6	54	34,080,768	38,490,778	0.114573158
3-1	51	31,850,496	31,329,436	0.016631643
3-2	51	31,850,496	27,114,768	0.174654933
3-3	54	34,080,768	39,027,600	0.126752145
3-4	54	34,080,768	37,118,625	0.081841852
3-5	26	23,003,136	20,690,432	0.111776496
3-6	57	35,930,112	42,870,656	0.16189498
4-1	54	34,080,768	39,246,389	0.131620287
4-2	29	26,542,080	20,703,155	0.282030686
4-3	54	34,080,768	37,850,024	0.099583979
4-4	54	34,080,768	37,037,000	0.079818344
4-5	30	28,532,736	22,880,064	0.247056652
4-6	54	34,080,768	40,088,756	0.14986716

4.3 Filament measurements and classification

Aspects of the filaments critical to this research visible in the SEM are the length of cracks/defects in the filament, shape of the filament, percent of the surface that is opaque, and the area of holes in the centerline. These factors were evaluated statistically to determine which of these factors related to the efficiency of the filaments, or if the interplay of any of these factors affected efficiency (e.g. if a filament had a particular

shape as well as large holes in the centerline). Surface features were evaluated in the region of the filament depressions only.

4.3.1 Gwyddion and Crack Measurement

For measuring total length of cracks on the filament surface, the Gwyddion software package was utilized. Gwyddion is typically used for scanning probe microscopy images, but has a number of useful features applicable to SEM imagery as well. When an image is loaded into Gwyddion, by providing measurements of the image being processed, Gwyddion can calculate the distance of any lines drawn on the image by doing a simple calculation of pixels to length. This was used for accurately measuring cracks and defects in the filament image, as in Figure 25, below.

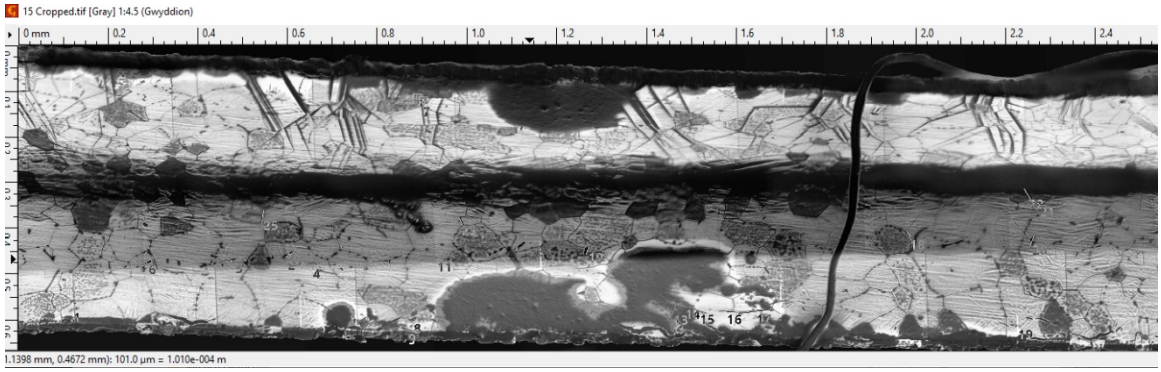

Figure 25. Crack analysis in Gwyddion. Note both the rulers along the top and left axis, as well as the numbers most visible in the center-bottom; each number is an identified crack.

All cracks were identified by eye. To delineate between a normal grain boundary and a crack requires some knowledge of how the SEM operates. The edge of a material in the SEM will typically appear brighter due to electrons escaping not just orthogonal to the electron beam but also out the sides of the sample; the exception is if there is a nonconductive region on the edge, it will appear dark, as electrons cannot escape a

nonconductive region. Thus, in areas were cracks/voids are present, the material adjacent to the void will appear significantly brighter, whereas a normal grain boundary will not have such a distinctive mark. An example of a crack demonstrating this phenomenon is in Figure 26. The near-vertical line is the bright spot where a crack between grains has appeared; grain boundaries in SEM imagery are black unless they have expanded as in this image. This type of brightness is distinct from the horizontal white lines on the bottom as they are not along a grain boundary; the brightness for the horizontal lines is due to surface topography.

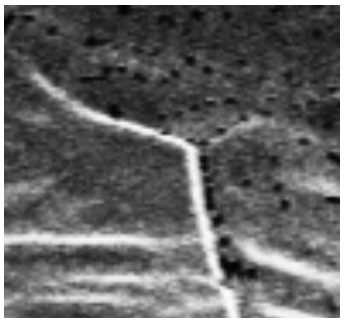

Figure 26. Note the bright whiteness between the grains along the center, compared to the normal grain boundary in the top right.

Three filaments, 1-1, 1-4, and 1-6, had so much of the surface opaque that crack measurements could not be conducted. The remainder of the filament measurements are in Table 9. The error values depicted in Table 9 are calculated by multiplying the Total Length of Cracks value in Table 9 by the percent error in the filament pixel count in Table 8 individually for each filament. Figure 27 is a scatter plot of filaments, separated by angular or curved filaments, and their associated crack lengths.

Table 9. Filament crack/defect total lengths

Filament	Angular or Curved (A=1, C=0)	Total Length of Cracks (μm)	Cracks Error (μm) (±)
1-1	0	-	-
1-2	1	600.19	92.50
1-3	0	774.07	119.30
1-4	0	-	-
1-5	1	621.63	95.81
1-6	0	-	-
2-1	1	1176.51	181.32
2-2	0	931.25	143.53
2-3	1	1793.81	276.46
2-4	1	3230.50	497.89
2-5	1	1623.53	250.22
2-6	1	281.88	43.44
3-1	0	376.64	58.05
3-2	0	1842.35	283.94
3-3	0	1583.99	244.13
3-4	0	2689.32	414.48
3-5	1	732.98	112.97
3-6	1	1663.41	256.37
4-1	1	280.13	43.17
4-2	1	2119.23	326.62
4-3	0	1576.69	243.00
4-4	0	1565.61	241.29
4-5	0	2748.13	423.54
4-6	1	1383.62	213.24

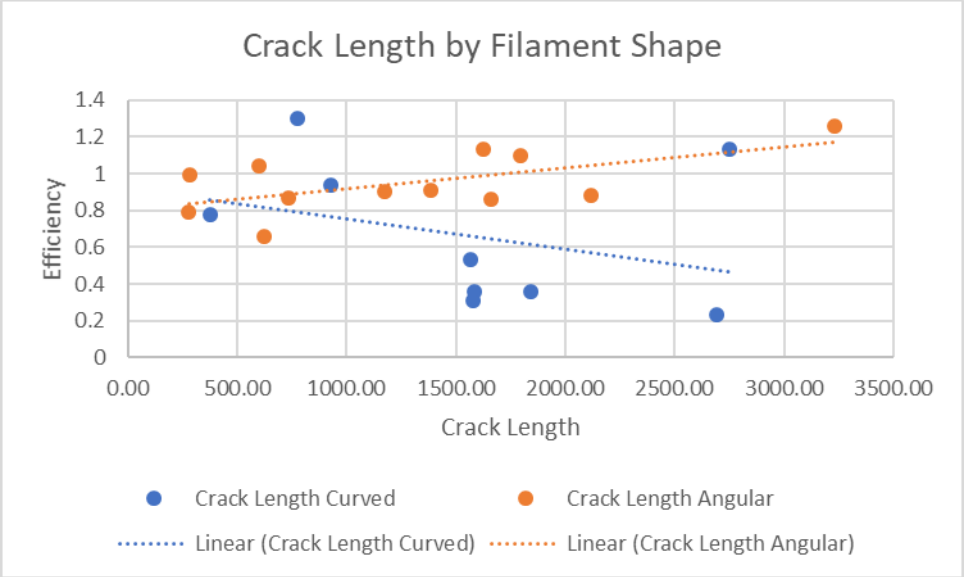

Figure 27. Scatter plot of crack length vs. efficiency. Curved filaments are blue circles, while angular filaments are red.

4.3.2 Shape of the Filament

Determining the shape of the filament depression was done, initially, via visual inspection of the filaments, and subsequently confirmed with 3-D surface plots generated from stereoscopic imaging of the filaments. Stereoscopic imaging is conducted by taking two images utilizing the same centerline, while adjusting the degree of tilt between 1 and 4 degrees, and then compiling the image together in a 3-D surface plot. Figure 28 shows the two images used to generate a surface plot of filament 1-5.

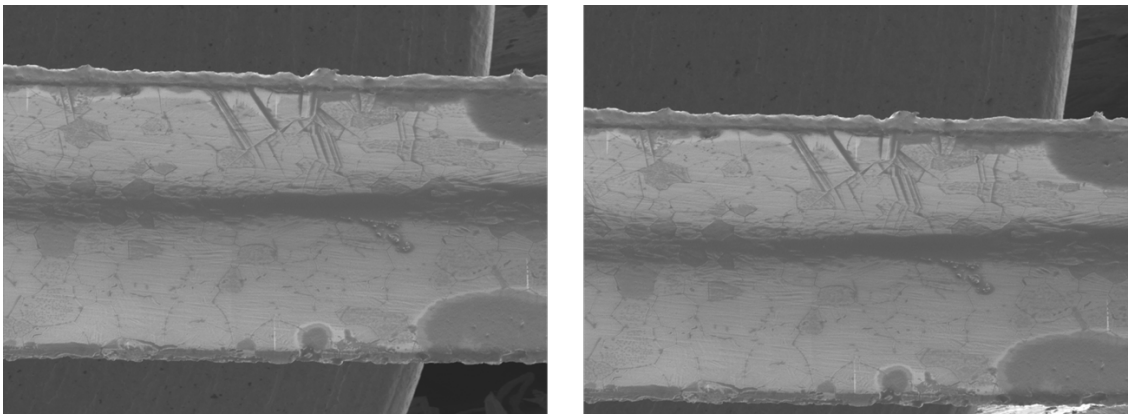

Figure 28. Composite images used to generate the stereoscopic image of filament 1-5.

Stereoscopic imaging confirmed that there were two distinct shapes of the filament depressions. Half of the filaments provided had curved depressions, while the other half had depressions that were much more angular, as Figure 29 demonstrates. This led to incorporating both filament shapes as a potential factor in filament efficiency, as well as utility for further analysis by measuring the radius of curvature of the filament depression region.

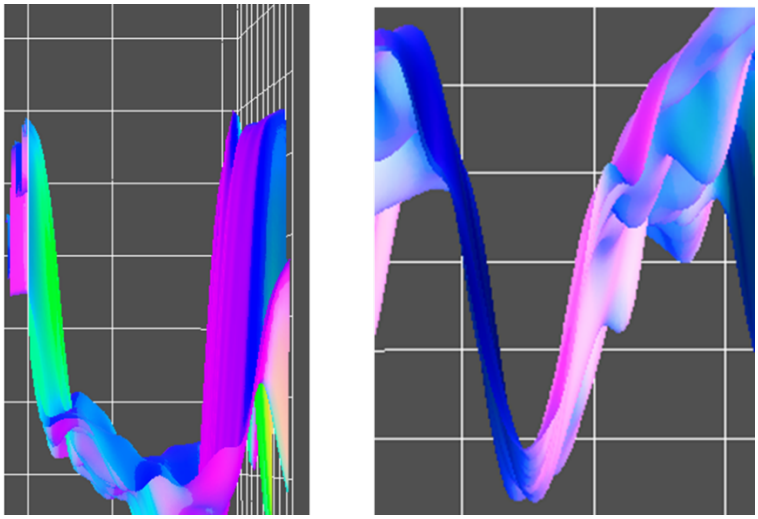

Figure 29. An example of 3-D surface plots generated by stereoscopic imaging of filaments 1-3 and 1-5, respectively, showcasing the two shapes of filament depressions. The image on the left, filament 1-3, shows a curved depression, while the filament on the right, filament 1-5, shows an angular depression.

Radii of curvature for filaments of both types were calculated using code contained in Appendix 3, referencing the 3-D surface plot images which are collected in Appendix 4. The code binarized the image so that the filament material was white and everything else black; it then calculated the radius of curvature by triangulating three points, including one point at the center and bottom of the dark region, and then circumscribing a circle around those points and calculating the radius. Note that three filaments were damaged in such a way that adequate imaging was impossible; these filaments twisted in upon themselves during removal from the tantalum posts, and so were unusable for these measurements.

These filament radius of curvature measurements have a low degree of confidence, as the macro used for measuring the radius does not take into account undulations or imperfections in the filament surface. The macro works well for smooth filament surfaces, such as filament 1-5 in Figure 29 above, but cannot compensate for the bends and folds of filament 1-3 in the same figure. Thus, some of these measurements appear to be non-physical, as the macro is calculating a curve which only is an artifact of the 3-D positioning of the filament surface. In other words, the macro cannot distinguish between the foreground and the background of the filament surface, but calculates them the same, which can give non-physical values for the radius of curvature measurements.

One additional observation noted during the course of tabulating this data was that two of the filaments, filaments 1-1 and 3-5, had depressions that were off-center, as depicted below in Figure 30. Table 10 collects all radius of curvature measurements

conducted for this experiment. Figure 31 is a scatter plot of filaments, separated by angular or curved filaments, and their associated radius of curvature.

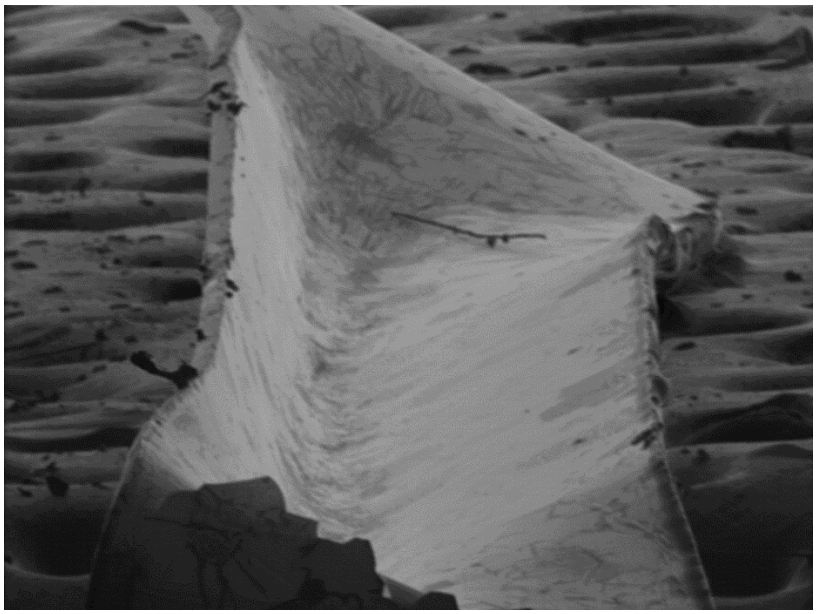

Figure 30. Filament 1-1, with off-set depression.

Table 10. Filament shape and radius of curvature by both pixel count and calculated size.

Filament	Angular or Curved (A=1, C=0)	Radius of Curvature (pixels)	Radius of Curvature (μm)	Radius of Curvature Error (μm) (±)
1-1	0	22.97	43.10	2.02
1-2	1	17.25	32.36	1.52
1-3	0	12.62	23.68	1.11
1-4	0	14.55	27.30	1.28
1-5	1	14.27	26.77	1.26
1-6	0	12.2	22.89	1.07
2-1	1	14.92	27.99	1.31
2-2	0	-	-	-
2-3	1	-	-	-
2-4	1	18.31	34.35	1.61
2-5	1	10.43	19.57	0.92
2-6	1	14.27	26.77	1.26
3-1	0	24.01	45.05	2.11
3-2	0	12.75	23.92	1.12
3-3	0	9.35	17.54	0.82
3-4	0	-	-	-
3-5	1	19.72	37.00	1.74
3-6	1	12.8	24.02	1.13
4-1	1	8.21	15.40	0.72
4-2	1	15.51	29.10	1.36
4-3	0	22.15	41.56	1.95
4-4	0	27.56	51.71	2.43
4-5	0	23.43	43.96	2.06
4-6	1	10.24	19.21	0.90

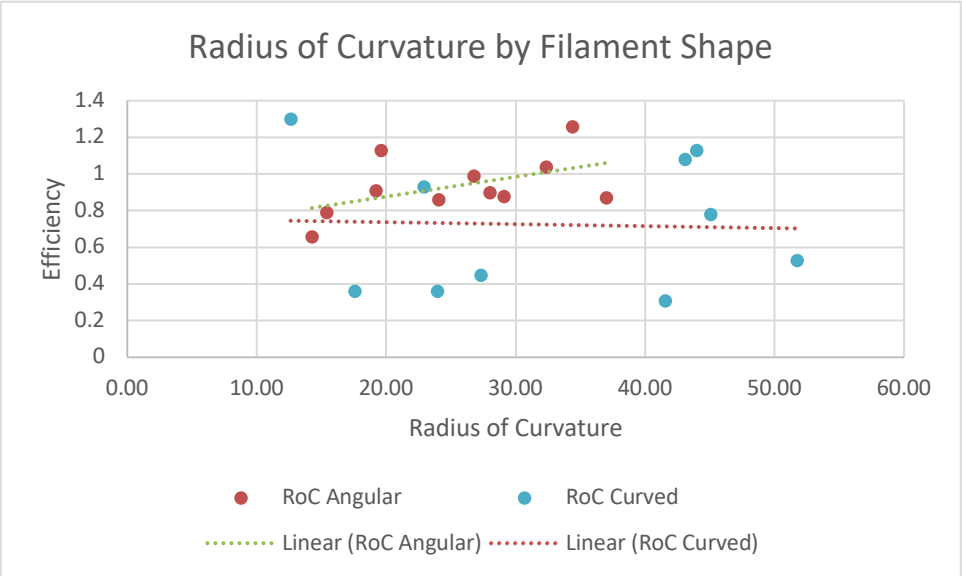

Figure 31. Scatter plot of radius of curvature vs. efficiency. Curved filaments are blue circles, while angular filaments are red.

4.3.3 Filament Opacity

Filaments measured had varying amounts of opacity, particularly in the depression in which samples are loaded. Opacity in SEM imagery is generally due to non-conductivity of the region in question. Electrons cannot conduct through the material, build up charge in the region in question, and are "lost" to the detector. As rhenium metal is conductive, non-conductive regions of an SEM image could either be excessive oxidation or some other material. While it is true that darker regions of an SEM image could also be related to surface topography or a change in Z, as lower Z elements appear darker, one method of checking is to observe the region for a short period of time. If the darkness is due to non-conductivity, the image will continuously distort and occasionally display patches of brightness, which is evidence of charge build up. The presence of this factor definitively shows that the darkness is due to non-conductivity and not the more mundane explanations. Identifying the exact composition

of the opaque regions is beyond the scope of this experiment, but may be analyzed in future work.

The charging phenomenon has an additional side-effect for imaging. Conductive regions adjacent to the opaque area become bright, as the excess electrical charge builds up with nowhere to go. This is amply illustrated in the stitched image of filament 1-1, in Figure 32. Filament 1-1 had a significant percent of the surface area opaque, and the few non-opaque regions, even with contrast adjustment, appear unusually bright.

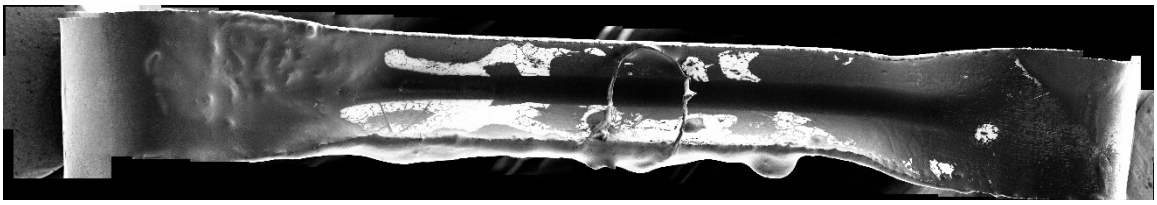

Figure 32. The white areas of the image are rhenium grains, driven to excess brightness by charge build up from the adjacent non-conductive regions. The black regions are all non-conductive.

Excess opacity detrimentally affects certain research objectives, as the opacity conceals much information that can be gleaned from surface examination of the filaments, as in Figure 28. These regions are completely opaque with the SEM even utilizing high energy (>20 kV) electrons, meaning that either the material is too thick to "shoot through" to examine the rhenium below, or is entirely nonconductive. This obfuscates the grain orientation and level of oxidation, particularly in the severely-coated filaments, as in Figure 33.

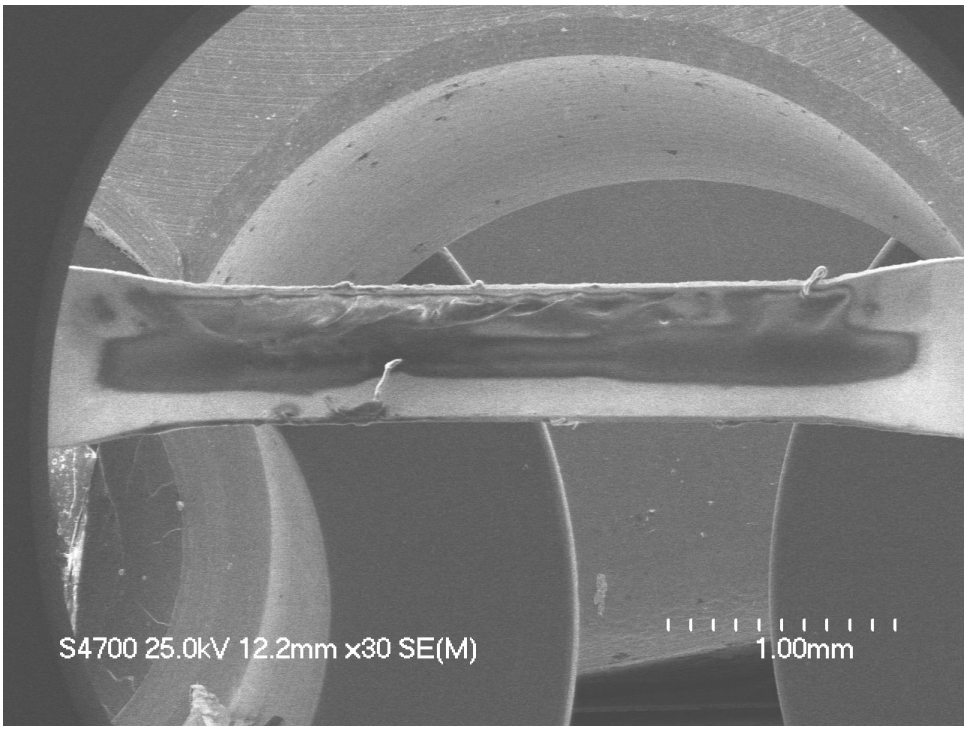

Figure 33. Filament 1-4 with significant material deposition in the sample depression.

Filament material defects have a wide range of possibilities, but the most probable will be cracks in the rhenium metal. These cracks have the potential to be detrimental due to the increased possibility of rhenium oxide formation at the site of the cracks, as hypothesized in Figure 34.

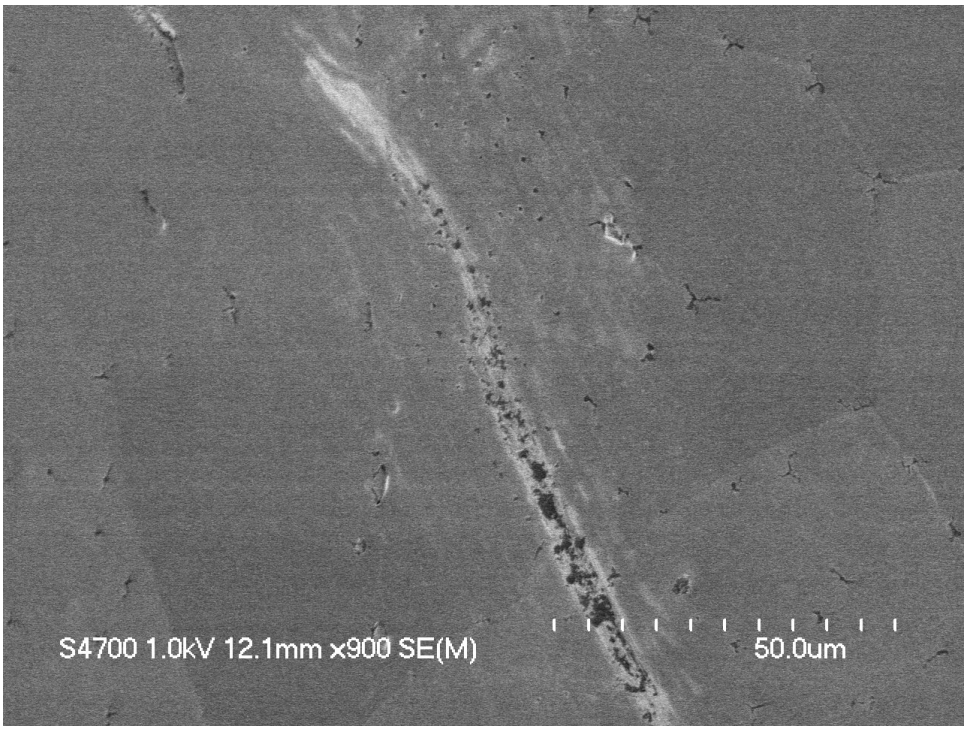

Figure 34. Filament 1-4 with significant potential oxidation along material defect.

Other defects may be due to mishandling of the filaments either prior to, or subsequent to, TIMS usage. Improper cleanliness procedures can lead to deposition of foreign material onto the filament which may or may not be burned off, and mishandling afterwards can lead to deposition of material as well. Discerning if the material was deposited before, during, or after TIMS operation is relatively straightforward in some sense; any organic material such as fibers must have been added after the fact as the extreme temperature of TIMS would have burned it off. Other material, such as the dark material below in Figure 35, will require further analysis in future work. Such defects may impede electrical conductivity, potentially degrading filament ionization efficiency.

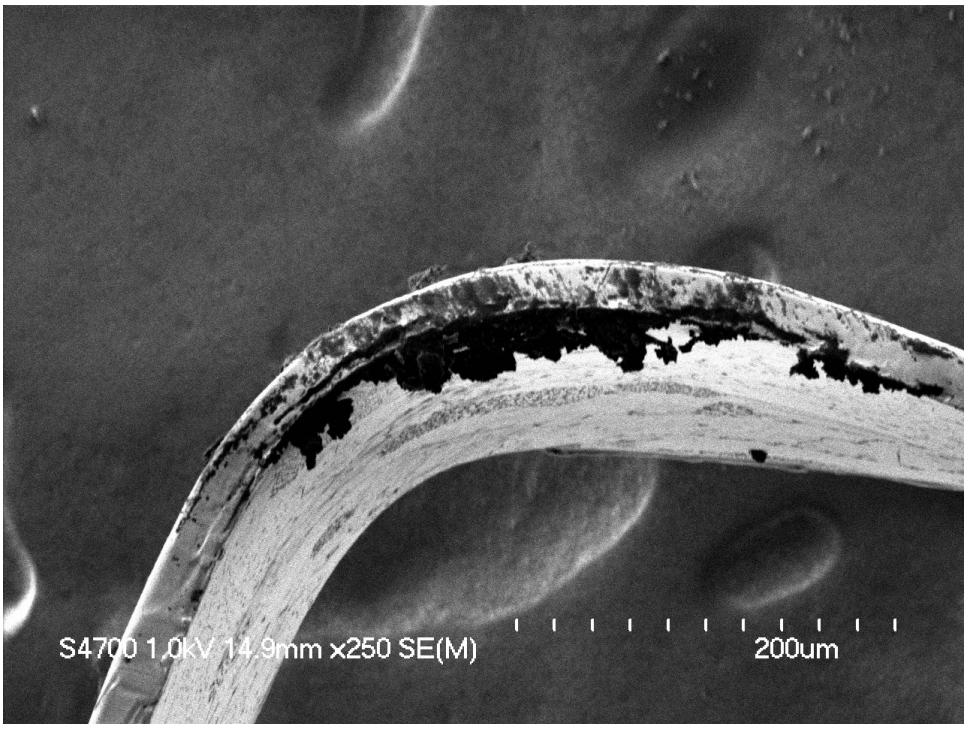

Figure 35. Filament 4-4 with significant cracking and opacity near where filament is spot-welded to the base.

As previously noted, oxidation of greater than 1% of rhenium grains in a filament can generally be associated with loss of efficiency [17]; something this research seeks to verify. Future work will be focused on identifying which, if any, of the opaque areas of the filaments are due to excessive oxidation. This can then potentially be used to backtrack through the filament preparation process to determine if the nonconductive regions were present on the filament prior to any preparation. Analysis on several images like Figure 36 below in future work will aid in determining if the image below is due to oxidation or some other cause; current literature suggests this image is similar to known images of rhenium oxide, but this requires further study [17].

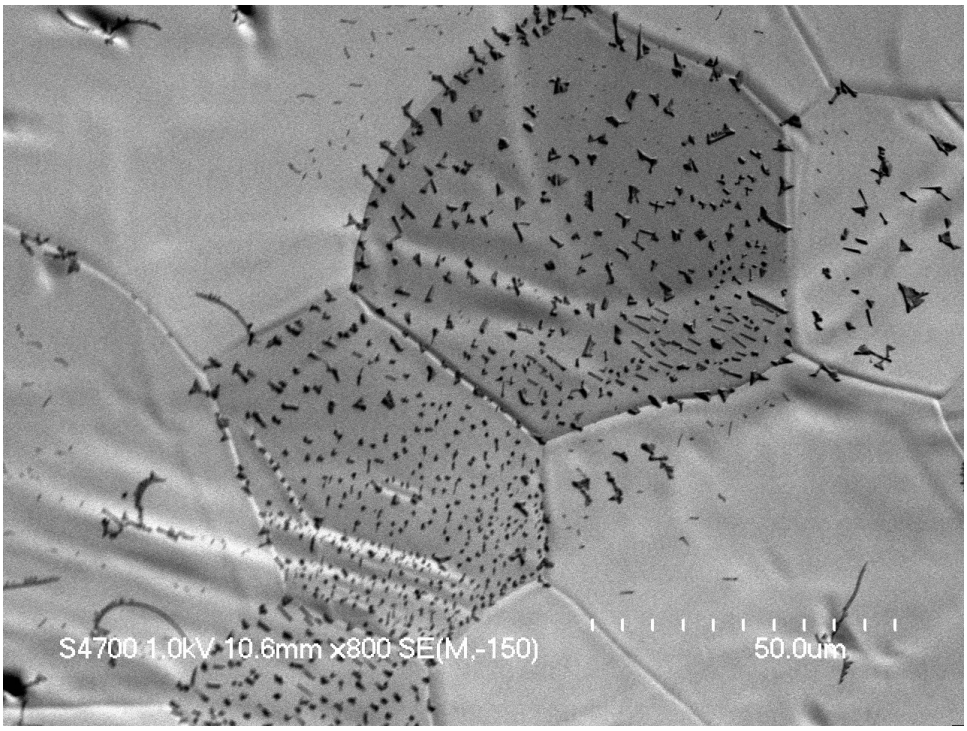

Figure 36. Significant opacity on certain grains in filament 4-4, which was a low efficiency filament with efficiency of only 0.53%. Note beginnings of opaque regions occurring along material defects in top left as well.

Oxidation is typically confined to specific grains and slowly begins to expand along grain boundaries and subsequently into adjacent grains [19]. Material defects are prime locations for oxidation to occur, but even on clean, untreated rhenium filaments the sticking probability – the probability that molecules become trapped on the surface of the material and become chemically adsorbed - of oxygen on a clean rhenium filament was 0.3 both at 298 and 1000 K. [51]

Determination of the percent of a filament's image which is opaque was done exclusively with FIJI, using threshold analysis. FIJI analyzes the greyscale image in a 256-color scheme, producing an image histogram where 0 is completely black and 255 is completely white – refer back to Figure 18. Threshold adjustments allow the user to slide

along the histogram values and highlight specific color combinations, typically in red, and FIJI provides the percent of the image within the given histogram value range. Each stitched filament image had its own unique color histogram for analysis, such as filament 4-5 in Figure 37. For this experiment, analyzing what was opaque as opposed to simply darkened grains due to orientation required some degree of intuition as a microscopist. The red shading area consists of the areas being evaluated in the histogram; these are the opaque parts of the filament image.

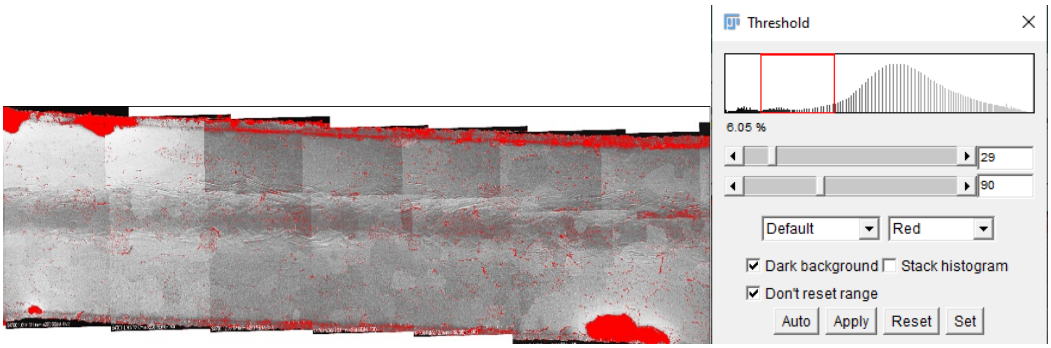

Figure 37. Image threshold for filament 4-5 with associated histogram

For some filaments, issues arose where certain areas that were not opaque were within the color range of the opaque area. This required the areas not intended to be counted to be highlighted with the select tool, have their pixel area counted, and then subtracting the percentage of the image those pixels comprised from the pixel percentage produced from the histogram analysis, to ensure that the percent opacity of the image was accurate and not counting excess areas that were dark due to topography or grain orientation. Table 11 has the range of filament opacity values. Percent error was calculated as the percent difference in opacity for ten histogram bins to either side of the selected histogram value. Figure 38 is a scatter plot of filaments, separated by angular or curved filaments, and their associated opacity.

Table 11. Filaments and associated percent opacity

Filament	Angular or Curved (A=1, C=0)	% image opaque	Opacity Error (±)
1-1	0	75.48	2.65
1-2	1	28.74	3.23
1-3	0	4.30	0.96
1-4	0	100.00	1.00
1-5	1	29.48	3.12
1-6	0	75.83	4.11
2-1	1	11.56	1.72
2-2	0	36.12	5.13
2-3	1	4.92	0.44
2-4	1	3.62	0.28
2-5	1	1.65	0.13
2-6	1	72.97	3.42
3-1	0	3.55	0.58
3-2	0	17.02	2.03
3-3	0	15.22	1.77
3-4	0	4.94	0.86
3-5	1	0.66	0.09
3-6	1	0.20	0.02
4-1	1	45.26	4.26
4-2	1	3.68	0.66
4-3	0	28.26	1.60
4-4	0	3.30	2.00
4-5	0	6.05	0.56
4-6	1	26.70	2.20

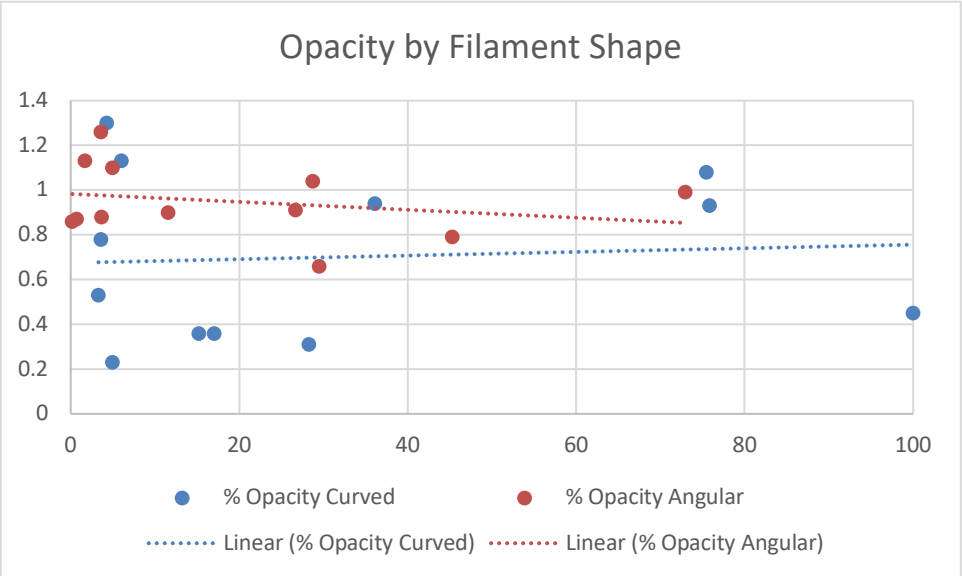

Figure 38. Scatter plot of efficiency vs. opacity. Curved filaments are in blue while angular filaments are in red.

4.3.4 Holes in Centerline – Optical Microscopy

Occasionally, the act of pressing the depression into the filament appears to cause undue stress on the centerline, producing holes that transmit through the entire depth of the filament. To analyze if there were holes that transmitted the entire depth of the filament was not possible with the SEM, and so a Zeiss Discovery V12 optical microscope, pictured in Figure 39, was used instead.

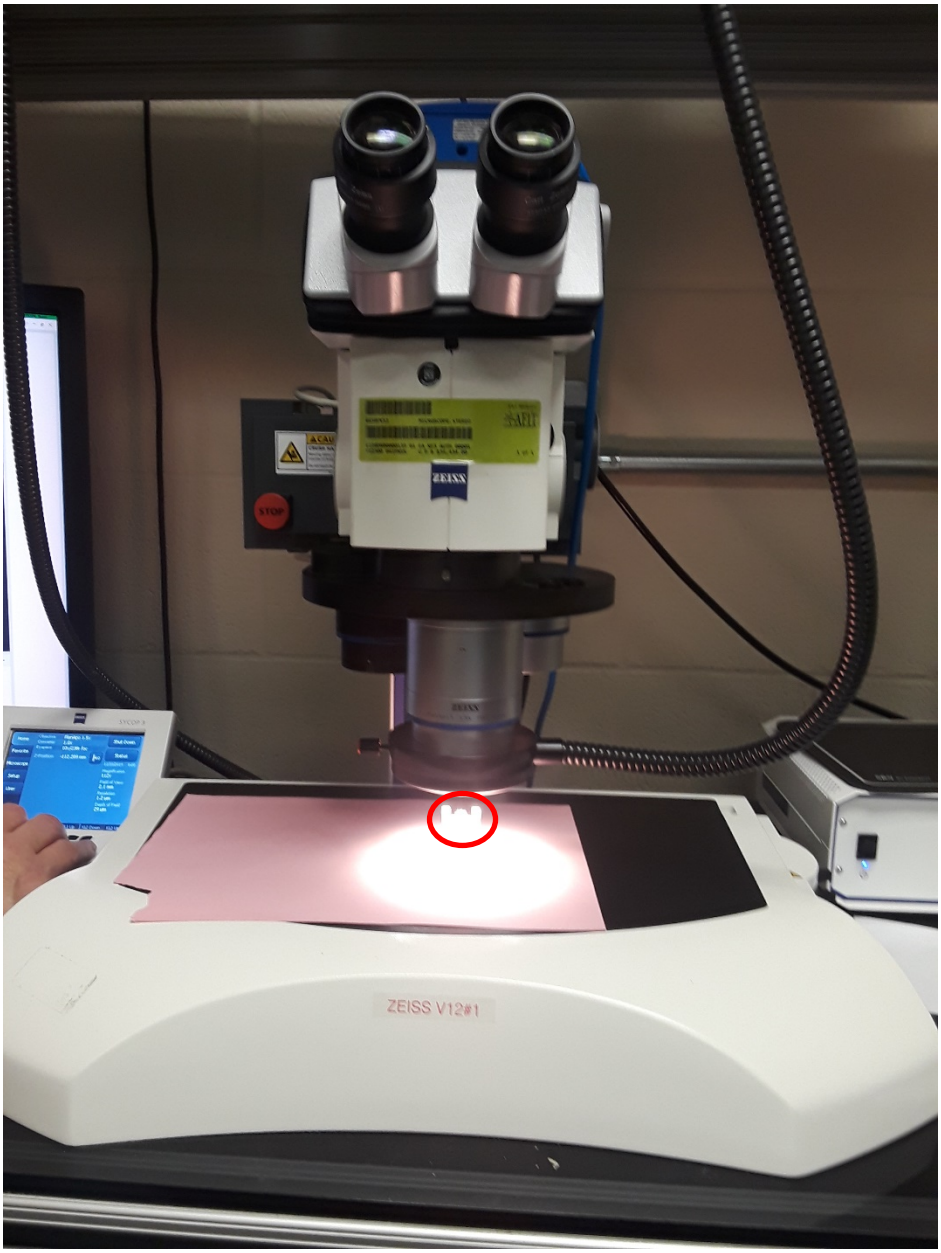

Figure 39. Zeiss V12 Discovery optical microscope with filament mounted on top of pink piece of paper. The filament is circled in red.

All images were taken at 110x magnification. A sheet of pink paper was placed below the filaments, which were placed under the optical microscope. If the filaments had no holes through the entirety of the filament's depth, the paper would not be visible.

There were two filaments that did have holes in them, however, and the pink paper was readily visible through the centerline of the filament, as demonstrated in Figure 40.

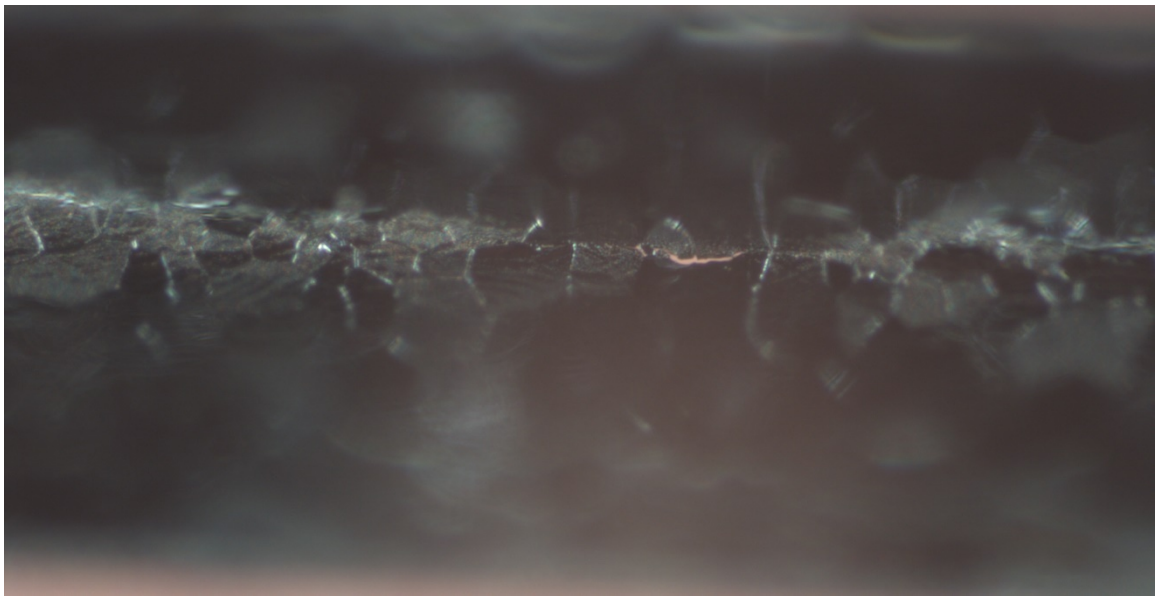

Figure 40. Centerline hole in filament 3-2. The pink paper is visible just to the right of the center of the image.

To calculate the area of the holes, images were converted to greyscale and a threshold analysis was done in FIJI. This gave the percent of the image that comprised the hole. The image was then loaded into Gwyddion, where the total area of the image was calculated. The total area was multiplied by the percentage of the image within the holes to give the area of just the holes. Gwyddion was then used to give approximate dimensions of the holes in terms of length and height.

Only two filaments had holes in the centerline. Filament 1-1 had four holes with a total area of 860.33 μm^2, while filament 3-2 had one hole with a total area of 933.96 μm^2. Table 11 collects all of the relevant data for holes in the filaments. Error was calculated by using the given standard error of the optical microscope model – in this instance, 0.37 μm – taking the square root of the microscope's standard error divided by

the length and height of the holes, summing those two values, then multiplying by the total area of the hole as given in Table 12 and the percent error from Table 7 for each respective filament.

Table 12. Area of holes in filaments

Filament	Area of Holes (μm)	Holes Error (μm) (±)
1-1	860.33	22.88
1-2	0.00	0.00
1-3	0.00	0.00
1-4	0.00	0.00
1-5	0.00	0.00
1-6	0.00	0.00
2-1	0.00	0.00
2-2	0.00	0.00
2-3	0.00	0.00
2-4	0.00	0.00
2-5	0.00	0.00
2-6	0.00	0.00
3-1	0.00	0.00
3-2	933.96	16.74
3-3	0.00	0.00
3-4	0.00	0.00
3-5	0.00	0.00
3-6	0.00	0.00
4-1	0.00	0.00
4-2	0.00	0.00
4-3	0.00	0.00
4-4	0.00	0.00
4-5	0.00	0.00
4-6	0.00	0.00

4.3.5 Electroconductivity Analysis

As an addition to surface features, electroconductivity analysis was conducted. Given that the filaments are heated via an electric current for use in TIMS, values for

filament resistance and resistivity, particularly those with higher resistance and resistivity, could potentially provide an indicator for low filament efficiency. Testing for these cannot be done via imaging like all of the other factors evaluated previously, but must be done using a probe station. Filaments were mounted on a probe station as in Figure 41. and subjected to tests measuring the filament's total resistance, and the resistivity of the filament. The rhenium filament is delineated by the red circle at the center of the image.

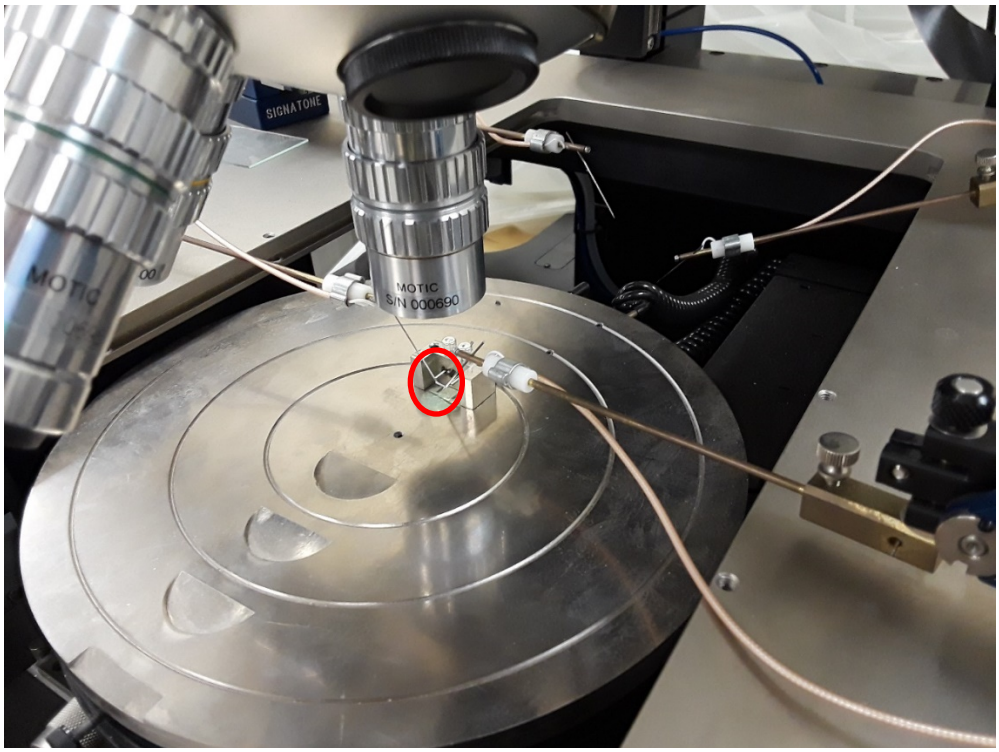

Figure 41. Filament mounted on probe station. The filament is circled in red.

Resistivity measurements involved using electronic calipers and measuring resistance with a distance of one millimeter between the probes and two millimeters between the probes. The slope of the line between these two data points was calculated as the resistivity. Both resistance and resistivity measurements were conducted from -2

volts to 2 volts. By the time the data was taken, several filaments had broken in such a manner that 2 straight millimeters of filament was not accessible, and so only 19 filaments had these measurements done. Results are below in Table 13. Percent error calculations includes the factory-determined percent error of 0.0012% in voltage for the voltages utilized to test the filaments. Figure 42 is a scatter plot of filaments, separated by angular or curved filaments, and their associated resistance, while Figure 43 is a scatter plot of resistivity for angular and curved filaments.

Table 13. Electrical resistance and resistivity measurements

Filament	Angular or Curved (A=1, C=0)	Resistivity (Ω·m)	Resistivity Error (Ω·m) (±)	Resistance (Ω)	Resistance Error (Ω) (±)
1-1	0	4.75E-03	5.70E-06	9.20E-02	1.10E-04
1-2	1	6.64E-02	7.96E-05	9.12E-02	1.09E-04
1-3	0	-	-	-	-
1-4	0	4.60E-02	5.52E-05	1.03E-02	1.24E-05
1-5	1	7.29E-02	8.75E-05	7.63E-02	9.15E-05
1-6	0	3.24E-02	3.89E-05	1.34E-02	1.61E-05
2-1	1	6.63E-03	7.95E-06	3.86E-02	4.64E-05
2-2	0	2.09E-02	2.51E-05	8.83E-03	1.06E-05
2-3	1	5.23E-04	6.27E-07	2.05E-02	2.46E-05
2-4	1	7.54E-02	9.04E-05	8.52E-02	1.02E-04
2-5	1	-	-	-	-
2-6	1	7.29E-02	8.75E-05	2.14E-02	2.56E-05
3-1	0	-	-	-	-
3-2	0	7.61E-02	9.14E-05	4.16E-02	4.99E-05
3-3	0	4.10E-02	4.92E-05	8.17E-02	9.81E-05
3-4	0	3.26E-02	3.92E-05	5.91E-02	7.10E-05
3-5	1	7.47E-02	8.96E-05	8.57E-02	1.03E-04
3-6	1	7.53E-02	9.04E-05	8.45E-02	1.01E-04
4-1	1	6.92E-04	8.30E-07	3.67E-02	4.40E-05
4-2	1	3.95E-02	4.74E-05	3.27E-02	3.92E-05
4-3	0	2.75E-02	3.30E-05	4.07E-02	4.88E-05
4-4	0	-	-	-	-
4-5	0	-	-	-	-
4-6	1	6.51E-02	7.82E-05	1.45E-02	1.74E-05

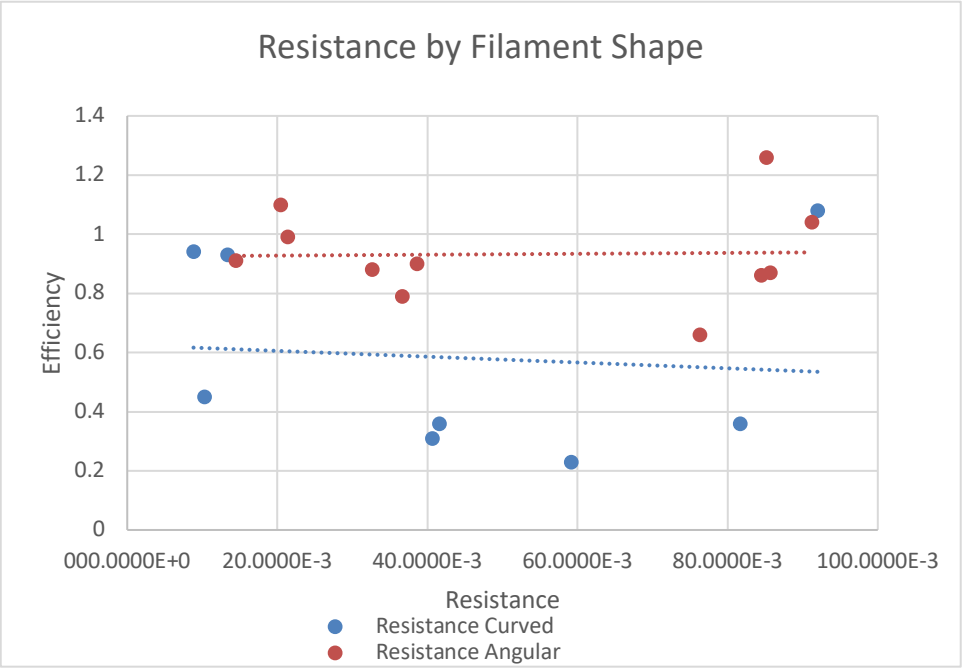

Figure 42. Scatter plot of efficiency vs. resistance. Curved filaments are in blue while angular filaments are in red.

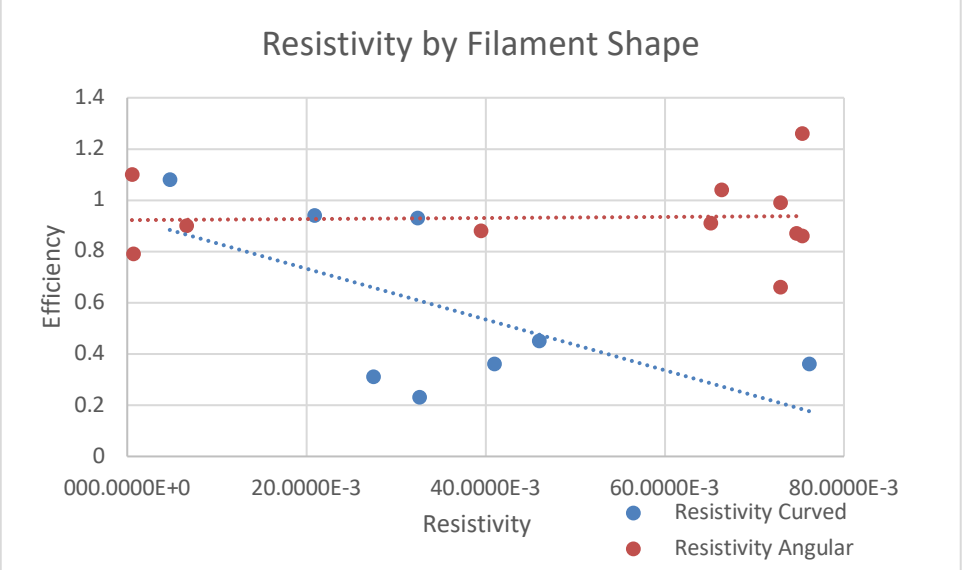

Figure 43. Scatter plot of efficiency vs. resistivity. Curved filaments are in blue while angular filaments are in red.

5. Analysis

5.1 General Statistical Analysis

Statistical analysis has been done on the tabulated filament efficiency to find the sample mean, $\bar{X}$ and the sample variance, S^2, which are displayed in Table 14. The assumption is that the distribution for the efficiency of the filaments is approximately normally distributed:

Table 14: Calculating $\bar{X}$ and S^2 for all filaments.

Filament	Efficiency (%)	xbar-eff	Squared
1-1	1.08	-0.26	0.068
1-2	1.04	-0.22	0.048
1-3	1.3	-0.48	0.230
1-4	0.45	0.37	0.137
1-5	0.66	0.16	0.026
1-6	0.93	-0.11	0.012
2-1	0.9	-0.08	0.006
2-2	0.94	-0.12	0.014
2-3	1.1	-0.28	0.078
2-4	1.26	-0.44	0.194
2-5	1.13	-0.31	0.096
2-6	0.99	-0.17	0.029
3-1	0.78	0.04	0.002
3-2	0.36	0.46	0.212
3-3	0.36	0.46	0.212
3-4	0.23	0.59	0.348
3-5	0.87	-0.05	0.003
3-6	0.86	-0.04	0.002
4-1	0.79	0.03	0.001
4-2	0.88	-0.06	0.004
4-3	0.31	0.51	0.260
4-4	0.53	0.29	0.084
4-5	1.13	-0.31	0.096
4-6	0.91	-0.09	0.008
Mean	**0.82**	**Variance**	**0.090**

This provides a baseline, and can also be used to conduct hypothesis testing. For this research, the null hypothesis is that the population mean, μ, is equal to 1% efficiency. This is the common efficiency noted throughout the literature for rhenium filaments in TIMS. For this research, the assumption is that the variance in the filament efficiency is unknown for the population. However, the sample variance, S^2 is considered an unbiased estimator for the population variance, σ^2, and thus the sample variance of 0.090 will be used in this research. [52]

5.2 Studentized t-test

The t-test can be used to determine if the sample of filaments in this experiment is statistically likely to be representative of the population of filaments. This test is useful in this case as the t-test is designed to function with small sample sizes, as in this research. The t-test will determine if there is a significant difference in the means between the two groups (the sample of 24 filaments versus the total population of filaments) by producing a confidence interval for $\mu_1 - \mu_2$. This experiment will use an α of 0.05 to achieve a 95% confidence interval.

If the confidence interval of $\mu_1 - \mu_2$ includes 0, that is an indication that the mean efficiencies of the sample and the population are the same, and thus that the sample potentially falls within normal statistical deviation of the population. If the interval does not contain zero, this rejects the null hypothesis and concludes that the means are dissimilar. This result would lead one to conclude, since the mean of the sample is different than the population mean, that something must be affecting the sample to bring about this difference in means. The t-value of the test will demonstrate how many

standard units the means of the two tests are apart. [52] Statistical analysis will further attempt to understand the signals in the data obscured by noise.

Given a population mean of 1% efficiency for rhenium filaments and a sample mean of 0.82%, the studentized t-test was utilized to determine if the sample mean was statistically probable to occur in a random sampling of the population of rhenium filaments. The null hypothesis is that the means are equal. A boxplot, showing all filament efficiencies, the population mean, and a 95% confidence interval on the true sample mean, is below in Figure 44.

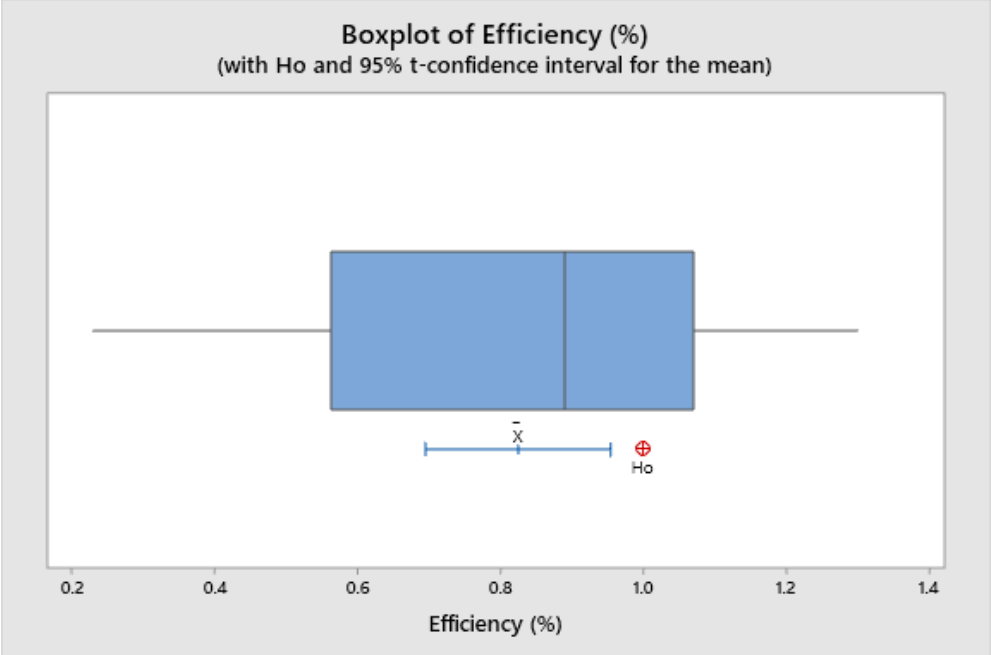

Descriptive Statistics

N	Mean	StDev	SE Mean	95% CI for μ
24	0.8246	0.3070	0.0627	(0.6949, 0.9542)

μ: mean of Efficiency (%)

Figure 44. Box plot and statistics for t-test

In the above figure, the red circle is the population mean. The blue box is the interquartile range box, which represents 50% of the data. The whiskers represent the top and bottom 25% of the data set. The left whisker is slightly longer than the right because there are more filaments below the interquartile range than above it; that is, there were more filaments with efficiencies less than 0.6% than there were filaments with efficiencies greater than 1.1%. The vertical line in the box is the calculated sample mean. The confidence interval below the box is the calculated, 95% confidence interval for the sample mean.

As shown above, the 95% confidence interval for the sample mean does not intersect with the population mean; in other words, $\mu_1 - \mu_2 \neq 0$ anywhere within the confidence interval. Thus, this rejects the null hypothesis and conclude that the sample mean is different from the population mean. The most likely conclusion is that there must be some factors that are affecting the efficiency of these filaments that causes them to have a lower mean efficiency.

5.3 Design of Experiments

Design of Experiments (DoE) is a methodology by which data is made to fit linear or quadratic models to permit holistic analysis of the data. DoE is most useful in that it allows multiple variables (known as factors) to be evaluated simultaneously rather than one at a time. DoE also permits one to observe the interplay between multiple factors and determine which factors, and which interplays of factors, directly affect the outcome of the model. Design of Experiments (DoE) techniques permit one to conduct an

Analysis of Variance (ANOVA) test to determine the relative effects of defects on filament efficiency. [53]

In this instance, all of the aforementioned factors from the previous sections – filament shape, area of centerline holes, length of cracks, percent opacity, radius of curvature, resistance, and resistivity – can be evaluated in groups to determine which, if any, affect the efficiency values for the rhenium filaments. Due to the small sample size, all seven factors cannot be evaluated concurrently as there are not enough degrees of freedom to model error, necessitating several designs with three to five factors each instead of one model with all seven factors.

Two types of models were evaluated, using the Minitab software package: a linear model, which will be a Factorial Design, and a quadratic model, which is a Response Surface Design. For all statistical models, all factors had a predefined $p < 0.05$ significance level, and used the following data in Table 15.

Table 15. Data for all runs of DoE analysis.

Filament	Efficiency (%)	Angular or Curved (A=1, C=0)	Total Length of Cracks (μm)	% image opaque	Area of Holes (μm)	Resistivity (Ω·m)	Resistance (Ω)	Radius of Curvature (μm)
1-1	1.08	0	-	75.48	860.33	4.75E-03	9.20E-02	43.10
1-2	1.04	1	600.19	28.74	0.00	6.64E-02	9.12E-02	32.36
1-3	1.3	0	774.07	4.30	0.00	-	-	23.68
1-4	0.45	0	-	100.00	0.00	4.60E-02	1.03E-02	27.30
1-5	0.66	1	621.63	29.48	0.00	7.29E-02	7.63E-02	26.77
1-6	0.93	0	-	75.83	0.00	3.24E-02	1.34E-02	22.89
2-1	0.9	1	1176.51	11.56	0.00	6.63E-03	3.86E-02	27.99
2-2	0.94	0	931.25	36.12	0.00	2.09E-02	8.83E-03	-
2-3	1.1	1	1793.81	4.92	0.00	5.23E-04	2.05E-02	-
2-4	1.26	1	3230.50	3.62	0.00	7.54E-02	8.52E-02	34.35
2-5	1.13	1	1623.53	1.65	0.00	-	-	19.57
2-6	0.99	1	281.88	72.97	0.00	7.29E-02	2.14E-02	26.77
3-1	0.78	0	376.64	3.55	0.00	-	-	45.05
3-2	0.36	0	1842.35	17.02	933.96	7.61E-02	4.16E-02	23.92
3-3	0.36	0	1583.99	15.22	0.00	4.10E-02	8.17E-02	17.54
3-4	0.23	0	2689.32	4.94	0.00	3.26E-02	5.91E-02	-
3-5	0.87	1	732.98	0.66	0.00	7.47E-02	8.57E-02	37.00
3-6	0.86	1	1663.41	0.20	0.00	7.53E-02	8.45E-02	24.02
4-1	0.79	1	280.13	45.26	0.00	6.92E-04	3.67E-02	15.40
4-2	0.88	1	2119.23	3.68	0.00	3.95E-02	3.27E-02	29.10
4-3	0.31	0	1576.69	28.26	0.00	2.75E-02	4.07E-02	41.56
4-4	0.53	0	1565.61	3.30	0.00	-	-	51.71
4-5	1.13	0	2748.13	6.05	0.00	-	-	43.96
4-6	0.91	1	1383.62	26.70	0.00	6.51E-02	1.45E-02	19.21

Finally, the null hypothesis for all models was that each factor did not affect filament efficiency. If any of the factors had a $p < 0.05$, this rejects the null hypothesis and concludes that that particular factor does in fact affect filament efficiency.

5.3.1 Factorial Design

This research used a total of seven factorial models, outlined in Table 16 below. One complete model will be displayed below; data from the remaining six models is in Appendix 5.

Table 16. All Factorial Design models evaluated.

Model	Sample Size	# Factors Modelled	Factors Modelled						
			Angular or Curved	% opaque	Total Length of Cracks	Area of Holes	Resistivity	Resistance	Radius of Curvature
1	24	3	x	x		x			
2	21	4	x	x	x	x			
3	21	4	x	x		x			x
4	19	5	x	x		x	x	x	
5	18	5	x	x	x	x			x
6	16	5	x	x		x	x		x
7	16	5	x	x		x		x	x

The response for all models is efficiency. Table 17 represent the Analysis of Variance (ANOVA) for Model 1. Again, factors are only statistically significant with a p-value of $p < 0.05$.

Table 17. ANOVA for factorial design Model 1.

Analysis of Variance

Source	DF	Adj SS	Adj MS	F-Value	P-Value
Model	5	0.80840	0.16168	2.14	0.107
Linear	3	0.16461	0.05487	0.73	0.549
Angular or Curved (A=1, C=0)	1	0.09317	0.09317	1.23	0.281
% image opaque	1	0.12915	0.12915	1.71	0.207
Area of Holes (µm)	1	0.01635	0.01635	0.22	0.647
2-Way Interactions	2	0.28297	0.14149	1.87	0.182
Angular or Curved (A=1, C=0)*% image opaque	1	0.02683	0.02683	0.36	0.559
% image opaque*Area of Holes (µm)	1	0.20794	0.20794	2.75	0.114
Error	18	1.35980	0.07554		
Total	23	2.16820			

In Table 17, DF stands for degrees of freedom, Adj SS is the Adjusted Sum of Squares, Adj MS is the adjusted mean squares, the F-value relates to the F-test, and the p-value determines if a factor is statistically significant.

The degrees of freedom are determined by the sample size and the DF term in the above table shows how much information that term uses in the model. As this model has a sample size of N=24, there are 23 degrees of freedom available, as DF is always equal to N-1. The greater number of DF in the error term, the better the model is able to fit the data to the model.

Adj SS are measures of variation for components of the model. It quantifies the amount of variation in the response data that is explained by each factor or interplay of factors. Adj MS explains how much variation a term explains. Unlike Adj SS, Adj MS considers degrees of freedom in its calculation. Adj MS of the error term is the variance of the fitted values.

The F-value is the test statistic to determine if the factor is associated with the response. F-value directly relates to the p-value. A large F-value indicates a small p-value; thus, the larger an F-value a factor has, the more likely it is to be significant.

As can be seen from Table 17, none of the factors nor their interactions in Model 1 are statistically significant in affecting filament efficiency – none of the p-values are less than 0.05. This fails to reject the null hypothesis that no factors affect the efficiency of the filaments.

The Normal Probability Plot of the residuals is in Figure 45. The Normal Probability Plot shows the standardized effects relative to a distribution fit line for the case when all the effects are 0. The standardized effects are t-statistics that test the null hypothesis that the effect is 0. Positive effects increase the response when the settings change from the low value of the factor to the high value. Negative effects decrease the response when the settings change from the low value of the factor to the high value of the factor. Effects further from 0 on the x-axis have greater magnitude and are more statistically significant. [55] The data is approximately linear, though none of it in this instance is statistically significant.

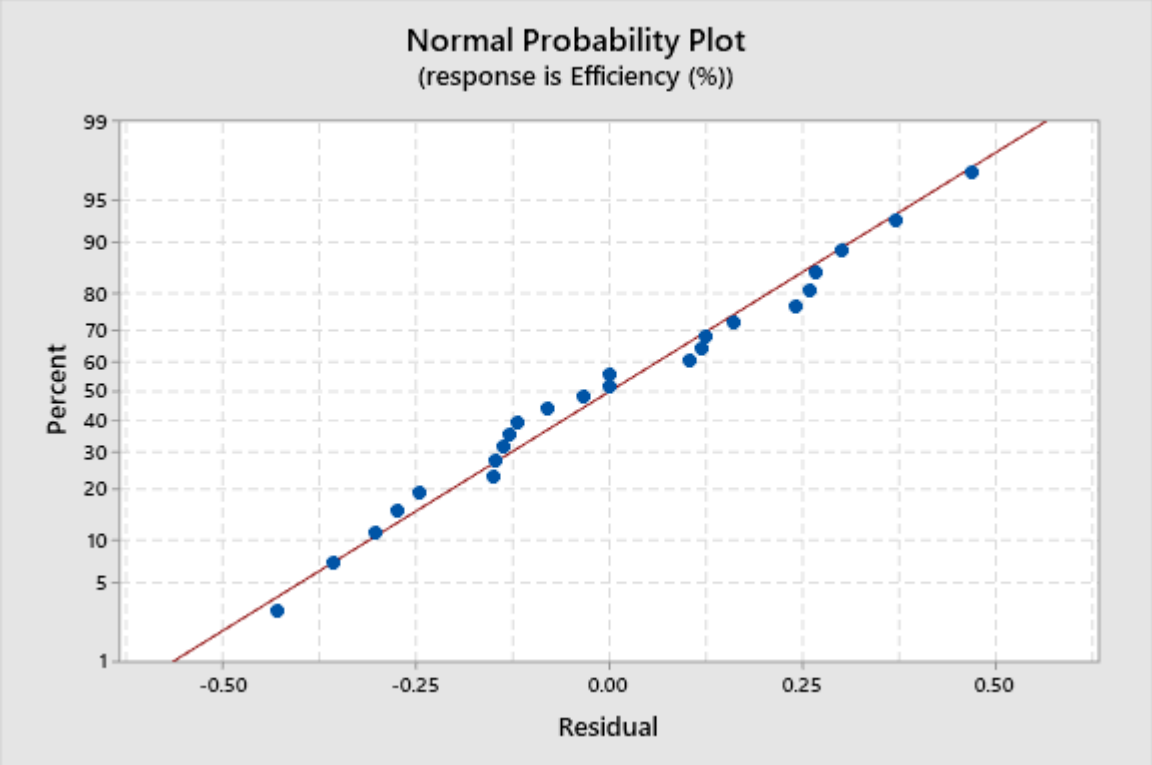

Figure 45. Residuals plot normalized for Model 1. The data is roughly linear.

Figure 46 is a Pareto chart of the factors; the red dashed line is the cut-off line for a factor to be statistically significant. For a factor to be considered significant, the

histogram bar must extend to the right of the dashed line. None of the factors extend past the dashed line, as none are statistically significant. X-axis values are the absolute value of the standardized effects, ranked from largest impact on the response (efficiency) to the smallest.

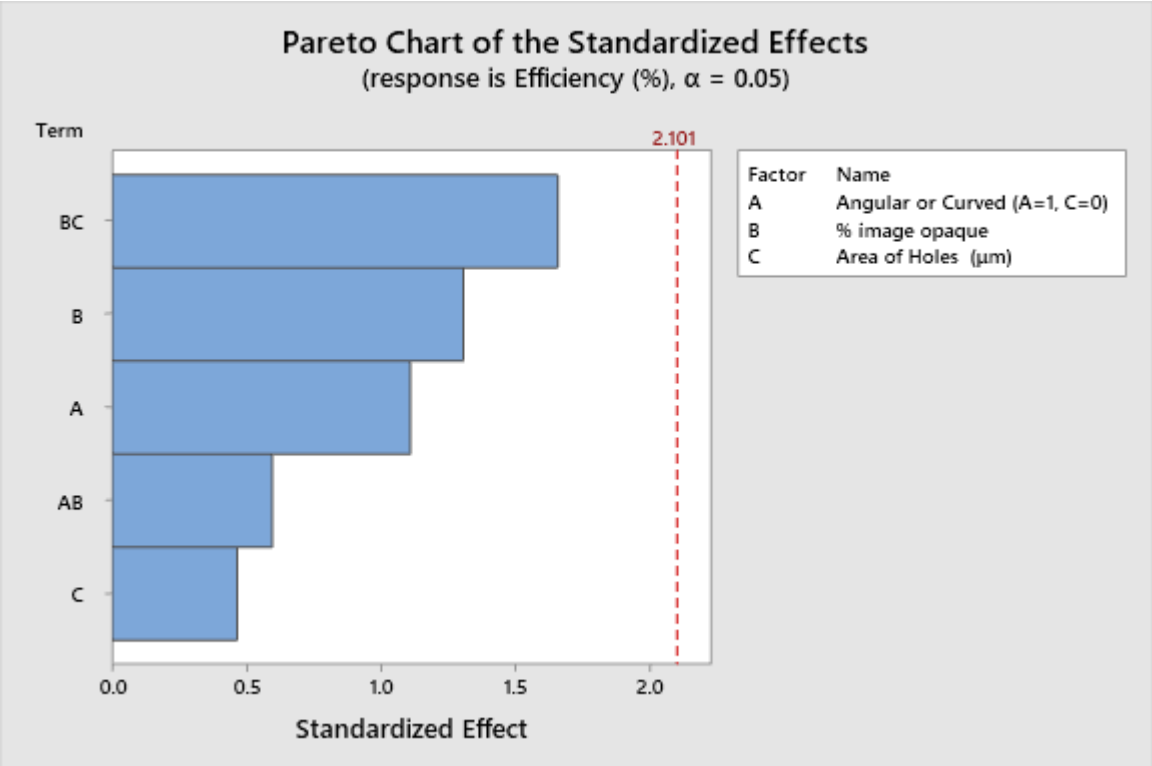

Figure 46. Pareto chart of factors in Model 1, a Factorial Design.

The equation for how efficiency related to the factors in this model is as follows:

Efficiency (%) = 0.659 + 0.351 Angular or Curved (A=1, C=0) + 0.00038 % image opaque - 0.000555 Area of Holes (µm) - 0.00285 Angular or Curved (A=1, C=0)*% image opaque + 0.000013 % image opaque*Area of Holes (µm) (Equation 7)

5.3.2 Response Surface Design

Four of the above models were also tested as a Response Surface Design. Due to the quadratic nature of the response surface design, some degrees of freedom are lost modeling squared terms, and so the three models with the smallest sample size could not be replicated with a Response Surface Design. The four Response Surface Design Models are displayed in Table 18, with the model numbering continuing from Table 16.

Table 18. All Response Surface Design models evaluated.

Model	Sample Size	# Factors Modelled	Factors Modelled						
			Angular or Curved	% opaque	Total Length of Cracks	Area of Holes	Resistivity	Resistance	Radius of Curvature
8	24	3	x	x		x			
9	21	4	x	x	x	x			
10	21	4	x	x		x			x
11	19	5	x	x		x	x	x	

The resulting ANOVA table is below for the outputs from Model 8 using the same factors as in 5.3.1. Given the nature of the data and the subsequent confirmation of the outputs, a linear model best serves this data, not a quadratic model, as the responses fit a linear data set, as can be seen in Figure 47. This design used the same parameters as the factorial design – the same three factors, the same response, efficiency, and a p-value of < 0.05 to determine significance. As demonstrated in Table 19, no factors were significant in this model.

Table 19. ANOVA for the response surface design. No factors are statistically significant.

Analysis of Variance

Source	DF	Adj SS	Adj MS	F-Value	P-Value
Model	6	0.81710	0.136183	1.71	0.178
Linear	3	0.27186	0.090619	1.14	0.361
Angular or Curved (A=1, C=0)	1	0.06108	0.061083	0.77	0.393
% image opaque	1	0.02304	0.023044	0.29	0.597
Area of Holes (µm)	1	0.08788	0.087879	1.11	0.308
Square	2	0.21664	0.108322	1.36	0.282
% image opaque*% image opaque	1	0.00870	0.008700	0.11	0.745
Area of Holes (µm)*Area of Holes (µm)	1	0.20146	0.201463	2.53	0.130
2-Way Interaction	1	0.03553	0.035529	0.45	0.513
Angular or Curved (A=1, C=0)*% image opaque	1	0.03553	0.035529	0.45	0.513
Error	17	1.35110	0.079476		
Total	23	2.16820			

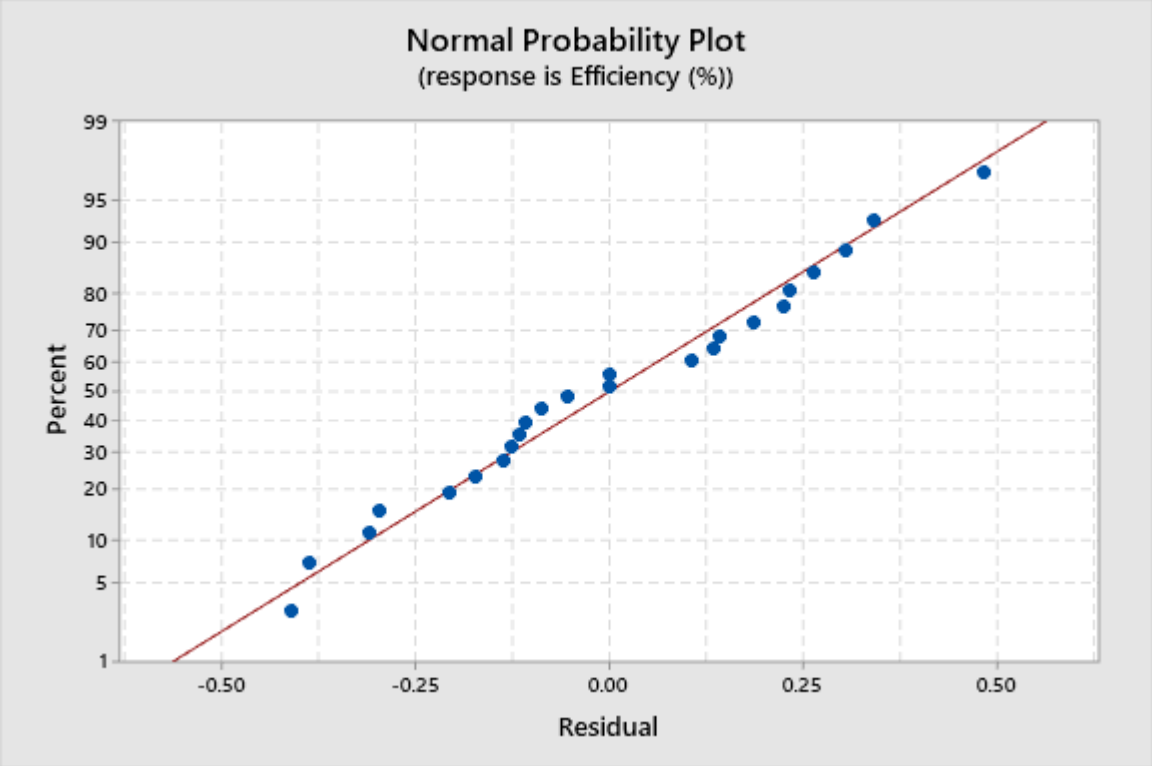

Figure 47. Data is approximately linear, and so a quadratic model is not appropriate.

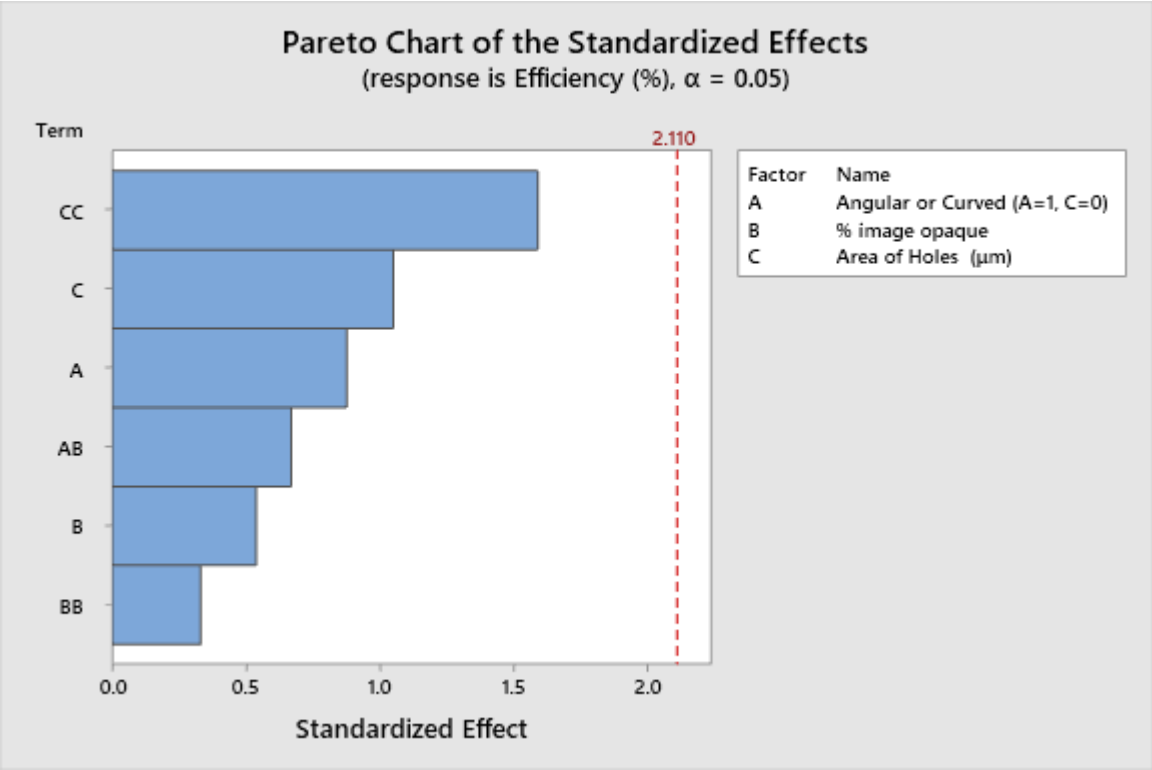

Figure 48. Pareto chart of factors in Model 1, a Response Surface Design.

Figure 47 shows that the residual plot is roughly linear, despite the model being quadratic. Figure 48 is the Pareto chart which also demonstrates that no factors are statistically significant. As in the linear model, no factors are statistically significant.

The equation for how efficiency related to the factors in this model is as follows:

(Equation 8)

Efficiency (%) = 0.627 + 0.370 Angular or Curved (A=1, C=0)
+ 0.00334 % image opaque
+ 0.00946 Area of Holes (µm)
- 0.000030 % image opaque*% image opaque
- 0.000010 Area of Holes (µm)*Area of Holes (µm)
- 0.00376 Angular or Curved (A=1, C=0)*% image opaque

5.3.3 Results from All Models

Of the eleven models evaluated, only one model, model 10, a Response Surface Design, showed any factors having any statistical significance. Model 10 indicated that % opacity and the interplay between % opacity and radius of curvature were both statistically significant. However, given discussion in section 4.3.2, the values for radius of curvature have a low confidence associated with them, and subsequently those results should be considered invalid. Furthermore, as % opacity is common to all 11 models, the fact that it is only significant for one of the models signifies that model 10 is an outlier.

5.4 Angular versus Curved Differences

When filaments were determined to have two distinct shapes in the filament depression, an analysis of the potential difference between these two sets of filaments followed. Table 20 shows the different means and variances for the curved and angular filaments.

Table 20. Curved and Angular Filament Means and Variances

Filament	Efficiency (%)	Angular or Curved (A=1, C=0)	xbar-eff	Squared
1-1	1.08	0	-0.38	0.14
1-3	1.30	0	-0.6	0.36
1-4	0.45	0	0.25	0.06
1-6	0.93	0	-0.23	0.05
2-2	0.94	0	-0.24	0.06
3-1	0.78	0	-0.08	0.01
3-2	0.36	0	0.34	0.12
3-3	0.36	0	0.34	0.12
3-4	0.23	0	0.47	0.22
4-3	0.31	0	0.39	0.15
4-4	0.53	0	0.17	0.03
4-5	1.13	0	-0.43	0.18
Mean	**0.70**		**Variance**	**0.13**
Filament	**Efficiency (%)**	**Angular or Curved (A=1, C=0)**	**xbar-eff**	**Squared**
1-2	1.04	1	-0.0908	0.0083
1-5	0.66	1	0.28917	0.0836
2-1	0.90	1	0.04917	0.0024
2-3	1.10	1	-0.1508	0.0228
2-4	1.26	1	-0.3108	0.0966
2-5	1.13	1	-0.1808	0.0327
2-6	0.99	1	-0.0408	0.0017
3-5	0.87	1	0.07917	0.0063
3-6	0.86	1	0.08917	0.0080
4-1	0.79	1	0.15917	0.0253
4-2	0.88	1	0.06917	0.0048
4-6	0.91	1	0.03917	0.0015
Mean	**0.95**		**Variance**	**0.024**

Curved filaments overall have a mean efficiency of 0.7 with a variance of 0.13, whereas angular filaments have a mean efficiency of 0.95 with a

variance of .024. Angular filaments have significantly less variance than curved. To determine if these two means are statistically separate, a two-sample t-test was conducted, with the results below in Figure 49. As with all other statistical models, all statistics are at a 95% confidence interval.

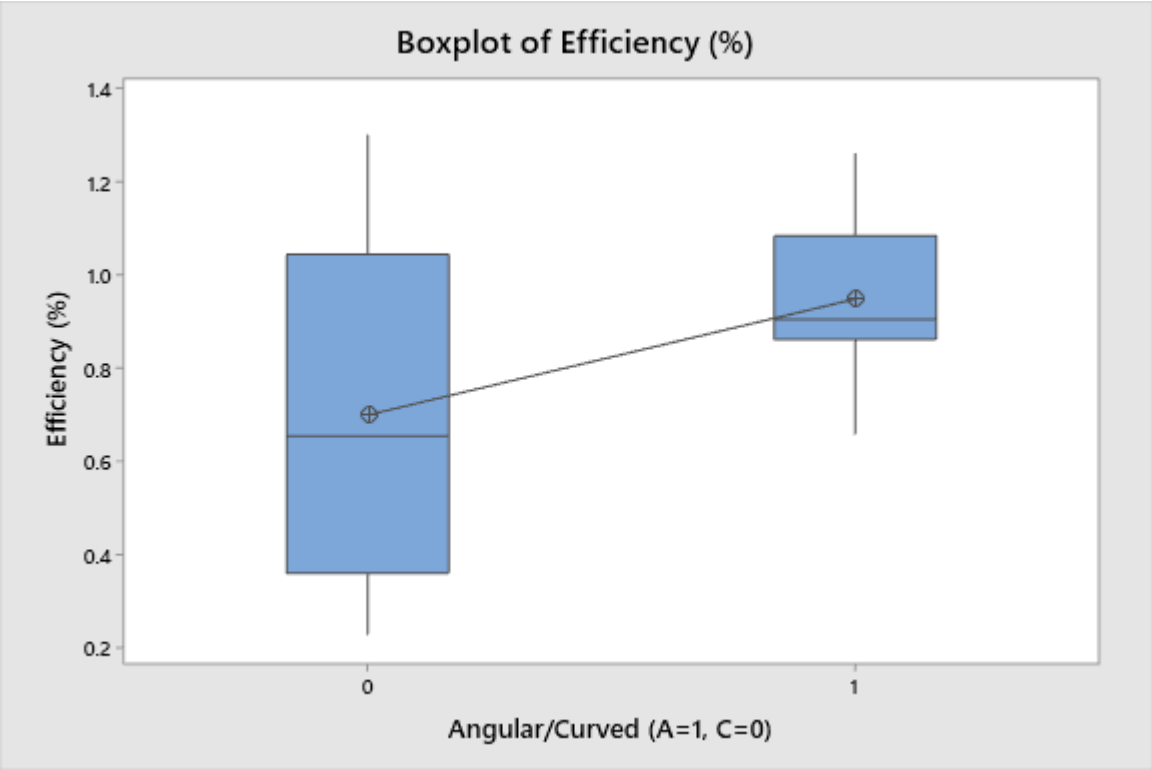

Figure 49. Boxplots of angular (right box) and curved (left box) filaments.

The t-test for these two values is below:

Test

Null hypothesis	$H_0: \mu_1 - \mu_2 = 0$
Alternative hypothesis	$H_1: \mu_1 - \mu_2 \neq 0$

T-Value	DF	P-Value
-2.14	15	0.050

Due to a p-value of 0.050, this rejects the null hypothesis and concludes that the means are different. Angular and curved filaments have different means and different variances. The angular filaments have a higher mean and lower variance than the curved filaments. Efficiency in curved filaments is more unpredictable due to the increased variance. For consistency, it is thus desirable for filaments used in TIMS measurements to be angular rather than curved.

5.5 Other Findings

Due to the necessity of re-imaging filaments whose first run of images could not be stitched, an additional phenomenon was discovered. The opacity of the filaments evolved in the intervening period between when the images were taken. Figure 50 shows the difference in opacity for filament 1-5 after three months and then after an additional two months. Red circles denote regions of difference between August and November, and yellow circles denote differences between November and January. The top right in particular had an increase in opacity, along with the bottom of the canoe. A number of factors could cause this change in opacity and is a possibility for future work. Appendix 6 contains all stitched images, along with the cropped image of the filament depression, that were used in this experiment.

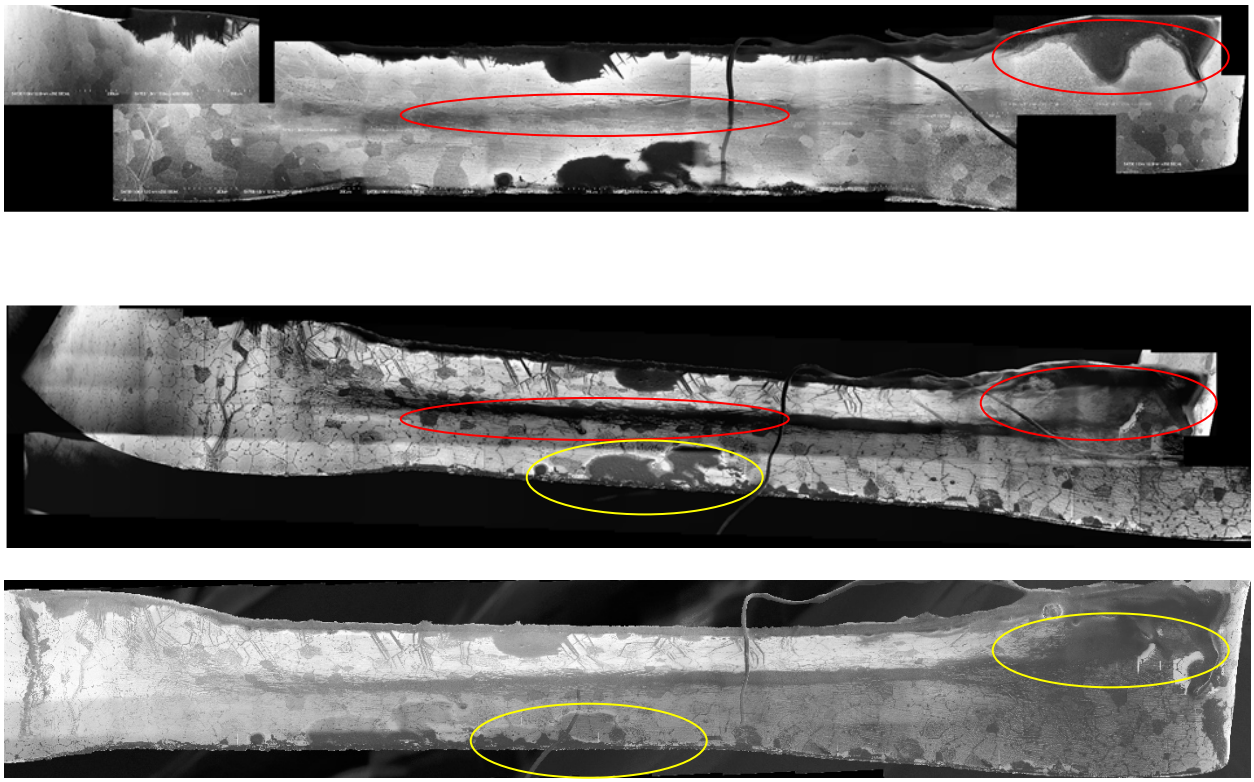

Figure 50. Time evolution of filament opacity. The top image was taken in August 2019, the middle in November 2019, and the bottom in January 2020.

6. Conclusions and Future Work

6.1 Reflections on Obtained Data

The results of the factorial and response surface design experiments demonstrate that none of the seven factors evaluated had an effect on the efficiency of the filaments. Model 10 was the only model to indicate that % opacity and radius of curvature were statistically significant, but due to the fact that there exists a low level of confidence in the values for radius of curvature, and the fact that % opacity occurs in all 11 models but was only significant in one of them, leads to the conclusion that Model 10 is an outlier. Furthermore, given that opacity has been demonstrated to change over time, it cannot be a reliable indicator of efficiency given its continually changing nature.

The shape of the filament depression did affect the variance of the data; angular filaments had less variance in their efficiency values than curved filaments did, and angular filaments had a higher mean efficiency than curved filaments. The shape of the data indicated that a linear model was the best model for this experiment. The fact that none of the factors identified affected filament efficiency is interesting, particularly given the existence of literature that directly contradicts these findings. The shape of rhenium filaments has been demonstrated to have an impact on ionization efficiency and this has been known for decades. [56] This experiment's findings that filament shape affects efficiency is in line with previous experiments by McHugh and Dietz that the v-shaped filament was the most efficiency single filament methods for TIMS. [56] [57] Holes in the filament depression would also adversely affect electrical conductivity, and thus ionization of a sample, while excessive cracks would permit oxidation, also known to

impede filament efficiency [16]. As filaments are heated by passing an electric current through them, it follows rationally that electrical resistance and resistivity would have bearing on filament efficiency as well, but once again, the data directly contradicts this.

Although the data suggests that none of the factors could be statistically correlated to ionization efficiency, the disparity in variances between angular and curved filaments is evident. Better process control to standardize the shape of the filament depressions in the angular form would be beneficial in reducing the disparity in calculated efficiencies.

6.2 Sample Size Limitations

As is always the case in statistics, the greater the sample size, the better. Naturally optimal sample size must be balanced against time and resources, although it is important to note that smaller sample sizes will result in decreased accuracy. A rule of thumb in linear regression analysis is that for each independent variable measured, at least 10 samples are optimal. [58] Given that there were seven independent variables evaluated in this experiment, at least 70 filaments would have been an optimum sample size. This may have been time-prohibitive, but the small sample size – particularly as all filaments could not be evaluated for all seven factors – means that the data is not as robust as it could be.

The small sample size limits how much can be extrapolated from the data, as well as limiting how representative of the total population of the rhenium filaments utilized by AFTAC the data produced actually is. A better idea of the actual population size – such as how many filaments are used in a year at this particular laboratory – would greatly

increase the confidence level in how accurate this sample could be of the population that it is representing.

6.3 Conclusions from the Data

Based on the data collected in this experiment, there exist three possibilities to conclude:

1. There are no surface features identifiable from SEM imagery that affect filament efficiency.
2. There are additional factors identifiable from other techniques besides SEM imagery that affect filament efficiency.
3. There are additional, unknown factors that affected the original calculation of filament efficiency.

Based on literary evidence, conclusion (1) is unlikely, as there have been numerous studies demonstrating factors that can be tied directly to filament efficiency. There is one set of surface features that this experiment did not analyze, and that pertains to grain size and orientation; this would be a fruitful path for further study. Conclusion (2) is possible, and is a candidate for future work. Recommendation is that most future work should focus on other analysis techniques to get a more complete picture of the structure and chemistry of the rhenium filaments. Aside from grain orientation, there is little additional work that can be done with solely an SEM system, and even grain orientation requires other resources such as Electron Backscatter Diffraction (EBSD).

Conclusion (3) bears further investigation. Process improvement in the manufacture of rhenium filaments to ensure more uniformity in the filaments themselves would aid in standardization, and thus a likely reduction in filament efficiency variance. Furthermore, the method by which rhenium filament efficiency is calculated deserves a closer look to ensure the most accurate data is available.

6.4 Recommendations for Process Improvement

Some of the variance is likely be due to the process by which the filaments are created, and efficiencies will be suggested to be built into the process to ensure uniformity. Recommendations could include applying the principles of Lean Six Sigma to the filament preparation process to reduce population variance, as the external factors that affect the filaments will be lessened. Cracks in the material are ripe for oxidation, and so should be minimized in filament preparation. The potential exists for Value Stream Mapping (VSM), Kaizen and Kanban implementation at AFTAC to improve process flow and filament uniformity. [59] Kaizen refers to the continuous improvement of a process by all staff, while Kanban refers to improving process flow to speed up processing time while maintaining efficiency.

A method of standardizing solution deposition on the filaments is likely to be most beneficial. Standardizing the means by which a filament's depression is stamped will prevent filaments that are stamped off-centerline as well as regulate the shape of the filaments. Angular filaments have less variance and a higher mean efficiency, and are thus more desirable for TIMS analysis. Better controls over the stamping process will aid in producing filaments that are shaped most beneficially for ionization efficiency. It is crucial that the ionization efficiency values are accurate, as if they are not, this could produce faulty data which incorrectly identifies the substances evaluated.

The process of preparing filaments for TIMS utilization must be continually refined and standardized to prevent filament defects occurring from mishandling of

filaments, improper rhenium filament sizes requisitioned, and uniformity in sample distribution on the filaments.

6.5 Future Work

Future work should focus on identifying which of the three potential conclusions postulated in section 6.3 are accurate. A simple way to determine if conclusion (1) or conclusion (3) are valid is to obtain a sample of rhenium filaments from a different laboratory and conducting the same experiment again, and see if there is a correlation between efficiency and surface features. If the filaments from the second lab also do not show a correlation between surface features and efficiency, then conclusion (1) becomes more likely. If the filaments from the second lab do, however, show a correlation, then conclusion (3) is more likely. One surface feature not evaluated in this experiment is average grain size, and this could be incorporated into future work as a potential variable that could affect efficiency.

Conclusion (2) can be observed utilizing a variety of different techniques to examine depth of carburization of the filament, certain types of mass spectrometry or X-ray fluorescence (XRF) to identify the composition of the opaque areas in the SEM imagery, and using an EBSD system to determine dominant grain orientation. Finally, once a method has been determined to definitively identify oxidized grains, a ratio of oxidized grains to non-oxidized grains would be fruitful; however, if the time evolution of the rhenium filament surface is caused by additional oxidation, time becomes in a factor in this analysis, as the filaments may continue to oxidize the longer they are stored.

Time evolution of rhenium filament, utilizing raw rhenium and carburized filaments and observing changes, specifically oxidation, over time, is another fruitful bit of experimentation worth exploring in the future. As one hopes to identify defective filaments before use, analyzing unused filaments prior to loading in TIMS and seeing if surface or material composition defects exist that affect ionization efficiency is crucial. Perhaps the use of a different filament material, such as tungsten, and observing if similar surface features identified via an SEM system can correlate to efficiency would also be of use in broadening knowledge for actinide evaluation in TIMS.

Bibliography

1. Office of the Secretary of Defense, "Nuclear Posture Review," 2018, accessed at https://dod.defense.gov/News/SpecialReports/2018NuclearPostureReview.aspx

2. Bodansky, David, *Nuclear Energy: Principles, Practices and Prospects*, Second Edition, Springer Science + Business Media, 2004.

3. International Atomic Energy Agency, "Treaty on the Non-Proliferation of Nuclear Weapons," 1970.

4. Baxter, Phillip, "The False Hope of Nuclear Forensics? Assessing the Timeliness of Forensics Intelligence," American Federation of Scientists, 2015.

5. Kraim, M., Richter, S., Kuhn, H., Aregbe, Y., *Development of an improved method to perform single particle analysis by TIMS for nuclear safeguards*, in Analytica Chimica Acta, Vol 688, 2011.

6. Becker, Johanna Sabine, "Inorganic Mass Spectrometry of Radionuclides," in *Handbook of Radioactivity Analysis,* edited by Michael F. L'Annubziata, Elsevier Inc., 2012.

7. Kristo, Michael, "Nuclear Forensics," in *Handbook of Radioactivity Analysis,* edited by Michael F. L'Annubziata, Elsevier Inc., 2012.

8. Makishima Akio, *Thermal Ionization Mass Spectrometry (TIMS)*, John Wiley & Sons Inc., 2016.

9. Wade, Leroy G., *Organic Chemistry 5th Edition*, Prentice-Hall Inc., 2002.

10. Mayer, Klaus, Wallenius, Maria, Varga, Zsolt, Hedberg, Magnus and Erdmann, Nicole, "Inorganic Mass Spectrometry as a Tool of Destructive Nuclear Forensic Analysis," in *The New Nuclear Forensics: Analysis of Nuclear Materials for Security Purposes*, edited by Vitaly Fedchenko, Oxford University Press, pages 48-49, 2015.

11. Glenn, John. *Strategic Reserves* at Electron Café Marketplace, Power Online.

12. Warneke, Thorsten, *High-Precision Isotope Ratio Measurements of Uranium and Plutonium in the Environment*, Ph.D. dissertation, University of Southampton, 2002.

13. Gall, N.R., Mikhailov S.N., Rut'kov E.V., Tontegode A.Y., *Carbon Interaction with the Rhenium Surface*, in Surface Science, Vol 191, Issues 1-2, pgs 185-202, 1969.

14. Robinson, Charles F. and Sharkey, A.G., *Rhenium as an Electron Emitter in Mass Spectrometry*, in Review of Scientific Instruments 29, 1958.

15. Pallmer, P.E. and Gordon, R.L., *The Work Function of Carburized Rhenium*, in Journal of Applied Physics Vol 51, Issue 7, 1980.

16. Shatynski, Stephen R., *The Thermochemistry of Transition Metal Carbides*, in Oxidation of Metals Vol 13, No. 2, 1979

17. Mannion, Joseph M., Wellons, Matthew S., Shick, Charles R., Fugate, Glenn A., Powell, Brian A., Husson, Scott M., *Ambient aging of rhenium filaments used in thermal ionization mass spectrometry: Growth of oxo-rhenium crystallites and anti-aging strategies*, in Heliyon, Vol 3, Issue 1, 2017.

18. Mannion, Joseph M., *Improved Sample Loading for Plutonium Analysis by Thermal Ionization Mass Spectrometry and Alpha Spectroscopy,* Ph.D. dissertation, Clemson University, 2017.

19. Mannion, Joseph and Fugate, Glenn, *Rhenium Filament Oxidation: Effect on TIMS Performance and the Roles of Carburization and Humidity*, in Talanta Vol 168, 2017.

20. Bramnik, Kirill G., *Ternary and quaternary phases in the alkali-earth - rhenium - oxygen system*, Ph.D. Dissertation, Vom Fachbereich Material- und Geowissenschaftender Technischen Universität Darmstad, 2001.

21. Shcheglov, P.A. and Drobot, D.V., *Heterogeneous Equilibria in the Rhenium-Oxygen System*, in Russian Journal of Physical Chemistry, Vol, 80, No. 11, 2006.

22. Office of the Secretary of the Interior, "Final List of Critical Minerals 2018," 2018.

23. Lasley, Shane, *Rhenium – The Hot Superalloy Element*, in North of 60 Mining News Online Column, 2019.

24. Royal Society of Chemistry, Periodic Table, Cambridge, UK 2019.

25. Millensifer, Tom A. *Rhenium and Rhenium Compounds*, in Kirk-Othmer Encyclopedia of Chemical Technology, John Wiley & Sons, Inc., 2010.

26. Ford, R.R. and Lichtman, David, *Ion Emission from Rhenium and Lanthaxum Hexaboride Coated Rhenium Filaments*, in Journal of Applied Physics, Vol. 40, Issue 13, 1970.

27. Kaoumi, Djamel, *Investigations of the Chemical Compatibility of Rhenium With Uranium Dioxide At Elevated Temperatures*, Master's Thesis, University of Florida, 2001.

28. ESPI Metals, *Rhenium Fact Sheet*, ESPI Metals, 2019.

29. Vallopplly, Shah, Private Correspondence regarding unpublished database at Nebraska Center for Materials and Neuroscience.

30. Greiner, Mark T., Rocha Tulio C.R., Johnson, Benjamin, Klyushin, Alexander, Knop-Gericke, Axel, and Schlogl, Robert, *The Oxidation of Rhenium and Identification of Rhenium Oxides During Catalytic Partial Oxidation of Ethylene: An In-Situ XPS Study*, in Physical Chemistry, Vol 228, 2014.

31. Delmore, J.E., *The Ionization of Selected Elements in the Nuclear Fuel Cycle*, Conference Notes, Netherlands, 1978.

32. Watrolus, Matthew G. and Delmore, James E., *Metal dicarbides as intermediate species in thermal ion formation mechanisms*, in International Journal of Mass Spectrometry, Vol 286, Issue 1, pages 7-10 2009.

33. Smith, David H., *Mass Spectrometric Investigation of Surface Ionization. X. Desorption of Uranium Ions and Neutrals from Carburized Rhenium,* in The Journal of Chemical Physics, Volume 55, Issue 8, 1971.

34. Jaffee, R.I. and Sims, C.T., *Technical Report on the Effect of Rhenium on the Fabricability and Ductility of Molybdenum and Tungsten*, Department of the Navy Office of Naval Research, 1958.

35. Smith, David H. "Mass Spectrometric Investigation of Surface Ionization. X. Desorption of Uranium Ions and Neutrals from Carburized Rhenium," in *The Journal of Chemical Physics,* 1971.

36. Zhang,Ling, Xiong, Penghui, Zhang, Hailu, Chen, Lumin, Xu, Jie, Wu, Haoxi, Qin, Zhen, "Mass Spectrometric Investigation of Surface Ionization. X. Desorption of Uranium Ions and Neutrals from Carburized Rhenium," in *Analytical Chemistry*, 2019.

37. Studier, Martin H., Sloth, Eric N., and Moore, Leon P., "The Chemistry of Uranium In Surface Ionization Sources," in *Journal of Physical Chemistry,* 1962, 133-134.

38. Studier, Martin H., "Gaseous Oxides of Rhenium," in *Journal of Physical Chemistry*, 1962, 189.

39. Lide, D.R. (Editor), "Ionization Potentials of Atoms and Atomic Ions" in *Handbook of Chemistry and Physics*, 1992, 10-211.

40. *Hitachi S-4700 FESEM Manual*, Hitachi Scientific Instruments, 2018.

41. Goldstein, Joseph I., Newbury, Dale E., Michael, Joseph R., Ritchie, Nicholas W.M., Scott, John Henry J., Joy, David C., *Scanning Electron Microscopy and X-Ray Microanalysis*¸ Fourth Edition, Springer Science + Business Media, 2018.

42. Joy, D.C. and Luo, S., *An Empirical Stopping Power Relationship for Low-Energy Electrons*¸ in Scanning, Vol. 11, pages 176-180, 1989.

43. Hafner, Bob, *Scanning Electron Microscopy Primer*, University of Minnesota – Twin Cities Characterization Facility, 2007.

44. Liao, Yougui, *Practical Electron Microscopy and Database*, GlobalSino, 2018.

45. *X-Ray Transition Energies Database*, National Institute of Standards and Technology, Physical Measurements Laboratory, 2020, accessed at https://physics.nist.gov/PhysRefData/XrayTrans/Html/search.html on 9 February 2020.

46. Bulloss, Nick, *Technical Note TN-002 Pitfalls of Energy-Dispersive X-Ray Spectroscopy: Dead Time and Peak Artifacts*, Boise State University, 2017.

47. Montgomery, Douglas C., *Design and Analysis of Experiments,* Arizona State University, Eighth Edition, 2013.

48. S. Preibisch, S. Saalfeld, P. Tomancak (2009) "Globally optimal stitching of tiled 3D microscopic image acquisitions", Bioinformatics, 25(11):1463-1465.

49. *INCA Energy Operator Manual*, Oxford Instruments Analytical, 2006.

50. Raynald, Gauvin, "What is CASINO?," Université de Sherbrooke, accessed at https://www.gel.usherbrooke.ca/casino/What.html on 2 September 2019.

51. Gasser, R.P.H. and Marsay, C.J., *The Reaction of Oxygen with Rhenium*, in Surface Science Vol 20, Issue 1, 1970.

52. Milton, Susan J. and Arnold, Jesse C., *Introduction to Probability and Statistics: Principles and Applications for Engineering and the Computing Sciences Fourth Edition*, McGraw Hill Education (India) Private Limited, 2003.

53. Siegle, Del, *T-Test*, University of Connecticut Educational Research Basics, 2019.

54. Morris, Max D., *Design of Experiments: An Introduction Based on Linear Models*, CRC Press, 2011.

55. "Effects plots for Analyze Factorial Design," Minitab '18 Support, Minitab LLC, 2019, accessed at https://support.minitab.com/en-us/minitab/18/help-and-how-to/modeling-statistics/doe/how-to/factorial/analyze-factorial-design/interpret-the-results/all-statistics-and-graphs/effects-plots/

56. McHugh, James A. *Surface Ionization – the Rhenium V-type Single Filament*, in International Journal of Mass Spectrometry and Ion Physics, Vol 3, Issues 3-4, October 1969, pages 267-276.

57. Dietz, Leonard A. *Optics for the V-Type Surface Ionization Filament Used in Mass Spectrometry*, in Review of Scientific Instruments, Issue 30, 1959, pages 235-241.

58. "Sample Size Formula," Statistics Solutions, USA, 2019, accessed at https://www.statisticssolutions.com/sample-size-formula/

59. Rastogi, Ankit, "A Brief Introduction to Lean, Six Sigma, and Lean Six Sigma," GreyCampus, 2018.

Appendix 1: CRM-129 Specifications

New Brunswick Laboratory
U.S. Department of Energy

Certificate of Analysis
CRM 129-A
Uranium Oxide (U_3O_8) Assay and Isotopic Standard

Uranium Assay (Mass Fraction) .....0.847698 ± 0.000090 kg U/kg

Isotopic Ratios	$^{234}U/^{238}U$	$^{235}U/^{238}U$	$^{236}U/^{238}U$
Atom Ratios	0.000053350 ± 0.000000039	0.0072614 ± 0.0000039	0.000000097 ± 0.000000012

Isotopic Abundance	^{234}U	^{235}U	^{236}U	^{238}U
Atom Fraction (x 100)	0.0052962 ± 0.0000038	0.72087 ± 0.00039	0.0000097 ± 0.0000012	99.27382 ± 0.00039
Mass Fraction (x 100)	0.0052075 ± 0.0000038	0.71183 ± 0.00039	0.0000096 ± 0.0000012	99.28295 ± 0.00039

Relative Atomic Mass of Uranium .....238.028894 ± 0.000012

Reported numerical uncertainties are expressed as expanded uncertainties (U) at the 95% level of confidence, where $U = k \cdot u_c$, k is the coverage factor, and u_c is the combined standard uncertainty. The last figure in the reported values and their uncertainties is provided for information purposes only and is not intended to convey a significant degree of reliability.

This Certified Reference Material (CRM) is an assay (elemental concentration) and isotopic standard primarily for use in uranium determinations. Each unit of CRM 129-A contains approximately 1 gram of uranium (nominally normal) oxide (U_3O_8) contained in a glass jar. Before use, follow the recommended procedure for ignition of material.

NOTE: *The material should be handled under proper radiologically-controlled conditions at all times.*

RECOMMENDED PROCEDURE FOR IGNITION OF MATERIAL

To ensure accurate measurement results for uranium determination, CRM 129-A must be ignited in an open dish or crucible in a muffle furnace at 800°C for one hour and cooled in a desiccator prior to use. The ignition temperature, 800°C, was determined to provide the greatest weight loss stability for this specific lot of material.

The source material for CRM 129-A was prepared in 1984, at NLO, Inc., Cincinnati, OH, from a supply of highly pure UO_2 pellets. The pellets were crushed, dissolved in nitric acid, the solution precipitated with hydrogen peroxide, then filtered, dried, calcined at 900°C, milled, and screened. The final product was blended and shipped to New Brunswick Laboratory.

March 1, 2008
Argonne, Illinois

www.nbl.doe.gov
Page 1 of 2

Jon Neuhoff, Director
New Brunswick Laboratory

(Editorial revision of NBL Certificate dated November 30, 2003)

A random sample of the units was taken for uranium assay (elemental concentration) and isotopic abundance analyses. The uranium assay was determined by the NBL High Precision Titrimetric Method using National Institute of Standards and Technology (NIST) Standard Reference Material (SRM) 136e, Potassium Dichromate ($K_2Cr_2O_7$) Oxidimetric Standard, as the titrant. NBL CRM 112-A, Uranium Metal Assay Standard, and NBL CRM 129, Uranium Oxide (U_3O_8) Assay Standard were used as controls to verify proper performance of the measurement systems. Uranium assay measurements were performed by two analysts each using independent titration systems. Prior to titration preparation, CRM 129-A analysis samples were ignited at 800°C to constant weight to determine the recommended procedure for ignition.

The uranium isotopic composition and the relative atomic mass of uranium were determined by thermal ionization mass spectrometry (TIMS). The following relative atomic masses were used in calculations: ^{234}U - 234.0409456, ^{235}U - 235.0439231, ^{236}U - 236.0455619, and ^{238}U - 238.0507826. Uranium isotopic ratio measurements were performed by two analysts each using a different mass spectrometer. One TIMS instrument, utilizing the Total Evaporation procedure, was used to generate values for the certification of only the $^{235}U/^{238}U$ ratio. A second TIMS instrument, utilizing the NBL-Modified Total Evaporation procedure, was used to generate values for the $^{235}U/^{238}U$ ratio. The $^{234}U/^{238}U$ and $^{236}U/^{238}U$ ratios were also measured on this instrument using an energy/direction filter lens assembly and a high signal-intensity static multi-collector method with the ^{236}U measured using a secondary electron multiplier. The minor ratios were corrected internally using the $^{235}U/^{238}U$ ratio determined by the Total Evaporation and NBL Modified Total Evaporation methods. Mass discrimination correction factors applied to measured CRM 129-A $^{235}U/^{238}U$ isotopic ratios were determined from multiple analyses of NBL CRM U030-A, Uranium Isotope Standard (3% enriched), run sequentially with CRM 129-A. Measurements of NBL CRM U500, Uranium Isotopic Standard (50% enriched), were used as a control to verify proper performance of the measurement system for the $^{235}U/^{238}U$ measurements. Measurements of NBL CRM U010, Uranium Isotopic Standard (1.0% enriched), were used as a control to verify proper performance of the measurement system for the $^{234}U/^{238}U$ and $^{236}U/^{238}U$ measurements. Mass spectrometric measurements indicate that there is no detectable ^{232}U and no significant heterogeneity in the isotopic abundances of ^{234}U, ^{235}U, and ^{238}U within and between units. Isotopic heterogeneity was, however, observed in the abundance of ^{236}U. The uncertainties calculated for the ^{236}U isotopic abundance and $^{236}U/^{238}U$ isotopic ratio incorporate the observed variability.

The expanded uncertainty (U) for a certified property of CRM 129-A defines an interval around the value of the property and is calculated according to the ANSI/NCSL Guide[1]. The magnitude of this interval is obtained by multiplying the combined standard uncertainty (u_c) by a coverage factor (k). The coverage factor, k, is the Student's t factor based on the effective degrees of freedom to provide a 95% level of confidence. The combined standard uncertainty (u_c) for uranium assay consists of Type A components derived from standard deviations associated with analyst-to-analyst differences and titration measurements; and a Type B component based on the standard uncertainty taken from the NIST SRM 136e certificate. The combined standard uncertainties (u_c) for uranium isotopic parameters consist of Type A components derived from standard deviations associated with isotopic ratio measurements of the samples and the measurements of the $^{235}U/^{238}U$ ratio of NBL CRM U030-A, and estimates of isotopic inhomogeneity of the samples; and a Type B component based on the standard uncertainty derived from the uncertainties associated with the NBL CRM U030-A certified value for the $^{235}U/^{238}U$ ratio.

Project coordination was provided by A. M. Voeks. High precision titrimetric assay measurements were performed by G. J. Orlowicz and A. M. Voeks. Isotopic abundance measurements were performed by R. M. Essex and S. Richter. Health physics support was provided by H. S. Gruhn. The statistical plan of analysis for assay measurements was prepared by M. D. Soriano and for isotopic measurements by R. M. Essex and S. A. Goldberg. The statistical evaluation of data was performed by M. D. Soriano and reviewed by W. C. Losinger. Technical guidance for CRM 129-A certification and issuance was provided by M. A. Legel and U. I. Narayanan. Project supervision was provided by S. A. Goldberg, U. I. Narayanan and J. W. Neuhoff.

[1] American National Standard for Calibration - U.S. Guide to the Expression of Uncertainty in Measurement [GUM]. ANSI/NCSL Z540-2-1997.

March 1, 2008
Argonne, Illinois

Jon Neuhoff, Director
New Brunswick Laboratory

(Editorial revision of NBL Certificate dated November 30, 2003)

Appendix 2: Bethe Equation MATLAB Code

```
A=186.21;

NA=6.022E23;

p=21.02;

z=75;

i=1;

for Ei=5:1:30

   range(i,:)=(0.0276.*A.*Ei.^(1.67))./(z.^(0.89).*p);

   energy(i)=Ei;

   i=i+1;

end


d=-7.85*((z*p)/(A*Ei)*log((1.166*Ei/(9.76*z+58.5*z^(-0.19))*10^(-3))))


figure

plot(energy,range);

xlabel('Energy(keV)')

ylabel('Range(um)')

title('Bethe Eqn Range vs Energy')

grid on

grid minor
```

Appendix 3: Radius of Curvature Measurement FIJI Code

```
//initial set-up, derived from imagej-macro "curvatureRadius" (Herbie G., 05. December 2018)
requires( "1.52i" );
setOption("BlackBackground", true);
//designates size and crops
w=getWidth();
h=getHeight()-20;
makeRectangle(0,20,w,h);
run("Crop");
//sets threshold for greyscale
setAutoThreshold("Intermodes dark");
//converts image to binary black and white image
run("Convert to Mask");
h*=0.5;
//"clicks" on the pixel at the coordinates (0,h)
doWand(0,h);
run("Make Inverse");
run("Interpolate", "interval="+h);
//sets coordinates for points of triangle
x = newArray(3);
y = newArray(3);
```

```
getSelectionCoordinates(xx, yy);
rank = Array.rankPositions(xx);
for ( i=0; i<3; i++) {
   x[i] = xx[rank[i]];
   y[i] = yy[rank[i]];
}
// the following calculates the perimeter of the triangle and then the circumcircle
// which is the circle whose circumference passes through the three points
// of the triangle, derived from code at
// https://bitbucket.org/davemason/threepointcircumcircle/src/master/
d1=sqrt((x[0]-x[1])*(x[0]-x[1])+(y[0]-y[1])*(y[0]-y[1]));
d2=sqrt((x[1]-x[2])*(x[1]-x[2])+(y[1]-y[2])*(y[1]-y[2]));
d3=sqrt((x[2]-x[0])*(x[2]-x[0])+(y[2]-y[0])*(y[2]-y[0]));
// calculate radius of curvature
r=(d1*d2*d3)/sqrt((d1+d2+d3)*(d2+d3-d1)*(d3+d1-d2)*(d1+d2-d3));
print("Radius: "+d2s(r, 2));
exit();
```

Appendix 4: Rhenium Filament 3-D Surface Plots

Filament 1-1 3-D Surface Plot

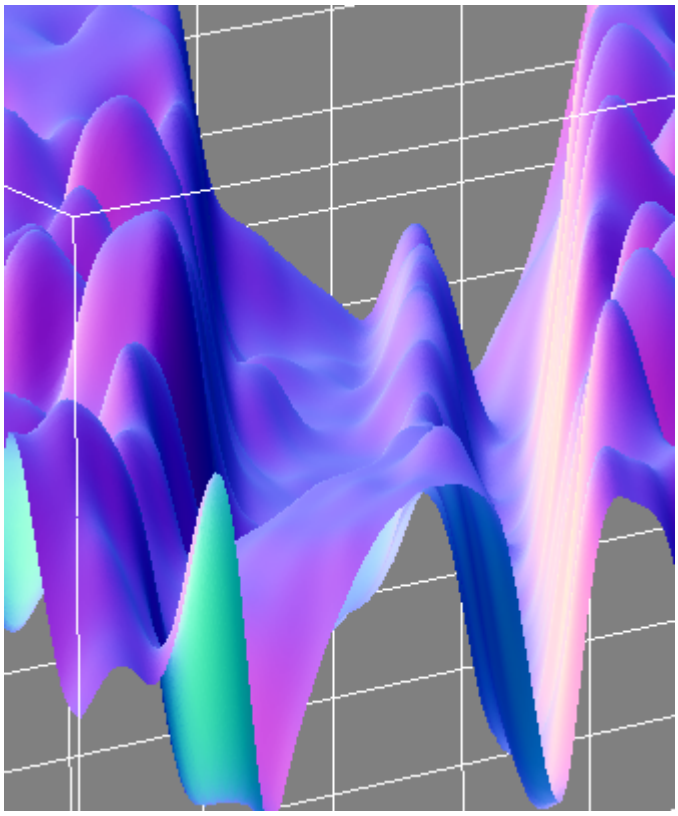

Filament 1-2 3-D Surface Plot

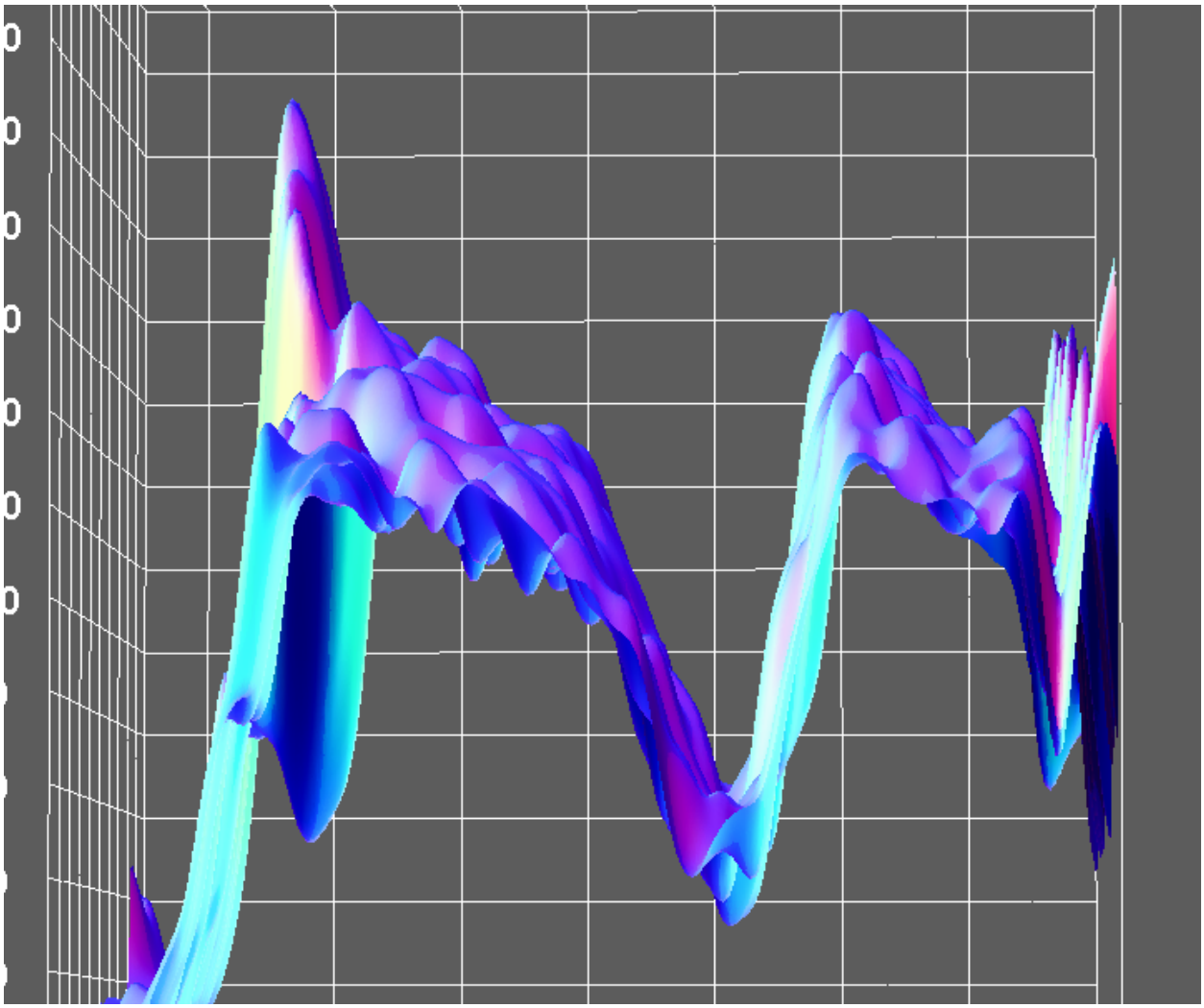

Filament 1-3 3-D Surface Plot

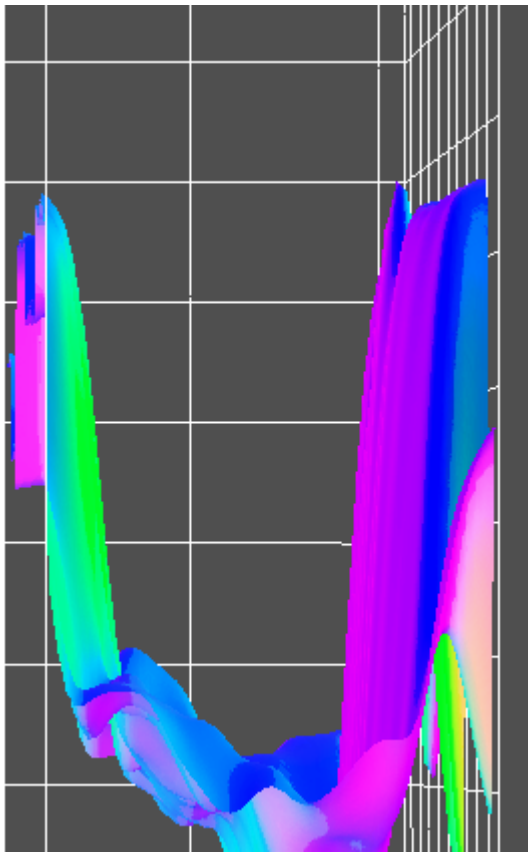

Filament 1-4 3-D Surface Plot

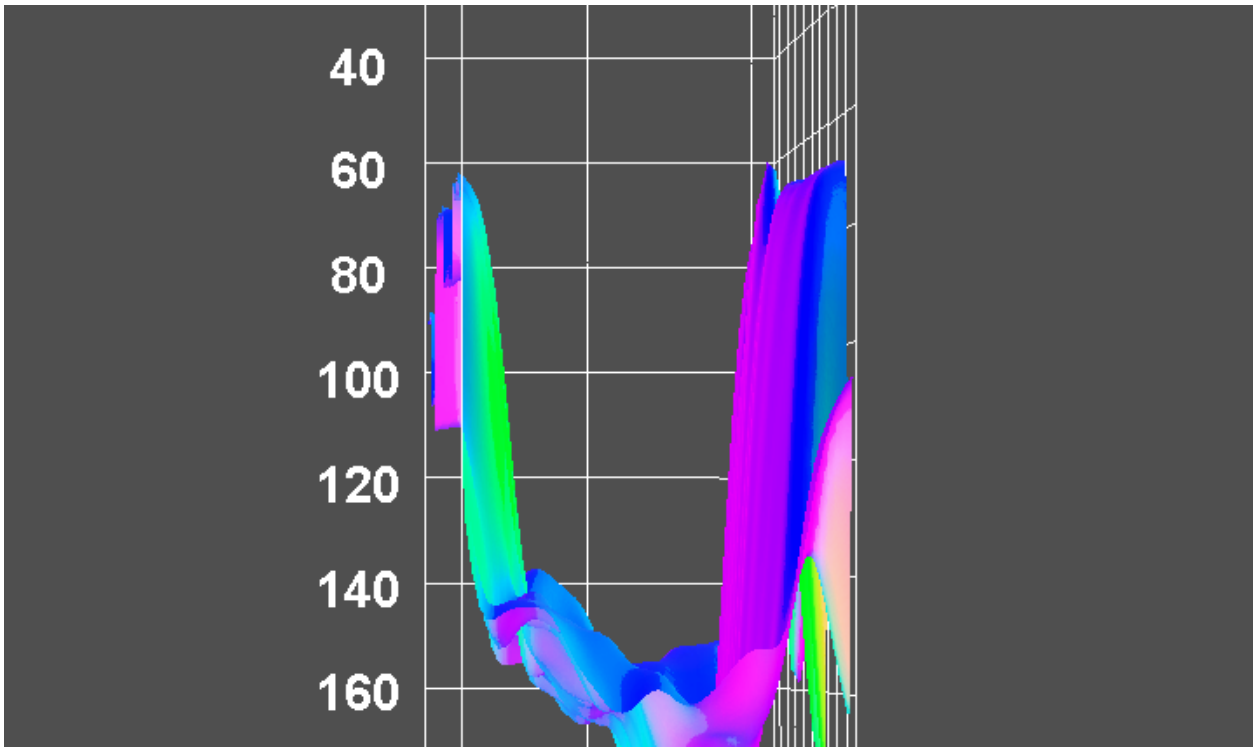

Filament 1-5 3-D Surface Plot

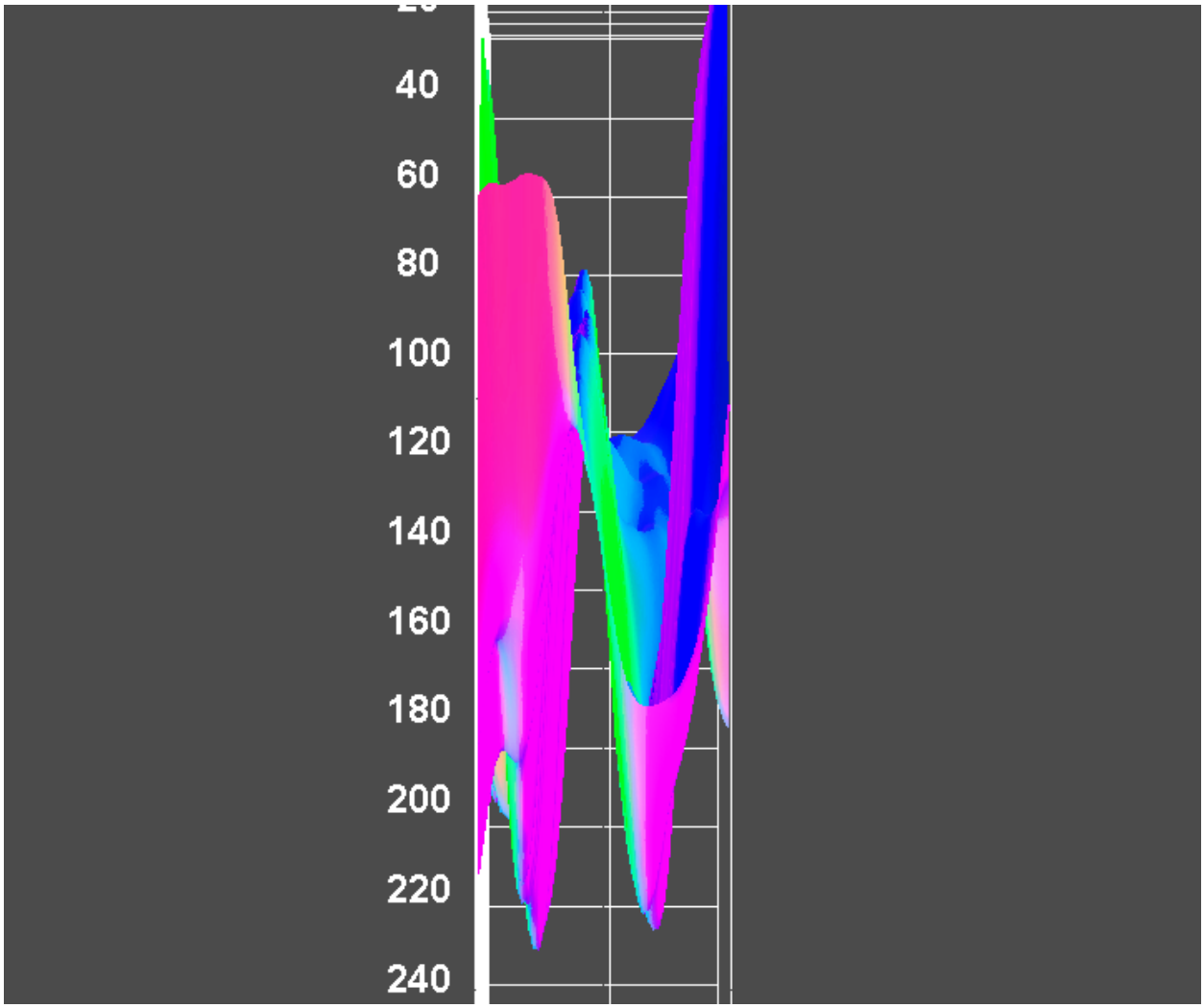

Filament 1-6 3-D Surface Plot

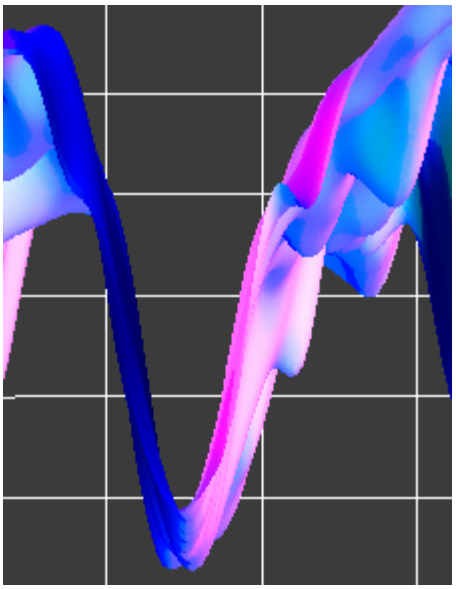

Filament 2-1 3-D Surface Plot

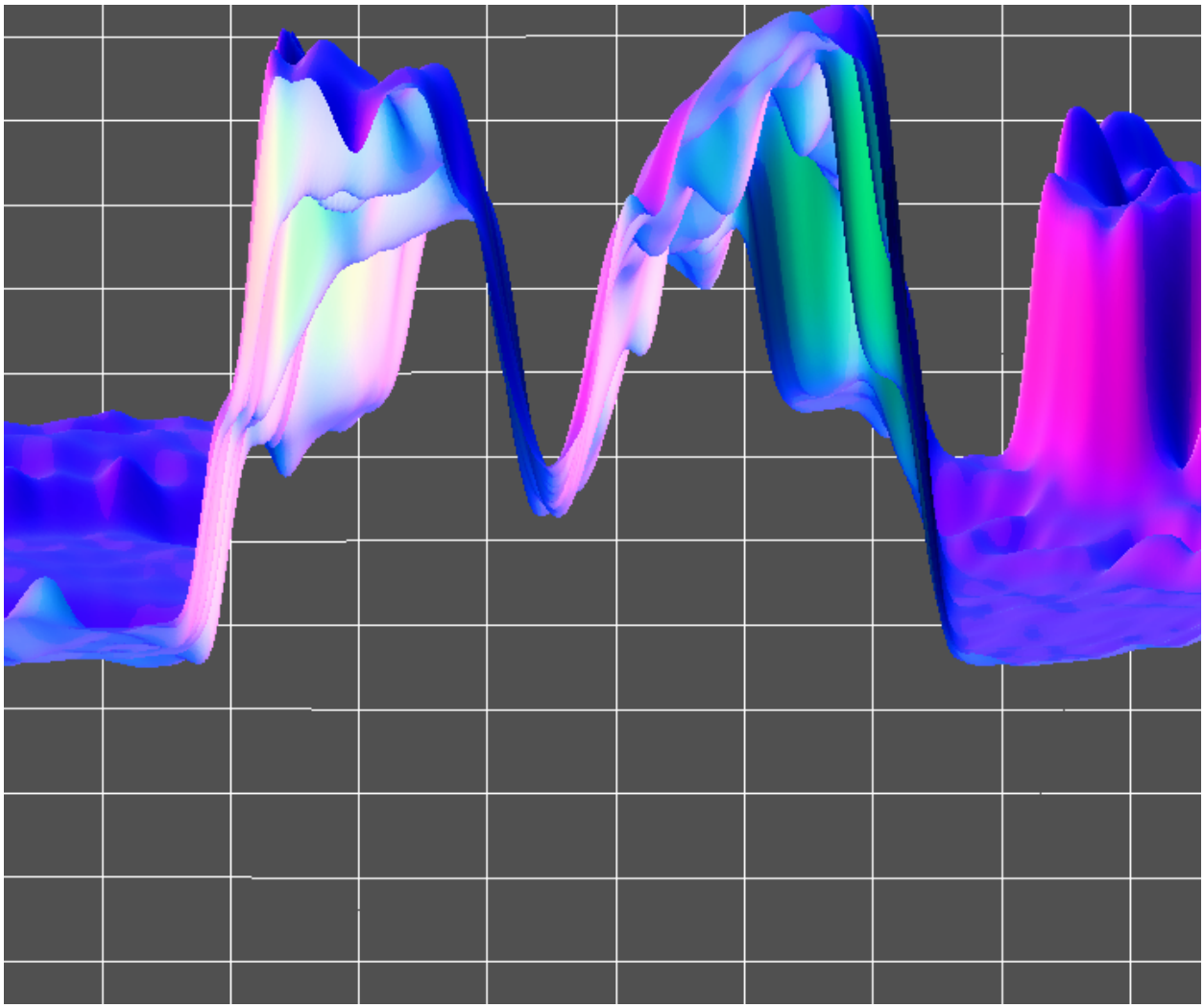

Filament 2-2 3-D Surface Plot

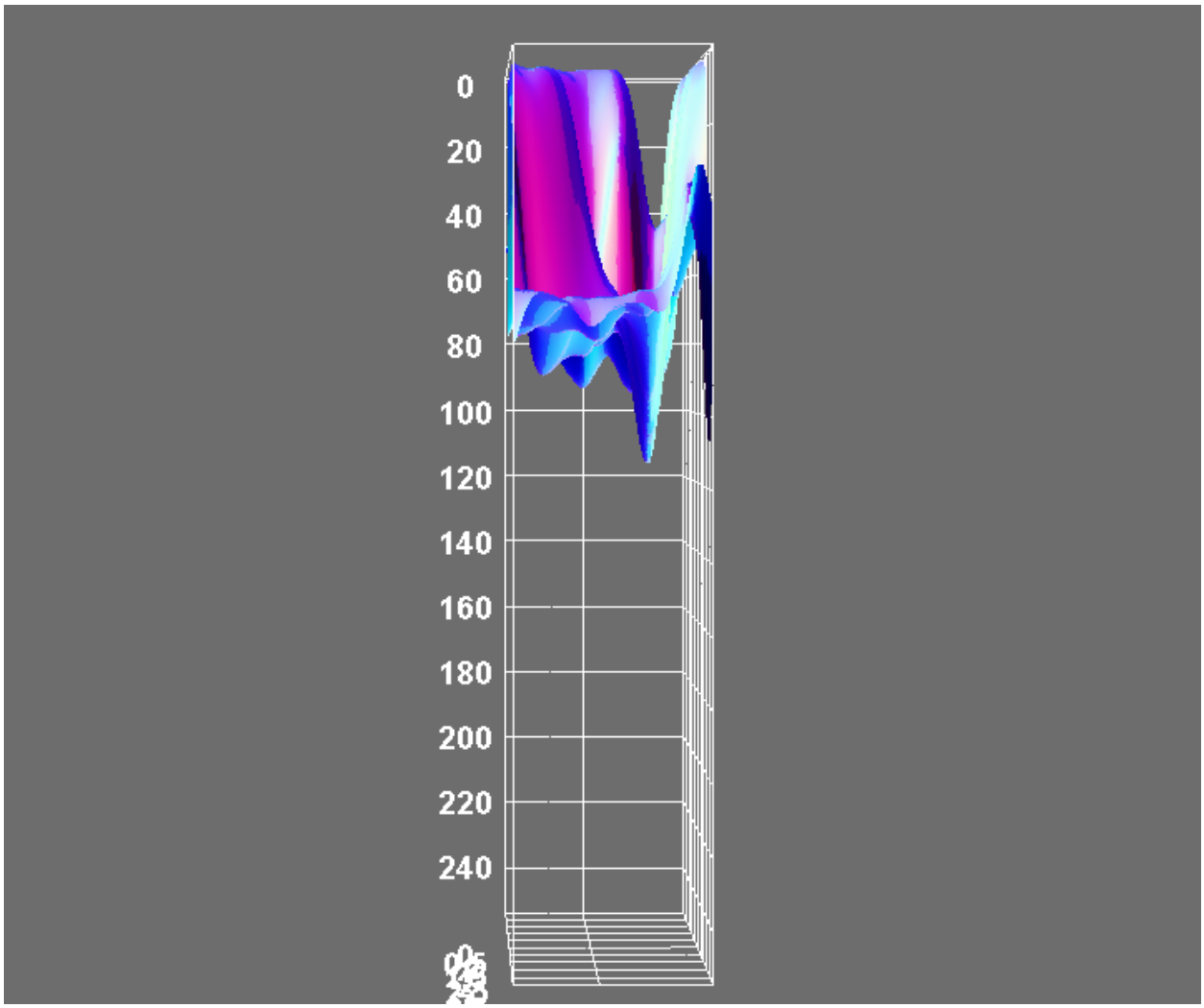

Filament 2-3 3-D Surface Plot

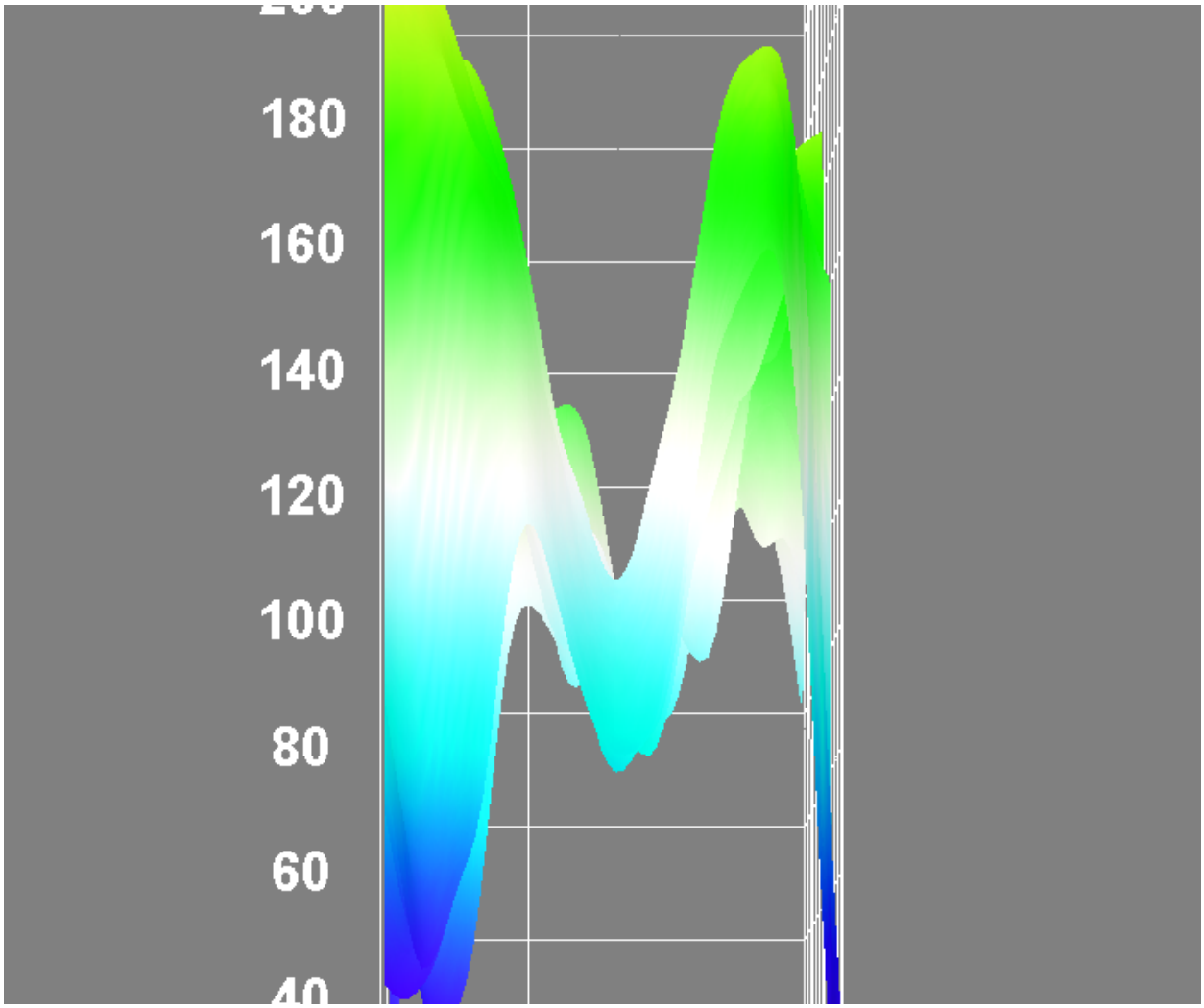

Filament 2-4 3-D Surface Plot

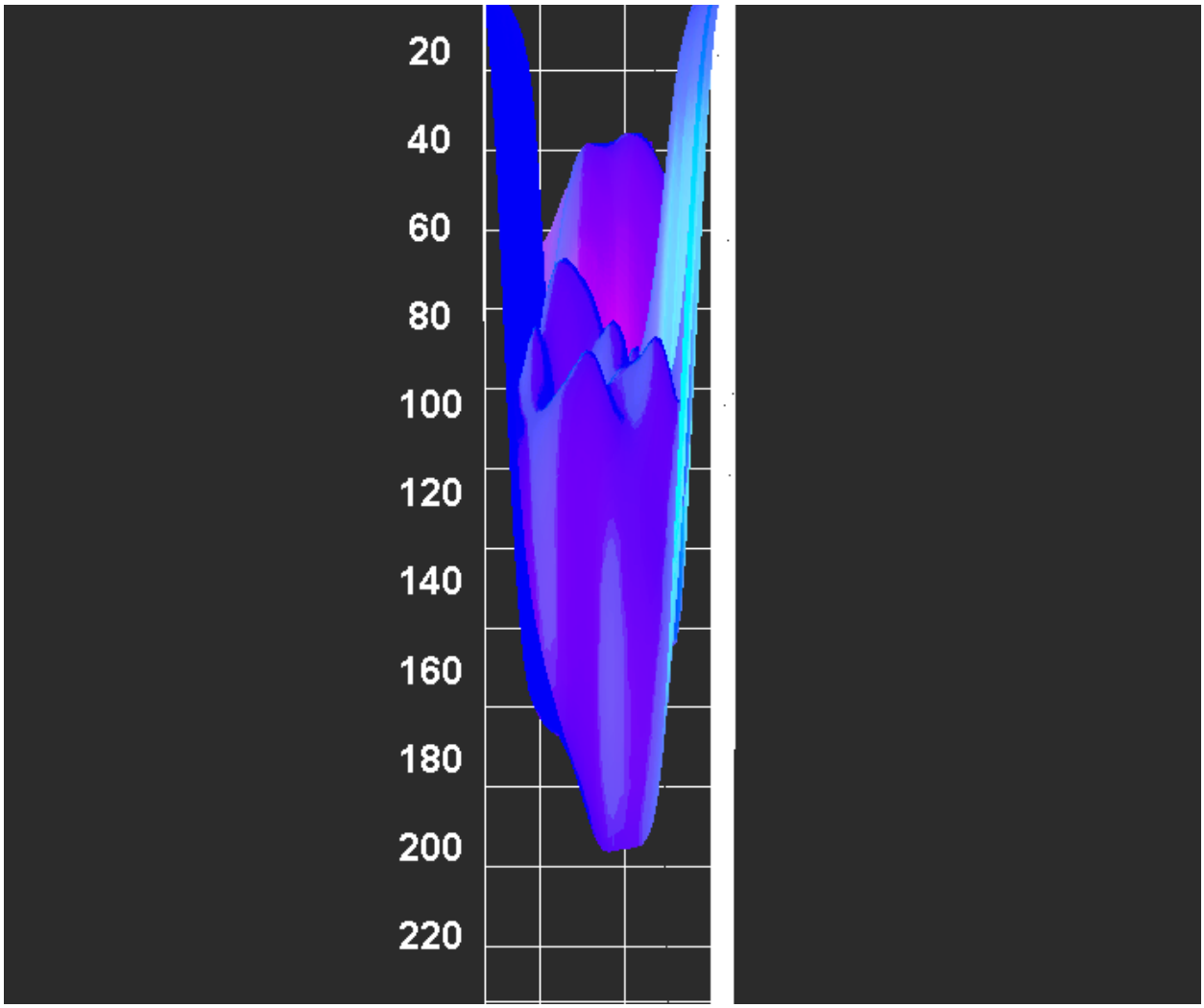

Filament 2-5 3-D Surface Plot

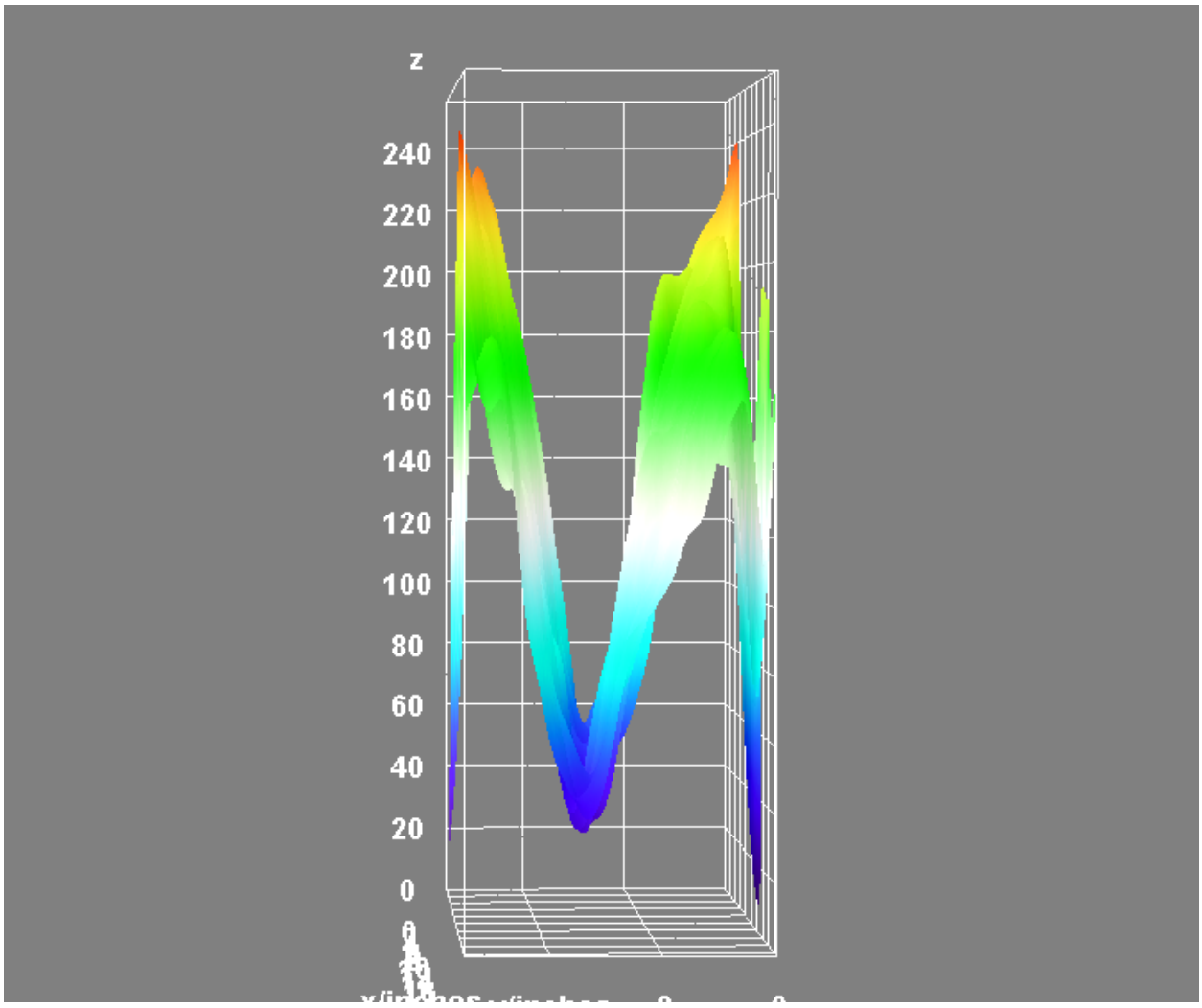

Filament 2-6 3-D Surface Plot

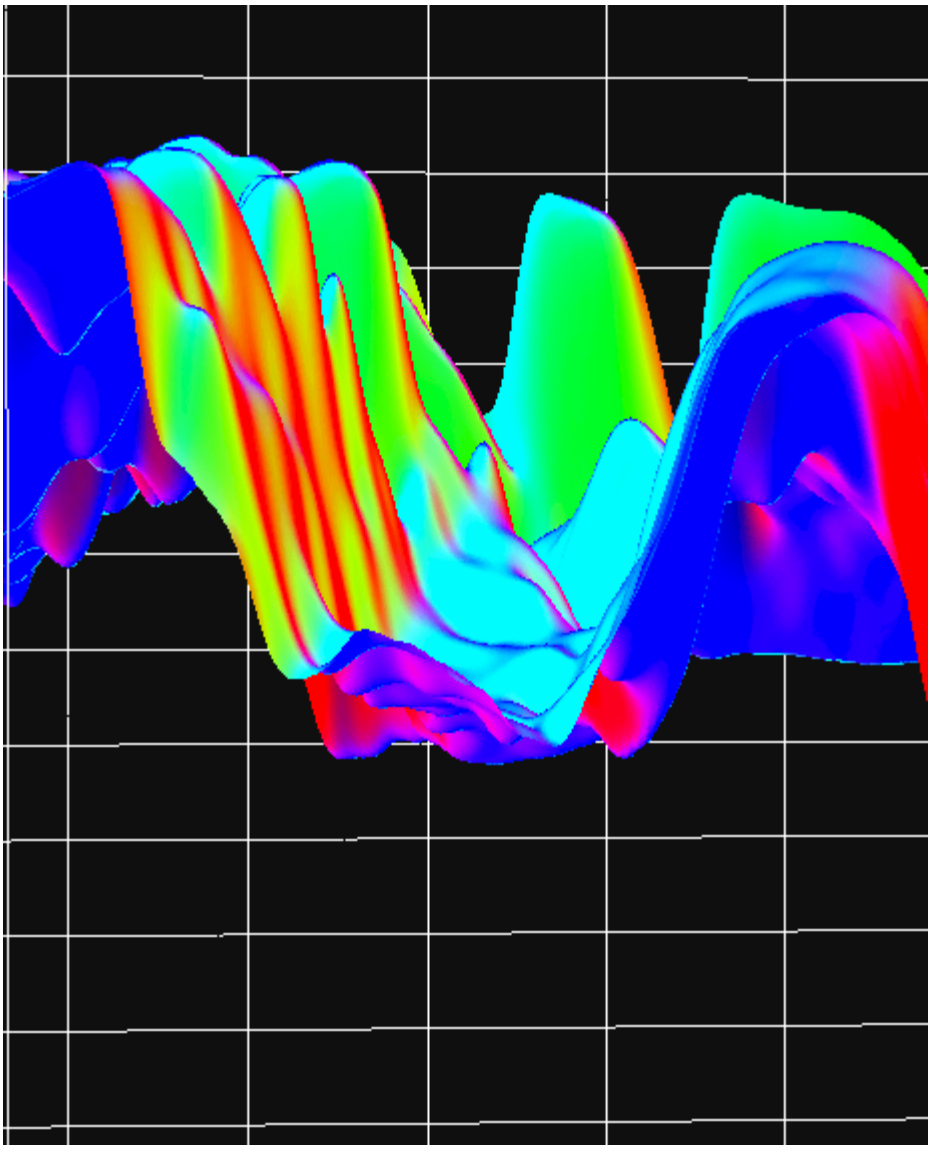

Filament 3-1 3-D Surface Plot

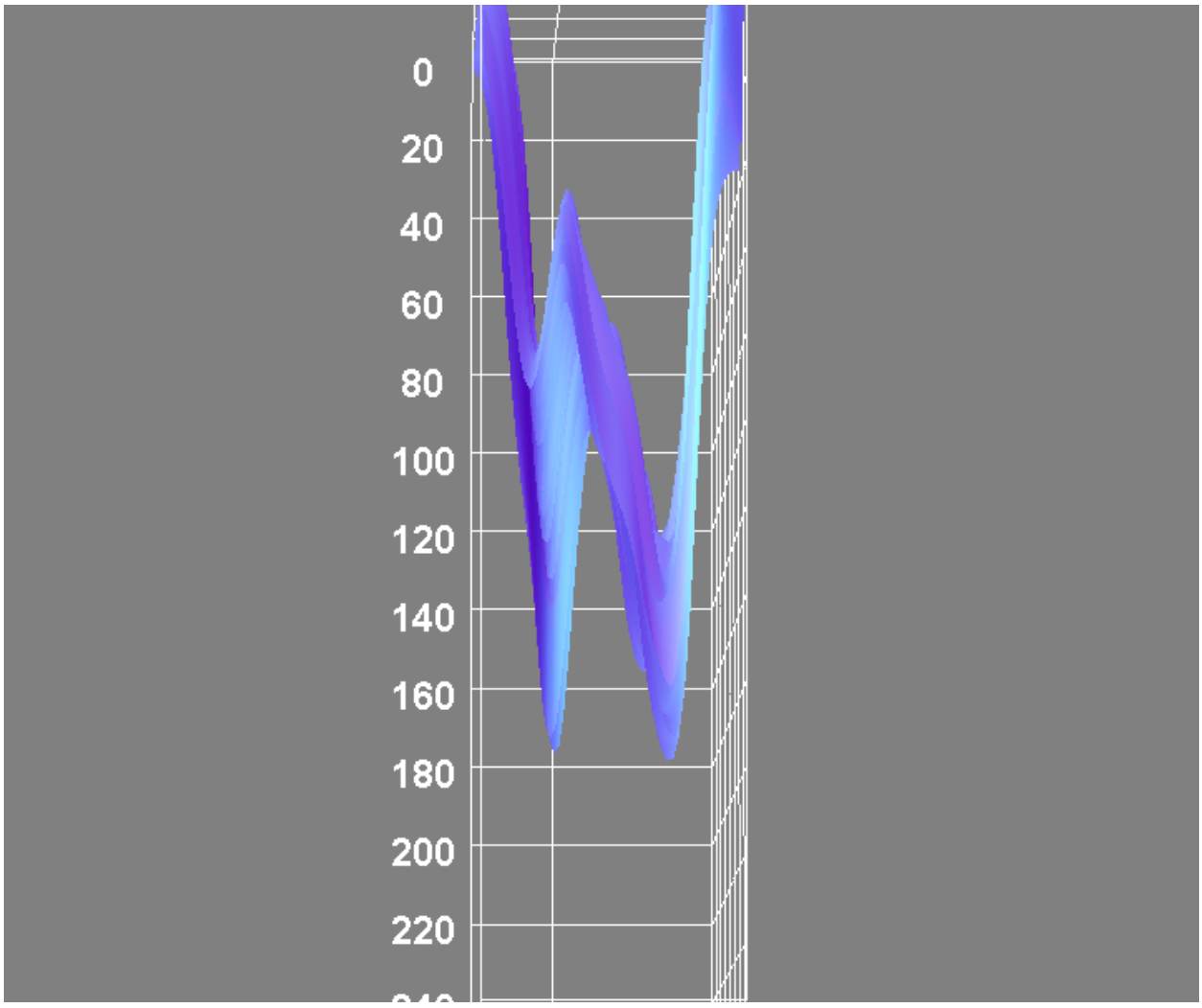

Filament 3-2 3-D Surface Plot

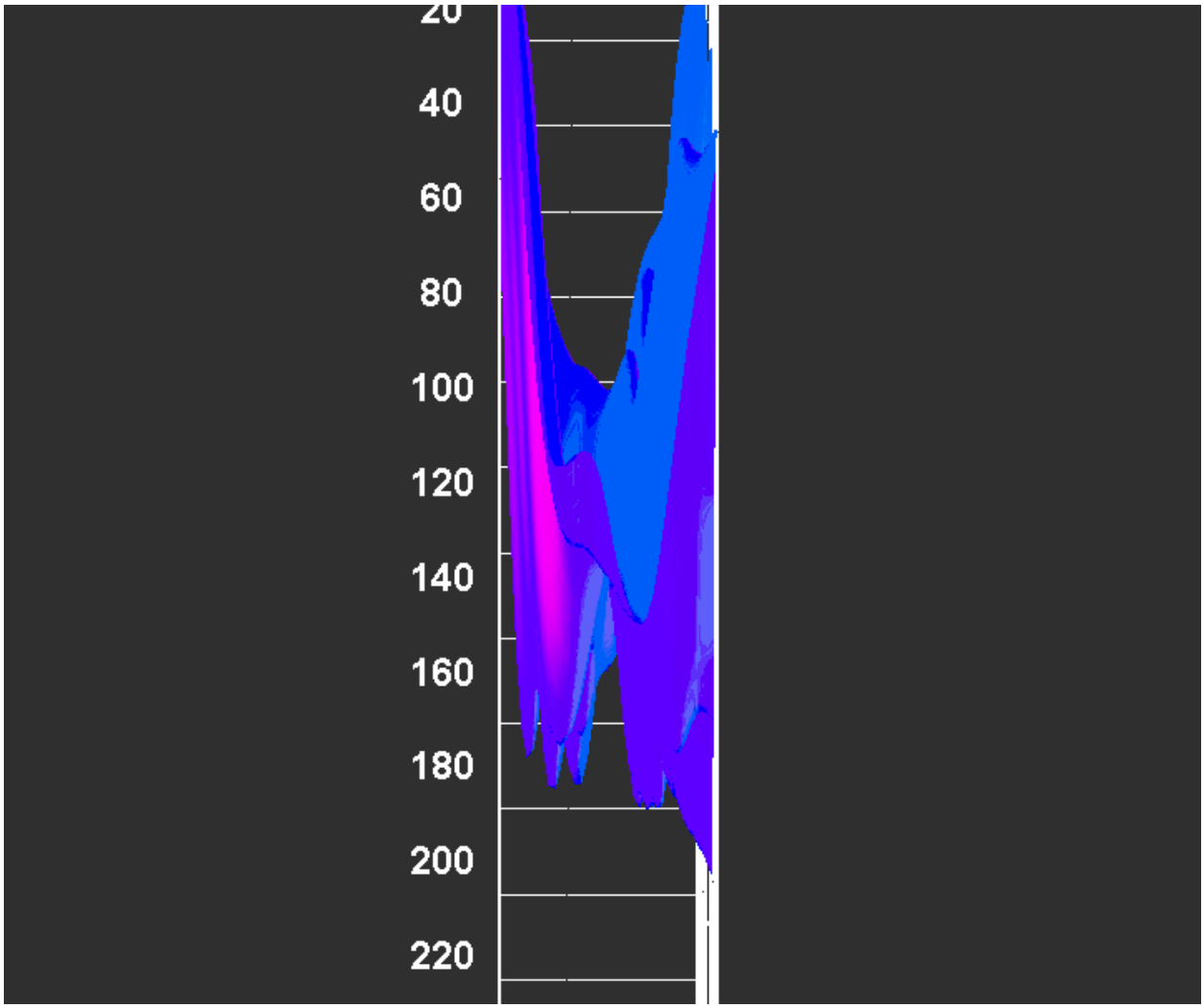

Filament 3-3 3-D Surface Plot

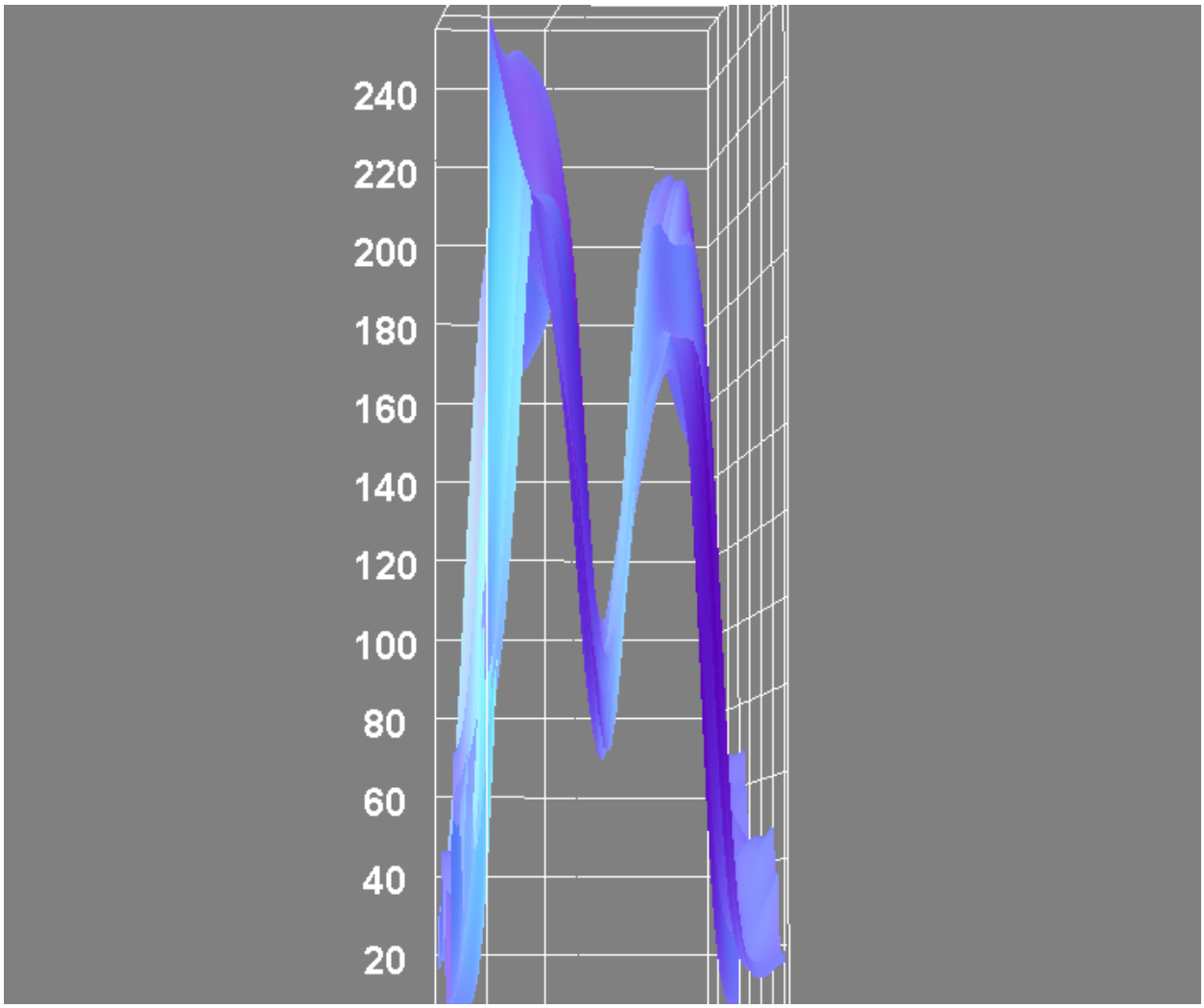

Filament 3-4 3-D Surface Plot

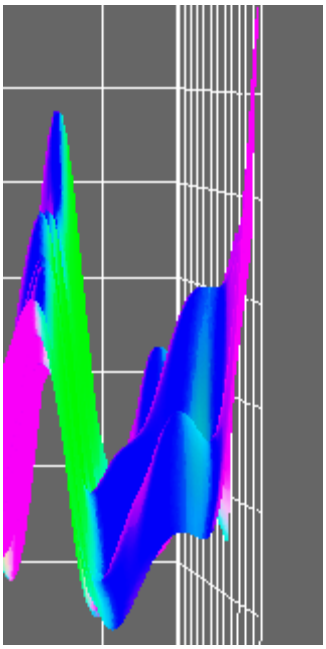

Filament 3-5 3-D Surface Plot

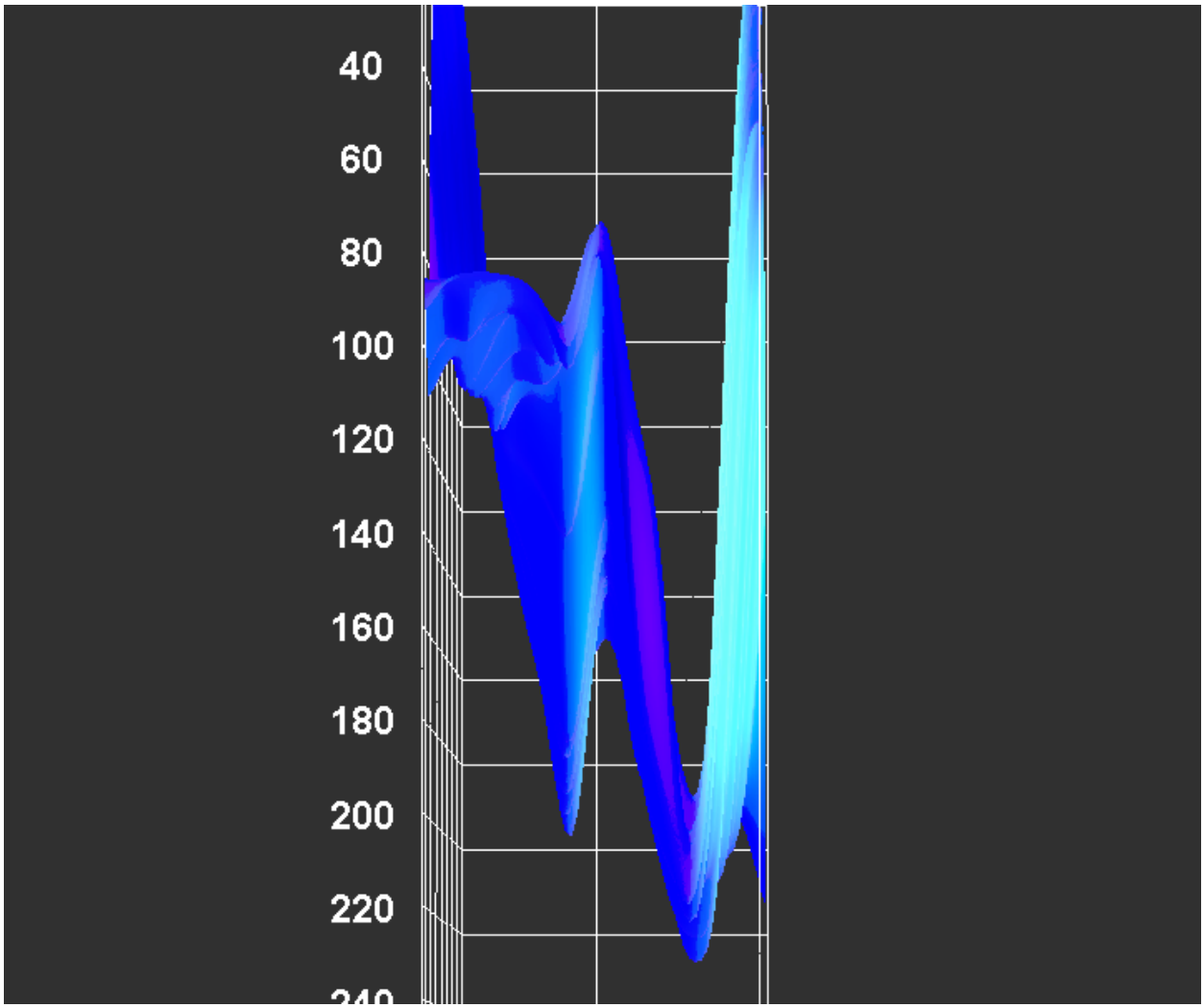

Filament 3-6 3-D Surface Plot

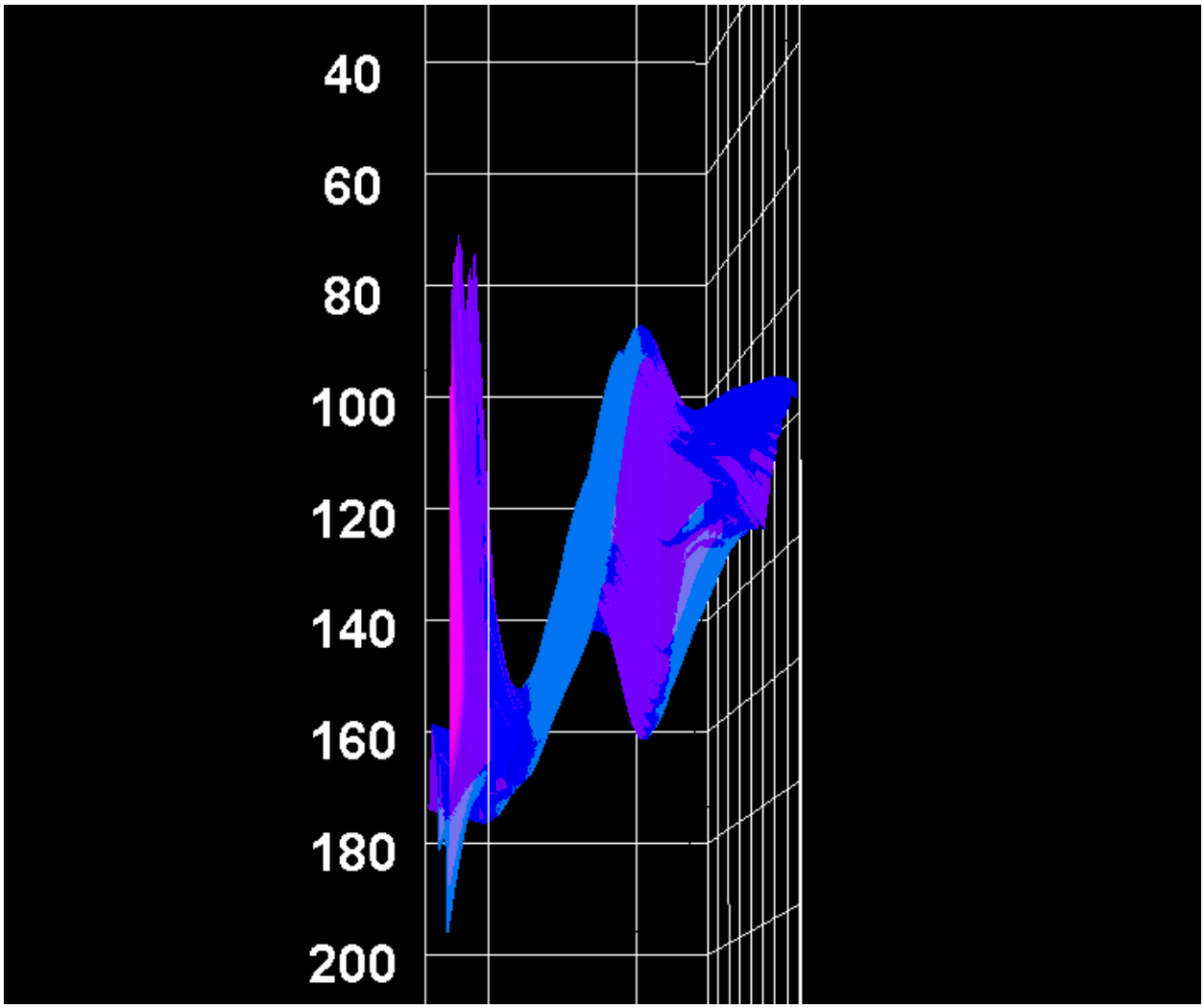

Filament 4-1 3-D Surface Plot

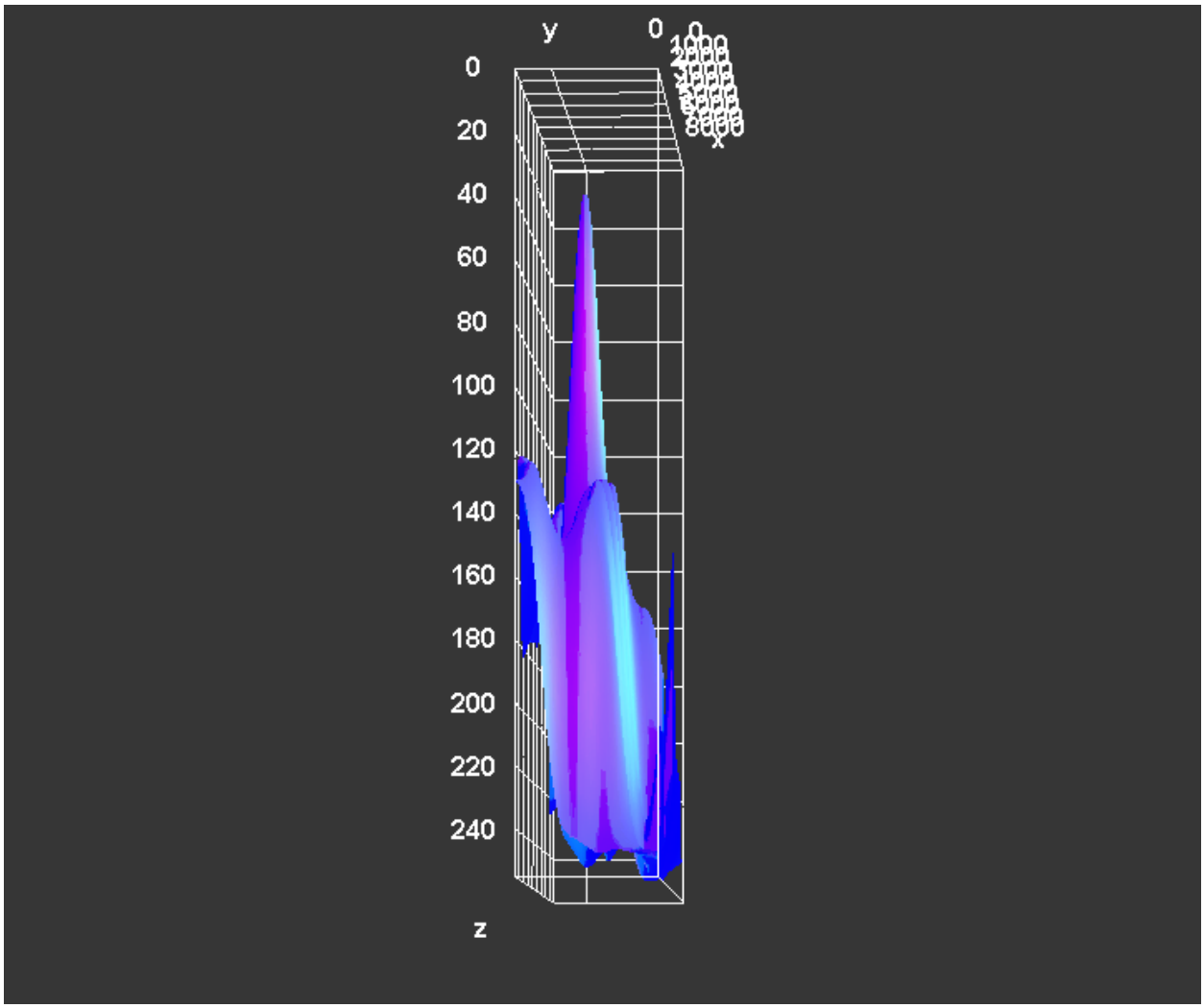

Filament 4-2 3-D Surface Plot

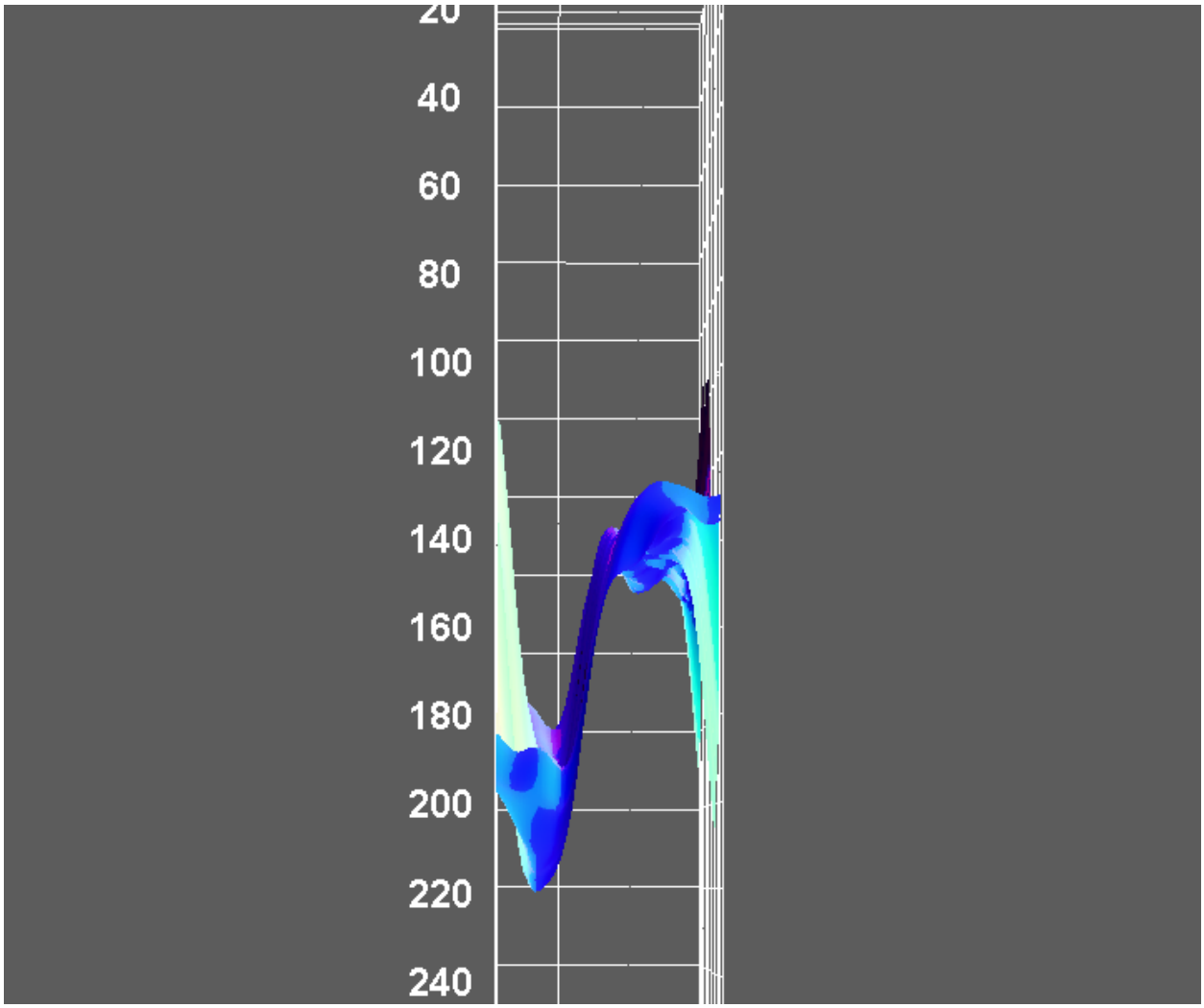

Filament 4-3 3-D Surface Plot

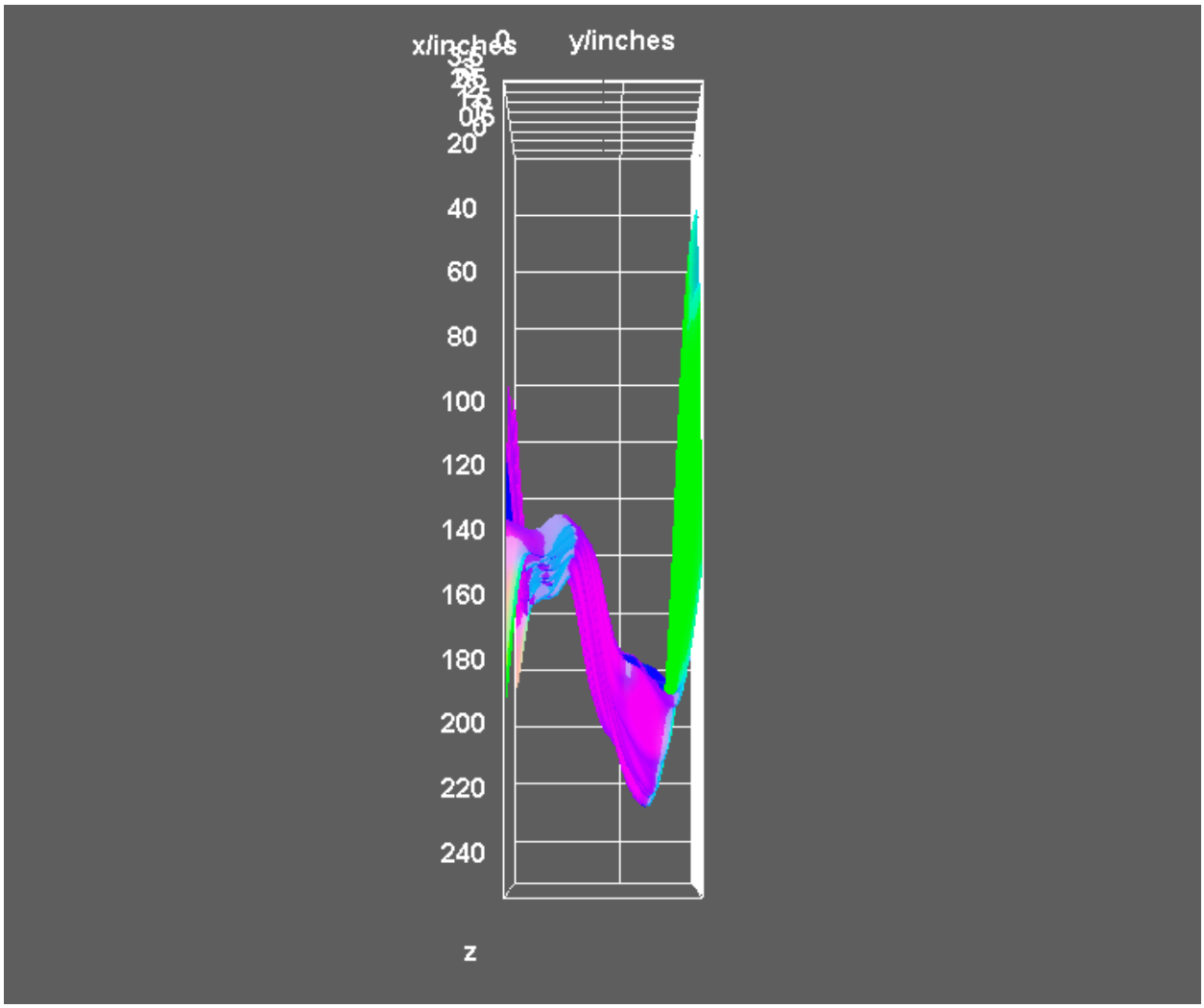

Filament 4-4 3-D Surface Plot

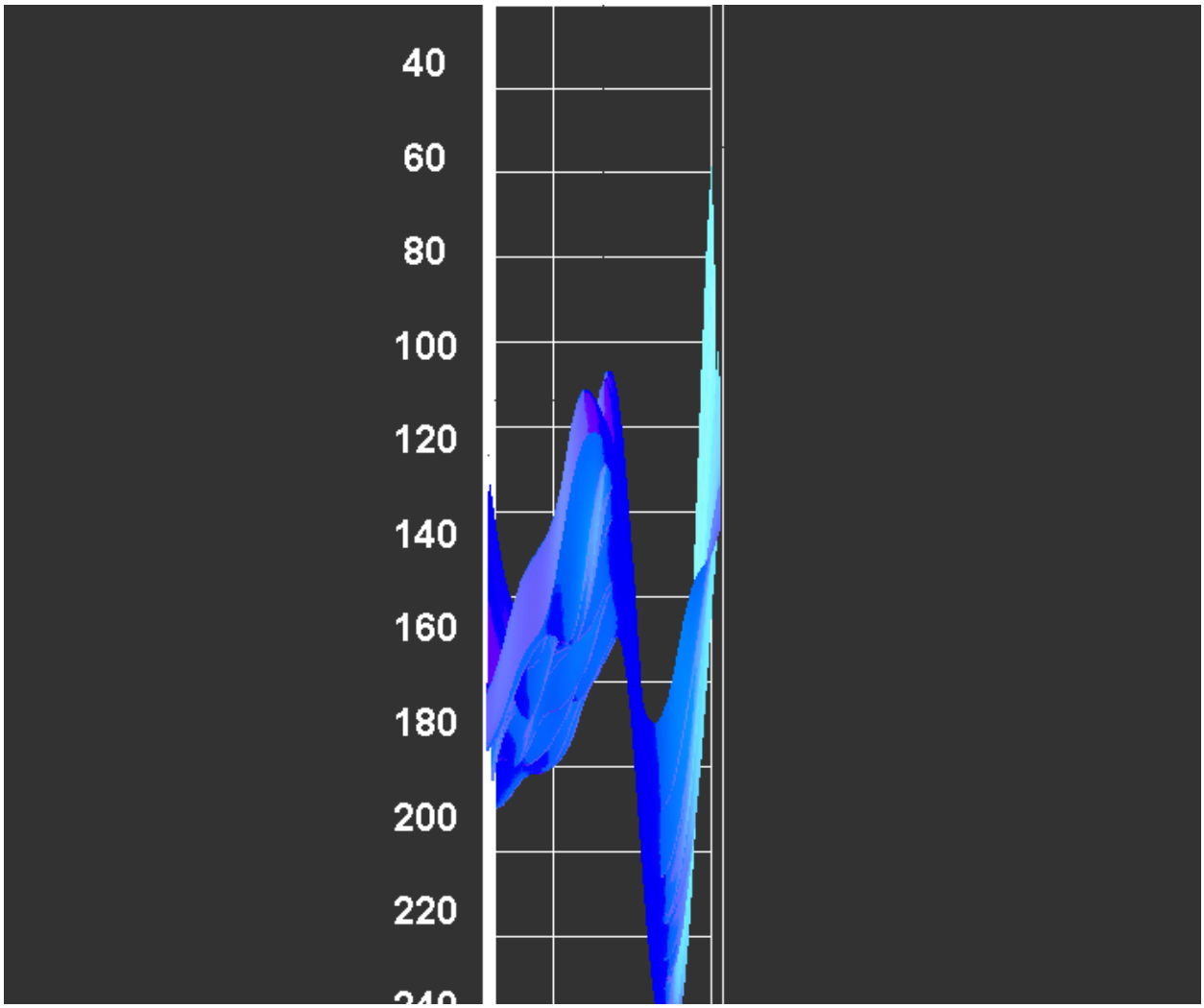

Filament 4-5 3-D Surface Plot

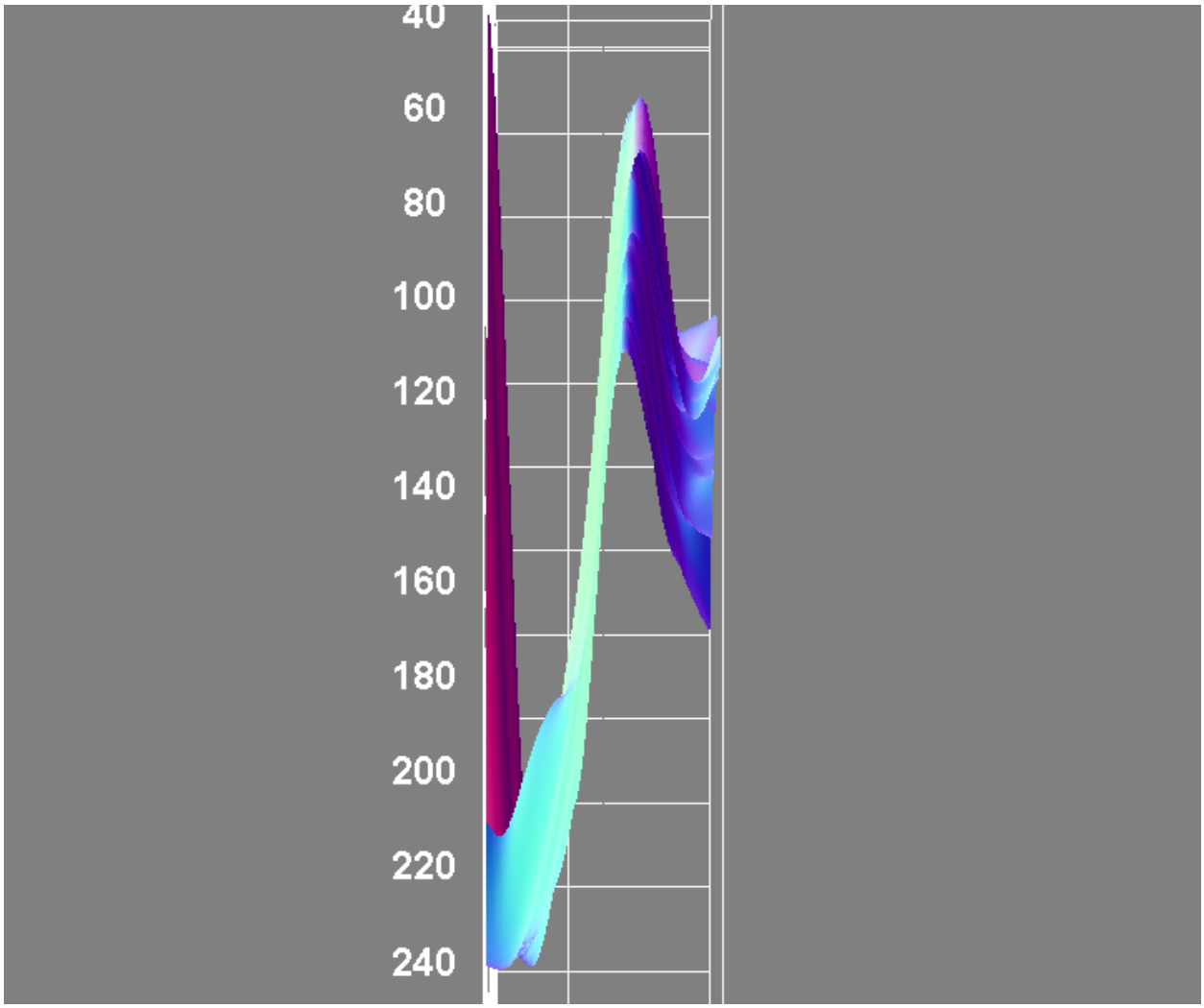

Filament 4-6 3-D Surface Plot

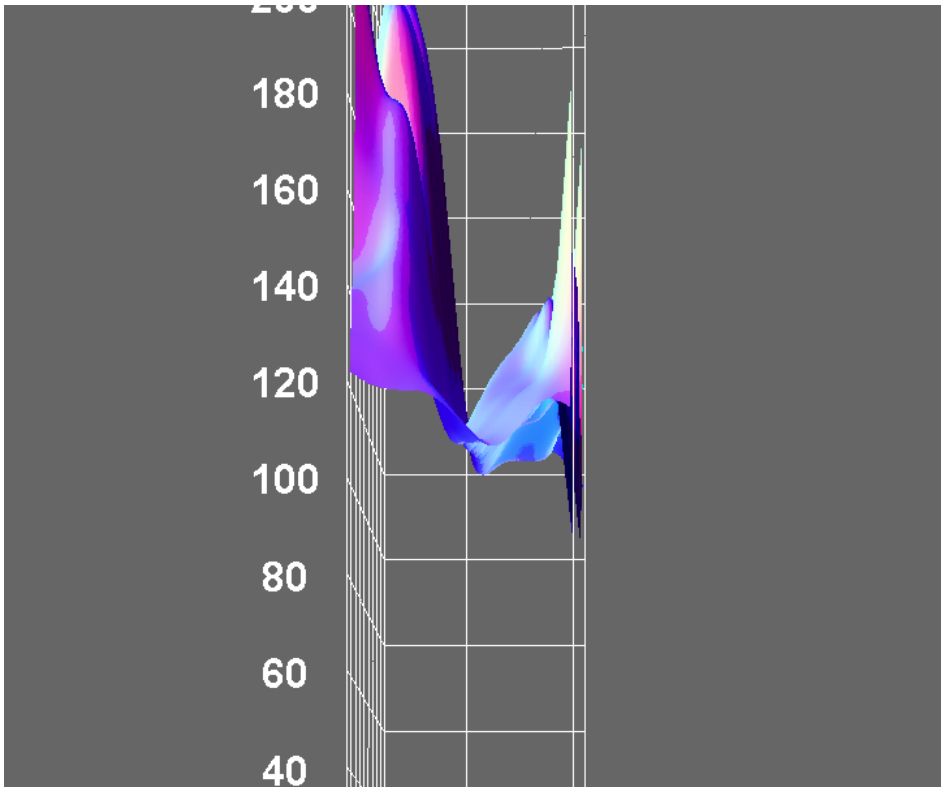

Appendix 5: Design of Experiments Results all Models

Model 1

Analysis of Variance

Source	DF	Adj SS	Adj MS	F-Value	P-Value
Model	5	0.80840	0.16168	2.14	0.107
Linear	3	0.16461	0.05487	0.73	0.549
Angular or Curved (A=1, C=0)	1	0.09317	0.09317	1.23	0.281
% image opaque	1	0.12915	0.12915	1.71	0.207
Area of Holes (µm)	1	0.01635	0.01635	0.22	0.647
2-Way Interactions	2	0.28297	0.14149	1.87	0.182
Angular or Curved (A=1, C=0)*% image opaque	1	0.02683	0.02683	0.36	0.559
% image opaque*Area of Holes (µm)	1	0.20794	0.20794	2.75	0.114
Error	18	1.35980	0.07554		
Total	23	2.16820			

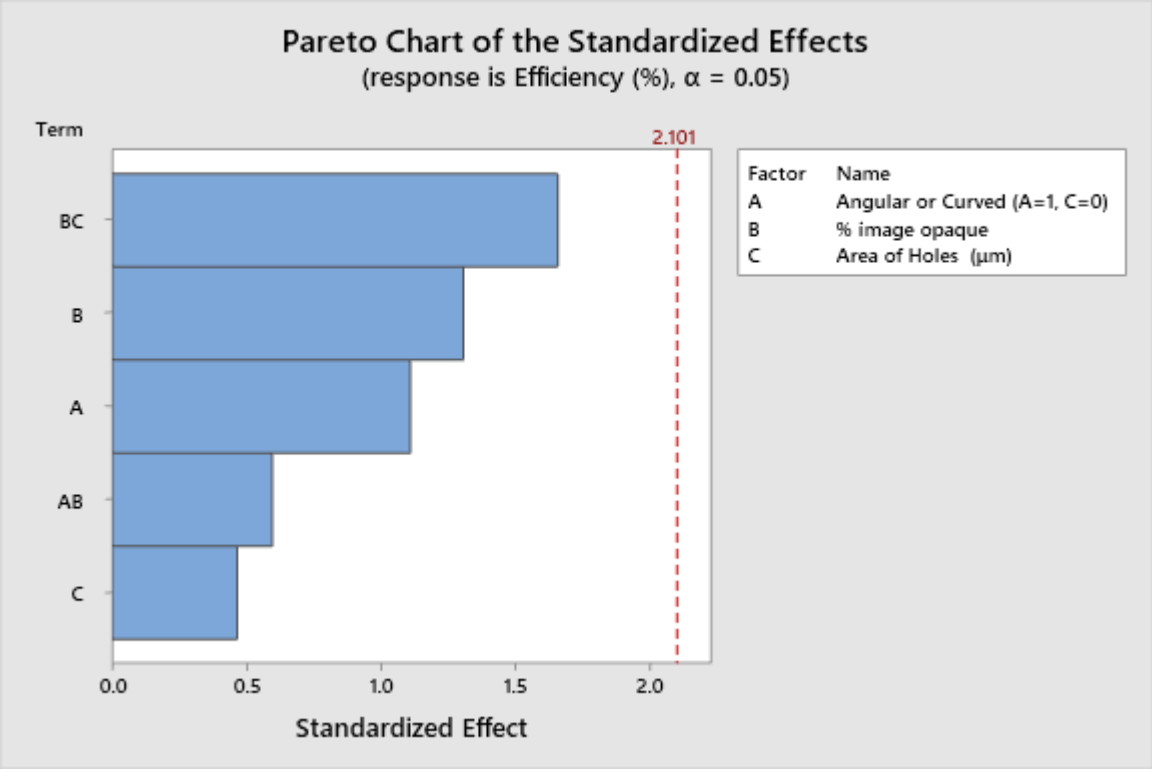

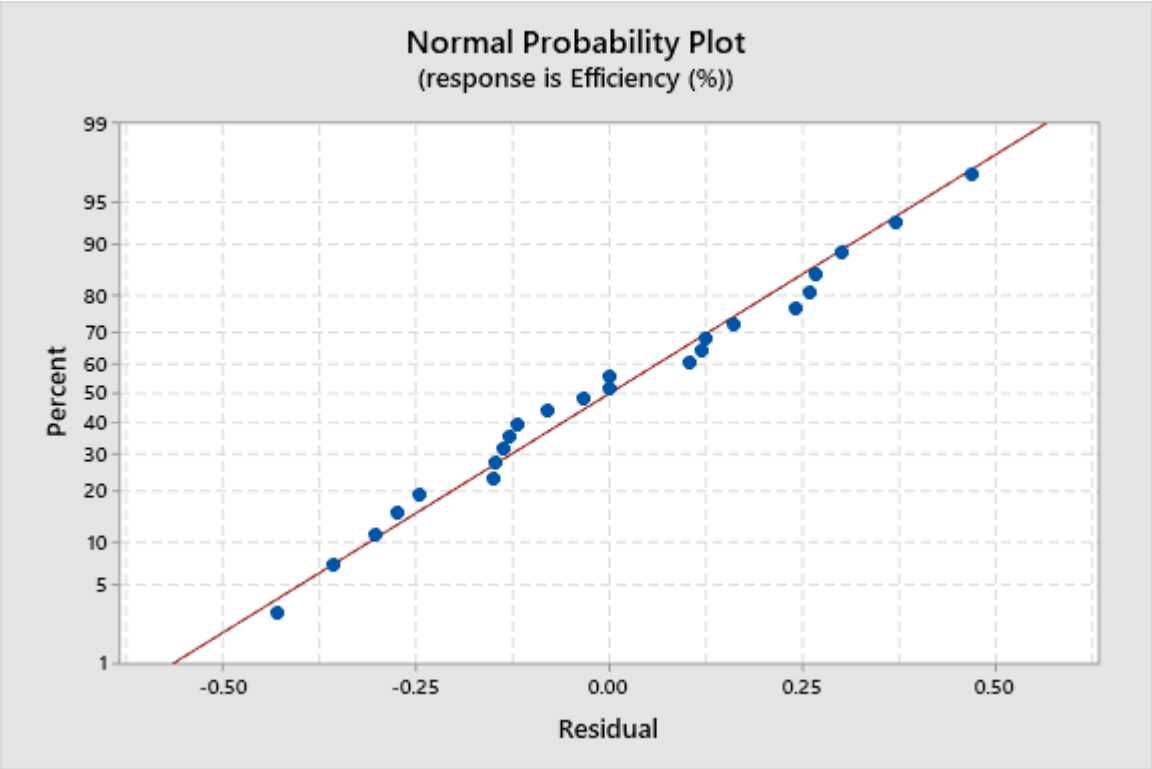
Normal Probability Plot
(response is Efficiency (%))
Percent
99
95
90
80
70
60
50
40
30
20
10
5
1
-0.50
-0.25
0.00
0.25
0.50
Residual

Model 2

Analysis of Variance

Source	DF	Adj SS
Model	8	1.11278
Linear	4	0.41426
Angular or Curved (A=1, C=0)	1	0.09853
Total Length of Cracks (µm)	1	0.22067
% image opaque	1	0.11704
Area of Holes (µm)	1	0.00069
2-Way Interactions	3	0.38901
Angular or Curved (A=1, C=0)*Total Length of Cracks (µm)	1	0.16490
Angular or Curved (A=1, C=0)*% image opaque	1	0.02172
Total Length of Cracks (µm)*% image opaque	1	0.24828
3-Way Interactions	1	0.12276
Angular or Curved (A=1, C=0)*Total Length of Cracks (µm)*% image opaque	1	0.12276
Error	12	0.83874
Total	20	1.95152

Source	Adj MS
Model	0.139098
Linear	0.103564
Angular or Curved (A=1, C=0)	0.098530
Total Length of Cracks (µm)	0.220669
% image opaque	0.117039
Area of Holes (µm)	0.000694
2-Way Interactions	0.129671
Angular or Curved (A=1, C=0)*Total Length of Cracks (µm)	0.164903
Angular or Curved (A=1, C=0)*% image opaque	0.021722
Total Length of Cracks (µm)*% image opaque	0.248284
3-Way Interactions	0.122759
Angular or Curved (A=1, C=0)*Total Length of Cracks (µm)*% image opaque	0.122759
Error	0.069895
Total	

Source	F-Value	P-Value
Model	1.99	0.136
Linear	1.48	0.268
Angular or Curved (A=1, C=0)	1.41	0.258
Total Length of Cracks (µm)	3.16	0.101
% image opaque	1.67	0.220
Area of Holes (µm)	0.01	0.922
2-Way Interactions	1.86	0.191
Angular or Curved (A=1, C=0)*Total Length of Cracks (µm)	2.36	0.150
Angular or Curved (A=1, C=0)*% image opaque	0.31	0.587
Total Length of Cracks (µm)*% image opaque	3.55	0.084
3-Way Interactions	1.76	0.210
Angular or Curved (A=1, C=0)*Total Length of Cracks (µm)*% image opaque	1.76	0.210
Error		
Total		

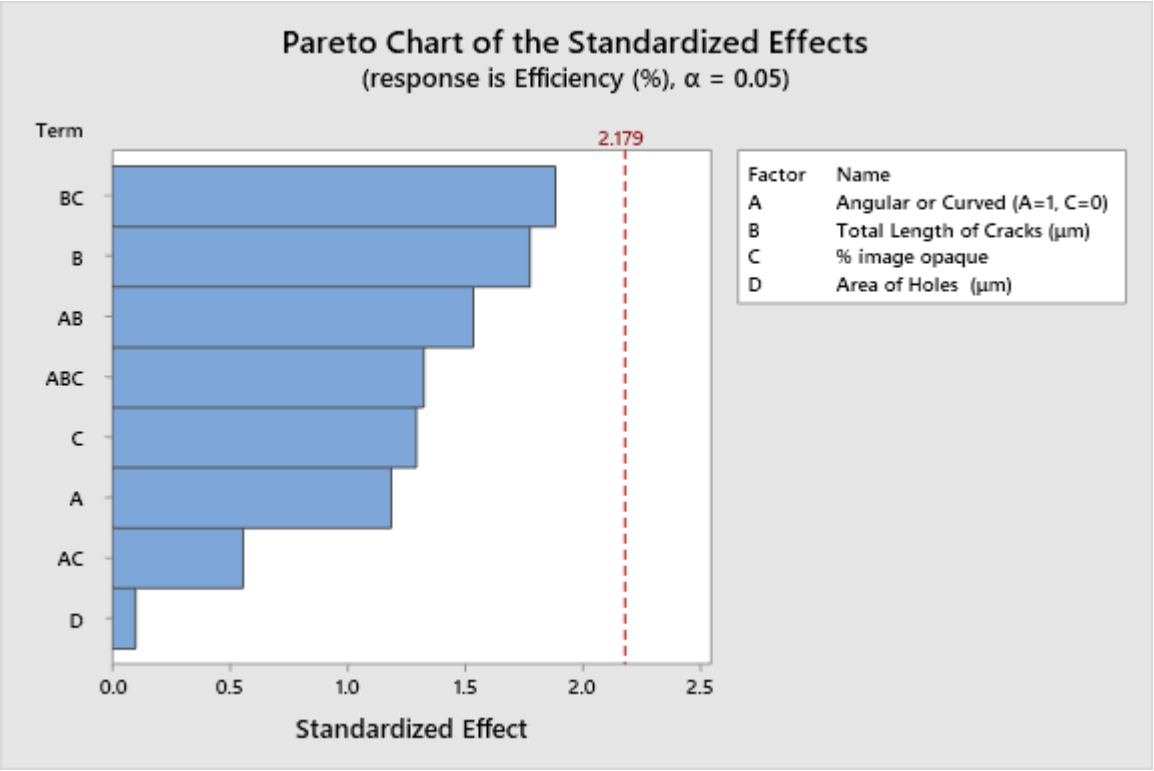
Pareto Chart of the Standardized Effects
(response is Efficiency (%), α = 0.05)
Term
2.179
BC
B
AB
ABC
C
A
AC
D
0.0
0.5
1.0
1.5
2.0
2.5
Standardized Effect
Factor Name
A Angular or Curved (A=1, C=0)
B Total Length of Cracks (µm)
C % image opaque
D Area of Holes (µm)

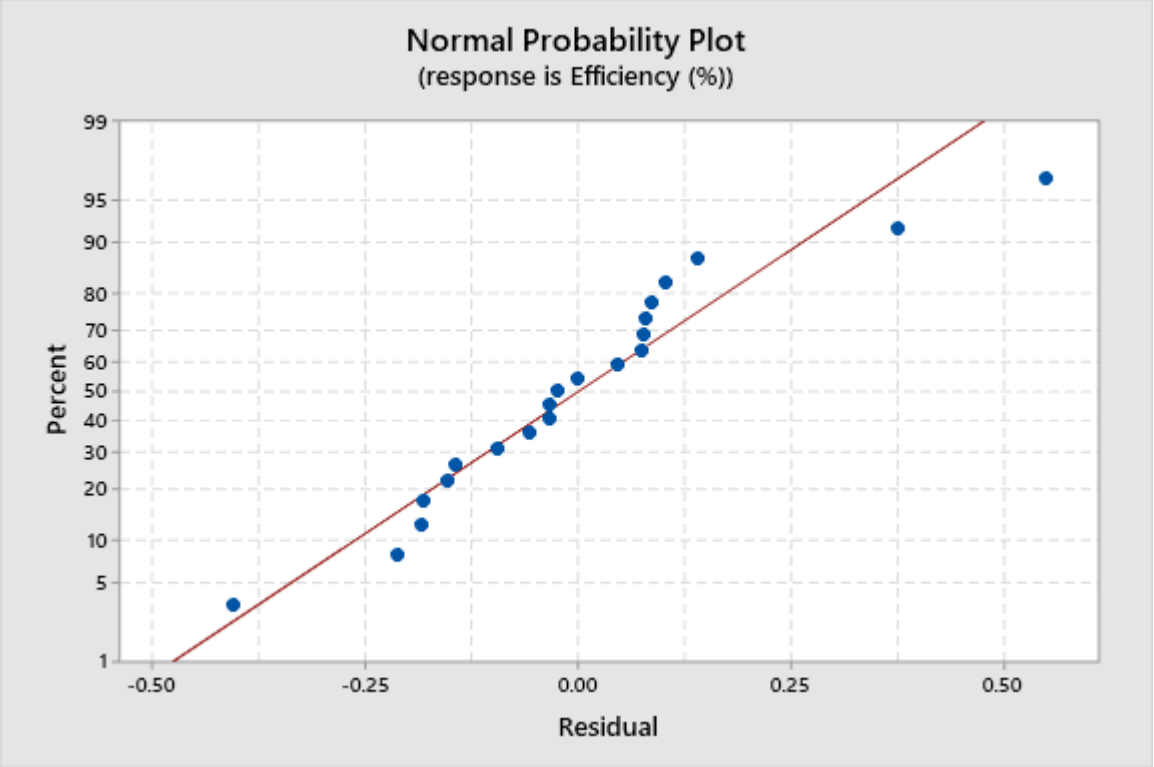
Normal Probability Plot
(response is Efficiency (%))
Percent
99
95
90
80
70
60
50
40
30
20
10
5
1
-0.50
-0.25
0.00
0.25
0.50
Residual

Model 3

Analysis of Variance

Source	DF	Adj SS
Model	9	1.01941
Linear	4	0.44909
Angular or Curved (A=1, C=0)	1	0.04616
Radius of Curvature (µm)	1	0.19642
% image opaque	1	0.17973
Area of Holes (µm)	1	0.21245
2-Way Interactions	4	0.54352
Angular or Curved (A=1, C=0)*Radius of Curvature (µm)	1	0.02361
Angular or Curved (A=1, C=0)*% image opaque	1	0.03460
Radius of Curvature (µm)*% image opaque	1	0.17979
Radius of Curvature (µm)*Area of Holes (µm)	1	0.22148
3-Way Interactions	1	0.03129
Angular or Curved (A=1, C=0)*Radius of Curvature (µm)*% image opaque	1	0.03129
Error	11	0.70410
Total	20	1.72351

Source	Adj MS	F-Value
Model	0.11327	1.77
Linear	0.11227	1.75
Angular or Curved (A=1, C=0)	0.04616	0.72
Radius of Curvature (µm)	0.19642	3.07
% image opaque	0.17973	2.81
Area of Holes (µm)	0.21245	3.32
2-Way Interactions	0.13588	2.12
Angular or Curved (A=1, C=0)*Radius of Curvature (µm)	0.02361	0.37
Angular or Curved (A=1, C=0)*% image opaque	0.03460	0.54
Radius of Curvature (µm)*% image opaque	0.17979	2.81
Radius of Curvature (µm)*Area of Holes (µm)	0.22148	3.46
3-Way Interactions	0.03129	0.49
Angular or Curved (A=1, C=0)*Radius of Curvature (µm)*% image opaque	0.03129	0.49
Error	0.06401	
Total		

Source	P-Value
Model	0.184
Linear	0.208
Angular or Curved (A=1, C=0)	0.414
Radius of Curvature (µm)	0.108
% image opaque	0.122
Area of Holes (µm)	0.096
2-Way Interactions	0.146
Angular or Curved (A=1, C=0)*Radius of Curvature (µm)	0.556
Angular or Curved (A=1, C=0)*% image opaque	0.478
Radius of Curvature (µm)*% image opaque	0.122
Radius of Curvature (µm)*Area of Holes (µm)	0.090
3-Way Interactions	0.499
Angular or Curved (A=1, C=0)*Radius of Curvature (µm)*% image opaque	0.499
Error	
Total	

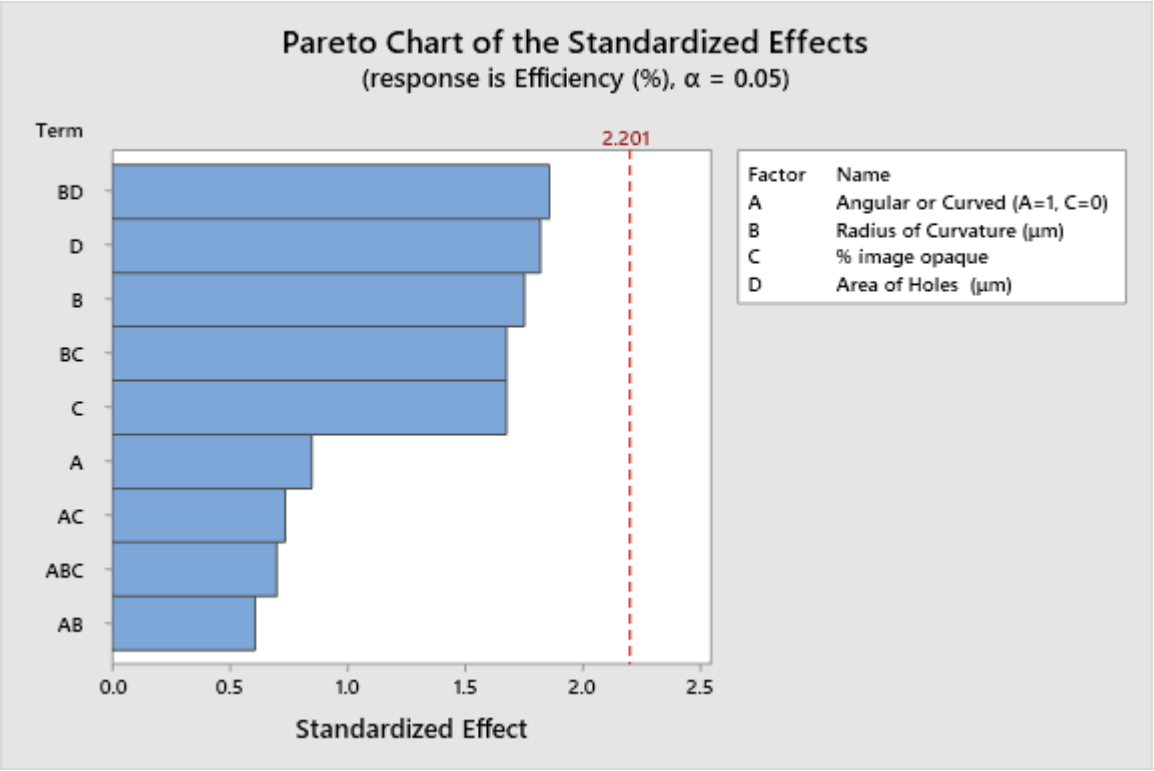
Pareto Chart of the Standardized Effects
(response is Efficiency (%), α = 0.05)
Term
2.201
BD
D
B
BC
C
A
AC
ABC
AB
0.0
0.5
1.0
1.5
2.0
2.5
Standardized Effect
Factor Name
A Angular or Curved (A=1, C=0)
B Radius of Curvature (µm)
C % image opaque
D Area of Holes (µm)

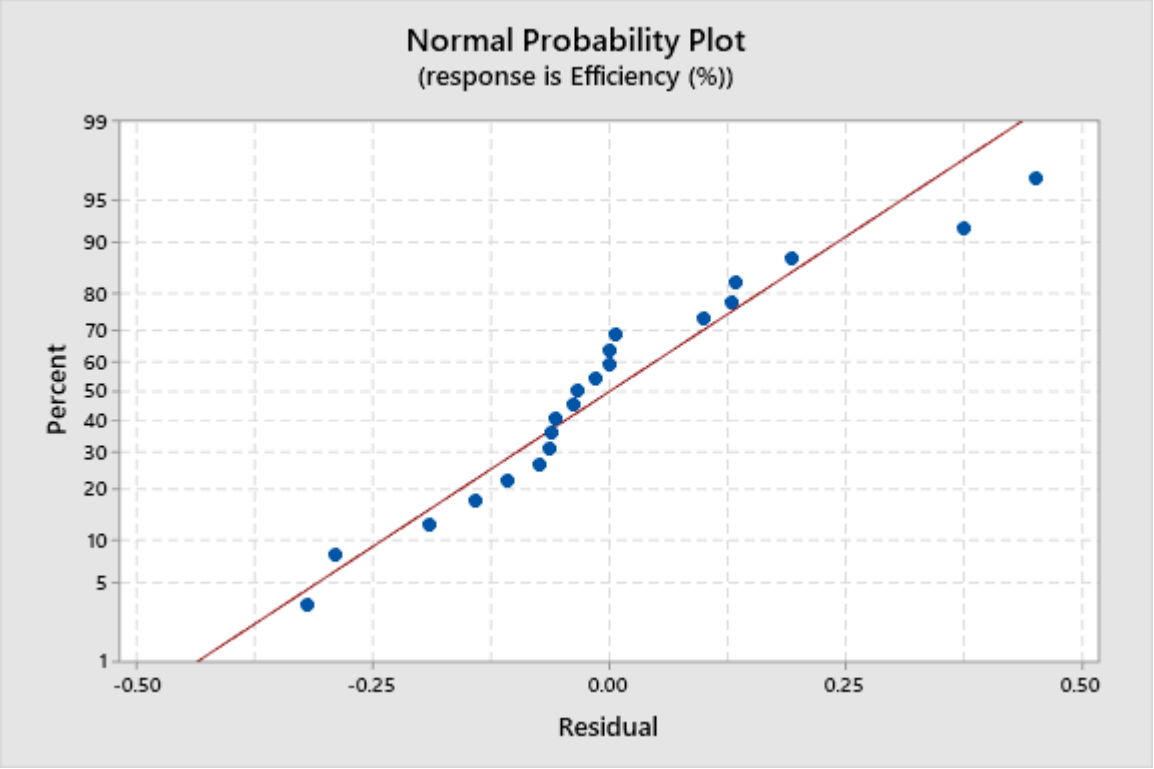
Normal Probability Plot
(response is Efficiency (%))
Percent
99
95
90
80
70
60
50
40
30
20
10
5
1
-0.50
-0.25
0.00
0.25
0.50
Residual

Analysis of Variance

Source	DF	Adj SS	Adj MS	F-Value
Model	16	1.52042	0.095026	1.62
Linear	5	0.09305	0.018610	0.32
Angular or Curved (A=1, C=0)	1	0.00386	0.003858	0.07
% image opaque	1	0.02031	0.020309	0.35
Area of Holes (µm)	1	0.00987	0.009865	0.17
Resistivity	1	0.00658	0.006578	0.11
Resistance	1	0.01419	0.014193	0.24
2-Way Interactions	7	0.39445	0.056350	0.96
Angular or Curved (A=1, C=0)*% image opaque	1	0.00742	0.007418	0.13
Angular or Curved (A=1, C=0)*Resistivity	1	0.00864	0.008641	0.15
Angular or Curved (A=1, C=0)*Resistance	1	0.00728	0.007278	0.12
% image opaque*Area of Holes (µm)	1	0.02044	0.020436	0.35
% image opaque*Resistivity	1	0.00559	0.005592	0.10
% image opaque*Resistance	1	0.01014	0.010141	0.17
Resistivity*Resistance	1	0.00958	0.009585	0.16
3-Way Interactions	4	0.16190	0.040476	0.69
Angular or Curved (A=1, C=0)*% image opaque*Resistivity	1	0.00366	0.003658	0.06
Angular or Curved (A=1, C=0)*% image opaque*Resistance	1	0.00685	0.006846	0.12
Angular or Curved (A=1, C=0)*Resistivity*Resistance	1	0.00009	0.000094	0.00
% image opaque*Resistivity*Resistance	1	0.00701	0.007006	0.12
Error	2	0.11705	0.058526	
Total	18	1.63747		

Source	P-Value
Model	0.448
Linear	0.869
Angular or Curved (A=1, C=0)	0.821
% image opaque	0.615
Area of Holes (µm)	0.721
Resistivity	0.769
Resistance	0.671
2-Way Interactions	0.597
Angular or Curved (A=1, C=0)*% image opaque	0.756
Angular or Curved (A=1, C=0)*Resistivity	0.738
Angular or Curved (A=1, C=0)*Resistance	0.758
% image opaque*Area of Holes (µm)	0.614
% image opaque*Resistivity	0.786
% image opaque*Resistance	0.718
Resistivity*Resistance	0.725
3-Way Interactions	0.663
Angular or Curved (A=1, C=0)*% image opaque*Resistivity	0.826
Angular or Curved (A=1, C=0)*% image opaque*Resistance	0.765
Angular or Curved (A=1, C=0)*Resistivity*Resistance	0.972
% image opaque*Resistivity*Resistance	0.762
Error	
Total	

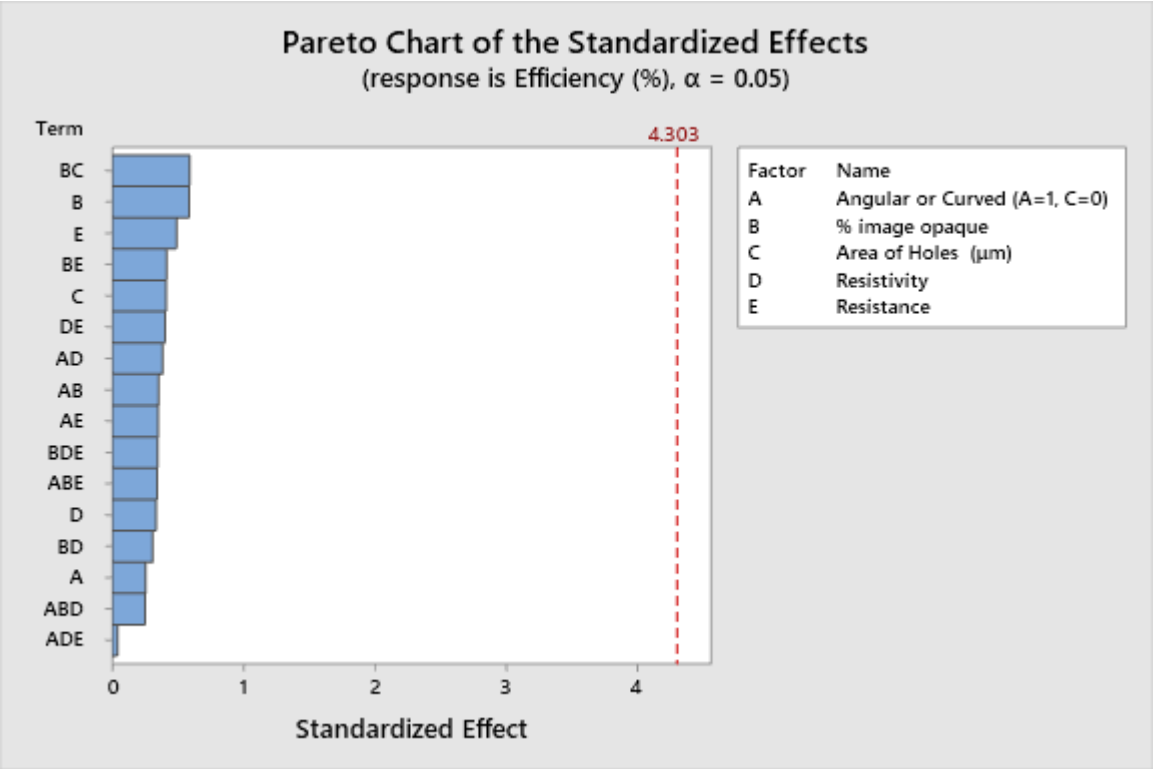
Pareto Chart of the Standardized Effects
(response is Efficiency (%), α = 0.05)
Term
BC
B
E
BE
C
DE
AD
AB
AE
BDE
ABE
D
BD
A
ABD
ADE
4.303
0
1
2
3
4
Standardized Effect
Factor Name
A Angular or Curved (A=1, C=0)
B % image opaque
C Area of Holes (µm)
D Resistivity
E Resistance

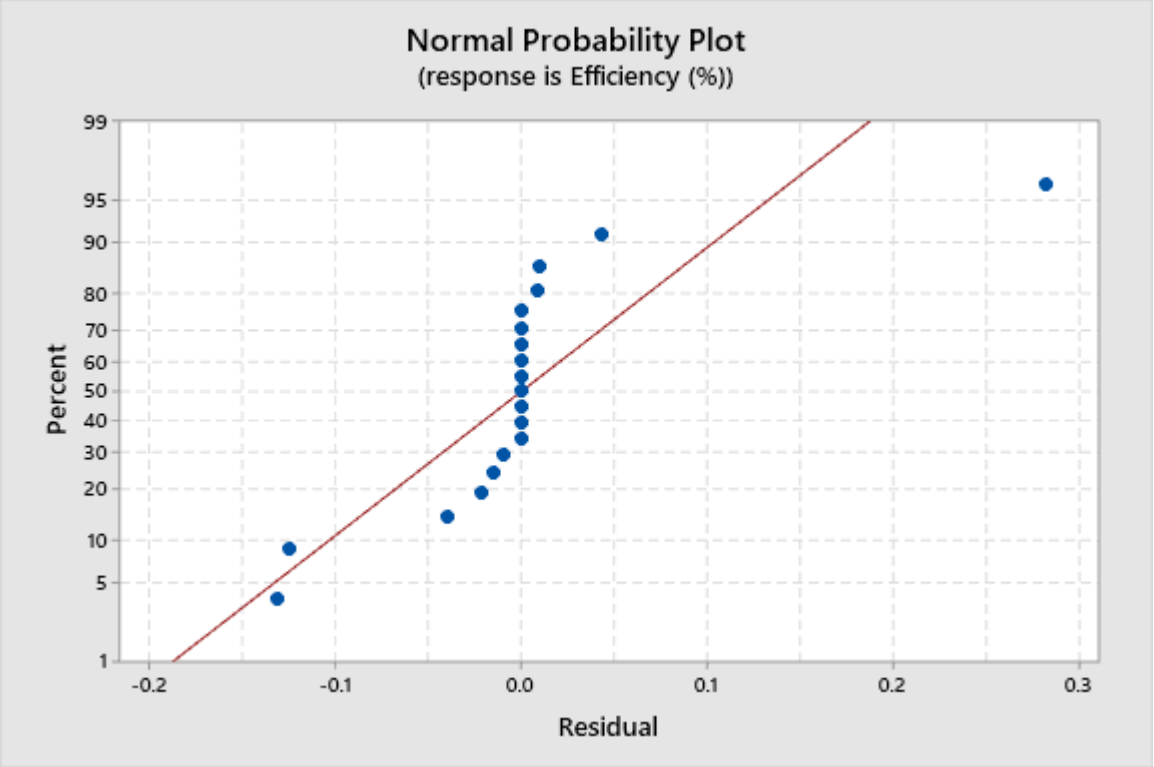
Normal Probability Plot
(response is Efficiency (%))
Percent
99
95
90
80
70
60
50
40
30
20
10
5
1
-0.2
-0.1
0.0
0.1
0.2
0.3
Residual

Model 5

Analysis of Variance

Source	DF	Adj SS
Model	15	1.41984
Linear	5	0.68358
Angular or Curved (A=1, C=0)	1	0.01577
Total Length of Cracks (µm)	1	0.00171
Area of Holes (µm)	1	0.06446
% image opaque	1	0.08670
Radius of Curvature	1	0.00009
2-Way Interactions	6	0.49821
Angular or Curved (A=1, C=0)*Total Length of Cracks (µm)	1	0.02475
Angular or Curved (A=1, C=0)*% image opaque	1	0.15216
Angular or Curved (A=1, C=0)*Radius of Curvature	1	0.00060
Total Length of Cracks (µm)*% image opaque	1	0.23247
Total Length of Cracks (µm)*Radius of Curvature	1	0.22433
% image opaque*Radius of Curvature	1	0.11190
3-Way Interactions	4	0.56862
Angular or Curved (A=1, C=0)*Total Length of Cracks (µm)*% image opaque	1	0.31459
Angular or Curved (A=1, C=0)*Total Length of Cracks (µm)*Radius of Curvature	1	0.28139
Angular or Curved (A=1, C=0)*% image opaque*Radius of Curvature	1	0.07613
Total Length of Cracks (µm)*% image opaque*Radius of Curvature	1	0.00254
Error	2	0.08636
Total	17	1.50620

Source	Adj MS
Model	0.094656
Linear	0.136716
Angular or Curved (A=1, C=0)	0.015775
Total Length of Cracks (µm)	0.001706
Area of Holes (µm)	0.064461
% image opaque	0.086695
Radius of Curvature	0.000089
2-Way Interactions	0.083035
Angular or Curved (A=1, C=0)*Total Length of Cracks (µm)	0.024746
Angular or Curved (A=1, C=0)*% image opaque	0.152158
Angular or Curved (A=1, C=0)*Radius of Curvature	0.000597
Total Length of Cracks (µm)*% image opaque	0.232474
Total Length of Cracks (µm)*Radius of Curvature	0.224330
% image opaque*Radius of Curvature	0.111899
3-Way Interactions	0.142155
Angular or Curved (A=1, C=0)*Total Length of Cracks (µm)*% image opaque	0.314593
Angular or Curved (A=1, C=0)*Total Length of Cracks (µm)*Radius of Curvature	0.281394
Angular or Curved (A=1, C=0)*% image opaque*Radius of Curvature	0.076129
Total Length of Cracks (µm)*% image opaque*Radius of Curvature	0.002535
Error	0.043182
Total	

Source	F-Value
Model	2.19
Linear	3.17
Angular or Curved (A=1, C=0)	0.37
Total Length of Cracks (µm)	0.04
Area of Holes (µm)	1.49
% image opaque	2.01
Radius of Curvature	0.00
2-Way Interactions	1.92
Angular or Curved (A=1, C=0)*Total Length of Cracks (µm)	0.57
Angular or Curved (A=1, C=0)*% image opaque	3.52
Angular or Curved (A=1, C=0)*Radius of Curvature	0.01
Total Length of Cracks (µm)*% image opaque	5.38
Total Length of Cracks (µm)*Radius of Curvature	5.19
% image opaque*Radius of Curvature	2.59
3-Way Interactions	3.29
Angular or Curved (A=1, C=0)*Total Length of Cracks (µm)*% image opaque	7.29
Angular or Curved (A=1, C=0)*Total Length of Cracks (µm)*Radius of Curvature	6.52
Angular or Curved (A=1, C=0)*% image opaque*Radius of Curvature	1.76
Total Length of Cracks (µm)*% image opaque*Radius of Curvature	0.06
Error	
Total	

Source	P-Value
Model	0.358
Linear	0.257
Angular or Curved (A=1, C=0)	0.607
Total Length of Cracks (µm)	0.861
Area of Holes (µm)	0.346
% image opaque	0.292
Radius of Curvature	0.968
2-Way Interactions	0.381
Angular or Curved (A=1, C=0)*Total Length of Cracks (µm)	0.528
Angular or Curved (A=1, C=0)*% image opaque	0.201
Angular or Curved (A=1, C=0)*Radius of Curvature	0.917
Total Length of Cracks (µm)*% image opaque	0.146
Total Length of Cracks (µm)*Radius of Curvature	0.150
% image opaque*Radius of Curvature	0.249
3-Way Interactions	0.246
Angular or Curved (A=1, C=0)*Total Length of Cracks (µm)*% image opaque	0.114
Angular or Curved (A=1, C=0)*Total Length of Cracks (µm)*Radius of Curvature	0.125
Angular or Curved (A=1, C=0)*% image opaque*Radius of Curvature	0.316
Total Length of Cracks (µm)*% image opaque*Radius of Curvature	0.831
Error	
Total	

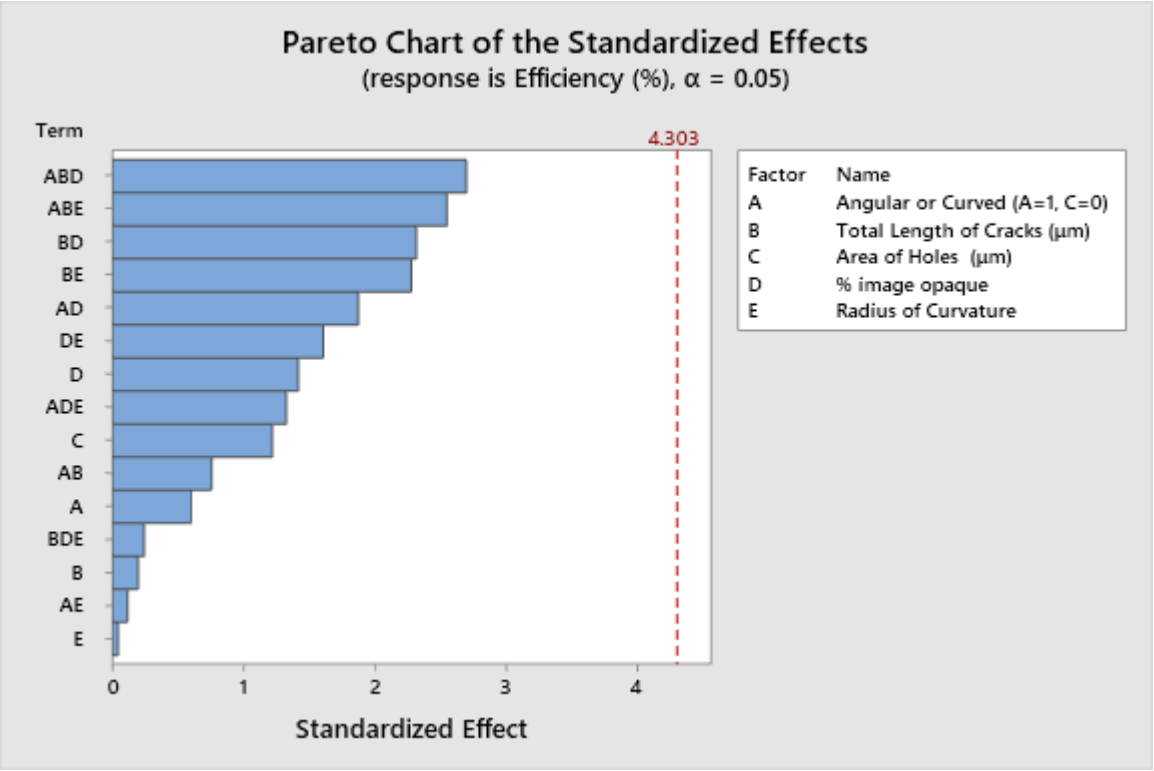
Pareto Chart of the Standardized Effects
(response is Efficiency (%), α = 0.05)
Term
4.303
ABD
ABE
BD
BE
AD
DE
D
ADE
C
AB
A
BDE
B
AE
E
0
1
2
3
4
Standardized Effect
Factor Name
A Angular or Curved (A=1, C=0)
B Total Length of Cracks (µm)
C Area of Holes (µm)
D % image opaque
E Radius of Curvature

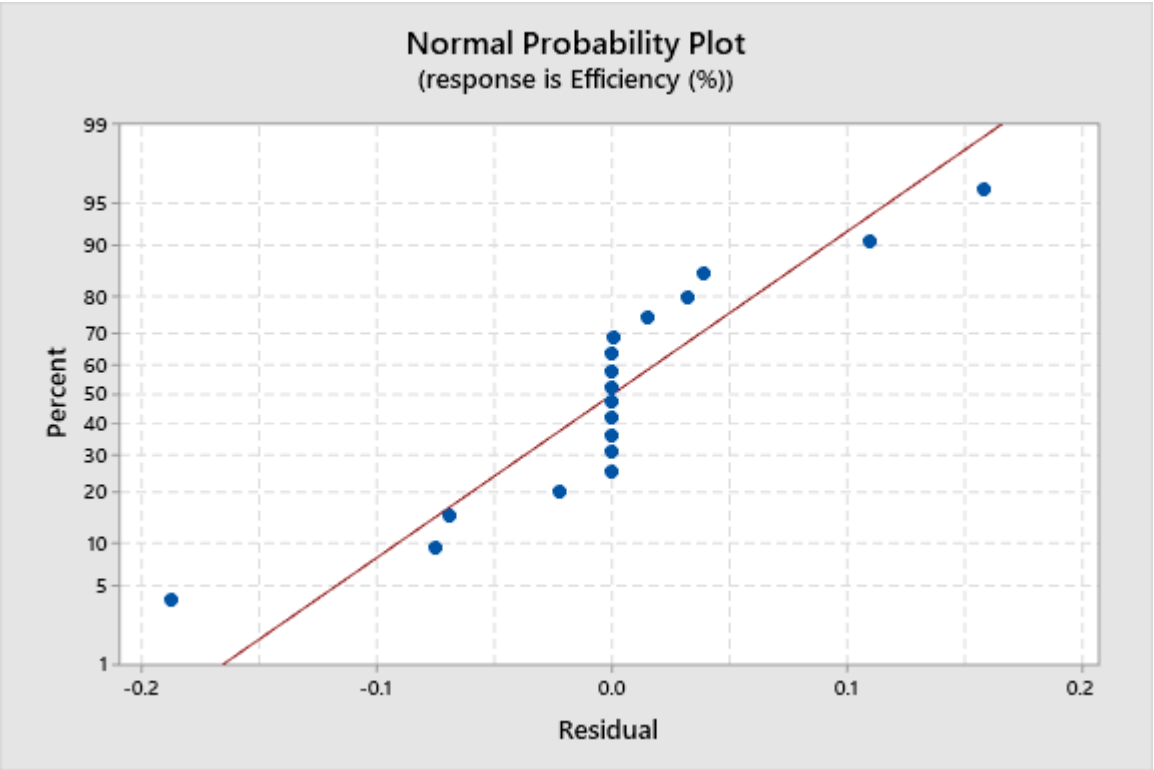
Normal Probability Plot
(response is Efficiency (%))
Percent
99
95
90
80
70
60
50
40
30
20
10
5
1
-0.2
-0.1
0.0
0.1
0.2
Residual

Model 6

Analysis of Variance

Source	DF	Adj SS	Adj MS	F-Value
Model	14	1.08674	0.07762	0.65
Linear	5	0.26029	0.05206	0.44
Angular or Curved (A=1, C=0)	1	0.02132	0.02132	0.18
% image opaque	1	0.02546	0.02546	0.21
Area of Holes (µm)	1	0.02738	0.02738	0.23
Resistivity	1	0.02897	0.02897	0.24
Radius of Curvature	1	0.02754	0.02754	0.23
2-Way Interactions	7	0.55552	0.07936	0.67
Angular or Curved (A=1, C=0)*% image opaque	1	0.02553	0.02553	0.21
Angular or Curved (A=1, C=0)*Resistivity	1	0.02560	0.02560	0.22
Angular or Curved (A=1, C=0)*Radius of Curvature	1	0.02251	0.02251	0.19
% image opaque*Area of Holes (µm)	1	0.02614	0.02614	0.22
% image opaque*Resistivity	1	0.03113	0.03113	0.26
% image opaque*Radius of Curvature	1	0.02646	0.02646	0.22
Resistivity*Radius of Curvature	1	0.02610	0.02610	0.22
3-Way Interactions	2	0.06860	0.03430	0.29
Angular or Curved (A=1, C=0)*% image opaque*Resistivity	1	0.02844	0.02844	0.24
% image opaque*Resistivity*Radius of Curvature	1	0.02586	0.02586	0.22
Error	1	0.11895	0.11895	
Total	15	1.20569		

Source	P-Value
Model	0.764
Linear	0.809
Angular or Curved (A=1, C=0)	0.745
% image opaque	0.724
Area of Holes (µm)	0.715
Resistivity	0.708
Radius of Curvature	0.714
2-Way Interactions	0.740
Angular or Curved (A=1, C=0)*% image opaque	0.724
Angular or Curved (A=1, C=0)*Resistivity	0.723
Angular or Curved (A=1, C=0)*Radius of Curvature	0.739
% image opaque*Area of Holes (µm)	0.721
% image opaque*Resistivity	0.699
% image opaque*Radius of Curvature	0.719
Resistivity*Radius of Curvature	0.721
3-Way Interactions	0.796
Angular or Curved (A=1, C=0)*% image opaque*Resistivity	0.710
% image opaque*Resistivity*Radius of Curvature	0.722
Error	
Total	

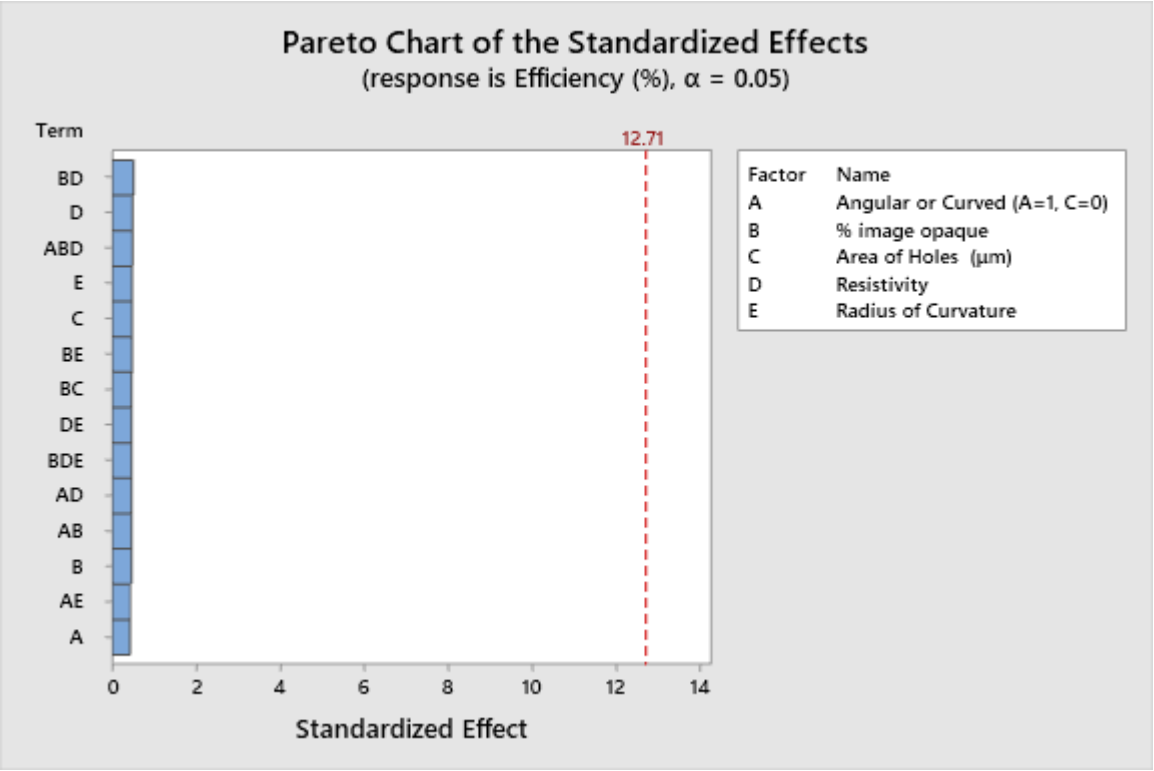
Pareto Chart of the Standardized Effects
(response is Efficiency (%), α = 0.05)
Term
12.71
BD
D
ABD
E
C
BE
BC
DE
BDE
AD
AB
B
AE
A
0
2
4
6
8
10
12
14
Standardized Effect
Factor Name
A Angular or Curved (A=1, C=0)
B % image opaque
C Area of Holes (µm)
D Resistivity
E Radius of Curvature

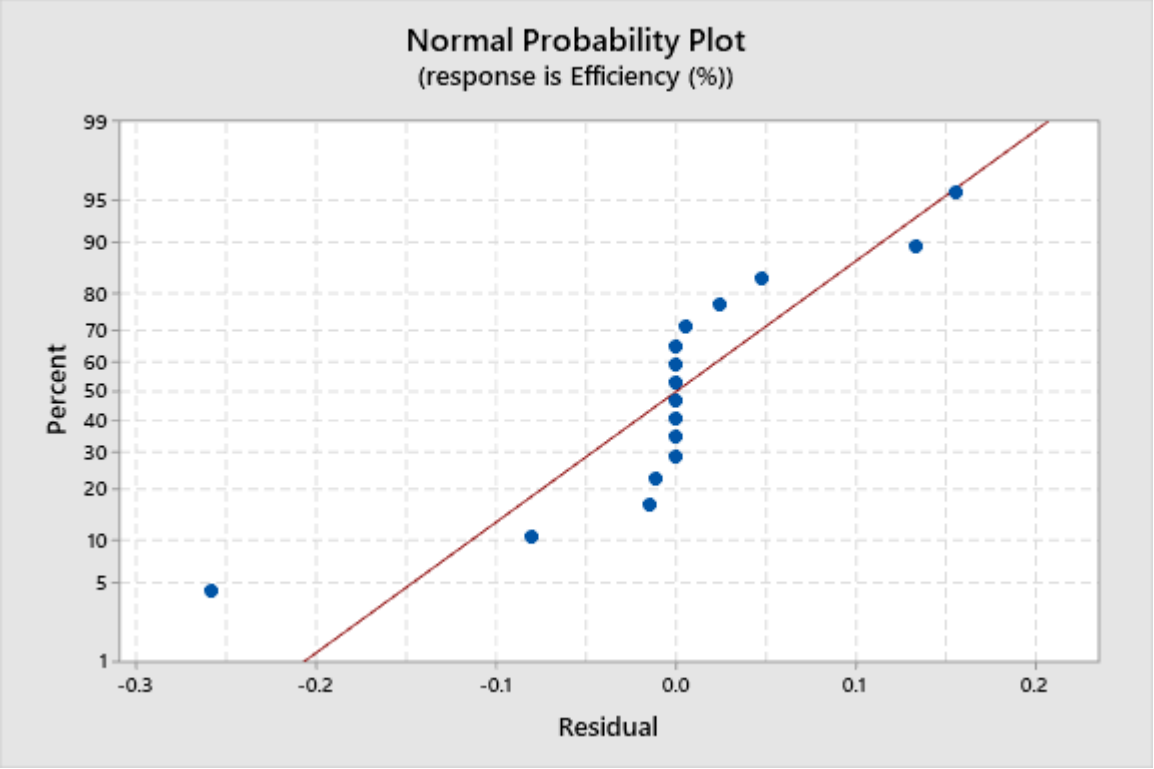
Normal Probability Plot
(response is Efficiency (%))
Percent
99
95
90
80
70
60
50
40
30
20
10
5
1
-0.3
-0.2
-0.1
0.0
0.1
0.2
Residual

Model 7

Analysis of Variance

Source	DF	Adj SS	Adj MS	F-Value
Model	14	1.14675	0.081911	1.39
Linear	5	0.28404	0.056807	0.96
Angular or Curved (A=1, C=0)	1	0.01879	0.018786	0.32
% image opaque	1	0.09937	0.099374	1.69
Area of Holes (µm)	1	0.00497	0.004974	0.08
Resistance	1	0.00194	0.001943	0.03
Radius of Curvature	1	0.02538	0.025377	0.43
2-Way Interactions	7	0.55879	0.079828	1.35
Angular or Curved (A=1, C=0)*% image opaque	1	0.01478	0.014781	0.25
Angular or Curved (A=1, C=0)*Resistance	1	0.01401	0.014012	0.24
Angular or Curved (A=1, C=0)*Radius of Curvature	1	0.00898	0.008977	0.15
% image opaque*Area of Holes (µm)	1	0.00238	0.002381	0.04
% image opaque*Resistance	1	0.01184	0.011837	0.20
% image opaque*Radius of Curvature	1	0.00480	0.004797	0.08
Resistance*Radius of Curvature	1	0.03639	0.036386	0.62
3-Way Interactions	2	0.23712	0.118560	2.01
Angular or Curved (A=1, C=0)*% image opaque*Resistance	1	0.01496	0.014960	0.25
% image opaque*Resistance*Radius of Curvature	1	0.02882	0.028816	0.49
Error	1	0.05894	0.058943	
Total	15	1.20569		

Source	P-Value
Model	0.589
Linear	0.645
Angular or Curved (A=1, C=0)	0.673
% image opaque	0.418
Area of Holes (µm)	0.820
Resistance	0.886
Radius of Curvature	0.630
2-Way Interactions	0.581
Angular or Curved (A=1, C=0)*% image opaque	0.704
Angular or Curved (A=1, C=0)*Resistance	0.711
Angular or Curved (A=1, C=0)*Radius of Curvature	0.763
% image opaque*Area of Holes (µm)	0.874
% image opaque*Resistance	0.732
% image opaque*Radius of Curvature	0.823
Resistance*Radius of Curvature	0.576
3-Way Interactions	0.446
Angular or Curved (A=1, C=0)*% image opaque*Resistance	0.703
% image opaque*Resistance*Radius of Curvature	0.612
Error	
Total	

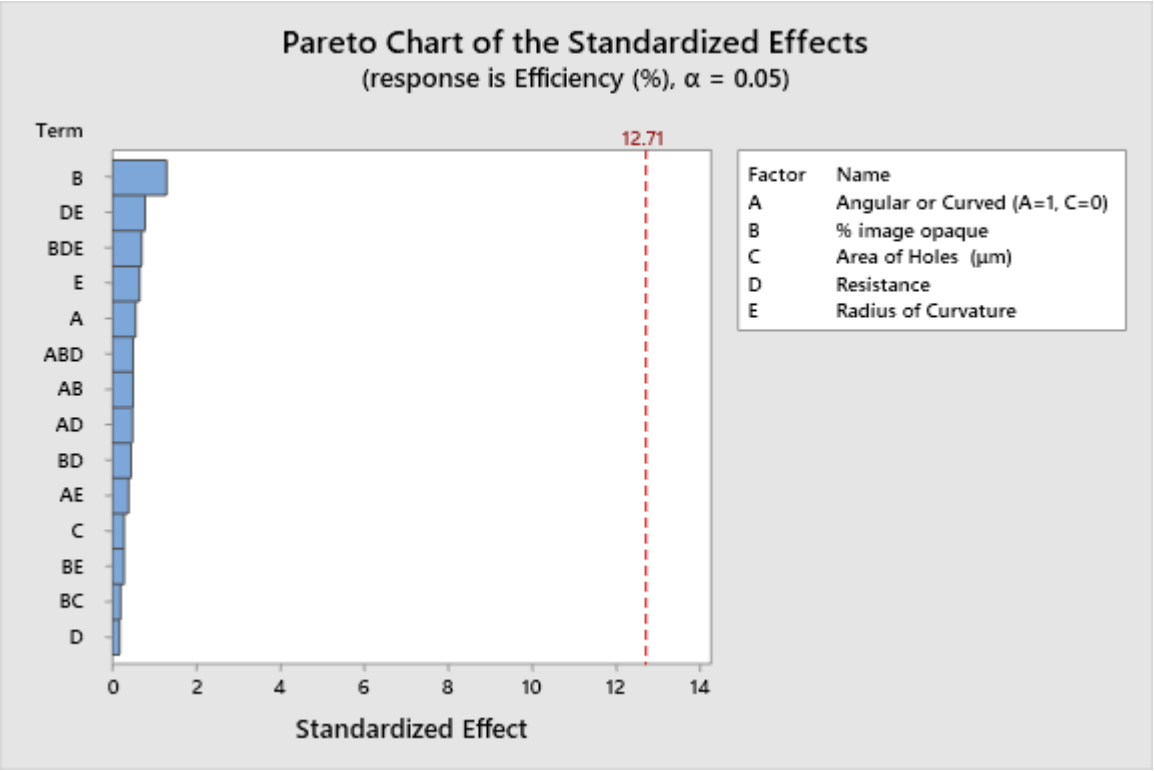
Pareto Chart of the Standardized Effects
(response is Efficiency (%), α = 0.05)
Term
B
DE
BDE
E
A
ABD
AB
AD
BD
AE
C
BE
BC
D
12.71
0
2
4
6
8
10
12
14
Standardized Effect
Factor Name
A Angular or Curved (A=1, C=0)
B % image opaque
C Area of Holes (µm)
D Resistance
E Radius of Curvature

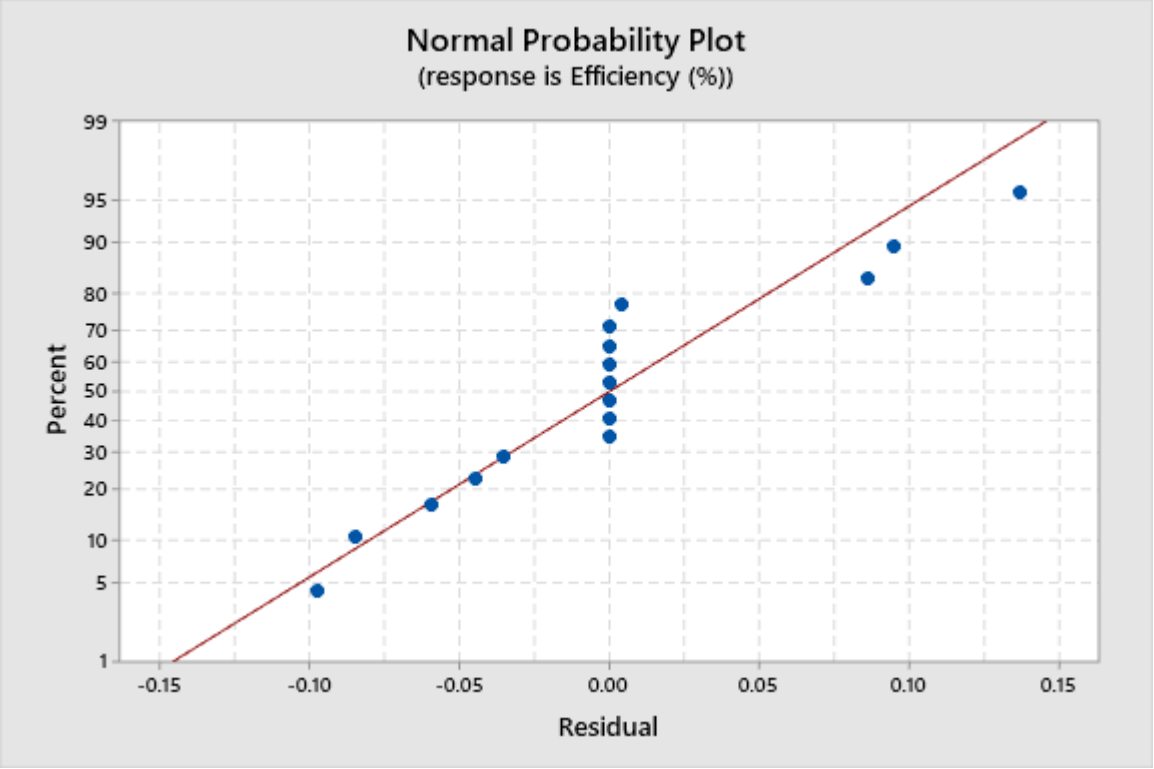
Normal Probability Plot
(response is Efficiency (%))
Percent
99
95
90
80
70
60
50
40
30
20
10
5
1
-0.15
-0.10
-0.05
0.00
0.05
0.10
0.15
Residual

Model 8

Analysis of Variance

Source	DF	Adj SS	Adj MS	F-Value	P-Value
Model	6	0.81710	0.136183	1.71	0.178
Linear	3	0.27186	0.090619	1.14	0.361
Angular or Curved (A=1, C=0)	1	0.06108	0.061083	0.77	0.393
% image opaque	1	0.02304	0.023044	0.29	0.597
Area of Holes (µm)	1	0.08788	0.087879	1.11	0.308
Square	2	0.21664	0.108322	1.36	0.282
% image opaque*% image opaque	1	0.00870	0.008700	0.11	0.745
Area of Holes (µm)*Area of Holes (µm)	1	0.20146	0.201463	2.53	0.130
2-Way Interaction	1	0.03553	0.035529	0.45	0.513
Angular or Curved (A=1, C=0)*% image opaque	1	0.03553	0.035529	0.45	0.513
Error	17	1.35110	0.079476		
Total	23	2.16820			

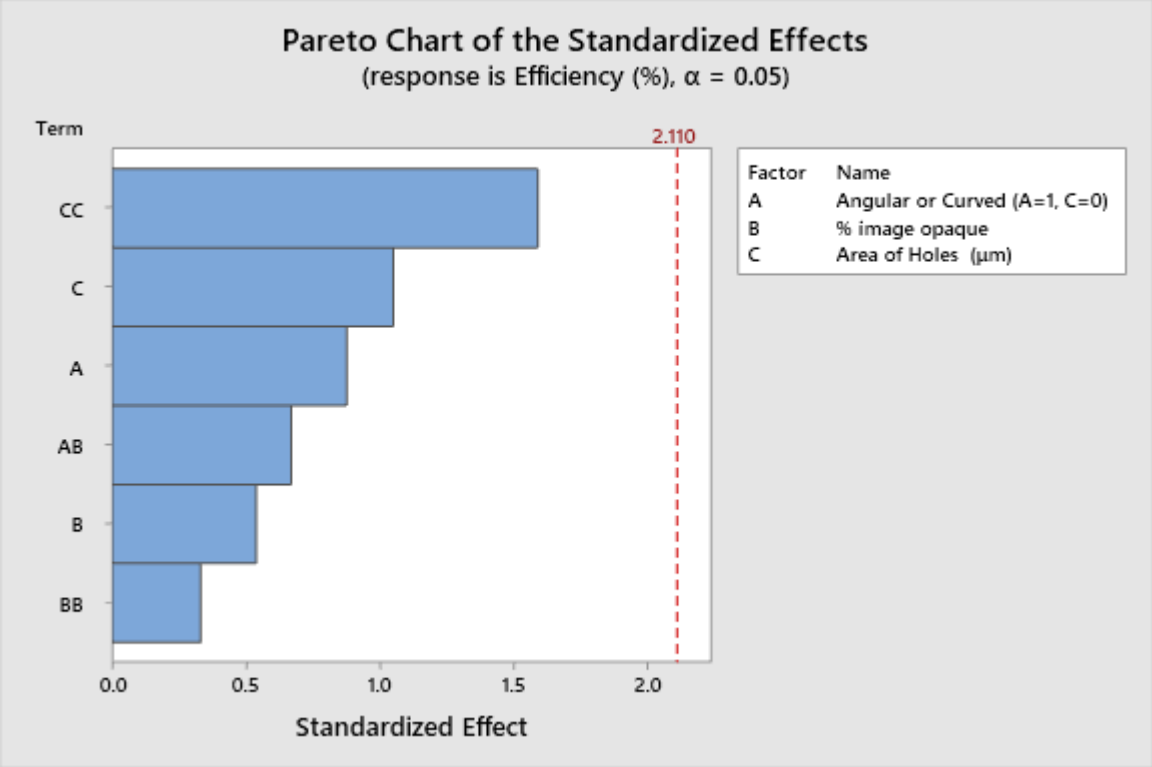

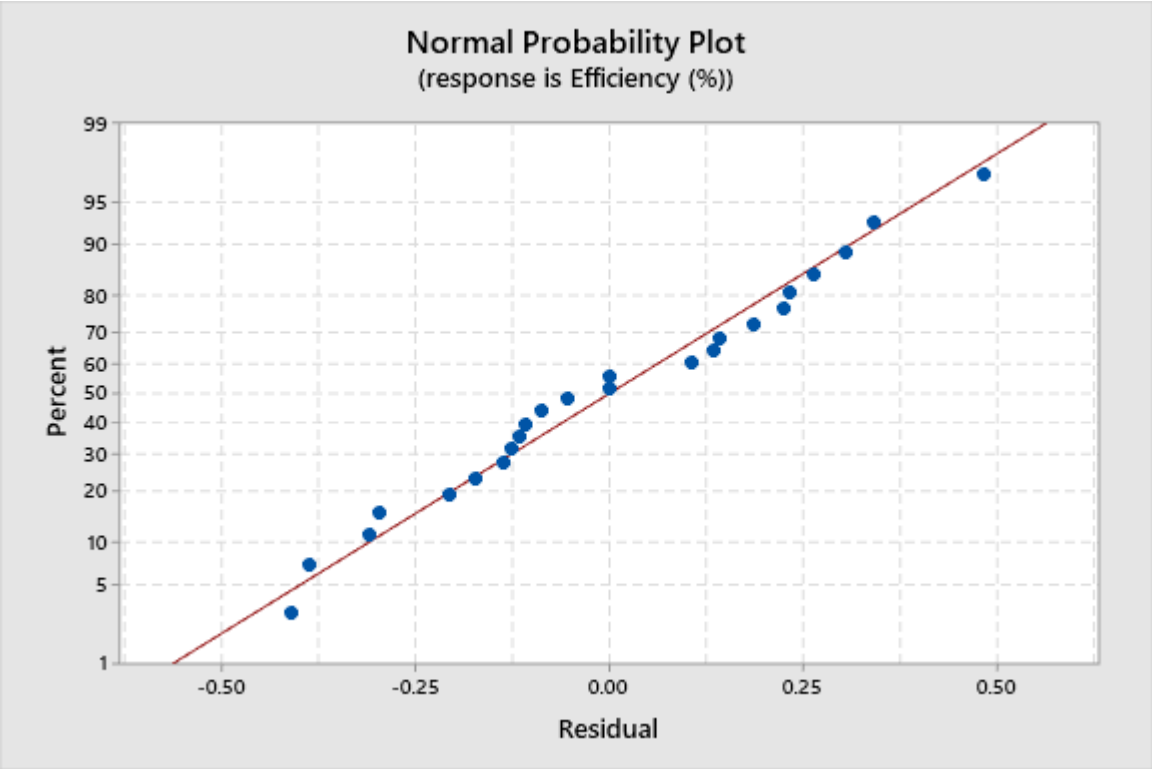
Normal Probability Plot
(response is Efficiency (%))
Percent
99
95
90
80
70
60
50
40
30
20
10
5
1
-0.50
-0.25
0.00
0.25
0.50
Residual

Model 9

Analysis of Variance

Source	DF	Adj SS	Adj MS	F-Value
Model	9	1.07323	0.119248	1.49
Linear	4	0.07087	0.017717	0.22
Total Length of Cracks (µm)	1	0.00389	0.003888	0.05
% image opaque	1	0.00000	0.000000	0.00
Area of Holes (µm)	1	0.02114	0.021136	0.26
Angular or Curved (A=1, C=0)	1	0.00120	0.001198	0.02
Square	2	0.08321	0.041605	0.52
Total Length of Cracks (µm)*Total Length of Cracks (µm)	1	0.07966	0.079664	1.00
% image opaque*% image opaque	1	0.02547	0.025465	0.32
2-Way Interaction	3	0.26323	0.087742	1.10
Total Length of Cracks (µm)*% image opaque	1	0.00500	0.004999	0.06
Total Length of Cracks (µm)*Angular or Curved (A=1, C=0)	1	0.02640	0.026400	0.33
% image opaque*Angular or Curved (A=1, C=0)	1	0.11448	0.114477	1.43
Error	11	0.87829	0.079845	
Total	20	1.95152		

Source	P-Value
Model	0.261
Linear	0.921
Total Length of Cracks (µm)	0.829
% image opaque	0.999
Area of Holes (µm)	0.617
Angular or Curved (A=1, C=0)	0.905
Square	0.608
Total Length of Cracks (µm)*Total Length of Cracks (µm)	0.339
% image opaque*% image opaque	0.584
2-Way Interaction	0.391
Total Length of Cracks (µm)*% image opaque	0.807
Total Length of Cracks (µm)*Angular or Curved (A=1, C=0)	0.577
% image opaque*Angular or Curved (A=1, C=0)	0.256
Error	
Total	

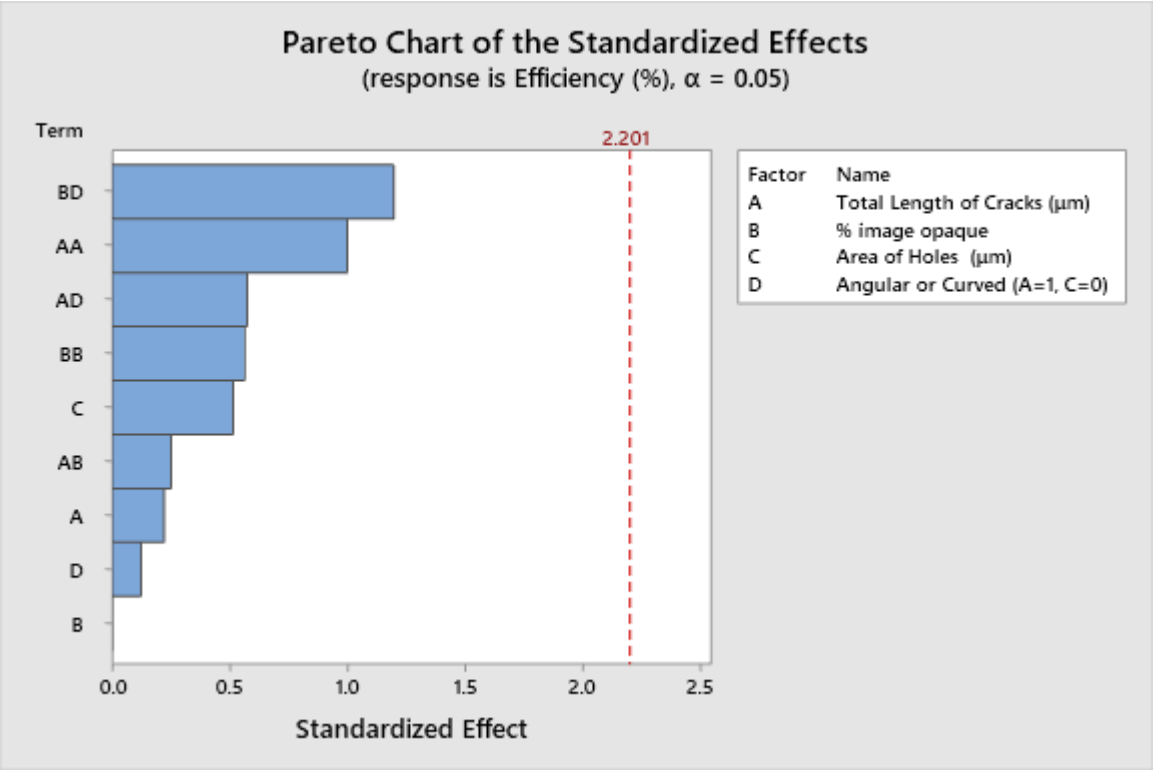
Pareto Chart of the Standardized Effects
(response is Efficiency (%), α = 0.05)
Term
2.201
BD
AA
AD
BB
C
AB
A
D
B
0.0
0.5
1.0
1.5
2.0
2.5
Standardized Effect
Factor Name
A Total Length of Cracks (µm)
B % image opaque
C Area of Holes (µm)
D Angular or Curved (A=1, C=0)

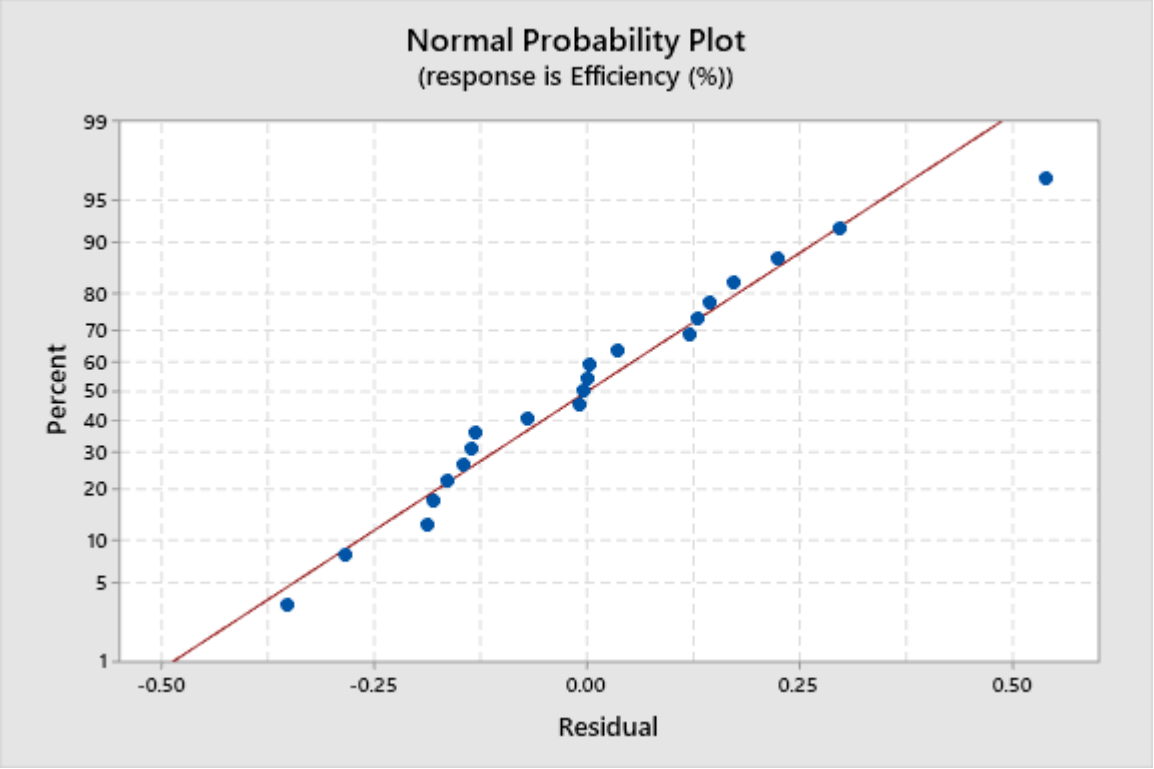
Normal Probability Plot
(response is Efficiency (%))
Percent
99
95
90
80
70
60
50
40
30
20
10
5
1
-0.50
-0.25
0.00
0.25
0.50
Residual

Model 10

Analysis of Variance

Source	DF	Adj SS	Adj MS	F-Value
Model	10	1.10311	0.110311	1.78
Linear	4	0.60837	0.152092	2.45
Radius of Curvature (µm)	1	0.20565	0.205647	3.31
% image opaque	1	0.36646	0.366464	5.91
Area of Holes (µm)	1	0.05687	0.056869	0.92
Angular or Curved (A=1, C=0)	1	0.02348	0.023480	0.38
Square	3	0.38117	0.127058	2.05
Radius of Curvature (µm)*Radius of Curvature (µm)	1	0.07131	0.071307	1.15
% image opaque*% image opaque	1	0.03336	0.033363	0.54
Area of Holes (µm)*Area of Holes (µm)	1	0.29200	0.292004	4.71
2-Way Interaction	3	0.36661	0.122204	1.97
Radius of Curvature (µm)*% image opaque	1	0.36481	0.364807	5.88
Radius of Curvature (µm)*Angular or Curved (A=1, C=0)	1	0.00395	0.003945	0.06
% image opaque*Angular or Curved (A=1, C=0)	1	0.00016	0.000163	0.00
Error	10	0.62041	0.062041	
Total	20	1.72351		

Source	P-Value
Model	0.189
Linear	0.114
Radius of Curvature (µm)	0.099
% image opaque	0.035
Area of Holes (µm)	0.361
Angular or Curved (A=1, C=0)	0.552
Square	0.171
Radius of Curvature (µm)*Radius of Curvature (µm)	0.309
% image opaque*% image opaque	0.480
Area of Holes (µm)*Area of Holes (µm)	0.055
2-Way Interaction	0.183
Radius of Curvature (µm)*% image opaque	0.036
Radius of Curvature (µm)*Angular or Curved (A=1, C=0)	0.806
% image opaque*Angular or Curved (A=1, C=0)	0.960
Error	
Total	

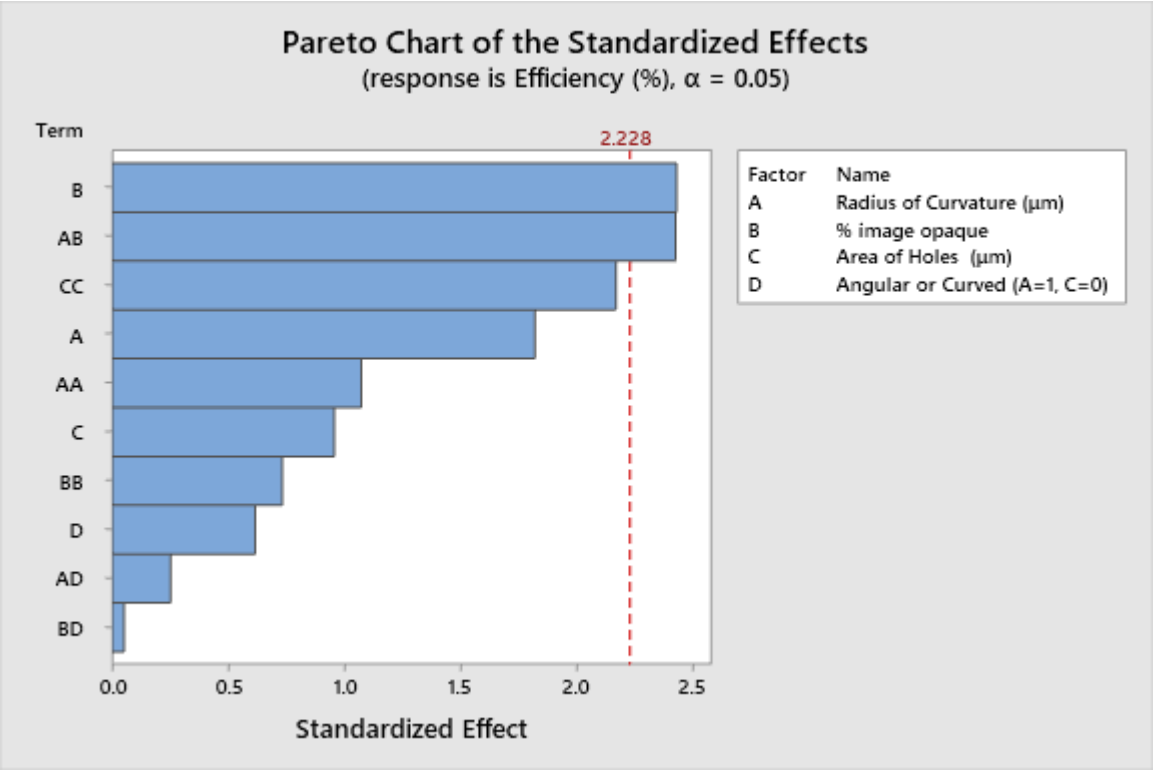
Pareto Chart of the Standardized Effects
(response is Efficiency (%), α = 0.05)
Term
2.228
B
AB
CC
A
AA
C
BB
D
AD
BD
0.0
0.5
1.0
1.5
2.0
2.5
Standardized Effect
Factor Name
A Radius of Curvature (µm)
B % image opaque
C Area of Holes (µm)
D Angular or Curved (A=1, C=0)

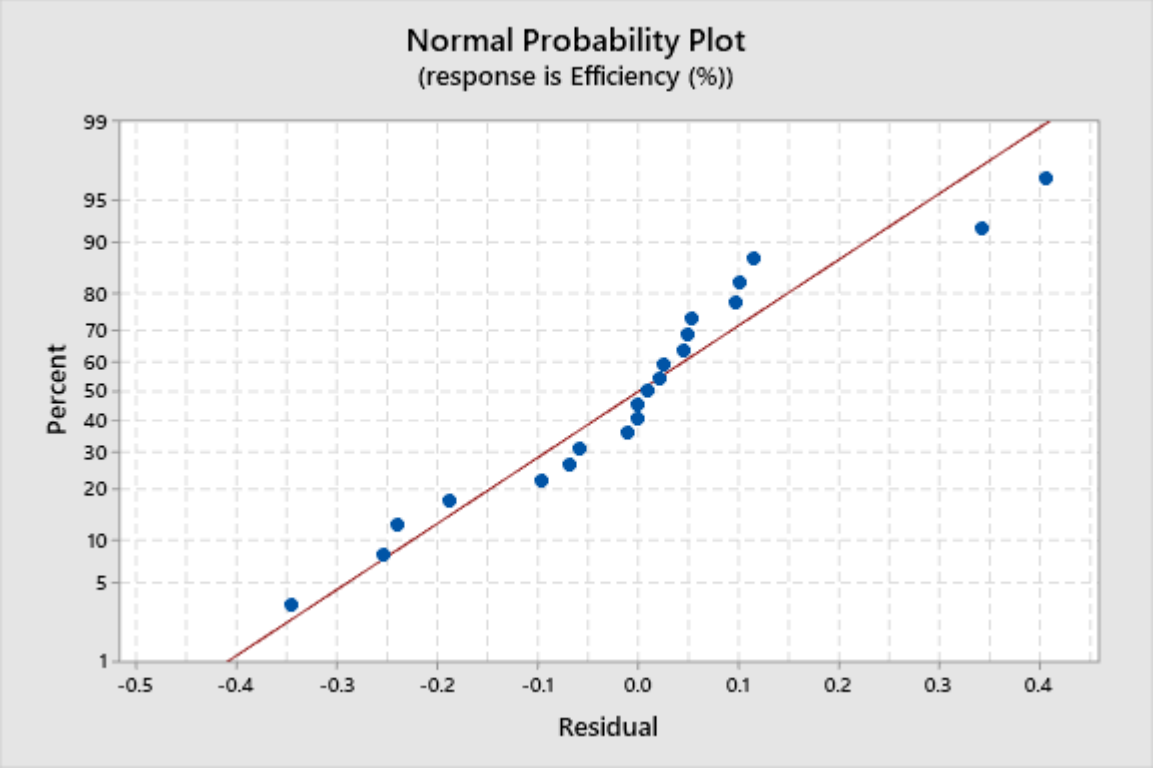
Normal Probability Plot
(response is Efficiency (%))
Percent
99
95
90
80
70
60
50
40
30
20
10
5
1
-0.5
-0.4
-0.3
-0.2
-0.1
0.0
0.1
0.2
0.3
0.4
Residual

Model 11

Analysis of Variance

Source	DF	Adj SS	Adj MS	F-Value	P-Value
Model	15	1.53208	0.102139	2.91	0.206
Linear	5	0.29123	0.058246	1.66	0.359
% image opaque	1	0.12067	0.120675	3.44	0.161
Area of Holes (µm)	1	0.00510	0.005100	0.15	0.729
Resistivity	1	0.12376	0.123759	3.52	0.157
Resistance	1	0.22735	0.227347	6.47	0.084
Angular or Curved (A=1, C=0)	1	0.02205	0.022051	0.63	0.486
Square	4	0.21539	0.053847	1.53	0.378
% image opaque*% image opaque	1	0.14108	0.141078	4.02	0.139
Area of Holes (µm)*Area of Holes (µm)	1	0.17984	0.179844	5.12	0.109
Resistivity*Resistivity	1	0.10035	0.100351	2.86	0.190
Resistance*Resistance	1	0.02503	0.025033	0.71	0.461
2-Way Interaction	6	0.30325	0.050541	1.44	0.412
% image opaque*Resistivity	1	0.05649	0.056493	1.61	0.294
% image opaque*Resistance	1	0.17043	0.170434	4.85	0.115
% image opaque*Angular or Curved (A=1, C=0)	1	0.00331	0.003311	0.09	0.779
Resistivity*Resistance	1	0.23106	0.231059	6.58	0.083
Resistivity*Angular or Curved (A=1, C=0)	1	0.05351	0.053513	1.52	0.305
Resistance*Angular or Curved (A=1, C=0)	1	0.01887	0.018867	0.54	0.517
Error	3	0.10539	0.035130		
Total	18	1.63747			

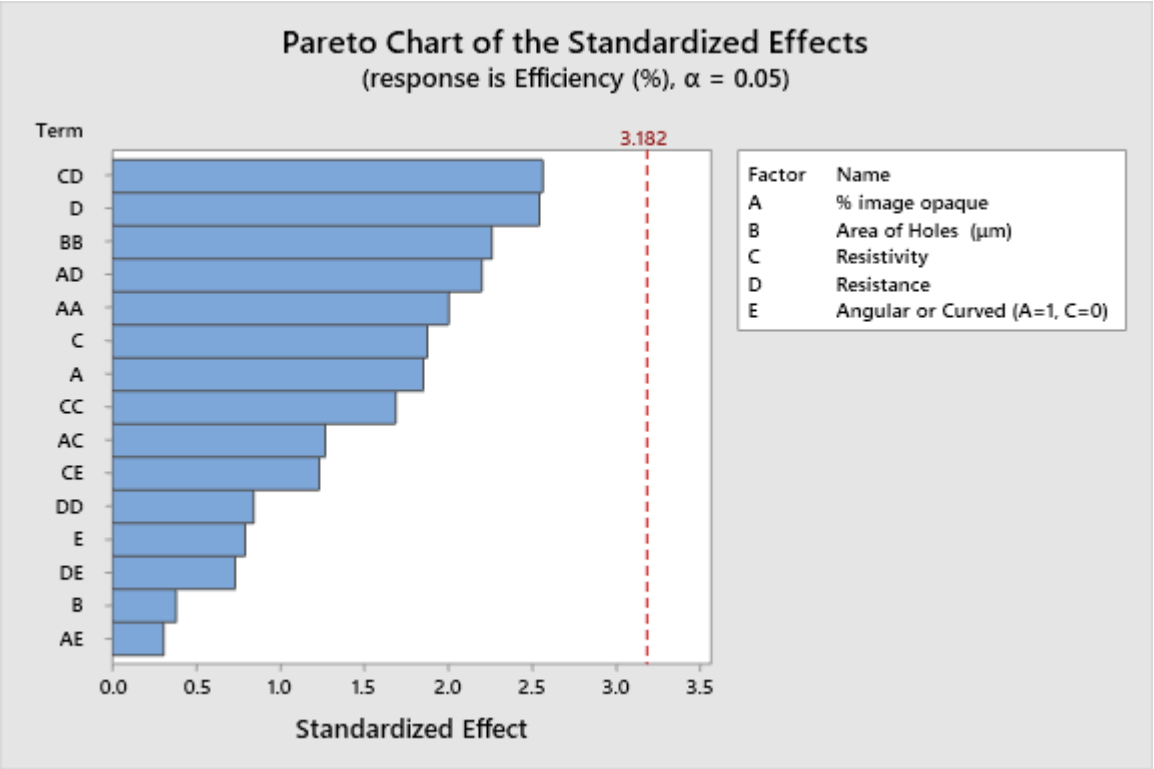
Pareto Chart of the Standardized Effects
(response is Efficiency (%), α = 0.05)
Term
3.182
CD
D
BB
AD
AA
C
A
CC
AC
CE
DD
E
DE
B
AE
0.0
0.5
1.0
1.5
2.0
2.5
3.0
3.5
Standardized Effect
Factor Name
A % image opaque
B Area of Holes (µm)
C Resistivity
D Resistance
E Angular or Curved (A=1, C=0)

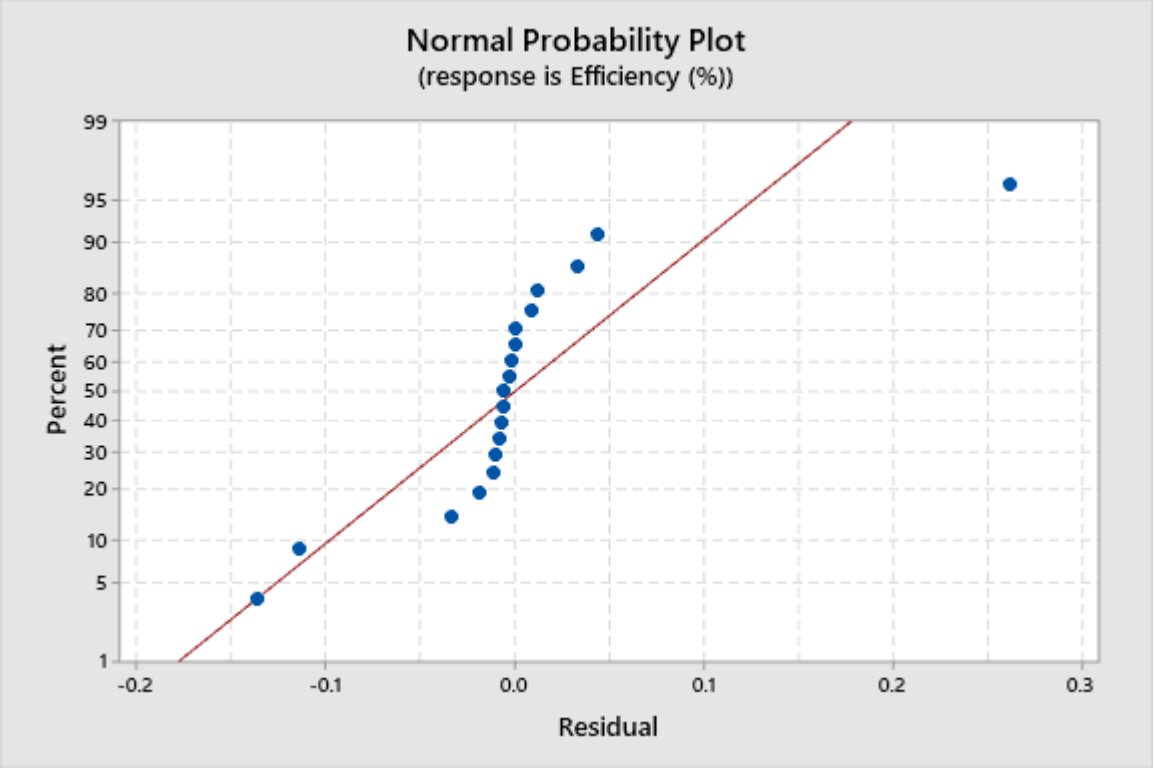
Normal Probability Plot
(response is Efficiency (%))
Percent
99
95
90
80
70
60
50
40
30
20
10
5
1
-0.2
-0.1
0.0
0.1
0.2
0.3
Residual

Appendix 6: All Stitched Rhenium Filament Images and Cropped Images Used for Analysis

Filament 1-1

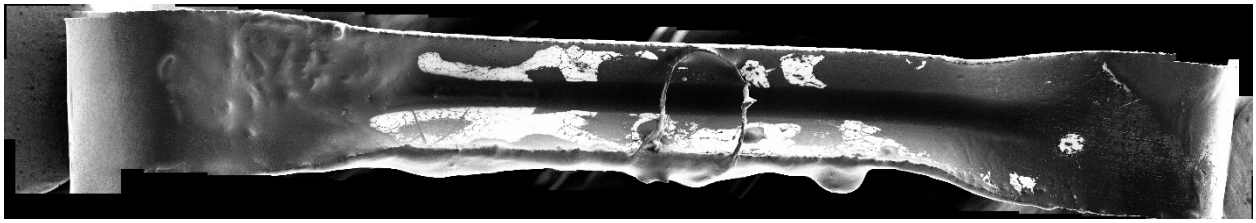

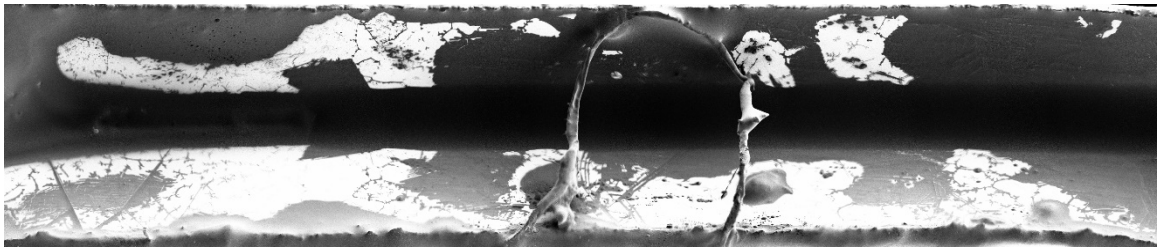

Filament 1-2

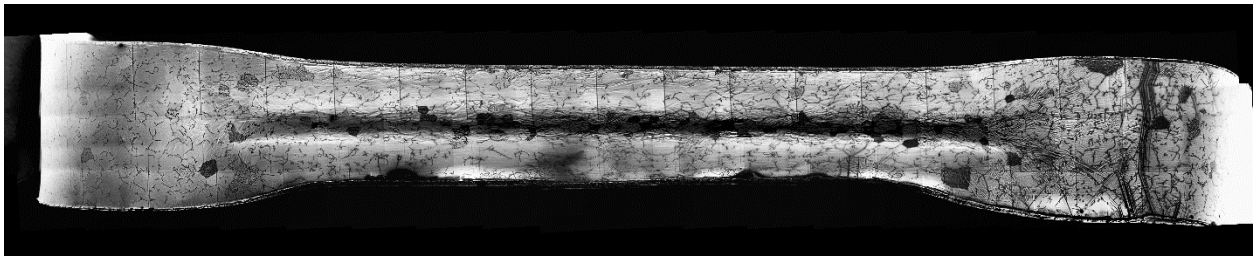

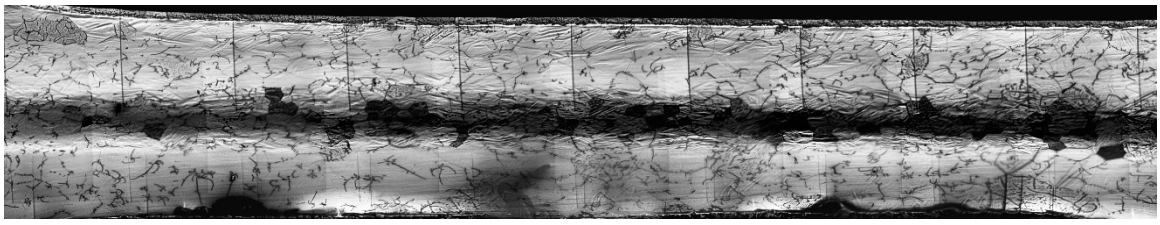

Filament 1-3

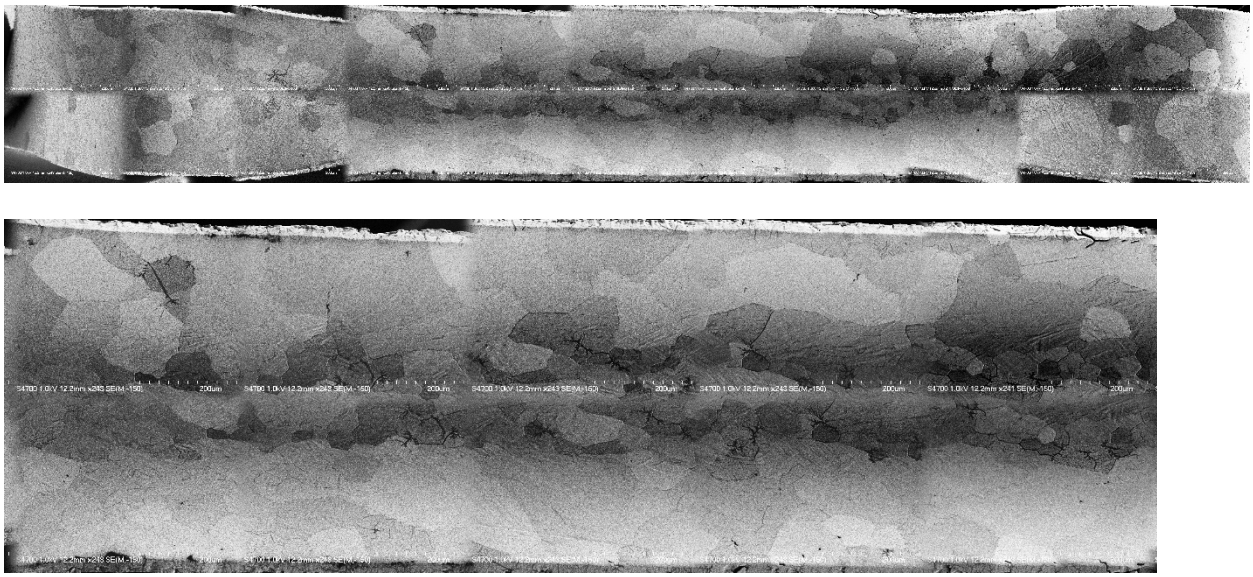

Filament 1-4

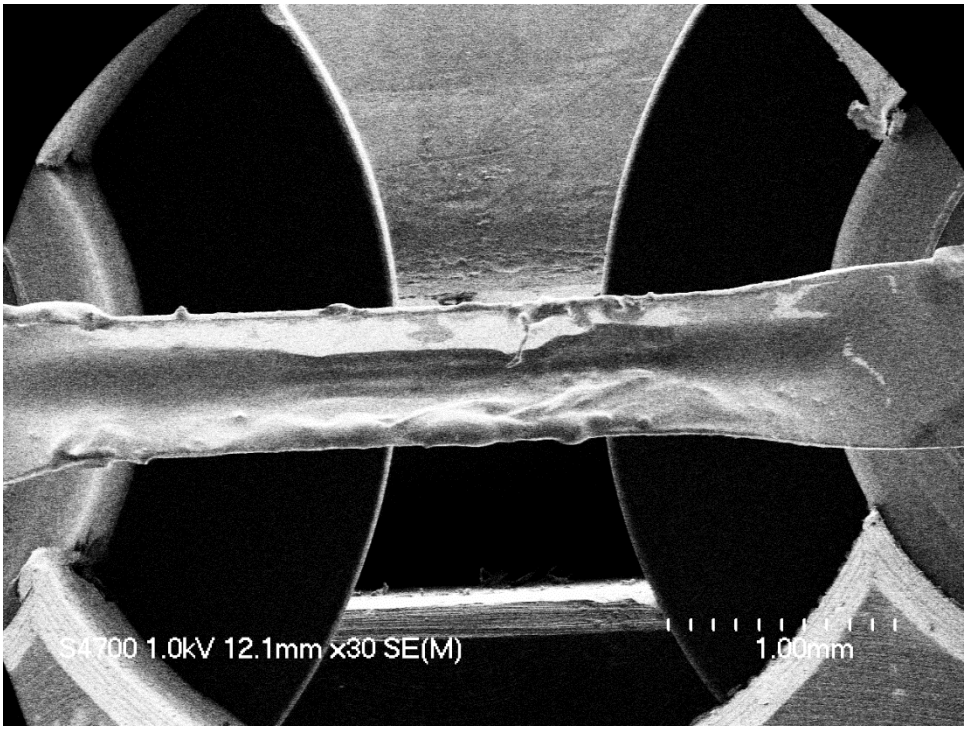

Filament 1-5

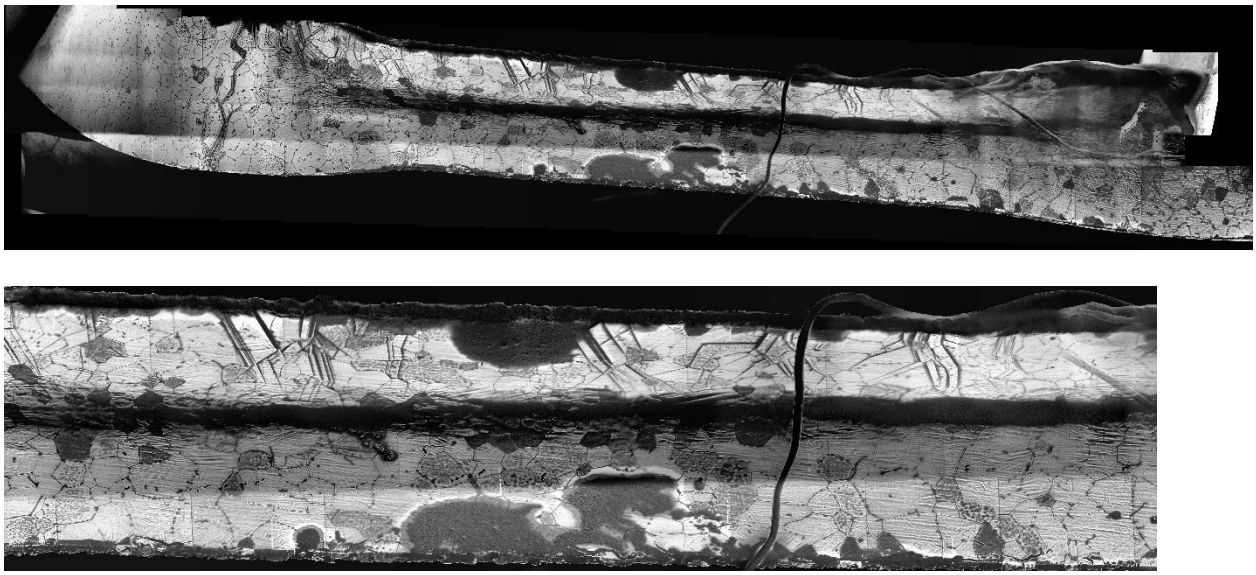

Filament 1-6

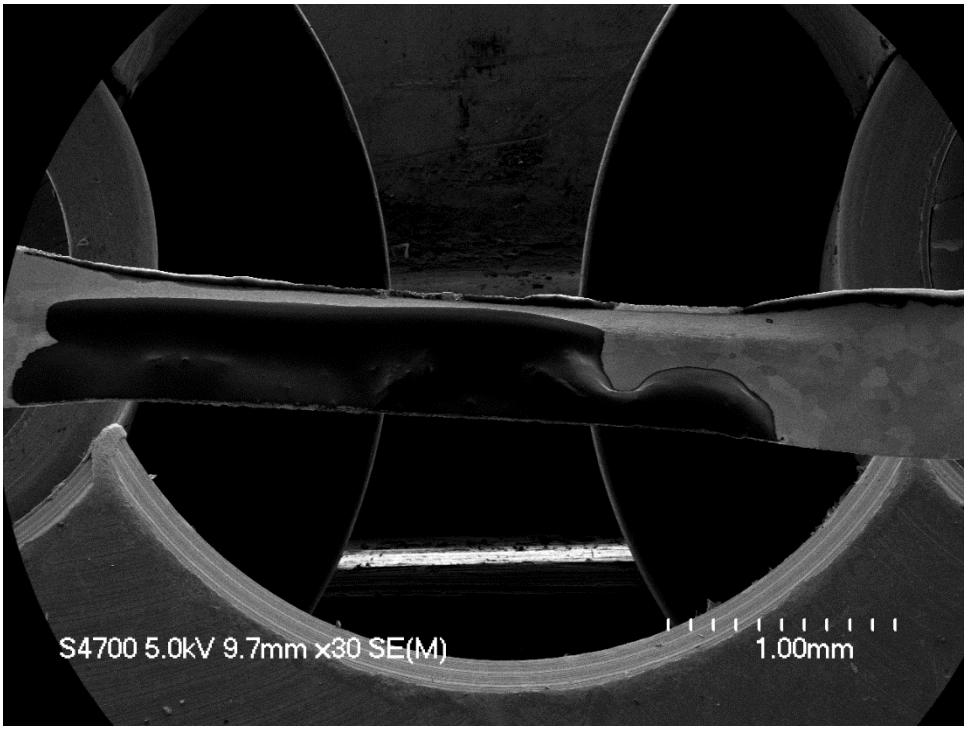

Filament 2-1

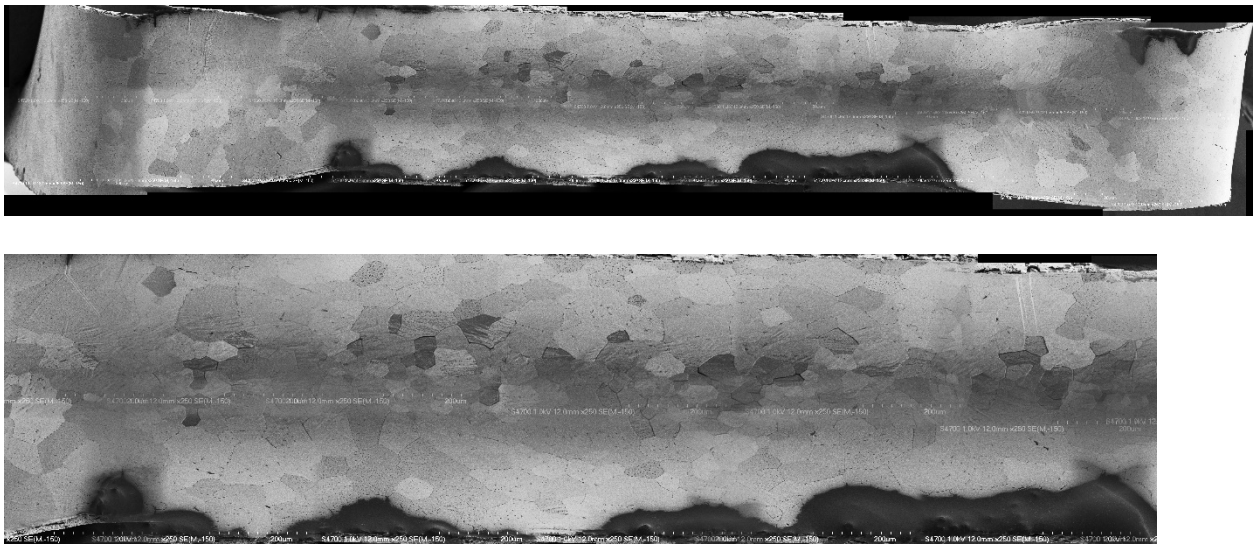

Filament 2-2

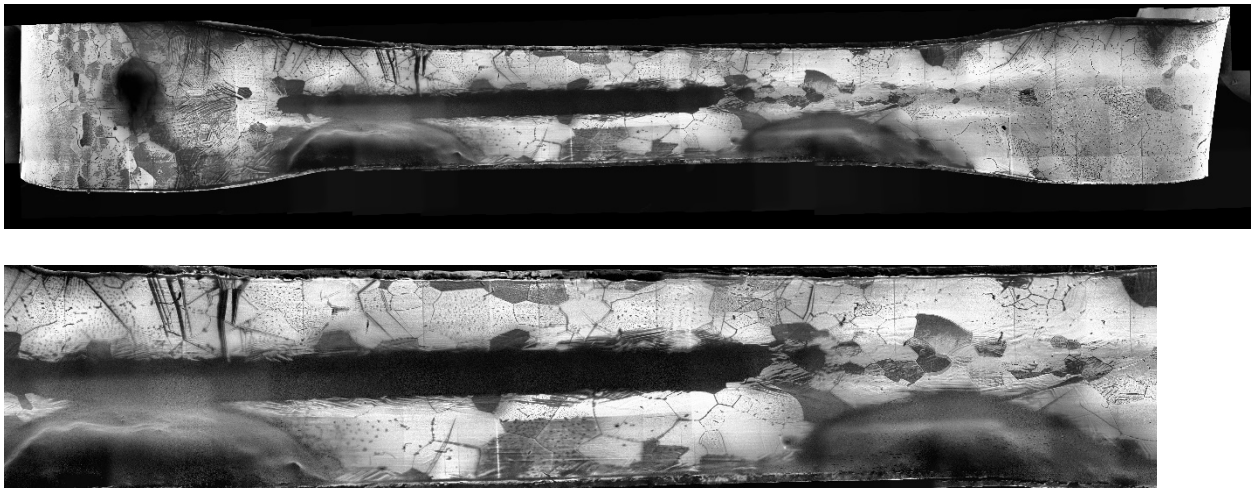

Filament 2-3

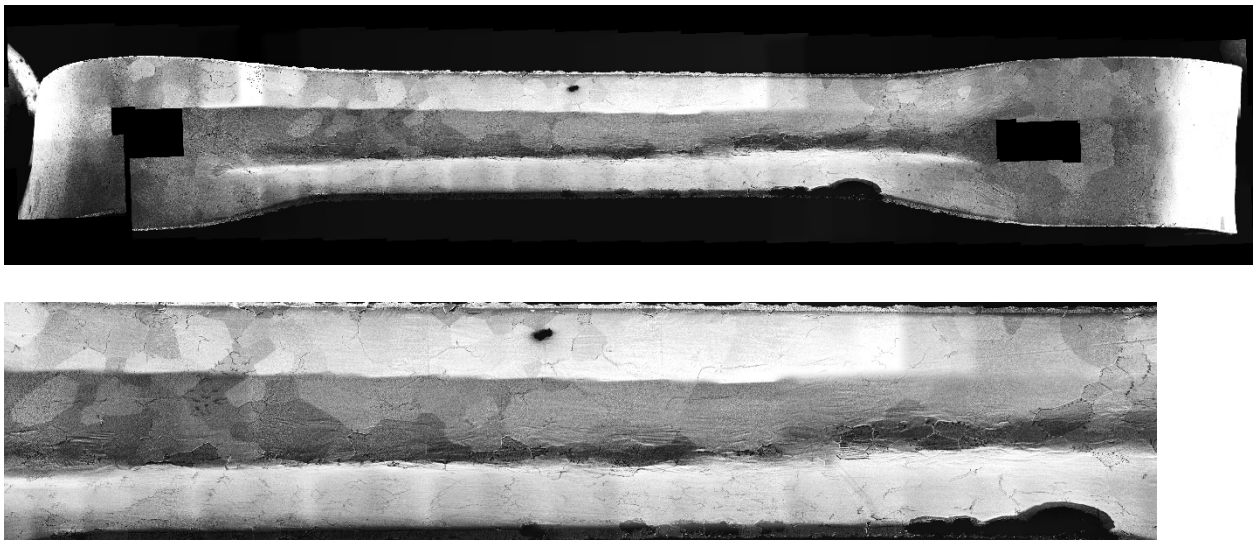

Filament 2-4

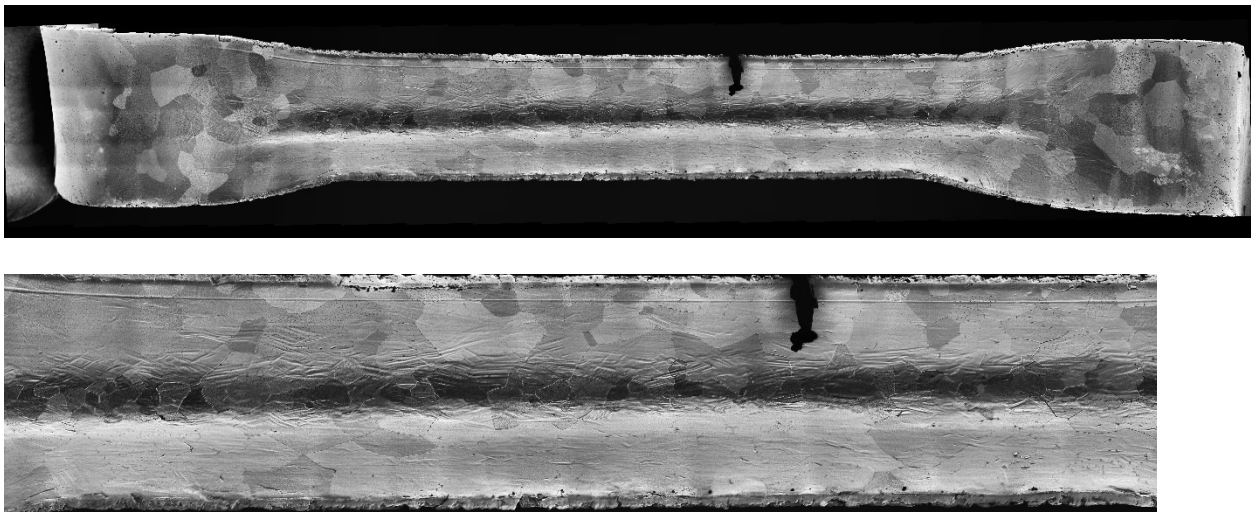

Filament 2-5

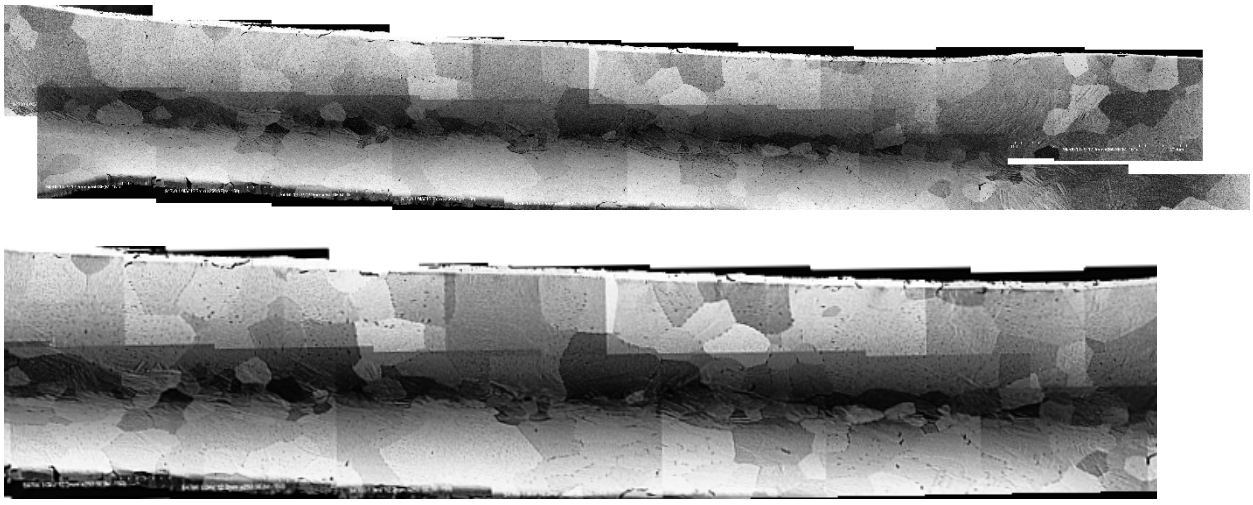

Filament 2-6

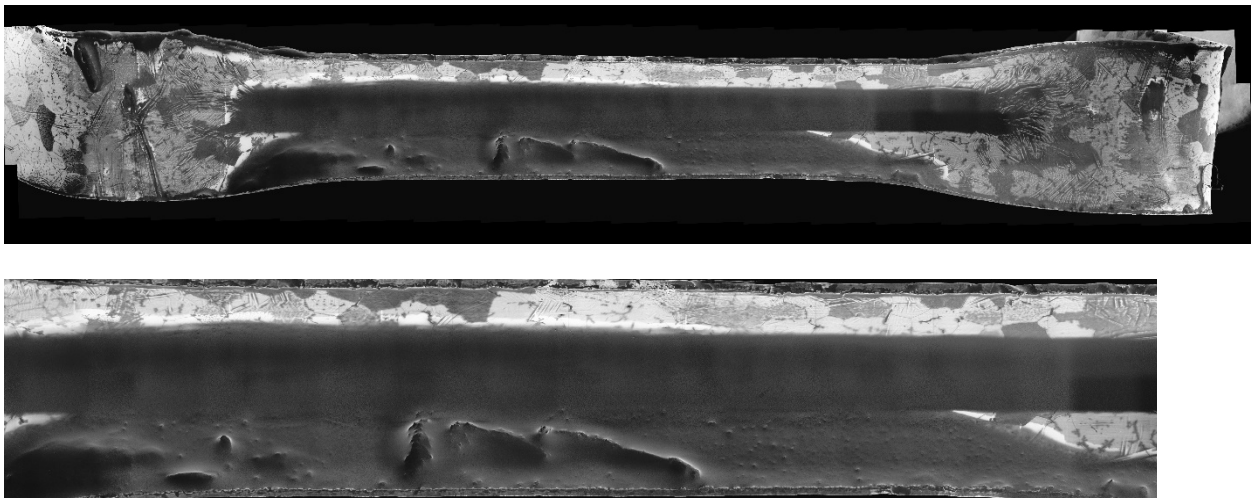

Filament 3-1

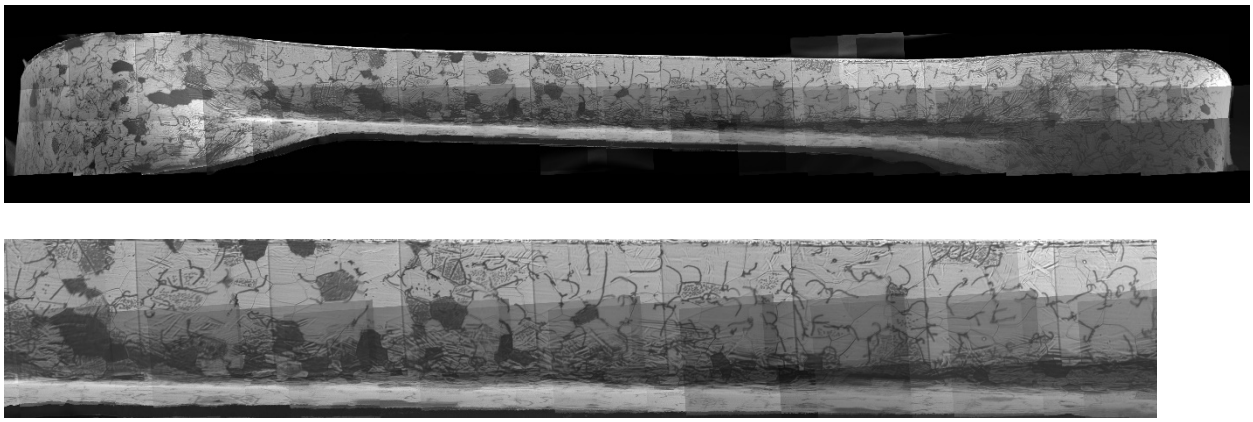

Filament 3-2

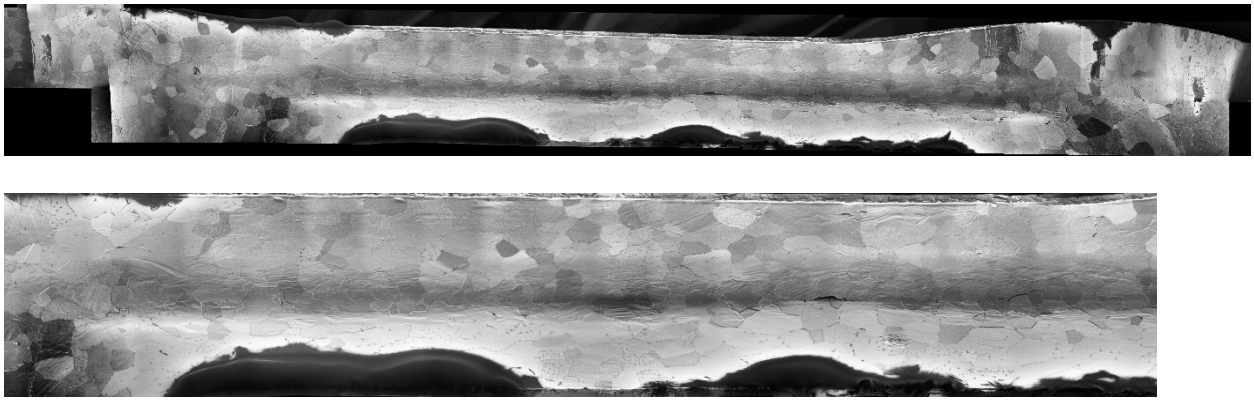

Filament 3-3

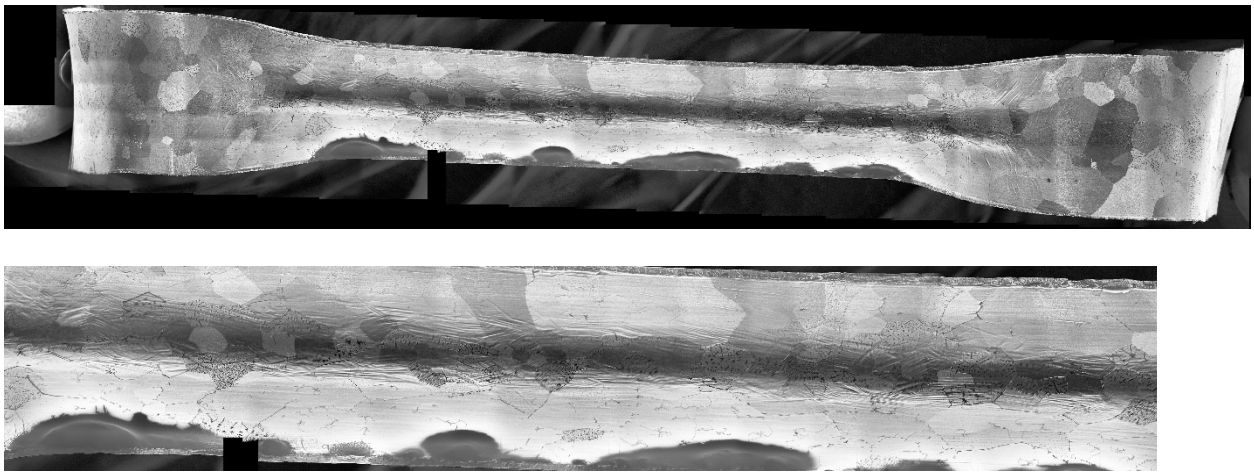

Filament 3-4

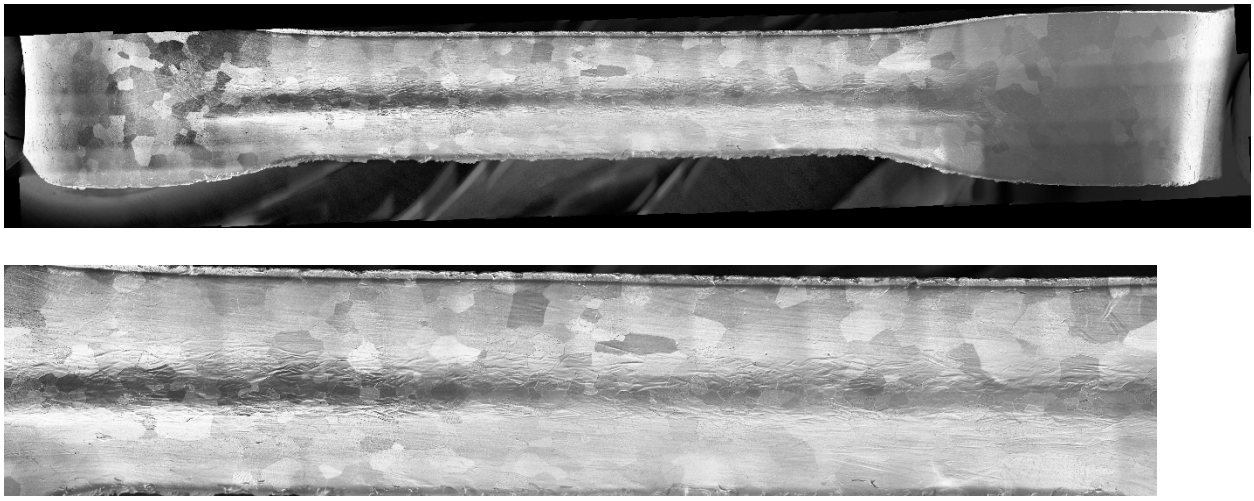

Filament 3-5

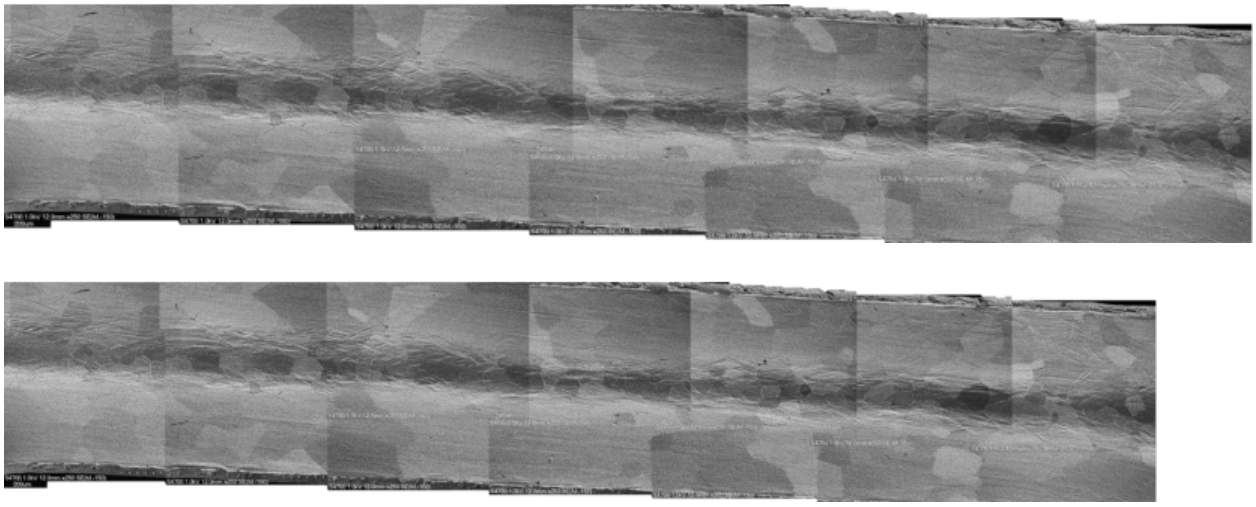

Filament 3-6

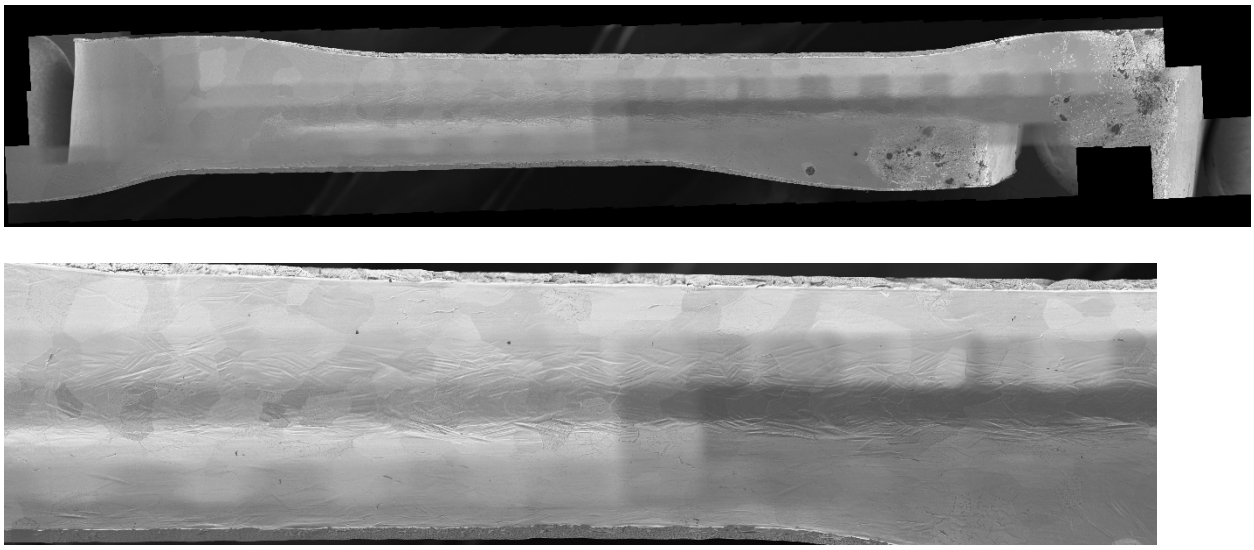

Filament 4-1

Filament 4-2

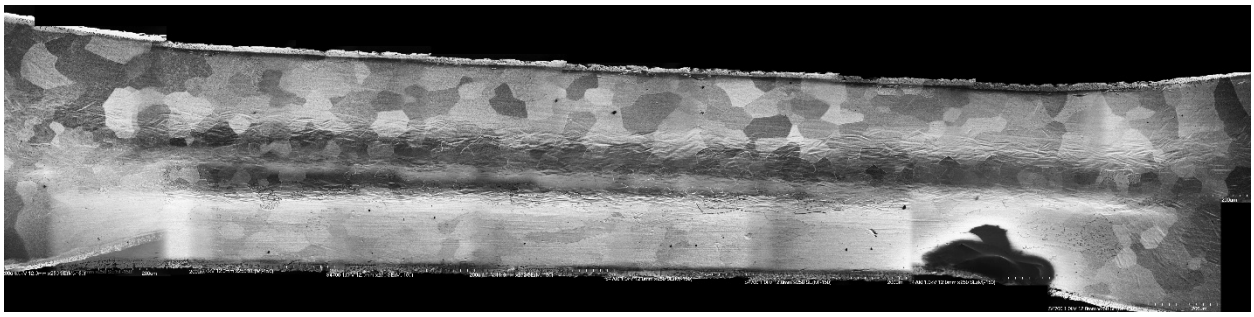

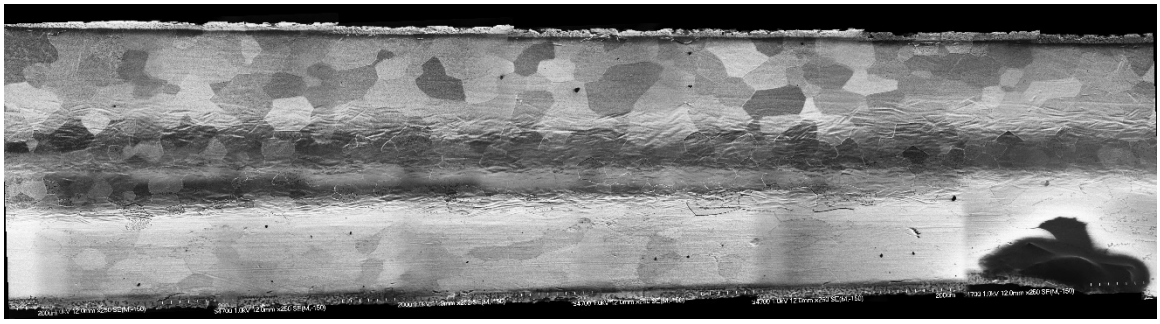

Filament 4-3

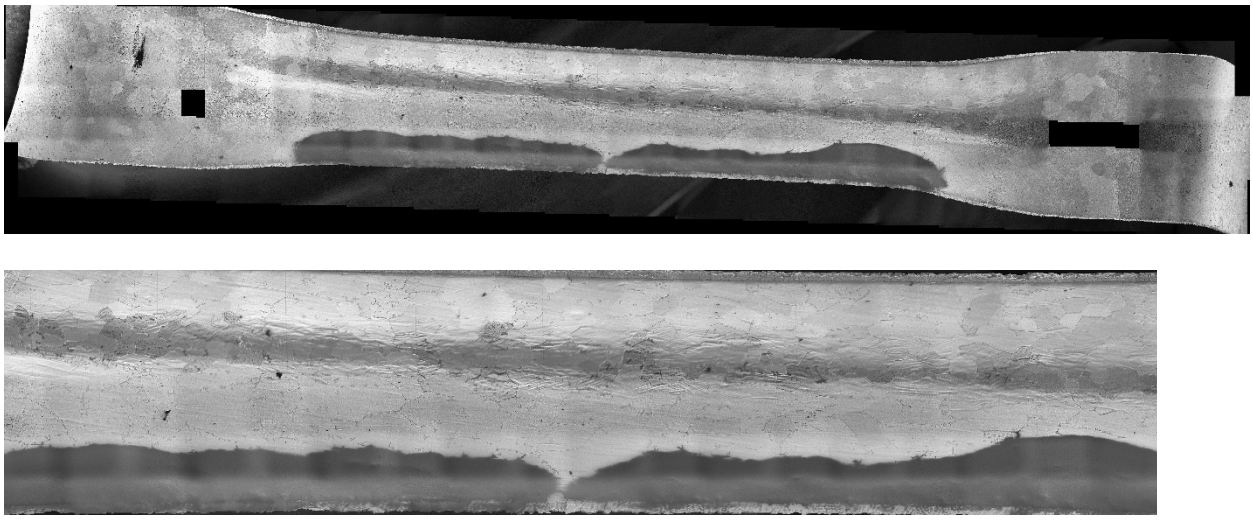

Filament 4-4

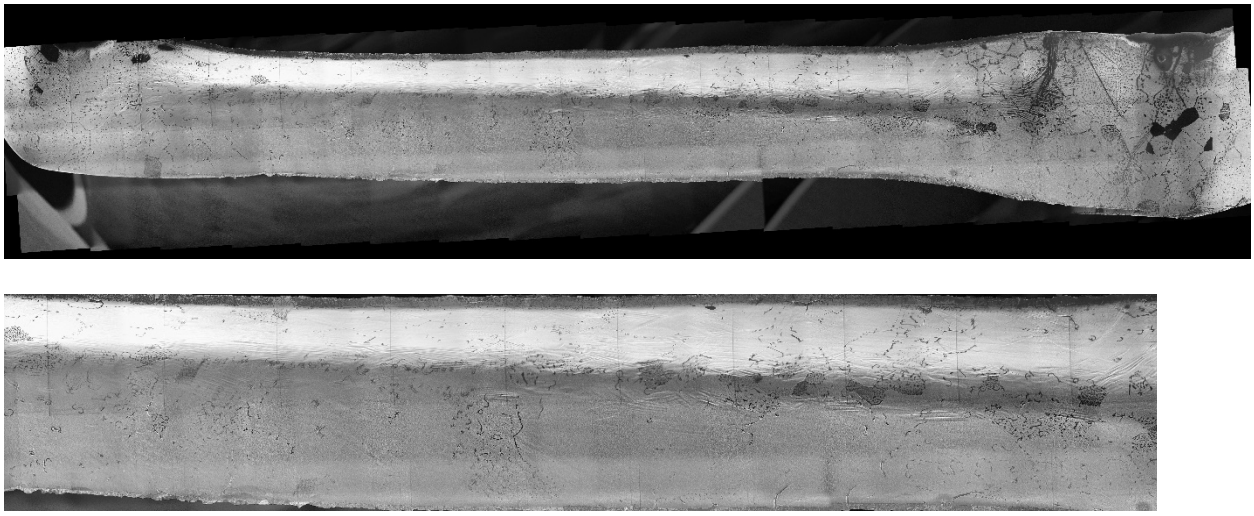

Filament 4-5

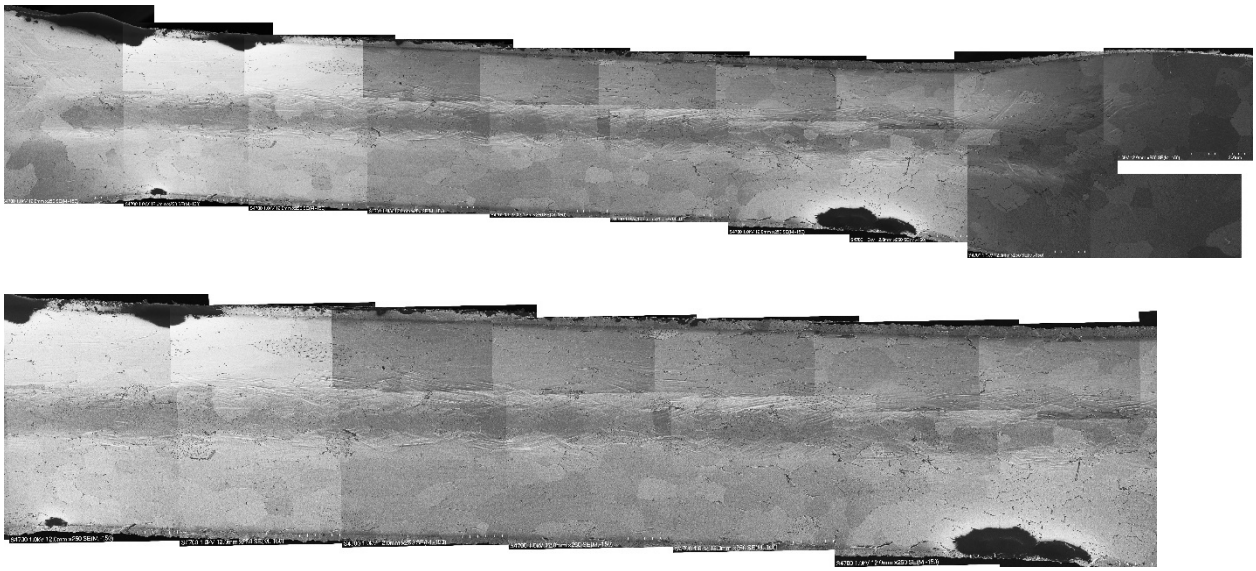

Filament 4-6

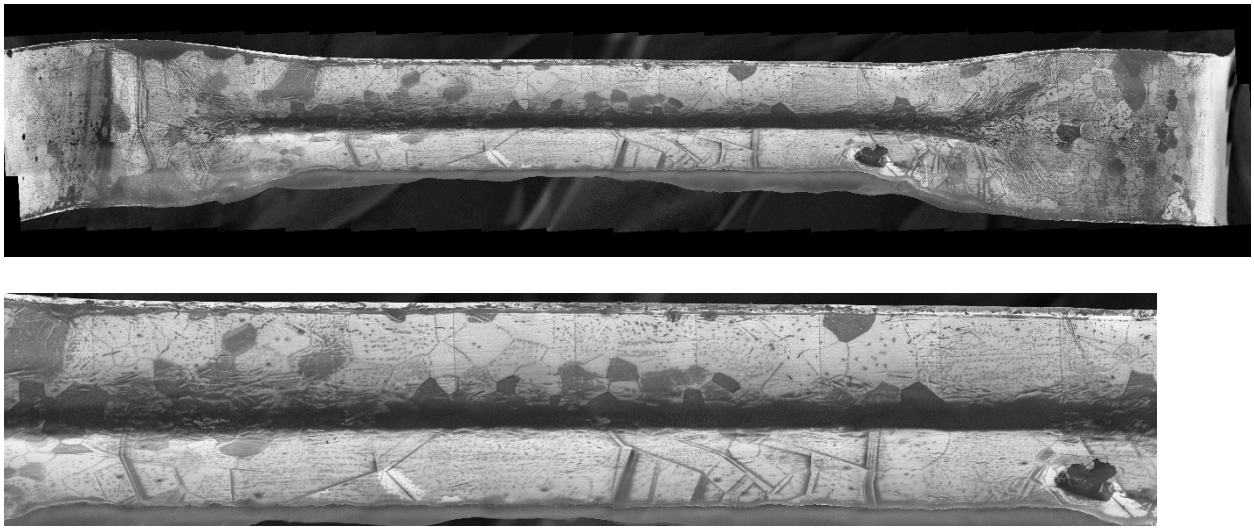

REPORT DOCUMENTATION PAGE

Form Approved
OMB No. 074-0188

1. REPORT DATE *(DD-MM-YYYY)*	**2. REPORT TYPE**	**3. DATES COVERED** *(From – To)*
01-03-2020	Master's Thesis	September 2018-March 2020

TITLE AND SUBTITLE

Analysis of the Correlation Between Re Filament Surface Features and TIMS Performance

5a. CONTRACT NUMBER

5b. GRANT NUMBER

5c. PROGRAM ELEMENT NUMBER

6. AUTHOR(S)

Mihal, Christopher J., Major, USA

5d. PROJECT NUMBER

5e. TASK NUMBER

5f. WORK UNIT NUMBER

7. PERFORMING ORGANIZATION NAMES(S) AND ADDRESS(S)
Air Force Institute of Technology
Graduate School of Engineering and Management (AFIT/ENY)
2950 Hobson Way, Building 640
WPAFB OH 45433-8865

8. PERFORMING ORGANIZATION REPORT NUMBER

AFIT-ENP-MS-20-M-107

9. SPONSORING/MONITORING AGENCY NAME(S) AND ADDRESS(ES)
Intentionally left blank

10. SPONSOR/MONITOR'S ACRONYM(S)

AFRL/RHIQ (example)

11. SPONSOR/MONITOR'S REPORT NUMBER(S)

12. DISTRIBUTION/AVAILABILITY STATEMENT
DISTRUBTION STATEMENT A. APPROVED FOR PUBLIC RELEASE; DISTRIBUTION UNLIMITED.

13. SUPPLEMENTARY NOTES
This material is declared a work of the U.S. Government and is not subject to copyright protection in the United States.

14. ABSTRACT

Thermal Ionization Mass Spectrometry (TIMS) is an invaluable tool in nuclear forensics as it enables isotopic assays of actinides to be measured, permitting analysis to include special nuclear material isotopic assays, nuclear reactor monitoring, and treaty verification. In one method of measurement for the TIMS system, samples are deposited in solution form on high-purity rhenium filaments. The filaments are heated to evaporate the solvent, and then further heated to cause sample ionization, permitting the sample to be transmitted through a magnetic field which separates ions based on mass to charge ratio into detectors for counting. Heavier ions will be deflected less by the magnetic field than lighter ions with equivalent charges.

Critical to the function of TIMS is the rhenium filaments themselves; any variability that suppresses ionization of the samples can lead to reduction in the number of ions detected. This research examines twenty-four filaments utilized in TIMS that have already been used for actinide analysis, with varying degrees of ionization efficiency. By examining the surface of the filaments using scanning electron microscopy (SEM), energy-dispersive x-ray spectroscopy (EDS), optical microscopy and electrical conductivity analysis, this research determined that there was correlation between filament shape and reported filament efficiency.

15. SUBJECT TERMS
Thermal ionization mass spectrometry, rhenium, scanning electron microscopy, nuclear forensics

16. SECURITY CLASSIFICATION OF:			**17. LIMITATION OF ABSTRACT**	**18. NUMBER OF PAGES**	**19a. NAME OF RESPONSIBLE PERSON**
a. REPORT	**b. ABSTRACT**	**c. THIS PAGE**			Dr. Abigail Bickley, AFIT/ENP
U	**U**	**U**	**UU**	175	**19b. TELEPHONE NUMBER** *(Include area code)* (937) 255-6565, ext 4555 (NOT DSN) (abigail.bickley@afit.edu)

Standard Form 298 (Rev. 8-98)
Prescribed by ANSI Std. Z39-18